

Tribology of MAX Phases and Their Composites

A Thesis

Submitted to the Faculty

of

Drexel University

By

Surojit Gupta

in partial fulfillment of the
requirements for the degree

of

Doctor of Philosophy

April 2006

© Copyright 2006.
Surojit Gupta, All Rights Reserved.

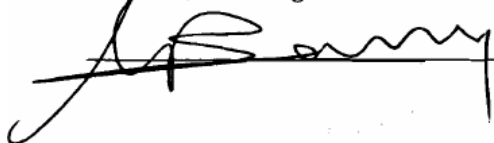
Thesis Approval Form

This thesis, entitled TRIBOLOGY OF MAX PHASES AND THEIR COMPOSITES

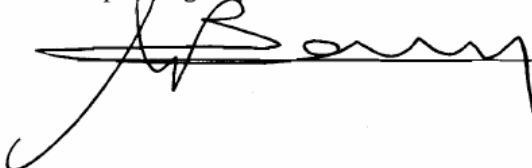
_____ and authored
by SUROJIT GUPTA, is hereby accepted and approved.

Signatures:

Chairman, Examining Committee:

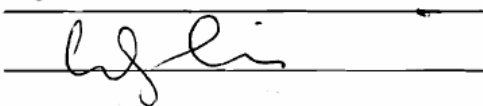


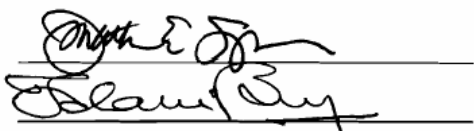
Supervising Professor:



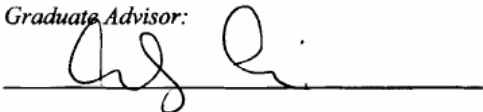
Committee Members:



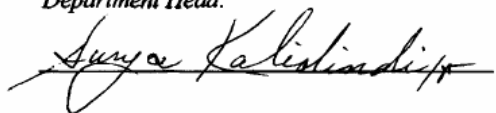




Graduate Advisor:



Department Head:



DEDICATIONS

This work is dedicated to my mother, my inspiration, who inspite of deadly disease “Thallasaemia” worked day and night to give us great education; my dad, who taught me principles, and hard work; my grandfather, who taught me Yoga; and my teacher, Prof. Barsoum, whose teachings during my study was inspirational, and consequently lead me from the darkness to light.....

ACKNOWLEDGEMENTS

During the course of this work, I received great help from numerous individuals. I would like to thank my committee members, Prof. J. Spanier, Dr. T. Palaniasamy, Prof. W. Shih, and Prof. Y. Gogotsi for kindly reviewing my work. Drs. D. Filimonov, and T. El-Raghy for numerous illuminating discussions, and help and suggestions during the entire duration of this work. Dr. Dellacorte for discussions. Eric Passman and Jim Piacek from Honeywell International for help during numerous experiments. Members of my group: Adrish, Liz, Aiguo, and Sandip for help. Dr. A. Murugaiah, and Dr. T. Zhen for help. Also Materials Science and Department as a whole for making this place a wonderful place to study. Judy and Crystal for help during numerous occasions. For financial support, I would like to thank O.N.R.

TABLE OF CONTENTS

LIST OF TABLES	viii
LIST OF FIGURES	ix
CHAPTER 1: INTRODUCTION	1
1.1 Introduction	1
1.2 Gas turbine engines	2
1.3 Air Bearings	3
1.4 Self Acting Foil Bearings	4
1.5 Current solid lubricant materials	11
1.6 The MAX Phases	18
1.7 Scope and Objective of Thesis	21
CHAPTER 2: ISOTHERMAL OXIDATION OF Ta ₂ AlC AND Ta ₂ AlC/Ag IN AIR	25
2.1 Introduction	25
2.2 Experimental Details	27
2.3 Results and Discussion	28
2.4 Conclusions	36
CHAPTER 3 - TRIBOLOGICAL BEHAVIOR OF SELECT MAX PHASES	37
3.1 Introduction	37
3.2 Experimental Details	37
3.3 Results	41
3.4 Discussion	56

3.5 Conclusions	61
CHAPTER 4 - SCREENING TESTS TO SELECT BEST COMPOSITIONS FOR FOIL BEARING RIG TESTS	62
4.1 Introduction	62
4.2 Experimental details	62
4.3 Synthesis of Ag-based composites	63
4.4 Mechanical properties, μ and WR of the laboratory samples	66
4.5 Conclusions	75
CHAPTER 5 - Ta₂AlC/Ag and Cr₂AlC/Ag: PROMISING MATERIALS FOR FOIL/GAS BEARING APPLICATIONS	76
5.1 Introduction	76
5.2 Experimental Details	76
5.3 Results	77
5.4 Discussion	97
5.5 Summary and Conclusions	99
CHAPTER 6 - STUDY OF TRIBOFILMS FORMED BETWEEN Ta₂AlC/Ag OR Cr₂AlC/Ag COMPOSITES AND Inc718 OR Al₂O₃	101
6.1 Introduction	101
6.2 Experimental Details	101
6.3 Results	102
6.4 Discussion	127
6.5 Conclusions	134
CHAPTER 7: TRIBOFILM ENGINEERING OF SELF-LUBRICATING Ta₂AlC/Ag–Inc718 or Cr₂AlC/Ag–Inc718 TRIBOCOUPLE	136
7.1 Introduction	136

7.2 Experimental Details	136
7.3 Results	137
7.4 Discussion	154
7.5 Comparison with literature	158
7.6 Conclusions	158
CHAPTER 8 – CLASSIFICATION OF TRIBOFILMS	160
8.1 Introduction	160
8.2 Classification of tribofilms	160
8.3 Philosophy of forming tribofilms	167
CHAPTER 9 - CONCLUSIONS AND FUTURE WORK	168
9.1 – Conclusions	168
9.2 Future work	171
LIST OF REFERENCES	173
APPENDIX A	179
APPENDIX B	181
VITA	183

LIST OF TABLES

1.	Characteristics of starting powders used in this work.	38
2.	Parameters used during the synthesis of MAX phases and MAX phase based composites.	40
3.	Summary of microstructure of MAX phases and its composites used during tribology study.	42
4.	Summary of WR and μ of different tribo-couples at 26 °C.	43
5.	Average of at least 3 EDS readings of a region homogenous at the micro scale. Each alphabet letter represents elemental ratios of “micro constituents”.	48
6.	Summary of μ and WR’s of different tribo-couples at high temperatures.	49
7.	Effect of interfacial film of different chemistries on μ	59
8.	Summary of WRs and μ of different tribocouples.	89
9A.	Average of at least 3 EDS readings of a region homogenous in micro scale, each alphabet letter represents elemental ratios of “micro constituents. The regions marked with grey color represent chemistry of analyzed tribofilms.	105
9B.	Average of at least 3 EDS readings of a region homogenous in micro scale, each alphabet letter represents elemental ratios of “micro constituents. The regions marked with grey color represent chemistry of analyzed tribofilms.	106
10.	Summary of WR’s and μ ’s when TaAg and CrAg composites were tested against Inc718 under different loading and temperature.	140
11.	Average of at least 3 EDS readings of a region homogenous in micro scale, each alphabet letter represents elemental ratios of “micro constituents”. The areas highlighted with grey areas denote chemistries of tribofilms.	154

LIST OF FIGURES

1.	Schematics showing different parts in a typical gas turbine engine [Ref. 4]	3
2.	Generation I foil bearing [Ref. 2].	4
3.	Generation II foil bearing [Ref. 2].	6
4.	Generation III foil bearing system [Ref. 2].	7
5.	Load capacity of Generation I, II, and III foil bearings [Ref. 2].	8
6.	Oil-Free engine for 30 kW microturbine [Ref. 2].	9
7.	Applications of Foil Bearing Technology [Ref. 19].	10
8.	Schematic illustration of layered structures of, (a) graphite, (b) MoS ₂ , (c) H ₃ BO ₃ , and (d) GaSe [Ref. 21].	12
9.	Oil free turbojet engine designed by Mohawk Innovative Technology, Inc., Albany, NY [Ref. 19].	18
10.	Unit cells of, a) 211, b) 312 and c) 413 phases. Unit cells are delineated by vertical arrow labeled c. The horizontal line is drawn through the centers of unit cells [Ref. 41].	19
11.	Normalized weight gains vs. time of Ta ₂ AlC samples isothermally oxidized in air at various temperatures.	28
12.	XRD diffraction patterns of the surface layers of Ta ₂ AlC samples after oxidation at 600 °C, 800 °C and 900 °C for 24 h.	29
13.	Cross- sectional BSE FESEM micrograph of a Ta ₂ AlC sample oxidized at 600 °C for 40 h.	30
14.	Cross-sectional BSE FESEM micrographs of Ta ₂ AlC samples oxidized at, a) 700 °C for 46 h, b) 800 °C for 32 h, and, c) 900 °C for 24 h.	32
15.	XRD of, (a) as synthesized Ta ₂ AlC/Ag composites, (b) oxidized at 600 °C for 96 h, and (c) oxidized at 700 °C for 10 h. Si was added as an internal standard.	33
16.	BSE FESEM micrographs of cross-section of TaAg11 composite sample after oxidation at 600 °C for 96h.	35

17. Plot of WR versus μ 's after dry sliding against, (a) Inc718, (b) alumina. A regression line has been fitted (solid line) to the data points and correlation coefficients, R, are shown.45
18. Change in μ as a function of sliding distance, when (a) Ti_3SiC_2 was tested against Inc718, and (b) Ta_2AlC was tested against Inc718. In both a and b, insets show evolution of μ 's during initial 10 m, and, (c) Plot of wear of Ti_3SiC_2 and Ta_2AlC as a function of sliding distance against Inc718. All the experiments were done at standard conditions at 26 °C.46
19. BSE FESEM micrographs of tribosurfaces after dry sliding of Ta_2AlC against Inc718 and at 26 °C: (a) Ta_2AlC surface, (b) Inc718 surface, and, (c) Al_2O_3 surface. In these micrographs, and all other shown in this thesis, letters are used to designate microconstituent.47
20. Change in μ as a function of sliding distance, when (a) Ti_3SiC_2 was tested against Inc718, (b) Ta_2AlC was tested against Inc718, and (c) Ta_2AlC was tested against Al_2O_3 . All experiments were done at 550 °C, and under standard conditions.51
21. (a) BSE FESEM micrograph showing tribofilms formed on Inc718 surface after 2 km dry sliding against Ta_2AlC . Inset shows the optical micrograph of the tribofilm (light blue) on Inc718 surface, (b) SE FESEM micrograph showing tribofilms formed on slightly gouged Inc718 surface after 2 km dry sliding testing against Ti_3SiC_2 . Inset shows the BSE FESEM micrograph of the tribofilms at higher magnification, (c) BSE FESEM micrograph showing tribofilms formed on Inc718 surface after 2 km dry sliding against Cr_2AlC . Inset shows the BSE FESEM micrograph of the tribofilm at *higher magnification*, and (d) SE FESEM micrograph showing tribofilms formed on Inc718 surface after 2 km dry sliding against Ti_2AlC . Inset shows the FESEM micrograph of the tribofilm. All the tribocouples were tested at 550 °C, and under standard conditions.52
22. FESEM micrographs showing tribofilms formed on Ta_2AlC surface after dry sliding for 2 km against Inc718 at 550 °C (a) SE image, & (b) BSE image of the region marked E at *higher magnification*. The experiment was done under standard testing condition.53
23. Laser profilometry on Inc718 surfaces after dry sliding for 2 km at 550 °C against, (a) Cr_2AlC , and, (b) Ta_2AlC . All the experiments were done under standard conditions.54
24. AFM analysis in scanning mode on 100 μm x 100 μm Ta_2AlC surface after testing against Inc718 for 2 km sliding at 550 °C, (a) isometric view, (b) top view, and (c) side view of the profile of the region marked by arrows on top view. All the experiments were done under standard conditions.54

25. (a) SE FESEM micrographs showing tribofilms formed on alumina surface after dry sliding for 2 km against Ta₂AlC at 550 °C, inset shows the region I at *higher magnification*, and (b) BSE FESEM micrograph of the Ta₂AlC surface. The experiment was done under standard testing condition.55
26. XRD patterns of the surfaces of Ta₂AlC counterparts after 2 km sliding: against Inc718 at (a) ambient temperature, and (b) 550 °C; and (c) against Al₂O₃ at 550 °C.56
27. BSE FESEM micrograph of the as-synthesized, (a) CrAg10, and (b) TaAg10 samples. Inset of the both figures show the microstructure at higher magnifications.64
28. BSE FESEM micrograph of synthesized CrAg11 samples.65
29. SE FESEM micrograph of the HIPed TaAg11P sample prepared from commercial powders. Inset shows the BSE FESEM micrograph at higher magnification.65
30. BSE FESEM micrograph of synthesized TaAg11 samples.66
31. (a) Plot of wear of Cr₂AlC-Ag composite samples as a function of sliding distance against Inc600, and, (b) influence of Ag additions on μ of Cr₂AlC sliding against Inc600. The tribocouples were tested under standard conditions.67
32. Stress - displacement curves during compression of Cr₂AlC-Ag sample at room temperature with, (a) 10 vol. %, and, (b) 20 vol. % Ag. In each figure, two set of data are plotted to show scatter during testing.68
33. Tribological properties of a TaAg10 sample against Inc600. Each data point represents – one heating/cooling down cycle. The test was done under standard conditions.69
34. Surface profilometry of Inc600 disc after wear tests against a TaAg10 sample for 24 km of dry sliding during thermal cycling.69
35. Tribological properties of the a CrAg10 sample tested against Inc600. Each data point represents a single heating and cooling down cycle. The tests were done under standard conditions.70
36. Tribological properties of the CrAg11 sample synthesized from commercial powders tested against Inc718. Each data point represents a heating up and cooling cycle.71

37. Laser profilometry of the Inc718 surfaces after, (a) first, (b) second, and (c) third heating and cooling cycles during testing against CrAg11 under standard conditions.72
38. Tribological properties of the TaAg11P sample synthesized from commercial powders.73
39. Laser profilometry of the Inc718 surfaces after, (a) first, (b) second, and (c) fourth heating and cooling cycles during testing against TaAg11P samples under standard conditions.73
40. Tribological properties of the dense TaAg11 composites tested against Inc718. .74
41. (a) Tensile strength of TaAg11 at 26 °C, (b) compressive strength of TaAg11 composites at 26 °C, (c) tensile strength of TaAg11 composites at 550 °C, and (d) tensile creep resistance of TaAg11 composites tested at 550 °C at 50 MPa for 1h.74
42. XRD spectra of synthesized, (a) TaAg11, and (b) CrAg11 samples.77
43. Variation in μ as a function of sliding distance at ambient temperature in different tribocouples; (a) Inc718 – TaAg11, (b) Al₂O₃ - TaAg11, (c) TiAlN coatings - TaAg11, (d) Inc718 - CrAg11, and (e) Al₂O₃ – CrAg11.81
44. Variation in μ as a function of sliding distance when Inc718 was tested at 350 °C against, (a) TaAg11, and, (b) CrAg11. All the tests were done under standard conditions.83
45. Variation in μ as a function of sliding distance during testing of different tribo-at 550 °C: (a) TaAg11 against Inc718 ($r_{\text{mean}} \sim 12$ mm), (b) TaAg11 against Inc718 ($r_{\text{mean}} \sim 18$ mm), (c) CrAg11 against Inc718 ($r_{\text{mean}} \sim 10$ mm), and (d) TaAg11 against Al₂O₃ ($r_{\text{mean}} \sim 19$ mm). All the tests were done under standard conditions.84
46. Variation in μ 's of, (a) TaAg11 - Inc718 tribocouple, and (b) CrAg11-Inc718 during heating and cooling in 26 to 500 °C temperature range. Black data points represent μ - during heating; red, μ – during cooling; blue – temperature during heating; green - temperature during cooling; black dotted line – stop and start; black solid line – donates end of one cycle, and start of next cycle.86
47. Laser profilometry on Inc718 surfaces after sliding against TaAg11 at, (a) room temperature, and (b) 550 °C.90
48. BSE FESEM micrograph showing tribofilms formed on alumina surface after sliding against TaAg11 at 550 °C for 2 km.90

49. Temperature dependencies of WRs of, (a) different ceramic-based materials, and (b) SA's, and, (c) of μ_{mean} . The WR of the phase encircled with a rectangular box is reported for each (a) and (b).
.....91
50. Laser profilometry of the Inc718 surfaces after, (a) one heating and cooling cycle, and (b) three heating and cooling cycles after testing against TaAg11 under standard conditions.92
51. Plot of wear as function of sliding distance of, (a) MAX/Ag composites against different substrates at ambient temperature, and (b) MAX/Ag composites against different substrates tested at 550 °C. All the tests were done under standard condition.94
52. WR as a function of sliding distance for, (a) TaAg11 against Inc718, and (b) CrAg11 against Inc718. Each data point represents, 1 heating and cooling cycle. All the tests were done at standard conditions.
Note: W_s – Wear rate of static partner (Ta₂AlC/Ag or Cr₂AlC/Ag), W_D – wear rate of dynamic partner (Inc718), and $W_T = W_D + W_s$95
53. (a) Ni-based SA top foil, and (b) TaAgR sample, after testing in foil bearing rig at Honeywell International Facility (Torrence, CA).96
54. (a) Ni-based SA top foil in testing rig, and (b) CrAg11 sample after testing in foil bearing rig at Honeywell International Facility (Torrence, CA).96
55. Figure 55: (a) SE FESEM micrograph of TaAg11 surface after testing against Inc718 at room temperature, (b) BSE FESEM micrograph of Inc718 surface after testing against TaAg11 and (c) BSE FESEM micrograph of alumina surface after testing against TaAg11. The experiment was done under standard conditions. 103
56. BSE FESEM micrograph of, (a) TaAg11 surface after testing against Inc718 at 550 °C for 2 km, and, (b) at a higher magnification. Experiment was done under standard condition.107
57. (a) SE micrograph of Inc718 surface after testing against TaAg11 for 2 km at 550 °C. Inset shows the optical micrograph of the tribofilm (blue color), (b) *higher magnification* of the region marked in a, and (c) BSE micrograph of the same region. Experiment was done under standard condition.108
58. (a) SE micrograph of CrAg11 surface after testing against Inc718 for 2 km at 550 °C, inset shows the optical picture of CrAg11 sample after rig testing, (b) *higher magnification* of the surface in one location in SE, inset shows the BSE image of the same region, and (c) BSE micrograph of another location. This experiment was done under standard conditions.
.....109

59. (a) SE micrograph of Inc718 surface after testing against CrAg11 for 2 km at 550 °C, (b) *higher magnification* of the region marked in a in SE, and (c) BSE micrograph of the same region. This experiment was done under standard conditions.110
60. BSE FESEM micrograph of, (a) Al₂O₃ surface after testing against TaAg11 at 550 °C for 2 km, (b) same as a but at higher magnification, and (c) TaAg11 surface after testing. The experiment was done under standard condition.111
61. FESEM micrograph of, (a) TaAg11 surface after testing against Inc718 during continuous thermal cycling from the 26 to 500 °C for 11 km in SE, and (b) SE micrograph at higher magnification, and (c) BSE micrograph of the same region. The test was done under standard conditions.113
62. (a) FESEM BSE micrograph of Inc718 surface after sliding against TaAg11 for 11 km after 3 heating and cooling cycles in the temperature range of 26 to 500 °C, and EDS mapping of the Inc718 surface for, (b) Ta, (c) Ni (d) Al, (e) Ag, and (f) Oxygen.114
63. FESEM micrograph of TaAgR surface, (a) after testing against Ni-based SA in *foil bearing rig* for 10,000 cycles in the 26 to 550 °C temperature range in SE, (b) at higher magnification in SE, and (c) BSE micrograph of the same region.116
64. FESEM micrograph of contact regions in Ni-based SA surface, (a) after testing against TaAgR in *foil bearing rig* for 10,000 cycles in the 26 to 550 °C temperature range in SE, (b) at higher magnification of region marked in a in SE, and (c) BSE micrograph of the same region.117
65. BSE FESEM micrograph of CrAg11 surface after testing against Ni-based SA in *foil bearing rig* for 3,000 cycles in the 26 to 550 °C temperature range. Inset shows the CrAg11 surface at higher magnification in SE.118
66. BSE FESEM micrograph of contact regions in Ni-based SA surface after testing against CrAg11 in *foil bearing rig* for 3,000 cycles in the 26 to 550 °C temperature range. Inset shows the Ni-based SA surface at higher magnification in BSE.119
67. SIMS images of positive ions Al, Ni, Ag and Ta distributions on the surface of TaAg11 (Region L in Fig. 55b) after 2 km sliding against Inc718 at 550 °C, plotted as function of spattering depth, (a) surface, (b) 0.5 μm, (c) 1 μm, and (d) color index to show qualitatively the distribution of ions as a function of depth.120
68. SIMS images of negative ions O, Ag and AlO distributions on the surface of Ta₂AlC/Ag (Region L in Fig. 55b) after 2 km sliding against Inc718 at 550 °C, plotted as function of number of spattering scans, (a) surface, (b) 0.5μm, (c) 1

- μm , and (d) color index to show qualitatively the distribution of ions as a function of depth.121
69. FESEM, (a) BSE micrograph, and (b) SE micrograph of cross-section of TaAg11 sample after 24 km thermocycling sliding against Inc600.123
70. XRD patterns on TaAg11 surfaces after sliding against Inc718, (a) at ambient temperature for 2km, (b) at 550 °C for 2km, (c) for 11 km thermal cycling, and, (d) after 2 km sliding against Al_2O_3 at 550 °C. All the tests were done under standard conditions.125
71. AFM analysis of $100 \times 100 \mu\text{m}^2$ TaAg11 surface after sliding against Inc718 at RT for 2 km, (a) isometric view, (b) top-View, and (c) linear profile of the section marked by line in b.125
72. AFM analysis of $100 \times 100 \mu\text{m}^2$ TaAg11 surface after sliding against Inc718 at 550 °C for 2 km, (a) isometric view, (b) top view, (c) linear profile of the region marked by line in b, (c) top view, and (e) linear profile of the region marked by line in d.126
73. Thermodynamic calculation of 2 moles of Ag and 1 mole of Al reacting with 10 moles of O_2 in 27 to 723 °C temperature range.127
74. XRD of as-synthesized, (a) TaAg11, and (b) TaAgR.137
75. Variation of μ as a function of sliding distance when TaAg11 and TaAgR samples were tested against Inc718 at 26 °C. Experiments were done under standard conditions.138
76. Variation of μ as a function of sliding distance when TaAgR and TaAg11 samples were tested against Inc718 at 550 °C under standard conditions.138
77. Dependence of μ on normal applied load when TaAgR and CrAg11 were tested against Inc718 at 26 °C, and TaAg11 was tested against Inc718 at 550 °C. All the tests were done under standard conditions.139
78. (a) Variations in μ 's as a function of sliding distance when TaAgR was tested against Inc718 at 18 N load for 1000 m at 26 °C, and subsequently tested at 3N load, and (b) variations in μ 's as a function of sliding distance when the same sample was tested against Inc718 at 3 N load for 2000 m at 26 °C after being cycled at conditions described in figure 78a, then at 550 °C for 2 km at 3 N load. Inset shows the schematic representation of the cycle, 1 is the starting point of the cycle, and 4 is the end point.140
79. (a) Variation in μ 's as a function of sliding distance when TaAgR-Inc718 tribocouple was tested at 550 °C, and 8N. On the same wear track, the tribocouple

- was subsequently tested at 26 °C, and 3 N. Inset shows the tribofilms formed on Inc718 surface. (b) Schematic representation of cycle. It is referred to as method-2 in the text.142
80. Variation in μ 's as a function of sliding distance when TaAgR was tested against, (a) Inc718 (sandblasted), and (b) Inc718 (FeCl₃ treated) under standard conditions at RT. Inset in a and b shows the tribofilms formed on Inc718 surface. (c) Variation in μ 's as a function of sliding distance when TaAgR was tested against Inc718 (sandblasted) by *method-3* described in text. Inset shows the digital picture of transfer film formed on Inc718 surface. (d) Variation in μ 's as a function of sliding distance when TaAgrig-Inc718 tribocouple was tested by by method 1, 2 and 3.143
81. WR of MAX/Ag as a function of normal loads when tested against Inc718 at 26 and 550 °C.145
82. Evolution of WR of TaAg composites tested under different normal loads, (a) at RT, and (b) at 550 °C.146
83. Evolution of WRs of TaAgR after testing under cyclic conditions - method 1 (Red), 2 (Blue) and 3 (Green).147
84. Laser profilometry of Inc718 surfaces after testing against TaAgR at 8 N load at 26 °C.148
85. Laser profilometry of Inc718 surfaces after testing by, (a) method 1, and (b) method 2.149
86. Laser profilometry of the Inc718 (surface treated) tested against TaAgR, (a) sandblasted and, (b) FeCl₃ treated under standard conditions at RT.150
87. BSE FESEM micrograph of, (a) Inc718 surface after tested against TaAgR, inset shows the higher magnification of the transfer film formed on Inc718 surface, and, (b) TaAgR surface. Inset shows the SE FESEM micrograph of the TaAgR surface. The experiment was done at RT and 8N load.151
88. SE FESEM micrograph of, (a) Inc718 (sandblasted) surface after tested against TaAgR, inset shows the BSE micrograph at higher magnification of the transfer film formed on Inc718 surface, and, (b) TaAgrig surface. Inset shows the SE FESEM micrograph of the TaAgR surface. The experiment was done under standard conditions.152
89. BSE FESEM backscattered micrograph of, (a) Inc718 surface, (b) higher magnification of Inc718 surface, and (c) TaAgR surface. The TaAgR-Inc718 tribocouple was tested by method 2.153

90. Schematic presentation of tribo-interactions of MAX phases against different tribo-partners: (a) and (a1) MAX-Inc718 tribocouples before and after dry sliding experiment at RT, (b) and (b2) MAX-Inc718 tribocouples before and after dry sliding experiment at 550 °C, (c) and (c1) MAX-alumina tribocouples before and after dry sliding experiment at RT, and (d) and (d1) MAX-alumina tribocouples before and after dry sliding experiment at 550 °C. All the tests were done under standard conditions.161
91. Schematic presentation of tribo-interaction of MAX/Ag against different tribo-partners: (a) and (a1) MAX/Ag-Inc718 tribocouples before and after dry sliding experiment at RT under standard conditions, (a2) MAX-Inc718 tribocouples after dry sliding experiment at RT and 8N load, (b) and (b2) MAX/Ag-Inc718 tribocouples before and after dry sliding experiment Inc718 at 550 °C under standard conditions, (b2) MAX-Inc718 tribocouples after dry sliding experiment at 550 °C and 8N load, (c) and (c1) MAX/Ag-alumina tribocouples before and after dry sliding experiment at RT under standard conditions, and, (d) and (d1) MAX/Ag-alumina tribocouples before and after dry sliding experiment at 550 °C under standard conditions.163
92. Schematic presentation showing different parameters required for forming LO's during tribochemical interaction of MAX/Ag composites against Inconel.166

ABSTRACT

Tribology of MAX Phases and Their Composites

Surojit Gupta

Michel. W. Barsoum, PhD

Currently there is a need for triboactive materials for high-speed turbomachinery applications in industry, which possess: (a) adequate mechanical strength, both at room and elevated temperatures and, (b) low wear rates, WRs, and low friction coefficients, μ , over a wide temperature range. If such materials can be found, the impact would be huge since they would result in increased efficiencies and reduced pollution. This is an outstanding problem that many in industry have been trying to solve for the past 20 years.

In this work, the tribological behavior of the MAX phases, and their composites with Ag have been studied for foil-bearing application. Initially, the tribological behavior - at 26 °C and 550 °C – of the following layered ternary carbides: Ti₂AlC, Cr₂AlC, Ta₂AlC, Ti₃SiC₂, Ti₂AlN, Ti₄AlN₃, Cr₂GeC, Cr₂GaC, Nb₂SnC and Ti₂SnC, tested against Ni-based superalloys (Inc718 and Inc600) and alumina, Al₂O₃, were studied. The high temperature tribo-properties were acceptable and in some cases, exceptional; but at room temperatures, the WRs were too high.

Since the addition of Ag is known to improve the tribological behavior at room temperature, it was used to liquid-phase sinter Ta₂AlC or Cr₂AlC composites. They were tested against a Ni-based superalloy (In718) and alumina. For foil-bearing applications, Ni-based superalloys are the best of choice for the foils. The tribocouples were tested for the most part using a force of 3N at 1 m/s at 25°C, 350 °C and 550 °C for at least 1 km of dry sliding. Over the entire temperature range, the WRs were $\leq 10^{-4}$ mm³/N-m and $\mu \leq$

0.5. Essentially similar results were obtained when the temperature was cycled between ambient and 550 °C. Finally, hot isostatically pressed Ta₂AlC/Ag and Cr₂AlC/Ag cylinders were machined and successfully tested in a foil-bearing rig test for 10,000 and 3,000 stop-start cycles, respectively.

When processed in the presence of liquid Ag, Al from the basal planes of the MAX phases reacts with the Ag to form Ag₂Al. This grain boundary phase prevents the formation of abrasive third bodies. As a result, the WRs of the MAX/Ag pins were reduced by ≈ 3 orders of magnitude as compared to the pure MAX phases. During testing at 550 °C and under thermal cycling conditions, the MAX/Ag lubricating tribooxides, comprised mainly of the elements of the Inc718 (Ni, Fe, Cr) and Al from the MAX phases, were formed. The presence of these layers is responsible for the low WRs of MAX/Ag composites ($\leq 10^{-5}$ mm³/N-m), and relatively high WR ($\sim 10^{-4}$ mm³/N-m) of the Inc718, accompanied by μ 's of ~ 0.5 . The films formed after rig testing were essentially the same as those obtained in the pin-on-disk experiments. As important, the lab-scale results obtained with the tribometer correlated well with pilot testing of the samples under stringent rig-testing conditions.

CHAPTER 1: INTRODUCTION AND LITRATURE REVIEW

1.1 Introduction

Global warming and the looming energy crisis are some of the more serious problems faced by humankind in the near future. The automobile and aerospace industries are adversely affected by this development. There is a frantic effort all over the world to increase the efficiency of existing systems, decrease consumption of ecotoxic oils and to reduce pollution [1-2]. Today's engine bearing systems - oil lubricated roller and ball bearings, are largely the same as those of three decades ago. Oil provides both a lubrication effect, as well as, critical cooling for key internal engine structures.

Without oil lubrication, the aviation industry would not have been able to get off the ground. The oil lubrication systems, however, have also imparted significant engineering limitations on aircraft propulsion engines, which have shaped current technology and is constraining major improvements in future engines. For instance, despite dedicated research over the past thirty years, turbine oil cannot operate over 180 °C, necessitating designs encumbered with oil coolers, filters and temperature sensors and seals. Performance improvements of current engines have predominantly been achieved through higher operating temperature alloys and cooling methods and the increased reliance on high bypass ratio fans. Following this technological development path, today's engine technology is quite mature and investments to further improve performance can yield only modest gains [2 - 5].

Dellacorte et al. [2] has summarized, “In order to dramatically improve aircraft propulsion systems, the technology used for the very foundation, the shaft support and lubrication system must be fundamentally changed.”

1.2 Gas turbine engines

Most modern passenger and military aircraft are powered by gas turbine engines, also known as jet engines [3,4]. Jet engines come in a variety of shapes and sizes but all jet engines have certain parts in common (Fig. 1). At the front of the engine, to the left, is the inlet. At the exit of the inlet is the compressor, which is colored cyan. The compressor is connected by a blue colored shaft to the turbine, (magenta). The compressor and the turbine are composed of many rows of small airfoil shaped blades. Some rows are connected to the inner shaft and rotate at high speed, while other rows remain stationary. The rows that spin are called rotors and the fixed rows are called stators. The combination of the shaft, compressor and turbine is called the turbomachinery. Between the compressor and the turbine flow path is the combustion section or burner, which is colored red. This is where the fuel and the air are mixed and burned. The hot exhaust then passes through the turbine and out the nozzle.

The nozzle performs two important tasks: It is shaped to accelerate the hot exhaust gas to produce thrust, and it sets the mass flow through the engine [4]. In current gas turbine engines, oil lubricated bearings (e.g. ball and roller) are used between the rotating and stationary parts of turbomachinery [2,5]. These bearings require an oil lubrication system that provides a thin film of oil between the moving parts of the bearing. Without oil, the metal-to-metal contact would cause the engine to grind to a halt [2].

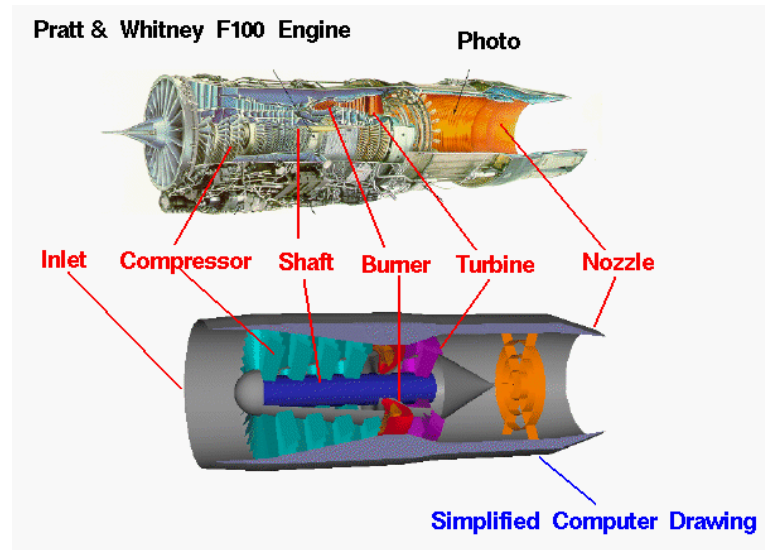


Figure 1: Schematics showing different parts in a typical gas turbine engine [Ref. 4].

1.3 Air Bearings

It is well established in the literature that under certain hydrodynamic conditions air, or gas, can be used as a lubricant [6,7]. The use of air as lubricant has certain advantages over oil lubrication. For example, it completely eliminates the use of ecotoxic oils; it can be used for cryogenic and high temperature applications since the viscosity of air does not change much with temperature [7]. There are different types of contact devices (i.e. air bearings) which use air as lubricant. They can be classified as self-acting, if the lubricant film exists because of relative tangential motion; squeeze, if due to relative normal motion, and externally pressurized, if due to an external source [7]. This work deals with self-acting foil bearings.

1.4 Self Acting Foil Bearings

In order to eliminate oil from turbomachinery, self-acting air bearings have great promise [2], and are the most studied bearing system for oil-free engines. Early foil

bearing designs were simple like those shown in Fig. 2; which will henceforth be referred to as generation I bearings [2]. They are composed of a shaft placed in an enclosure made with thin metal sheets of generally Ni-based superalloys, also called top foils. It is surrounded with a bump foil for elastic support. The entire system is then enclosed in a bearing sleeve. At rest, the top foil is preloaded against the shaft, with a stress ≤ 0.1 MPa. As the shaft rotates, viscous air is circumferentially dragged in between the top foil and shaft causing the top foil to separate or “lift-off” the shaft surface and press against its compliant support structure. The shaft surface can be visualized as a viscous pump and the top foil as a smooth impermeable membrane seal that traps the gas film creating a hydrodynamic pressure [2, 8].

From an engineering perspective, the load capacity of the bearing is defined as the maximum constant load that can be supported by a bearing operating at a constant speed and steady state conditions [8]. Air leakage at the edges of the bearing results in a reduction in maximum load capacities. For example, a shaft of 51 mm in diameter and a length of 38 mm can support a load < 150 N at 20000 rpm [2].

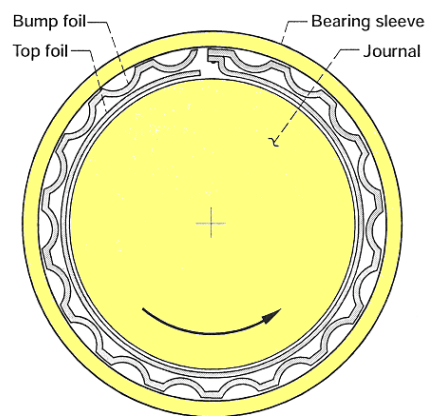


Figure 2 – Generation I foil bearing [Ref. 2].

In 1980's, with slight modifications, a new type of foil bearing was invented, henceforth referred to as generation II. In these bearings, the elastic stiffness of the support springs was tailored in one direction, typically axially, to accommodate for hydrodynamic effects such as edge leakage. Figure 3 shows this type of bearing which exhibits load capacities nearly double the more primitive Generation I designs. Based on these designs (e.g. generation I and II) foil bearings have been successfully commercialized in high speed rotating machines called air cycle machines or ACM's. An ACM is at the heart of the Environmental Control System (ECS) that is managing the cooling, heating and pressurization of aircraft. ACM's were first introduced in 1969 and used in the ECS systems of the DC-10's. With subtle modifications in design, this technology is currently being used in civilian planes (Airbus A-300, Boeing 767/757, etc.), fighter jets (F-15/F-14, F-16) and the B-2 stealth bomber [2, 9, 10].

Solid lubricant materials generally, Teflon (DuPont) or imide-based coatings that are only effective up to 250-370 °C are used for solid lubrication during initial start up between foils and shafts [2]. This technology has been successful in eliminating the oil-mist problem in cabins, since the entire system is oil free. However despite serious research efforts, these bearings were not able to support even small gas turbine engines. Moreover the temperature encountered in gas turbines is higher (> 500 °C), and there were no high temperature solid-state lubricants that can lubricate the foil/bearing contacts at that temperature [2].

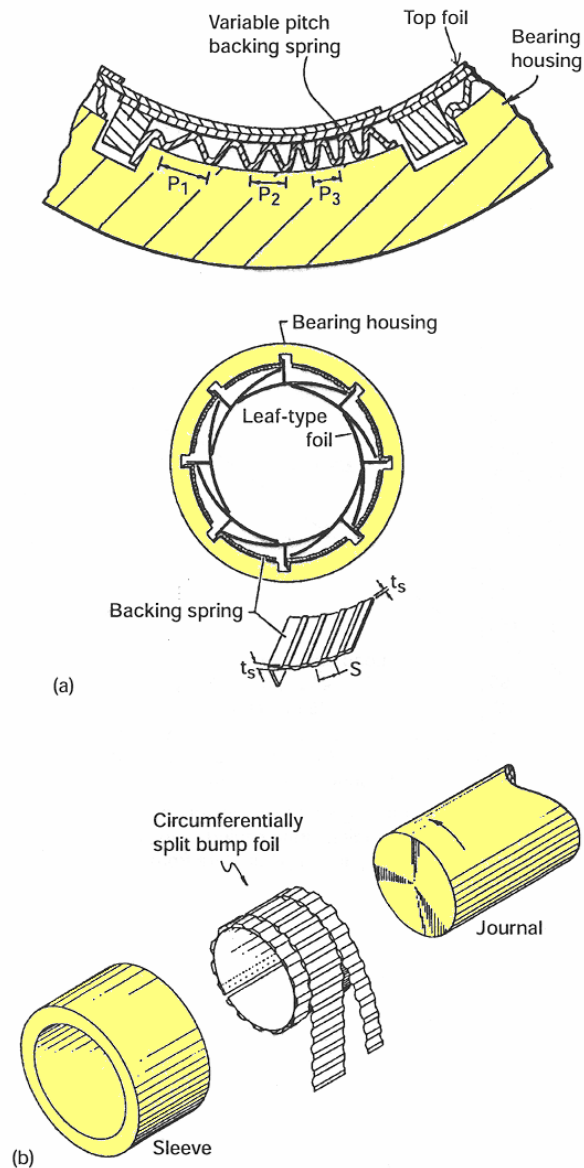


Figure 3 – Generation II foil bearing [Ref. 2].

The quest for oil free engines based on foil bearing technology got its impetus in the early 1990's with the invention of a third generation of foil bearings. The resulting Generation III bearings have more complex elastic spring support structures in which the stiffness is tailored in at least two directions, typically circumferential and axial (Fig. 4)

[2, 9, 11-14]. These Generation III bearings doubled the load capacity of Generation II bearings enabling re-consideration of more challenging gas turbine applications. A rule of thumb - ROT - model [2,8] was consequently developed to estimate load capacity.

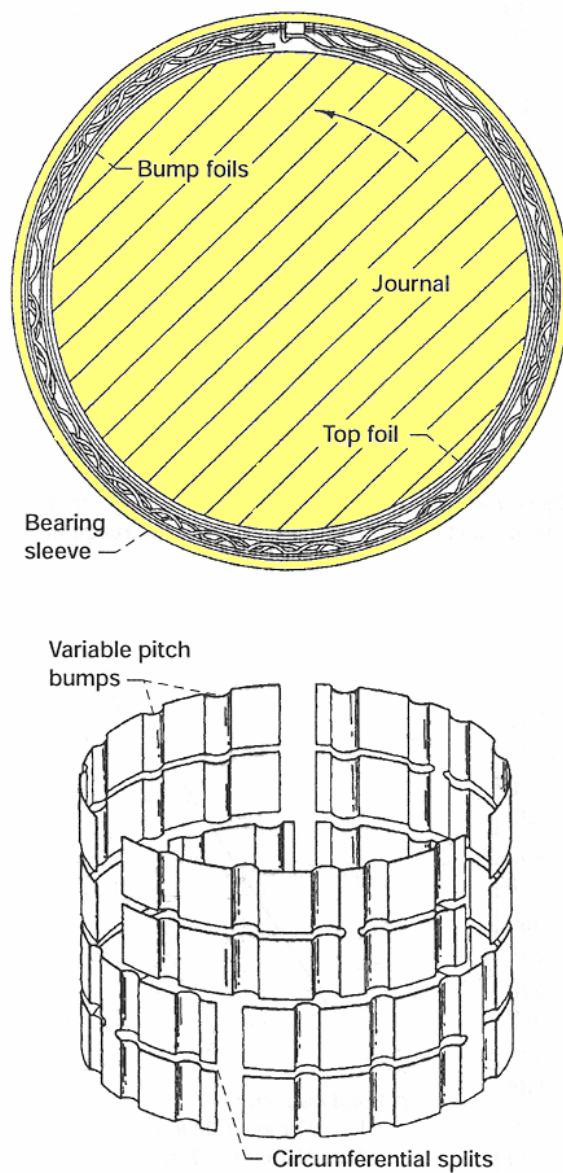


Figure 4 – Generation III foil bearing system [Ref. 2].

Rule-Of-Thumb (ROT) model relates bearing size, speed and design features with load capacity and is expressed in the following equation:

$$W = D_j(DL)(DN) \text{ -----(1.1)}$$

where:

W is load capacity in N (lbs)

D_j is the bearing load capacity coefficient, N/ (mm³.krpm) or (lbs/in³.krpm)

D is shaft diameter, mm (inches)

L is bearing length, mm (inches)

N is shaft speed in thousands of rpm (krpm)

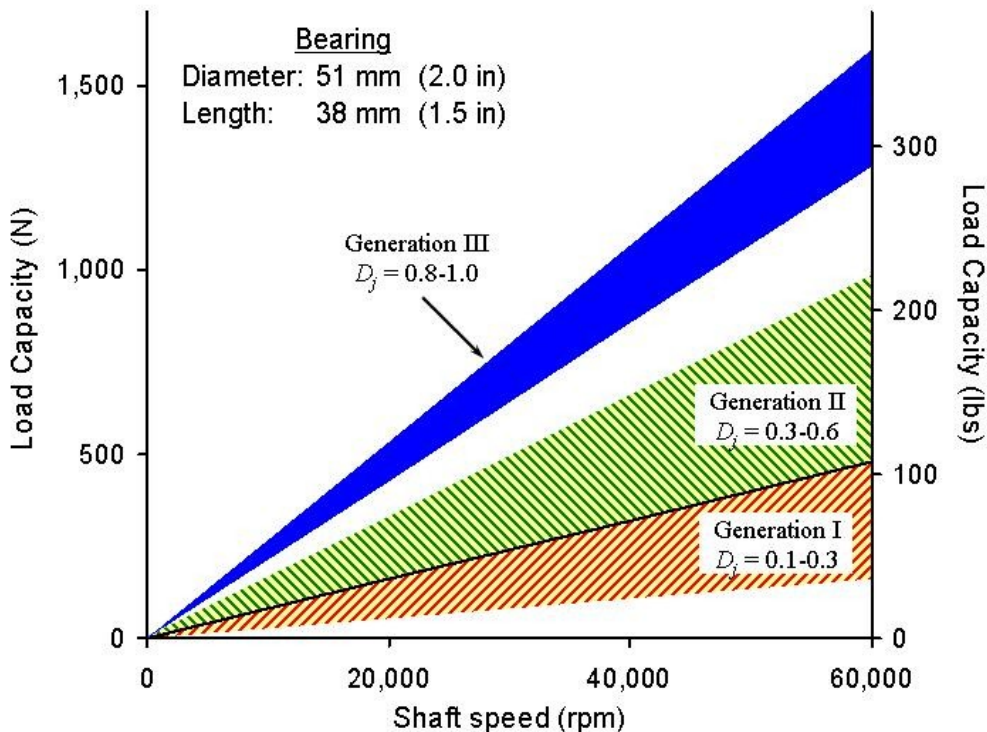


Figure 5 – Load capacity of Generation I, II, and III foil bearings [Ref. 2]

Figure 5 shows the comparison of load bearing capacity of different generation of bearings [2]. For a typical generation I foil bearings D_j is between 0.1 and 0.3 lbs/in³ .

krpm, for generation II, D_j , is between 0.3 and 0.6 lbs/in³.krpm, and for generation III, D_j , is between 0.8 and 1.0 , lbs/in³.krpm. Oil-free turbine based systems have made gradual inroads in power generation. Using type-III foil bearing designs, to date, over 2500 oil free generators (30-60 kW) or microturbine units are in operation and larger units - up to 400 kW - are being developed (Fig. 6). These products take advantage of the low cost, no maintenance and low friction benefits that foil bearings provide [2]. It has been estimated, that the integration of oil-free technologies in aircraft engines could result in a weight reduction of approximately 15%, a power density increase of 20%, a maintenance cost reduction of 50%. and a reduction of 8% in direct operating cost [2]. The advantages roughly translate into savings of \$400,000 per year on the operational costs of a Boeing 737 [15].

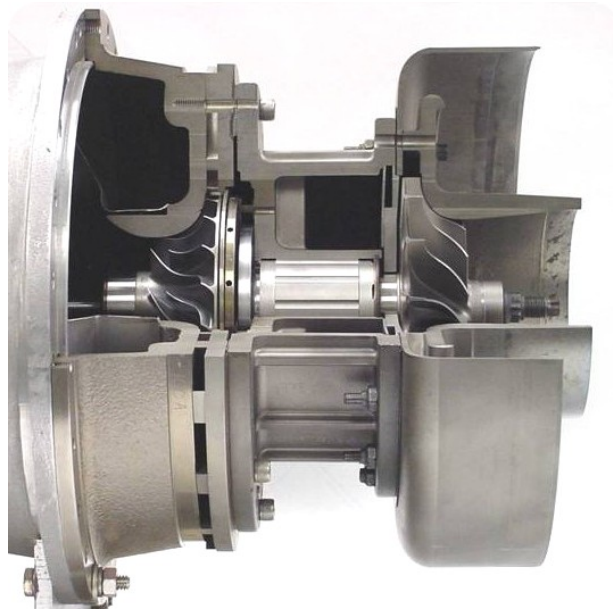


Figure 6 – Oil-Free engine for 30 kW microturbine [Ref. 2].

The technical hurdle that has to date prevented the integration of foil bearings in oil free gas turbine engines is the lack of a solid state material which can effectively lubricate the contacts between the foils and shaft during initial start and subsequent stop cycles. The absence of solid lubricant materials during start and stop conditions, decreases the load bearing capacity of generation III foil bearings from $D_j \sim 1$ to 0.3 , lbs/in³. krpm [8,16].

It is known that turbomachinery based systems have applications in power plants [17], automobiles [18], auxillary power units (APU's) [2], and numerous other applications [19]. Figure 7 presents the entire spectrum of potential foil bearing applications [19]. If high temperature lubricant materials can be found then, coupled with effective designs, and a case-by-case approach for each application, the entire outlook of our modern transport and other industries can be changed for the better.

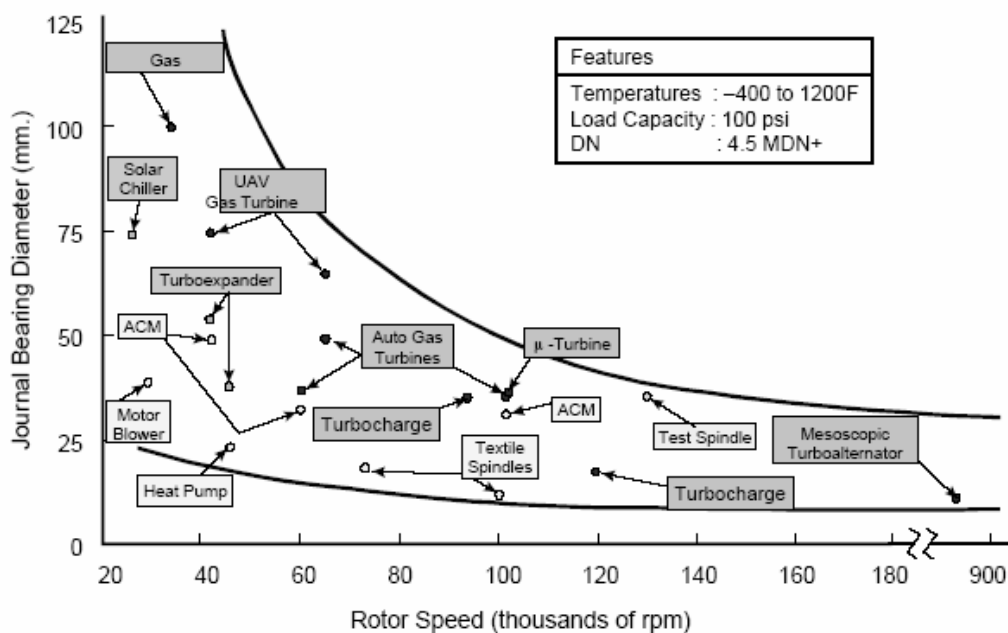


Figure 7: Applications of Foil Bearing Technology [Ref. 19]

1.5 Current solid lubricant materials

1.5.1 Lubrication in the room temperature to 300 °C temperature range

1.5.1.1 Layered Solids

Lamellar solids like graphite, MoS₂, H₃BO₃ and GaSe are excellent solid lubricants [20-22]. Graphite has a sheet – like crystal structure (Fig. 8a) in which all the C-atoms line in a plane and are bonded only weakly to the graphite sheets above and below. Each carbon atom in the plane joins to the three neighboring C atoms at a 120° angle and at a distance of 0.1415 nm. The distance between atomic layers is 0.335 nm and the layers are held together by weak Van der Waals forces [22]. Graphite is not intrinsically self lubricating; it requires the presence of water or hydrocarbons to develop solid lubricating properties [22].

Covalent bonds join sulphur and Mo atoms in the planar arrays of hexagonal S-Mo-S “sandwiches”, whereas weak Van der Waals interactions between adjacent S planes allow easy-shear parallel to the sliding direction (Fig. 8b). They are intrinsically self-lubricating and perform excellently at room temperature under vacuum and dry sliding conditions [21].

H₃BO₃ has a triclinic unit cell [21] in which boron, oxygen, and hydrogen atoms are arrayed to form extensive atomic layer parallel to the basal plane of the crystal. Because of the triclinic crystal structure (Fig. 8c), the c-axis is inclined to the basal plane at an angle of 101°. This inclination causes shifting of alternate layers along the c-axis. Bonding between the atoms lying on the same plane is of covalent/ionic & hydrogen type; the layers are 0.318 nm apart and held together only by weak Van der Waals forces. It is because of its structure it is self-lubricating.

Monochalcogenides, like GaSe, are also layered solids (Fig. 8 d). Their crystal structure is composed of double layers of Ga sandwiched between Se ions [21]. It is because of its layered structure that it is excellent solid lubricant. Tribooxidation/thermal oxidation of graphite and MoS₂ at 400 °C, and higher temperature is responsible for the loss of self-lubrication of these solids. H₃BO₃ decomposes at 170 °C, and loses its lubrication property [21].

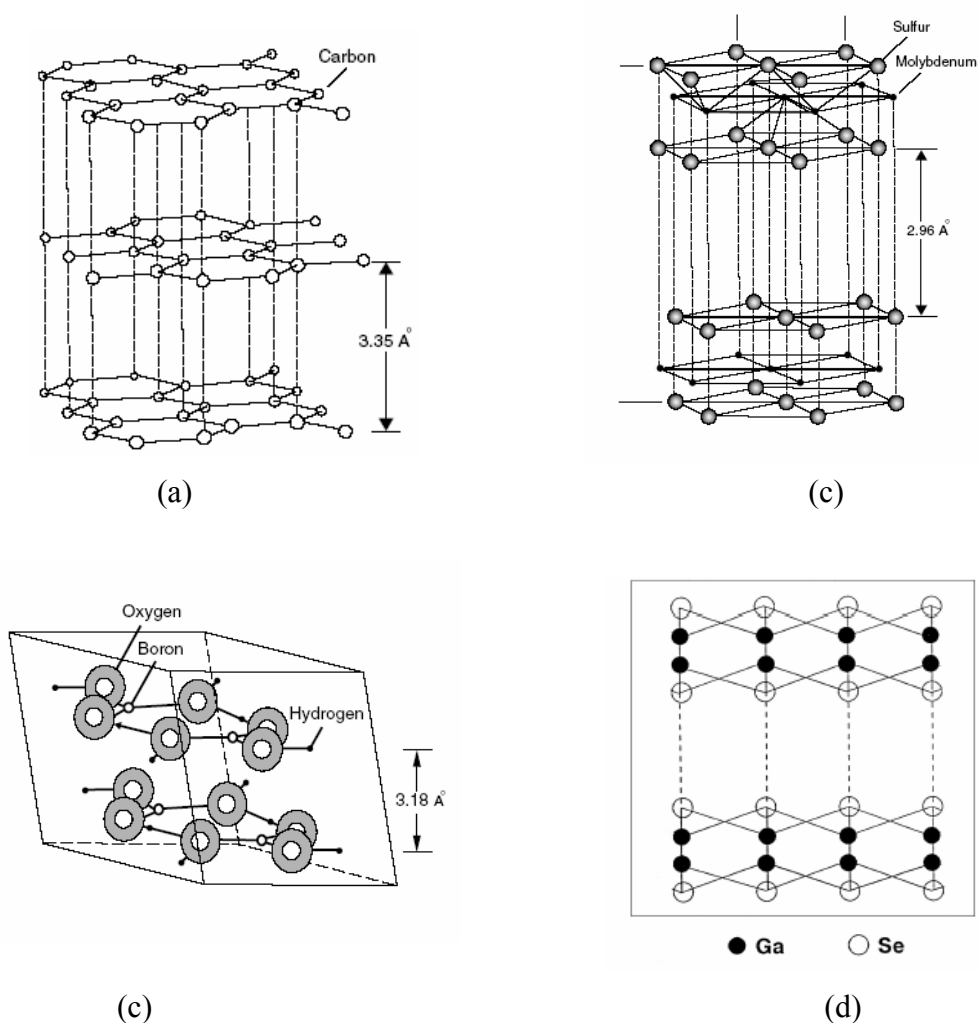


Figure 8: Schematic illustration of layered structures of, (a) graphite, (b) MoS₂, (c) H₃BO₃, and (d) GaSe [Ref. 21].

1.5.1.2 Binary Ceramics

Ceramics like alumina, Al_2O_3 , [23] and Si_3N_4 [24] display friction coefficients, μ , of 0.6-0.8 during dry sliding at room temperature. Al_2O_3 in the presence of moisture forms a lubricating hydroxide layer due to a tribo-chemical reaction. The μ 's are decreased to 0.3, and the wear rate, WR, is decreased by two orders of magnitude. Si_3N_4 similarly reacts with moisture to form an amorphous protective layer. The μ 's remains the same, but the WR is decreased by two orders of magnitude. Unfortunately hydroxides are not stable at higher temperatures, and cannot be used for lubrication [25].

1.5.2 Lubrication at 300 °C and higher temperatures

1.5.2.1 Lubricious oxides (LO's)

Self-mated tribocouples of Si_3N_4 – Si_3N_4 and SiC-SiC have μ 's > 0.6 at 400 °C, and higher temperature, and WRs $\sim 10^{-4}$ $\text{mm}^3/\text{N}\cdot\text{m}$. The addition of TiB_2 and TiC to SiC lowers the WRs in the 10^{-5} – 10^{-6} $\text{mm}^3/\text{N}\cdot\text{m}$ range. The μ 's are ≥ 0.4 at 400 °C and higher temperatures. Similarly, the addition of TiN to Si_3N_4 increased μ 's, as compared to Si_3N_4 tribocouples accompanied by reduction in WRs in the range of 10^{-5} – 10^{-6} $\text{mm}^3/\text{N}\cdot\text{m}$ [26]. The wear resistance of these solids have been attributed to the presence multi-component oxides, predominant amongst them an anion-poor rutile, TiO_{2-x} , in the transfer film [27-28]. Ordered vacancies can be generated in rutile to form crystallographic shear systems also known as $\text{Ti}_n\text{O}_{2n-1}$ ($4 \leq n \leq 32$) – Magnéli phases. $\text{V}_n\text{O}_{2n-1}$ or $(\text{W},\text{Mo})_n\text{O}_{2n-1}$ are other members of this class of oxides [27-28]. Dry sliding of $\text{Ti}_4\text{O}_7/\text{Ti}_5\text{O}_9$ against Al_2O_3 displayed excellent antiwear properties in the 25 – 800 °C temperature range but depending on sliding conditions and temperature, the μ 's varied from 0.2 to 0.8 [28]. The

inherent brittleness of ceramic-based solids however prevents their usage in high temperature turbomachinery.

Ni-based binary alloys display, $\mu \sim 0.7$ when dry sliding against alumina at RT. As the temperature is increased, $\mu \sim 0.3$ to 0.4 is observed because of the formation of lubricious oxides at 400 °C, and higher temperatures. Self-mated tribocouples of Ni display, $\mu \sim 0.9$. A decrease in μ is observed at 600 °C, and higher temperatures [29]. Oxides generated by tribooxidation (Lubricating oxides) are excellent at higher temperatures as triboactive materials. But the inherent brittleness of oxides at room temperature limits their use during cyclic conditions [21, 29].

1.5.2.2 Carbonaceous vapors

High temperature lubrication via the in situ deposition of lubricous carbon surface films from the pyrolytic decomposition of hydrocarbon feed gas has been used on a variety of self-mated ceramic and metal alloy sliding contacts [30]. $\mu \approx 0.08$ were recorded for all metal alloys tested — AISI M50, 52100, 440C and 1018 steel, as well as K-Monel (500) and Hastalloy C276. Friction coefficients < 0.1 were found for alumina, silicon nitride, tungsten carbide and zirconia. Only soda lime glass showed no friction coefficient reduction upon acetylene admixture. In general, acetylene admixture also significantly reduced wear volume, with wear reductions of multiple orders of magnitude in many instances [30]. It may not be commercially viable in oil-free engines since it will need additional designs to install the setup for hydrocarbon feed gas lubrication.

1.5.2.3 Soft non-layered solids

Non-layered solids like CaF_2 , BaF_2 , SrF_2 , LiF , $\text{CaF}_2\text{-BaF}_2$ and MgF_2 are excellent solid lubricants at 500 °C and higher temperatures [20-22]. Several oxides (Re_2O_7 , MoO_3 ,

PbO, B₂O₃, NiO etc), rhenates, molybdates, tungstates and sulfates (CaSO₄, BaSO₄ and SrSO₄) become soft and shearable at such temperatures [21, 29-31]. However these solids are hard and brittle at room temperature and thus cannot be used during cycling operations in engines.

1.5.2.4 Soft Metals

The noble metals Ag, Au are also excellent solid lubricants when used as thin films (< 500 nm) between hard sliding surfaces [22,32]. Ag, for example has a melting point of 961 °C, and is oxidation resistant in air. If, however, the Ag film is too thick it can deform excessively, and can cause gross plowing due to plastic deformation under load resulting in high μ 's [32].

1.5.3 Lubrication in the 26 °C to 550 °C temperature range

1.5.3.1 Composite Coatings/Materials

The current philosophy is to prepare solid lubricant composite coatings on Ni-based SA shafts or foils. The coating formulas include high and room temperature lubricants [33 – 37]. For example, Bhusan et. al. developed CdO-graphite based coatings, which were successfully tested in a foil bearing application up to a temperature of 427 °C [33]. C-based materials are not stable in air above 400 °C [20-22]. Thus these coatings cannot be used for oil free engines. Dellacorte et al. [34-37] did pioneering work on PS-300 coatings on Ni-based superalloy surfaces, which were amongst the first candidate materials for oil-free applications. Their coatings were designed to reach target temperatures of 500 °C, or even higher. The composition of PS300 is 60 wt.% Cr₂O₃, 20 wt.% NiCr, 10 wt.% Ag, and 10 wt.% of a CaF₂-BaF₂ eutectic [34]. However, owing to thermal expansion mismatches with the SA substrates, thermal cycling induced fatigue

resulted in coating failure. In order to alleviate these problems, PS-304 comprised of 20 wt. % Cr_2O_3 , 60 wt. % Ni-Cr binders, 10 wt. % Ag, and a 10 wt. % CaF_2 - BaF_2 eutectic was developed. Interestingly, and despite the dramatic changes in composition, the wear and friction performances of both coatings were comparable when tested against Inc750 (Ni-based superalloy). Both the PS300-Inc750, and PS304-Inc750 tribocouples showed similar WRs of $\sim 10^{-4}$ $\text{mm}^3/\text{N}\cdot\text{m}$, and $\mu's \leq 0.5$ in the 26 to 650 °C temperature range [35]. The latter was subsequently tested as a prospective material for partial-arc foil bearing applications – which is a type of foil bearings. The results were promising; the $\mu's$ were ≤ 0.4 in the 26 °C to 650 °C temperature range. The wear was higher than the designed limit at room temperature, but the situation ameliorated at higher temperatures. The tribosurfaces of PS304 and Ni-based superalloy surfaces were inspected. At 26 °C, the foil WR was high, and no mass transfer from PS-304 surface is observed. At 200 °C, significant Fe and O peaks were detected on the PS-304 surfaces, most possibly belonging to Fe_3O_4 . Essentially Ni-based SA surface was the source of Fe. However at 427 °C and higher temperatures, intrinsic lubricants like (Ag, Ca, Ba) were responsible for solid state lubrication property of PS304-Inc750 tribocouples [36].

The load bearing capacity of PS-304 coated shafts (as-ground and run-in surfaces) was studied against uncoated Ni-based foils, soft polymer film coated (polyimide), and Al_2O_3 -coated foils at 25 °C and 30000 rpm. Compared to the uncoated baseline, the soft polymer coated foils showed a 120 % increase in load bearing coefficient when operating against an as-ground journal surface, and 85 % against run-in journals surface. Alumina coated surfaces showed a 40% increase against as-ground journal but did not have any effect when the bearing was operated against run-in journal. This study suggests that the

addition of solid lubricant films provide added lubrication when the air film is marginal, indicating that as the load capacity is approached foil air bearings transition from hydrodynamic to mixed and boundary lubrications [16]. Blanchet et al. evaluated discs of PS-304 against rings of Inc750 by thrust washer tests at low contact pressures of 40 kPa and sliding speeds of 5.4 m/s; the coatings showed a total specific WR $\sim 10^{-4}$ mm³/N-m similar to earlier results but the μ 's were ~ 0.5 in all cases [37].

Honeywell International, NJ tried to use PS304 coatings as a potential candidate for foil bearing applications. But porosity of PS-304 coating severely limited their load bearing capacity. Moreover, these coatings need run-in time before the actual start of the rig tests, and it uses MoS₂ as a sacrificial lubricant during initial start up [38].

In a recent paper by Heshmat et. al. [19], Korolon™ coatings were developed by Mohawk Innovative Technology, Inc., Albany, NY. Korolon™ 1350A (Nickel-chrome based with solid lubricants) with an overcoat of Korolon™ 800 (WS₂ based solid lubricants) on foil bearings (total thickness of the coatings ~ 50 μ m) against chrome-coated shafts showed promising results, and was successfully tested for 70 stop and start cycles. The foil bearings and journals installed and operated successfully in 240 lb thrust turbo jet, oil free engine at 54,000 rpm for 14 h. It clearly demonstrates the feasibility of high temperature turbomachinery for gas turbine engine application (Fig. 9) [19]. S-based solid lubricant materials are not oxidation resistant at 500 °C for elongated time [19,21]. Thus in literature, there are currently no solid-state structural material which can be used in foil bearing applications for oil free engines.



Figure 9: Oil free turbojet engine designed by Mohawk Innovative Technology, Inc., Albany, NY [Ref. 19].

1.6 The MAX Phases

By now, it is fairly well established that the $M_{n+1}AX_n$ (MAX) phases are thermodynamically stable nanolaminates displaying unusual and sometimes unique properties [39-41]. These phases are so-called because they possess a $M_{n+1}AX_n$ chemistry, where n is 1, 2, or 3, M is an early transition metal element, A is an A-group element and X is C or N. MAX phases are layered hexagonal (space group $D_{6h}^4 - P6_3/mmc$) with two formula units per cell. Figures 10a, b, & c compare the unit cells of 211, 312 and 413 phases, respectively. In each case near close-packed layers of M layers are interleaved with layers of pure group A-element, with the X -atoms filling the octahedral sites between the former. The A-group elements are located at the center of trigonal prisms that are larger than octahedral sites and thus better able to accommodate the larger A-atoms. The M_6X octahedra are edge sharing. The main difference between

the structures shown in Fig. 10 is the number of M-layers separating the A – layers; in the 211's there are two, in the 312's three and in the 413's four [41].

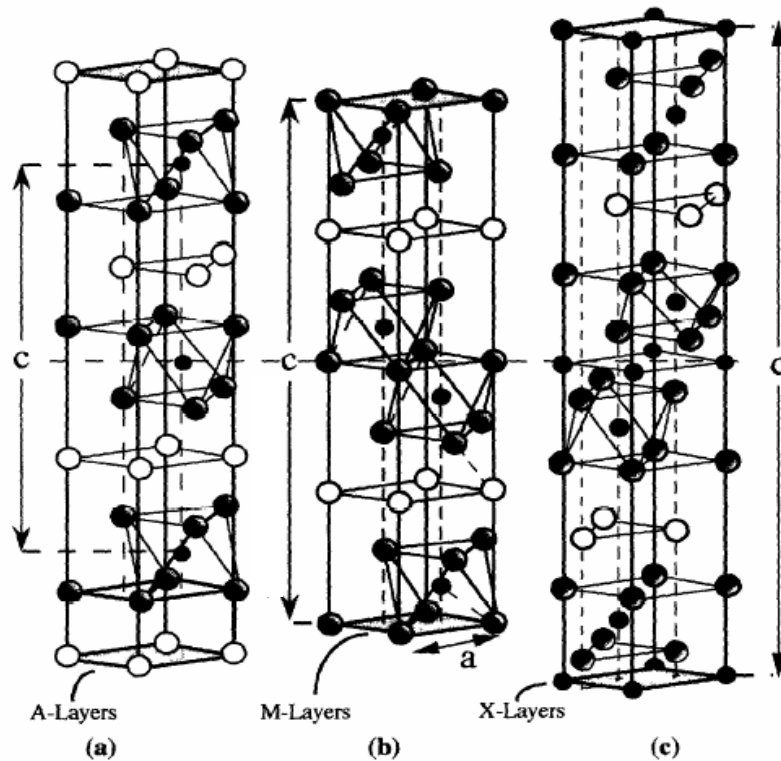


Figure 10: Unit cells of, a) 211, b) 312 and c) 413 phases. Unit cells are delineated by vertical arrow labeled c. The horizontal line is drawn through the centers of unit cells [Ref. 41].

They are highly damage tolerant, thermal shock resistant, readily machinable, and with Vickers hardness values of 2-5 GPa, are anomalously soft for transition metal carbides and nitrides [9-12]. Some of them display a ductile-brittle transition at temperatures > 1000 °C, while retaining decent mechanical properties at these elevated temperatures [42-46].

Moreover, their layered nature suggests they may have excellent promise as solid lubricant materials. Ti_3SiC_2 is the most studied member of these ternary carbides and nitrides. In the first paper on its properties its lubricious quality was noted [40]. This prompted Myhra et al. to study its tribological properties using an atomic force microscope with a Si_3N_4 tip [47]. They showed that indeed the friction coefficients, μ , of the basal planes were ultra-low (2 to 5×10^{-3}). The μ 's of other planes, however, were much higher. Later, El-Raghy et al. [48] studied the tribology of coarse-grained, CG, (25-50 μm) and fine-grained, FG, (4 μm) Ti_3SiC_2 samples, using a pin-on-disc method and a diamond belt abrasion test. The former tests were carried out using a 9.5-mm diameter 440C steel ball, a load of 5 N, with a sliding speed of 0.1 m/s. For both the microstructures, μ rose linearly from 0.15 to 0.4 and then to a steady state value of 0.8. The initial transition region was longer for CG than the FG samples. The average sliding wear rates were high, $1.34 \times 10^{-3} \text{ mm}^3/\text{N}\cdot\text{m}$ and $4.25 \times 10^{-3} \text{ mm}^3/\text{N}\cdot\text{m}$ for the fine- and coarse-grained samples, respectively.

Sun et al. [49] studied Ti_3SiC_2 with 7 wt. % TiC against 3.5 mm steel pins, under loads in the range of 7.7 to 14.7 N, for different numbers of cycles. The μ 's were not very sensitive to normal load, and displayed steady state values of 0.4-0.5. The average WR was $9.9 \times 10^{-5} \text{ mm}^3/\text{N}\cdot\text{m}$, and increased with load. Fine-grained, and partially compacted tribo-layers containing Fe were observed on the plane, along with ploughing on the steel pin. Zhang et al. [50] using an oscillating pin-on-disc method, with loads in the range of 1 to 10 N at a sliding speed of 13 mm/s to study the tribological properties between self-mated couples of Ti_3SiC_2 and between Ti_3SiC_2 and diamond. They reported μ 's of ~ 1 to 1.5 for the former and $\mu \sim 0.1$ for the latter. The low μ 's between Ti_3SiC_2 and diamond

were attributed to the formation of a tribo-film. Zhai et al. [51] evaluated Ti_3SiC_2 against low-carbon steel using a block-on-disc method at a sliding speed of 20 m/s and loads corresponding to stresses between 0.1 to 0.8 MPa. They also reported that the tribofilms formed were composed of TiO_2 , SiO_2 and Fe_2O_3 .

Souchet et al. [52] also studied the tribology of FG (4 μm) and CG (25-50 μm) samples against AISI 52100 steel and Si_3N_4 ball using a reciprocating type tribometer. They used balls with diameters varying between 4.5 and 12 mm and loads between 0.5 N to 6 N; the track length was 3.4 mm, and the sliding velocity was 1.35 mm/s. Two successive wear regimes were observed for the CG and FG samples against both counterparts. During regime I, sliding occurred between an oxycarbide tribofilm on the ball and the Ti_3SiC_2 surface, both the WRs and μ were low. Regime I was followed by Regime II; in the latter μ increased to 0.4-0.5 and wear became significant.

Sarkar et al. [53] studied the tribology of Ti_3SiC_2 against steel using a ball-on-disc method under fretting condition as the load was varied between 1 and 10 N. The μ 's they obtained varied between 0.5-0.55, and the WRs were between 11 and $37 \times 10^{-5} \text{ mm}^3/\text{N-m}$. Hongxiang et al. [54] tested Ti_3AlC_2 using a block-on-disc method against low carbon steel. At 60 m/s rotation speed and loads corresponding to stresses of $\approx 0.8 \text{ MPa}$, μ was ~ 0.1 and the specific WR was $\sim 2.5 \times 10^{-6} \text{ mm}^3/\text{N-m}$. It was argued that self-generating tribofilms, composed of Ti, O, Al and Fe were responsible for this behavior.

1.7 Scope and Objective of Thesis

In 2003, Drexel University and Honeywell Inc. were awarded a research and development contract from the US Department of the Navy to develop a high temperature tribocouple for applications in turbomachinery (Contract # N00421-03-C-0085 entitled

“MAX-Based High Temperature Foil Bearings”). The goal of the program was to develop novel tribocouple systems, with the following hard requirements:

- (a) Tribocouples with a $\mu < 0.5$, both dynamic and static in the temperature range of 26 to 550 °C.
- (b) $WR \sim 5 \text{ \AA/s}$, which translates in to specific wear rate, $WR \sim 10^{-6} \text{ mm}^3/\text{N-m}$, assuming a 36 mm^2 cross-sectional area, and 3 N load used for testing, which are the standard conditions used in this work. The above-mentioned, WR calculations were based for thin coatings. During the course of this work, it was discovered that $WRs < 10^{-4} \text{ mm}^3/\text{N-m}$, and $\mu \leq 0.5$ were adequate for successful rig tests of tribocouples made with bulk materials.
- (c) Enough tensile and compressive strength to withstand $> 50,000$ r.p.m. For example, a shaft made with a ceramics based material of density $\sim 10 \text{ g/c.c}$, diameter ~ 1.06 inch with a 0.25 inch hole, and rotating at 50 krpm should have a tensile strength of at least 80 MPa. Note, a safety factor of 2 has been taken into account in the calculations [38].

The main objective of this thesis is to present the research and development of a new generation of triboactive materials using MAX phases as starting materials, which can function in the entire temperature range of 26 to 550 °C. It has been divided into chapters to explain the step-wise development and understanding of the tribological performance of the MAX phases and their composites against Ni-based superalloys. Since preliminary studies showed that Ta_2AlC with Ag was one of the most promising materials for the foil bearing applications [55,56]. Chapter 2 is devoted to the synthesis and oxidation behavior of Ta_2AlC and $\text{Ta}_2\text{AlC}/\text{Ag}$ in air. Chapter 3 summarizes the

tribological behavior of pure MAX phases against Ni-based SA's and alumina in 26 to 550 °C temperature range. Chapter 4 explains the influence of Ag as an additive on the tribological behavior of the MAX phases, and the scale-up from lab samples to industrial/rig testing samples. Chapter 5 is a case study of Ta₂AlC/Ag and Cr₂AlC/Ag as prospective materials for foil bearing applications. In this chapter, experimental validation of the lab scale results in a rig test is reported. Chapter 6 is devoted to the understanding of the tribological behavior of the Ta₂AlC/Ag and Cr₂AlC/Ag composites against Inc718 and Al₂O₃. Chapter 7 will explain, by using the understanding in Ch. 6 – different methods to further enhance the tribological performance of Ta₂AlC/Ag. Chapter 8 summarizes the understanding developed in Chs. 2–7 to classify transfer films in different categories. Ch. 9 summarizes the conclusions.

In Appendix–A calculations needed for calculation of wear of Inc718 have been summarized. Appendix–B summarizes the tribochemistries of the tribofilms formed.

1.8 Some definitions

In this thesis we use a few terms that need definition.

1.8.1 Lubricating oxide (LO)

Any tribological oxide formed either by tribo- or thermal oxidation displaying a $\mu < 0.5$.

1.8.2 Lubricating mixture (LM)

Combination of two or more constituents at the nanoscale which show a $\mu < 0.5$.

1.8.3 Lubricating mixture (LM)

Combination of two or more phase-separated constituents, which show a $\mu < 0.5$ and display higher WRs than a LM of similar composition.

1.8.4 Specific Wear Rate (WRs)

During the course of this work most wear results have been reported as:

Specific Wear Rate, WR,

$$WR = \frac{\text{volume of material worn away}}{\text{Applied load x sliding distance}} \text{-----}(1.1)$$

The units are mm³/N-m. In this work a, WR > 10⁻⁴ mm³/N-m is considered high; a WR ≈ 10⁻⁴ mm³/N-m is tolerable and a WR ~ 10⁻⁵ to 10⁻⁶ mm³/N-m is considered excellent. WRs ~ 10⁻⁷ to 10⁻⁸ mm³/N-m are typical during mixed/boundary lubrication [44]. The latter have not been encountered in this work.

CHAPTER 2: ISOTHERMAL OXIDATION OF Ta₂AlC AND Ta₂AlC/Ag IN AIR

2.1 Introduction

The ternary carbide Ta₂AlC belongs to a larger class of layered solids with the general formula M_{n+1}AX_n, where M is an early transition metal, A an A-group (mostly IIIA and IVA) element, and X is C and/or N. These so-called MAX phases, with hexagonal symmetry, are built up from M carbide or nitride layers interleaved with pure A element layers. Some of them possess an unusual and sometimes a unique set of properties. With Vickers hardness values in the 3-5 GPa range, they are relatively soft, elastically stiff, electrically and thermally conductive and readily machinable [41].

These compounds decompose incongruently in inert atmospheres into MX-based compounds and an A-rich liquid. Typically, their oxidation results in the formation of A and M-based oxides [57-60]. In certain conditions, ternary oxides have been formed [57,60]. The oxidation can also be accompanied by phase separation in the oxide layers resulting in the formation of separate, alternating M- and A- rich oxide layers [57,59,60].

Recently Ta₂AlC, among some other MAX phases, has been identified as a possible material for high temperature (550 °C) tribological applications [55,56]. Before this material can be used in such applications, however, it is imperative to study its oxidation behavior in air.

Since this is the first report on the oxidation of Ta₂AlC, there are no studies with which to compare our results. It is thus useful to review the behavior of a number of related elements and compounds such as the Ta, Ta₂C, TaC and the isostructural Nb₂AlC.

Dense bulk TaC and Ta₂C samples oxidized in an oxygen atmosphere in the 700 to 850 °C temperature range oxidized notably at temperatures above 700 °C. The Ta₂O₅ oxide layers formed were not protective, resulting in interfacial reaction rate limited oxidation kinetic, presumably at the oxide/substrate interface [62].

The closest isomorphous analogue to Ta₂AlC, however, is Nb₂AlC. The isothermal oxidation of Nb₂AlC in air in a 650-800 °C temperature range was reported by Salama et al. [61]. The oxidation kinetics at 650 °C were subparabolic; at 700 °C and higher temperatures, the oxidation kinetics were linear, with rates comparable to those for the oxidation of pure Nb [61]. At 700 °C and short oxidation times, the oxidation products were Nb₂O₅ and Al₂O₃. At longer times and/or temperatures greater than 700 °C, the products were Nb₂O₅ and NbAlO₄. The layers that formed at 700 °C and higher, however, were not protective, resulting in linear oxidation kinetics.

Thermodynamically, α - and β -orthorhombic tantalum pentoxides (Ta₂O₅) are the only stable phases at elevated temperatures in air [63,64]. The low temperature β -form converts to higher temperature α phase at ~1360 °C. Consequently, β -Ta₂O₅ is the only high temperature oxidation product obtained when Ta metal is oxidized at 800 °C [65,66]. At temperatures below 500 °C, metastable tantalum suboxide phases, TaO_x, such as Ta₄O or Ta₂O form instead, or along with Ta₂O₅ [63,65,67].

The purpose of this chapter is to report on the oxidation behavior of Ta₂AlC and Ta₂AlC/Ag in the 600 to 900 °C temperature range in air. This paper is a continuation of our quest to understand the oxidation kinetics of the more than 50 ternary MAX phases known to exist [57, 59-61, 69,70].

2.2 Experimental Details

The Ta₂AlC sample was prepared by reactive hot isostatic pressing (HIPing) of Ta, Al and graphite powders (99.9%, Alfa Aesar, Ward Hill, MA). The powders were mixed in stoichiometric proportions by ball milling in a plastic container with alumina balls for 1 hour. The mixed powders were sealed in borosilicate glass tube under a mechanical vacuum, followed by heating at 650 °C for 10 h. The collapsed tubes with pre-reacted powders were HIPed at 100 MPa and 1600 °C for 8 h in Ar. After furnace cooling, the encapsulating glass was mechanically removed and rectangular specimens $\approx 2 \times 2 \times 8 \text{ mm}^3$ were cut using a diamond blade. All sides were polished with 1200 grit SiC paper prior to the oxidation runs.

The details of the powders used for the synthesis of Ta₂AlC-based composites can be found in Table 1 in Ch.3. The samples were synthesized by HIPing, 20 vol.% of Ag with Ta₂AlC powders at 1100 °C for 20 minutes under ~ 70 MPa pressure. The composites were $> 98\%$ dense. Henceforth this sample will be referred to as TaAg11.

The oxidation study was carried out using a thermobalance (D-101 CAHN). The samples were placed in an alumina crucible, hung by a Pt wire. The Ta₂AlC samples were oxidized in air between 600 °C and 900 °C for up to 40 h.

X-ray powder diffraction data were collected on a Siemens D-500 diffractometer using Cu K _{α} radiation, with a step scan of 0.02° and 1s per step.

The oxidized samples were mounted, ground, and polished to expose their cross-sections. The oxide layer morphologies and thicknesses were measured in a field emission scanning electron microscope, FESEM, (Phillips XL30) equipped with an energy dispersive spectroscope, EDS, (EDAX, Mahwah, NJ).

2.3 Results and Discussion

2.3.1 Oxidation of Ta₂AlC

XRD analysis of the Ta₂AlC HIPed samples indicated that they were predominantly single-phase, with small amounts of Ta₄AlC₃ as an impurity phase. All samples were greater than 98 % of theoretical density, viz. 11.82 g/cm³.

The time dependencies of the weight gain during the oxidation of Ta₂AlC in air, in the 700 °C to 900 °C temperature range, are shown in Fig. 11. (The weigh gain at 600 °C was lower than the sensitivity level of the thermobalance used.) At the higher temperatures the oxidation rates were linear. This suggests that the oxidation of Ta₂AlC in the given temperature range is most probably limited by a reaction at the oxide/carbide interface.

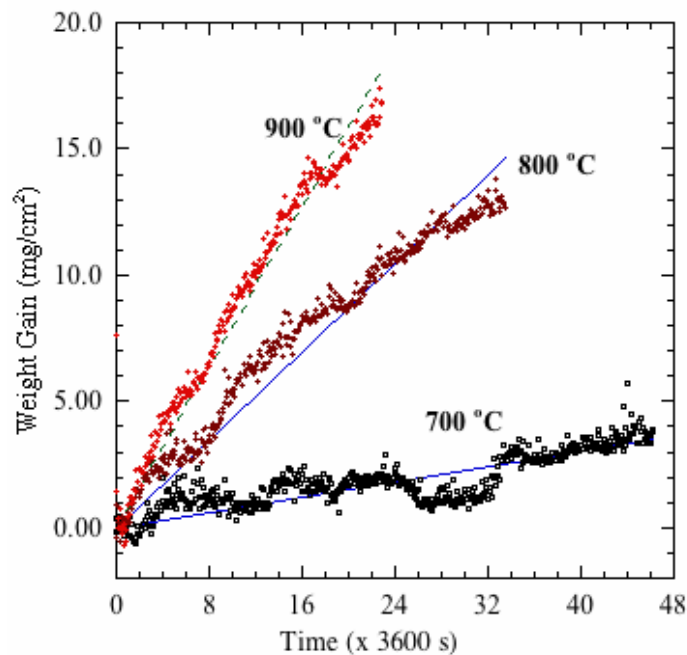


Figure 11: Normalized weight gains vs. time of Ta₂AlC samples isothermally oxidized in air at various temperatures.

Analysis of the XRD spectra of surfaces oxidized at 600 °C showed the presence of small amounts of Ta_2O_5 and, possibly, an even smaller amount of $TaAlO_4$ (Fig. 12). The peaks in the pattern are noticeably broadened, and slightly shifted compared to β - Ta_2O_5 presumably as a result of it being poorly crystallized and defective. It follows that it is more likely than not that the protective layer which forms is mostly amorphous.

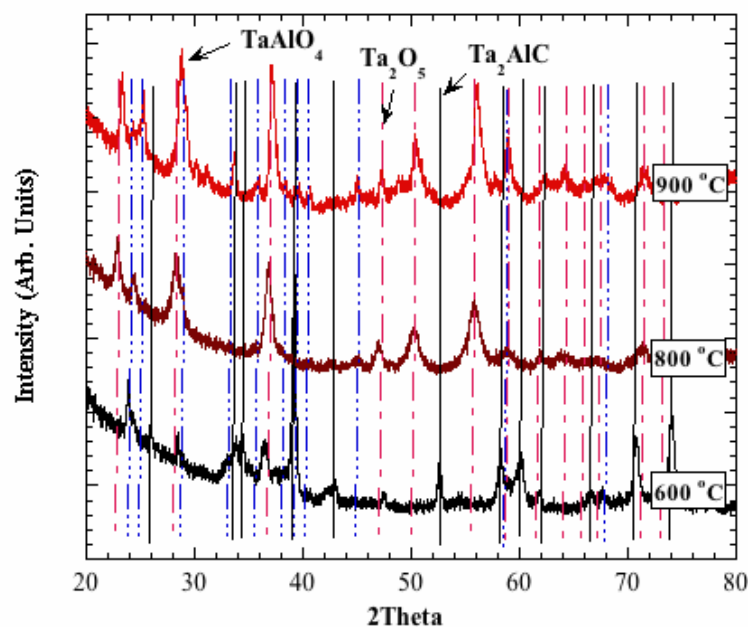


Figure 12: XRD diffraction patterns of the surface layers of Ta_2AlC samples after oxidation at 600 °C, 800 °C and 900 °C for 24 h.

After oxidation at 600 °C for 40 h, a thin ($< 10 \mu m$) oxide layer was formed (Fig. 13). According to EDS analysis the Ta:Al:O atomic ratio in the thin oxide layer was $\approx 2:1:6.5$, respectively, which corresponds to the Ta^{5+} and Al^{3+} oxidation states. In another experiment, a sample was oxidized for 100 h; no change in the morphology of the oxide layer was noted and no further weight gain was noted. However, the presence of the multiple cracks seen in Fig. 13 was not consistent with the passivating nature of the oxide

layer. To better understand the origin of these cracks, we thermal cycled a sample by heating it from room temperature to 600 °C in air and furnace cooling it five times while monitoring its weight. The oxidation rate during cycling was roughly one order of magnitude higher than in the isothermal case. We thus conclude that the cracks, most probably, form during cooling as a result of a thermal expansion mismatch. The thermal expansion coefficient of Ta₂O₅ is reported to be $2.9 \times 10^{-6} \text{ K}^{-1}$ in the 25 to 550 °C and $4 \times 10^{-6} \text{ K}^{-1}$ from 550 °C to 1200 °C [70]. Given that the bulk dilatometric thermal expansion coefficient of Ta₂AlC, measured herein, is $5.7 \times 10^{-6} \text{ K}^{-1}$, it follows that compressive stresses of the order of 450 MPa would develop in the oxide films upon cooling. Such stresses may have been sufficient to compromise the integrity of the thin film.

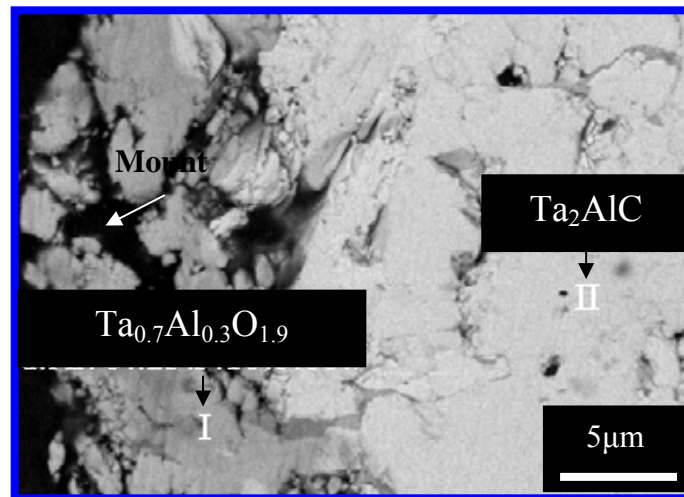


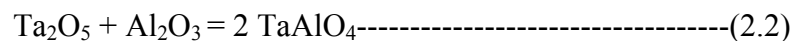
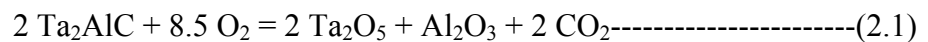
Figure 13: Cross- sectional BSE FESEM micrograph of a Ta₂AlC sample oxidized at 600 °C for 40 h.

The XRD spectra of the oxide layers formed at 800 and 900 °C are also shown in Fig. 12. According to these results, the oxide layers formed were mainly comprised of β-

Ta₂O₅, with AlTaO₄ as a secondary phase. Based on the relative intensities of the peaks of these phases, it is fair to conclude that the volume fraction of the AlTaO₄ phase increases with increasing temperature. Note that at all temperatures, the peaks in the XRD patterns are noticeably broadened implying that the oxide grains formed are quite small.

Cross-sectional SEM micrographs of samples oxidized at different temperatures for different times are shown in Fig. 14. All the oxide layers formed at temperatures 700 °C and above were porous and highly cracked. Compositionally, however, the oxide layers were rather uniform across their thicknesses. No well-formed grains of separate phases were observed. EDS analysis revealed that the oxide layers formed - within the resolution of our probe spot size of ~ 1 μm - were fully oxidized and maintained the same Ta/Al atomic ratio as for the matrix.

Based on these results it is reasonable to conclude that the oxidation of Ta₂AlC occurs according to the following reactions:



with higher temperatures favoring reaction 2.2. Although no Al₂O₃ peaks were observed in the XRD spectra, its formation was confirmed by EDS analysis of the oxidized layers. We thus assume that it forms, but is x-ray amorphous under our experimental conditions. As in all previous work on the oxidation of the MAX phases, the C is assumed to be completely oxidized. The main evidence is its lack of accumulation at the oxide/carbide interface [57,59-61,68,69].

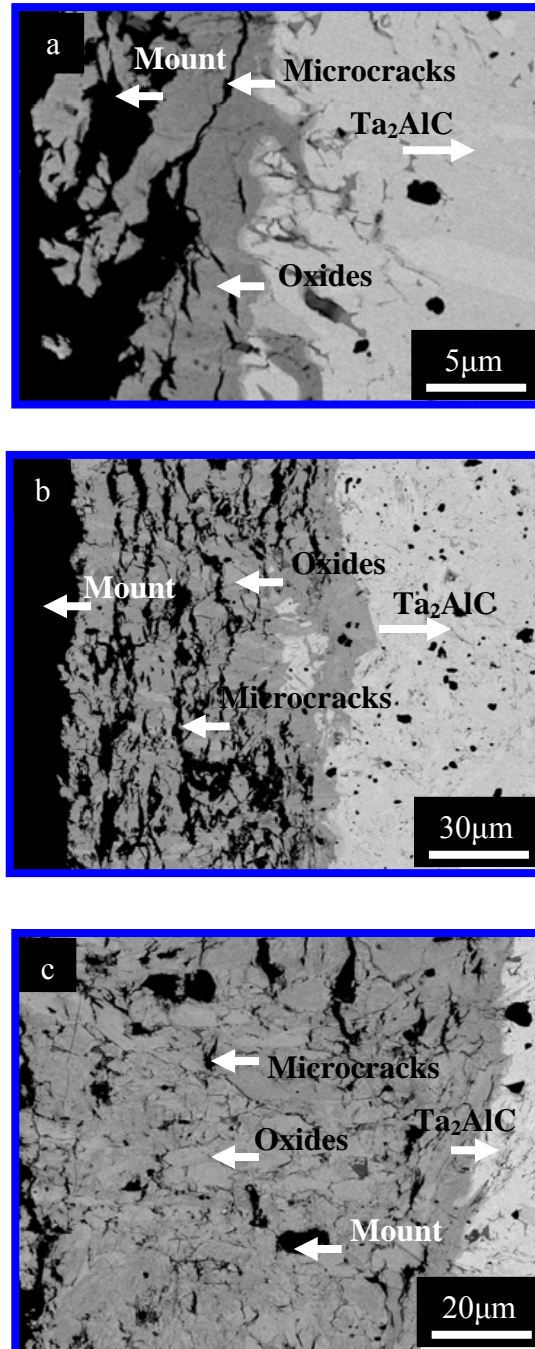


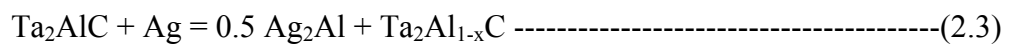
Figure 14: Cross-sectional BSE FESEM micrographs of Ta₂AlC samples oxidized at, a) 700 °C for 46 h, b) 800 °C for 32 h, and, c) 900 °C for 24 h.

As noted above, this reaction scheme is quite similar to the one that occurs during the oxidation of Nb₂AlC and its solid solutions in air [61].

Lastly, the cracked and porous nature of the oxides that form at 700 °C and above (Fig. 14) are consistent with the linear oxidation kinetics (Fig. 11). The cracks and fissures presumably provide fast diffusion paths for the oxygen toward the reaction interface, as well as the outward diffusion of CO₂. Given that the volume change for reaction 2.1 is 15.4%, while that for reaction 2.2 is 39.6%, it is not clear at this time, why the layers that form are not protective. This result, however, is consistent with the poor oxidation resistance of Ta, Ta₂C and TaC.

2.3.2 Oxidation of TaAg11

XRD analysis of the TaAg11 (Fig. 15) composites indicated that due to processing the following reaction had occurred.



where $x \geq 0.5$.

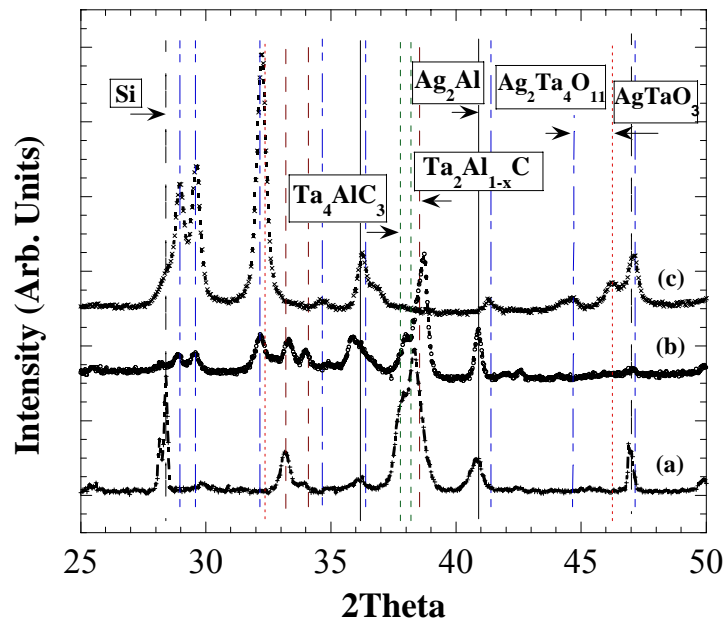


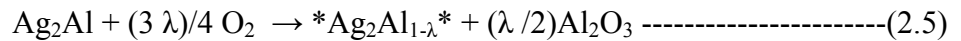
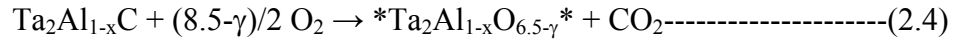
Figure 15: XRD of, (a) as synthesized Ta₂AlC/Ag composites, (b) oxidized at 600 °C for 96 h, and (c) oxidized at 700 °C for 10 h. Si was added as an internal standard.

When Ag reacted with Ta₂AlC grains, it selectively reacted with Al to form Ag₂Al at the grain boundaries. Ta₂AlC reacted with Ag to form Ta₂Al_{1-x}C ($x \geq 0.5$). In some grains the rate of reaction 2.3 was higher and Ta₂Al_{1-x}C recrystallized forming Ta₄AlC₃ and Ta₂C (Fig. 15).

When the samples were oxidized for 96 h at 600 °C, the weight gain was negligible. An oxide layer of (2-3) μm thick formed (Fig. 16). In BSE different regions were detected. To call these regions, phases is an oversimplification and in many cases is incorrect. So the chemistries of the regions designated by letters in the various SEM micrographs, determined by EDS analysis will be designated as *microconstituent*. An average of at least 3 spot analyses was done to estimate the composition of a particular microconstituent.

EDS analysis detected Ta-rich regions with atomic ratios, Ta:Al:O::20:6:68 - it most probably corresponds to the composition *Ta₂Al_{0.5}O_{6.5-γ}* (region TO1 in Fig. 16), Al-rich region with atomic ratios, O:Al:Ta:Ag :: 59:26:7:6 which most probably corresponds to alumina (region TO2 in Fig. 16), and O-deficient region with atomic ratios O:Al:Ta:Ag :: 51:22:10:12 (region TO3 in Fig. 16) at the oxide interface was observed (Fig. 16). Note – spot size during EDS analysis is ~ 1μm and hence the characterization of oxide scale is highly approximate.

XRD analysis of the surface of oxidized samples detected along with the original phases, several poorly crystallized products of oxidation i.e. Ta₂O₅, and Ta₄Ag₂O₁₁ (Fig. 15). Based on EDS and XRD analysis of the oxidized samples, the simplified oxidation reaction can be written as:



Note it is difficult to quantify γ and λ by EDS analysis. As it followed from the EDS and XRD analysis, the oxide layers formed at 600 °C are only partially crystalline. Al_2O_3 formed by reactions 2.5 and 2.6 are x-ray amorphous.

At 700 °C, the TaAg11 composite sample was completely oxidized in ~ 10 h. XRD analysis detected the presence of $\text{Ta}_4\text{Ag}_2\text{O}_{11}$ and AgTaO_3 (Fig.15). The Al_2O_3 formed during the oxidation reaction was XRD amorphous.

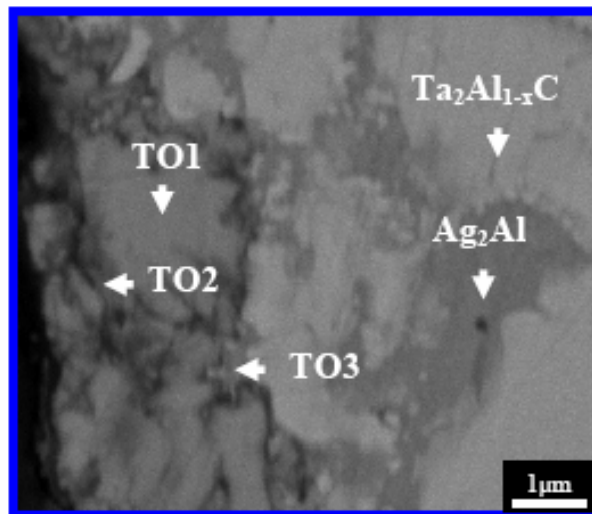


Figure 16: BSE FESEM micrographs of cross-section of TaAg11 composite sample after oxidation at 600 °C for 96h.

Clearly the presence of Ag_2Al lowers the oxidation resistance of TaAg11 composites as compared to Ta_2AlC . The formation of the triple oxides $\text{Ta}_4\text{Ag}_2\text{O}_{11}$ and AgTaO_3 , which causes stresses in the oxide scale, as well as possible melting of the

Ag_2Al (MP ~ 723 °C) most probably contribute to the catastrophic oxidation of the composites at 700 °C.

2.4 Conclusions

The oxidation in air of Ta_2AlC at 600 °C results in the formation of a thin protective (at least up to 100 h) oxide layer which prevents further oxidation. The main crystalline phase detected by XRD in this oxide layer was Ta_2O_5 , with the balance being x-ray amorphous. In the 700–900 °C temperature range, the oxide layers formed are compositionally quite uniform, but porous and highly cracked. They consisted of Ta_2O_5 and TaAlO_4 and some x-ray amorphous phases that are most probably Al_2O_3 .

The oxidation in air of $\text{Ta}_2\text{AlC}/\text{Ag}$ at 600 °C results in the formation of a thin protective (at least up to 100 h) oxide layer which prevents further oxidation. The crystalline phases detected by XRD in this oxide layer were Ta_2O_5 and $\text{Ta}_4\text{Ag}_2\text{O}_{11}$, with the balance being x-ray amorphous. At 700 °C, catastrophic oxidation ensued. The main phases detected by XRD were $\text{Ta}_4\text{Ag}_2\text{O}_{11}$ and AgTaO_3 . with the balance being XRD amorphous.

CHAPTER 3 - TRIBOLOGICAL BEHAVIOR OF SELECT MAX PHASES

3.1 Introduction

The goal of this work was to understand the tribological behavior of the pure MAX phases, and evaluate them as potential triboactive materials for foil bearing applications. In this chapter, we report on the tribological behavior - at 26 °C and 550 °C - of the following layered ternary carbides: Ti_2AlC , Cr_2AlC , Ta_2AlC , Ti_3SiC_2 , Ti_2AlN , Ti_4AlN_3 , Cr_2GeC , Cr_2GaC , Nb_2SnC and Ti_2SnC , tested against Ni-based superalloys (Inc718 and Inc600) and alumina, Al_2O_3 .

3.2 Experimental Details

The sources and characteristics of the powders used during the course of this work are summarized in Table 1. The Ti_2AlC , Ti_2AlN and Cr_2AlC samples used herein were commercially produced and purchased from 3-ONE-2, Voorhees, NJ. The processing parameters for synthesizing Ti_3SiC_2 [42,43], Ti_2SnC [68,72], Nb_2SnC [68,72], Ti_4AlN_3 [73], and Cr_2GaC [74] are summarized in Table 2.

In this chapter, we report on the processing of Cr_2GeC for the first time, and Ta_2AlC by a different processing route than the one described in Ch. 2. Cr_2GeC was prepared by ball milling stoichiometric amounts of Cr, Ge and C powders in plastic bottle for 1 h. The mixed powders were cold-pressed and annealed at 800 °C for 10 h. The annealed samples were placed in a graphite die, which was pre-coated with BN spray. The entire assembly was placed in a hot-press, HP, which was heated at the rate of 500 °C/h to a final temperature of 1375 °C. The samples were then uniaxially HPed under a

stress of 40 MPa at 1375 °C for 6 h. The Ta₂AlC samples were prepared by Hot Isostatic Pressing, HIPing of Ta₂AlC powders at 1600 °C for 8 h under a pressure of ~ 70 MPa.

Table 1: Characteristics of starting powders used in this work.

Powders	Source	Particle size	Purity
Ti	Alfa Aesar (Ward Hill, MA).	-325 mesh	99.50%
Cr			99%
Nb			99.80%
Sn	Aldrich (Milwaukee, WI).		99.80%
Ga	Alfa Aesar (Ward Hill, MA).	3 mm pellets	99.99%
Ge	Advanced Technology Inc., NJ.	-200 mesh	99.99%
TiN	Alfa Aesar (Ward Hill, MA).	(2-3) μm	99.80%
AlN		dm ≈ 3 μm	32 wt.% (N - min)
Graphite		-300 mesh	99%
SiC	Atlantic Eng. Equip., Bergenfield, NJ.	- 400 mesh	99.50%
TiH ₂	TIMET, Henderson, NV.	-325 mesh	99.30%
Ta ₂ AlC	3-ONE-2, Voorhese, NJ.	- 325 mesh	> 92%
Cr ₂ AlC	3-ONE-2, Voorhese, NJ.	- 325 mesh	> 95 %
Ag	Alfa Aesar (Ward Hill, MA).	- 325 mesh	99.90%

To determine the volume fraction of un-reacted A-group elements, such as Sn and Ga, present in many of the compositions, a small chip of the material to be studied was weighed, encased in an Al pan, and placed in a differential scanning calorimeter (DSC) [Perkin Elmer, Boston MA]. The details regarding the procedure used for calculating the un-reacted A-elements can be found elsewhere [68, 73]. The volume fractions of the binary carbides - that are always present in the ternaries - were determined from image

analysis of FESEM backscattered micrographs. The grain size was calculated by the linear intercept of at least 10 grains. Since the MAX phase-grains tend to grow as hexagonal plates, what is reported here is the average diameters of the plates.

The friction and wear tests were performed using a high temperature tribometer (CSM, Switzerland) capable of going up to 600 °C. In this thesis, μ 's, are referred to in different ways: μ_{mean} refers to the mean friction coefficient over the entire sliding distance; μ_s refers to the steady state value during sliding.

A tab-on-disc method was used for all tests. The MAX-phase based tab was in the form of a cuboid chip ($\sim 6 \times 6 \times 2 \text{ mm}^3$) with flat surfaces. The counter surfaces were 9.5 mm thick cylindrical (55 mm dia) discs of Inconel718, Inconel-600, henceforth referred to as Inc718 and Inc600, respectively, or Al_2O_3 (CerCo LLC, OH). The superalloy, SA, discs were commercially obtained (High Temp Metals, Inc., Sylmar, CA). The base composition of Inc718 is $\text{Ni}_{0.5}\text{Cr}_{0.25}\text{Fe}_{0.25}$, with small ($< 1 \text{ vol. \%}$) quantities of additions like Nb, C, Mo, Si, Mn, Si etc. For simplicity in this paper we assume the chemistry of the Inc718 to be $\text{Ni}_{0.5}\text{Cr}_{0.25}\text{Fe}_{0.25}$. Similarly, the base composition of Inc600 is $\text{Ni}_{0.7}\text{Cr}_{0.2}\text{Fe}_{0.1}$, with small ($< 1 \text{ vol. \%}$) quantities of additions like C, Si, Mn, Si, Cu etc.

All surfaces were polished to a 1 μm diamond finish, washed with acetone and dried prior to testing. Characterization of MAX–Inc718 tribocouples was carried out by EDS, and profilometric studies.

All the testing was done at a linear velocity of 100 cm/s and a load of 3 N. Henceforth, this particular set of condition will be referred to as standard condition. The MAX samples were tested on two tracks of the circular disc, an inner track of mean radius $r_{\text{mean}} = 10\text{-}12 \text{ mm}$ or an outer track of mean radius 18-19. The sliding distance at

Table 2: Parameters used during the synthesis of MAX phases and MAX phase based composites.

Composition	Process/Source Used	Parameters	Ref.
Ti ₂ AlC	3-ONE-2, Voorhese, NJ.	Commercially manufactured by 3-ONE-2, Voorhese, NJ.	NA
Ti ₂ AlN			
Cr ₂ AlC			
Ti ₄ AlN ₃	HIP	1275 °C for 24h under 70 MPa	73
Ti ₃ SiC ₂		1450 °C for 40 h under 40 MPa	42,43
Ta ₂ AlC		1600 °C for 8h under 70 MPa	Ch. 3
Cr ₂ GaC		1200 °C for 12 h under 70 Mpa	74
Cr ₂ GeC	HP	Explained in text	Ch. 3
Ti ₂ SnC	HIP	1325 °C for 4h under 70 MPa	68, 72
Nb ₂ SnC		1300 °C 4h under 70 MPa	
CrAg _{lab}	Liquid phase sintering	1200 °C for 10 minutes	Chs. 4 - 7
CrAg ₁₁	HIP	1100 °C for 20 min. under 70 Mpa	
TaAg _{lab}	Liquid phase sintering	1200 °C for 10 minutes	
TaAg ₁₁ (porous)	HIP	1100 °C for 20 min. under 70 Mpa	
TaAg ₁₁		1100 °C for 20 min. under 70 Mpa	
TaAg _R		1100 °C for 20 min. under 70 Mpa	

room temperature varied from 300 to 800 m; at 550 °C it was at least 2 km. The WRs of the MAX-phase tabs were determined by measuring their weights before and after testing in a scale with a resolution of 10⁻⁴ g. The WRs were calculated by normalizing the volumetric wear by the total sliding distance and applied load (Eq. 1.1).

The wear of the SA discs was measured by laser profilometry [Solarius Development, Sunnyvale, CA]. Profilometry of the MAX surfaces after testing were carried out by an atomic force microscope AFM, (Dimension-3000, Digital Instruments,

Santa Barbara, CA) at the University of SUNY in Stonybrook, NY, in a scanning mode over a $100\ \mu\text{m} \times 100\ \mu\text{m}$ contact area and a scan rate of 0.5 Hz. Roughness analysis was done to calculate the average root mean square roughness values, R_{RMS} of the scanned surfaces.

The phase and microconstituent phase chemistries were determined in a field emission scanning electron microscope, (FESEM, XL-30, FEI-Philips, Hillsboro, OR) equipped with an energy dispersive spectroscope, EDS, (EDAX, Mahwah, NJ). During this work, on the contact surfaces metastable and/or multicomponent regions are formed [26]. To call these regions phases is an oversimplification and in many cases is incorrect. So the chemistries of the regions designated by letters in the various SEM micrographs, determined by EDS analysis will be designated as *microconstituent*. An average of at least 3 spot analyses was done to estimate the composition of a particular microconstituent. Note, it is not possible to quantify C by EDS analysis. So based on the oxidation state of the different cations was estimated from knowledge of oxygen concentration. Most of EDS and surface profilometry were carried out on the Ta_2AlC surfaces since the preliminary tribology results on this MAX particular phase were quite promising [56, 57].

3.3 Results

3.3.1 Synthesis and Microstructure

The synthesized Cr_2GeC sample was $> 95\ \text{vol.}\%$ pure, its average grain size was $\approx 20\ \mu\text{m}$ and it contained $\sim 4\ \text{vol.}\%$ Cr_2O_3 and $\approx 1\ \text{vol.}\%$ Ge as impurity phases. A summary of all the microstructures used in this work can be found in Table 3.

Table 3: Summary of microstructure of MAX phases and its composites used during Tribology study.

Composition	Grain Size	Main Phase	Secondary Phases	Refs.
Ti ₂ AlC	≈ 45 μm	Ti ₂ AlC	Ti ₃ AlC ₂ (< 3 Vol. %) and TiAl ₃ (< 2 Vol. %)	3-ONE-2, NJ
Ti ₂ AlN	≈ 20 μm	Ti ₂ AlN	Ti ₄ AlN ₃ (~ 5 - 10 Vol.%) , TiN and Al ₂ O ₃ (< 1 Vol.%)	3-ONE-2, NJ
Ti ₄ AlN ₃	(20 - 30) μm	Ti ₄ AlN ₃	TiN (< 1 Vol.%) and Al ₂ O ₃ (< 1 Vol.%)	73
Ti ₃ SiC ₂	≈ 4 μm	Ti ₃ SiC ₂	SiC (≈ 2 Vol. %) and TiC (≈ 2 Vol. %)	42,43
Cr ₂ AlC	≈ 20 μm	Cr ₂ AlC	Cr ₇ C ₃ (≈ 3 Vol. %) and Al ₂ O ₃ (<1 Vol. %)	3-ONE-2, NJ
Ta ₂ AlC	≈ 20 μm	Ta ₂ AlC	Ta ₄ AlC ₃ (≈ 5 Vol. %), TaAl ₂ (≈ 2 Vol. %) and Al ₂ O ₃ (<1 Vol. %)	Ch. 3
Cr ₂ GaC	≈ 30 μm	Cr ₂ GaC	Cr ₇ C ₃ (<1 Vol.%) and Ga (<1 Vol. %)	74
Cr ₂ GeC	≈ 20 μm	Cr ₂ GeC	Cr ₂ O ₃ (< 3 Vol. %) and Ge (<1 Vol. %)	This work
Ti ₂ SnC	(5 - 10) μm	Ti ₂ SnC	Sn (5 Vol. %) and TiC _x (<1 Vol. %)	68, 72
Nb ₂ SnC	(5 - 10) μm	Nb ₂ SnC	NbC _x (<1 Vol. %) and Sn (4 Vol. %)	
CrAg1b	~ (2-5) μm	Cr ₂ AlC	Cr ₇ C ₃ and Ag ₂ Al are grain boundary phases	Chs. 4 -7
CrAg11				
TaAg1b		Ta ₂ Al _{1-x} C	Ta ₄ AlC ₃ , Ag ₂ Al and Ta ₂ C are grain boundary phases	
TaAg11 (porous)				
TaAg11				
TaAgR				

Table 4: Summary of WR and μ of different tribo-couples at 26 °C.

Specimen	Load (N)	Test Type	Dynamic Partner	WR (mm ³ /N-m)	μ_{mean}	Refs.
Ti ₂ AlC	3	Tab on Disc	Inc718	$\approx 5.5 \times 10^{-4}$	0.54±0.1	This Ch.
			Al ₂ O ₃	$\approx 1 \times 10^{-2}$	0.7±0.04	
Ti ₂ AlN			Inc718	$\approx 3 \times 10^{-2}$	0.8±0.15	
Ti ₄ AlN ₃			Inc718	$\approx 3 \times 10^{-2}$	0.8±0.15	
			Al ₂ O ₃	$\approx 1.2 \times 10^{-3}$	0.6±0.1	
Ti ₃ SiC ₂			Inc718	$\approx 2.5 \times 10^{-2}$	0.6±0.15	
Ti ₃ SiC ₂	5	Pin on Disc	Steel	1.4×10^{-3}	0.83	48
Cr ₂ AlC	3	Tab on Disc	Inc718	$\approx 1.2 \times 10^{-3}$	0.6±0.1	This Ch.
			Al ₂ O ₃	$\approx 4 \times 10^{-2}$	0.75±0.1	
Ta ₂ AlC			Inc718	$\approx 1.5 \times 10^{-2}$	0.5±0.1	
			Al ₂ O ₃	$\approx 2 \times 10^{-2}$	0.8 ± 0.05	
Cr ₂ GeC			Inc600	$\approx 1.2 \times 10^{-3}$	0.5±0.1	
			Al ₂ O ₃	$\approx 5.5 \times 10^{-4}$	0.7±0.1	
Cr ₂ GaC			Inc600	$\approx 4 \times 10^{-2}$	0.4±0.1	
Ti ₂ SnC			Inc600	$\approx 8 \times 10^{-3}$	0.63±0.1	
			Al ₂ O ₃	$\approx 3 \times 10^{-2}$	0.8±0.02	
Nb ₂ SnC			Inc600	$\approx 1.5 \times 10^{-2}$	0.63±0.1	
	Al ₂ O ₃	≈ 0.2	0.8±0.04			
Si ₃ N ₄	10	Pin on Disc	Si ₃ N ₄	$(1-5) \times 10^{-5}$	$(0.3-0.6)^{\ddagger}$	26
TiN - Si ₃ N ₄			TiN - Si ₃ N ₄	5×10^{-6}	0.6^{\ddagger}	
SiC			SiC	5×10^{-6}	0.6^{\ddagger}	
SiC - TiC			SiC - TiC	1×10^{-6}	0.3^{\ddagger}	
SiC - TiB ₂			SiC - TiB ₂	1×10^{-6}	0.6^{\ddagger}	

[‡] Friction coefficient refers to steady state.

3.3.2 Room temperature tribology results

At ambient temperatures, the WRs of all the MAX phases were $\geq 10^{-4}$ mm³/N-m, irrespective of the countersurface used (Table 4). The μ 's were also > 0.4 in all cases (Table 4).

From the profilometry and the microscopy results, the WRs of the SA and Al₂O₃ surfaces were low and difficult to quantify. The details are discussed below.

When the WRs of the MAX phases against Inc718 are plotted vs. μ , (Fig. 17a) no correlation was found (correlation coefficient, $R \sim 0.3$). The same is true for the MAX/Al₂O₃ couples (Fig. 17b); here R was ~ 0.5 .

Figures 18a and 18b plot the μ 's as a function of sliding distance against Inc718 for Ti₃SiC₂ and Ta₂AlC, respectively. In both cases, the initial μ 's were low (< 0.1 to 0.2), (insets of Figs. 18a and b) before increasing to ≈ 0.6 . This kind of transition was observed in all the other MAX phases tested (not shown) as well.

When the wear in mm³/N, of both these compounds, are plotted vs. sliding distance (Fig. 18c), it is obvious that the WR's are linear, i.e. more or less constant, with sliding distance. The WRs of the Ti₃SiC₂ samples are higher than those of Ta₂AlC.

When the Ta₂AlC pin and the Inc718 disc were examined in the SEM, on both surfaces, an oxy-carbide transfer film was detected (Fig. 19). Note that in the remainder of this thesis, we denote various areas in the SEM micrographs by letters. The chemistries of these, and similar areas, were determined - by averaging at least 3 EDS readings - and listed in Table 5, using the same letter used on the micrographs.

The partially oxidized transfer film on the MAX surface was pulverized (Fig. 19a) and the average composition was $A = [Ta_{0.7}Al_{0.3}]O_{0.1}$. The transfer film on the Inc718

surface (Fig. 19b) was smeared and had an average composition, $B = [Ta_{0.66}Al_{0.33}]O_{0.3}$ (Table 5). Sliding marks were observed on the Inc718 surfaces. The Al_2O_3 surfaces were also covered with an oxy-carbide transfer film (Fig. 19c) of average composition, $D = [Ta_{0.66}Al_{0.33}]O_{0.35}$ (Table 5).

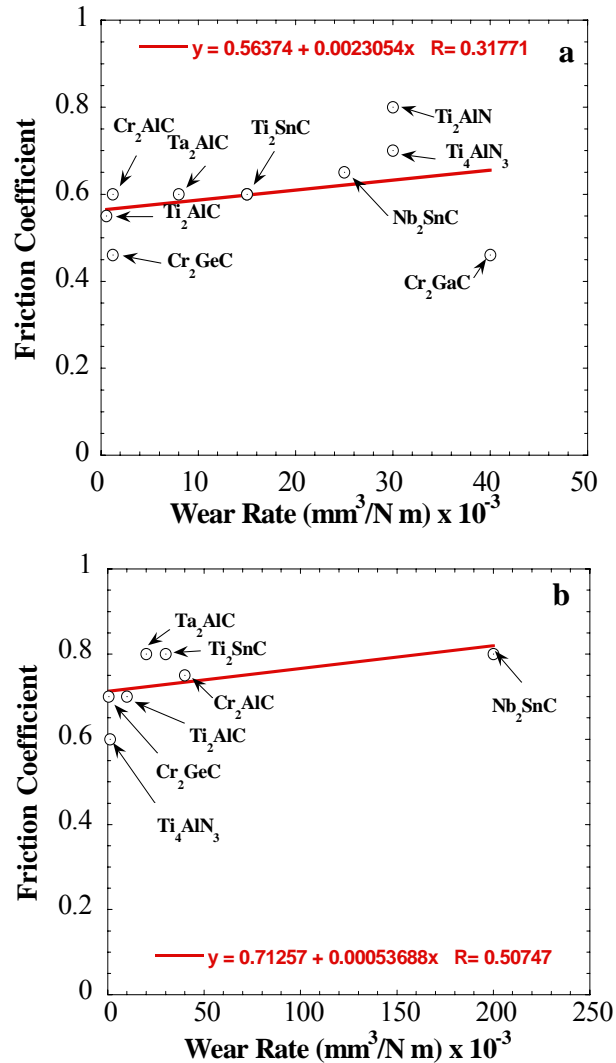


Figure 17: Plot of WR versus μ 's after dry sliding against, (a) Inc718, (b) alumina. A regression line has been fitted (solid line) to the data points and correlation coefficients, R , are shown.

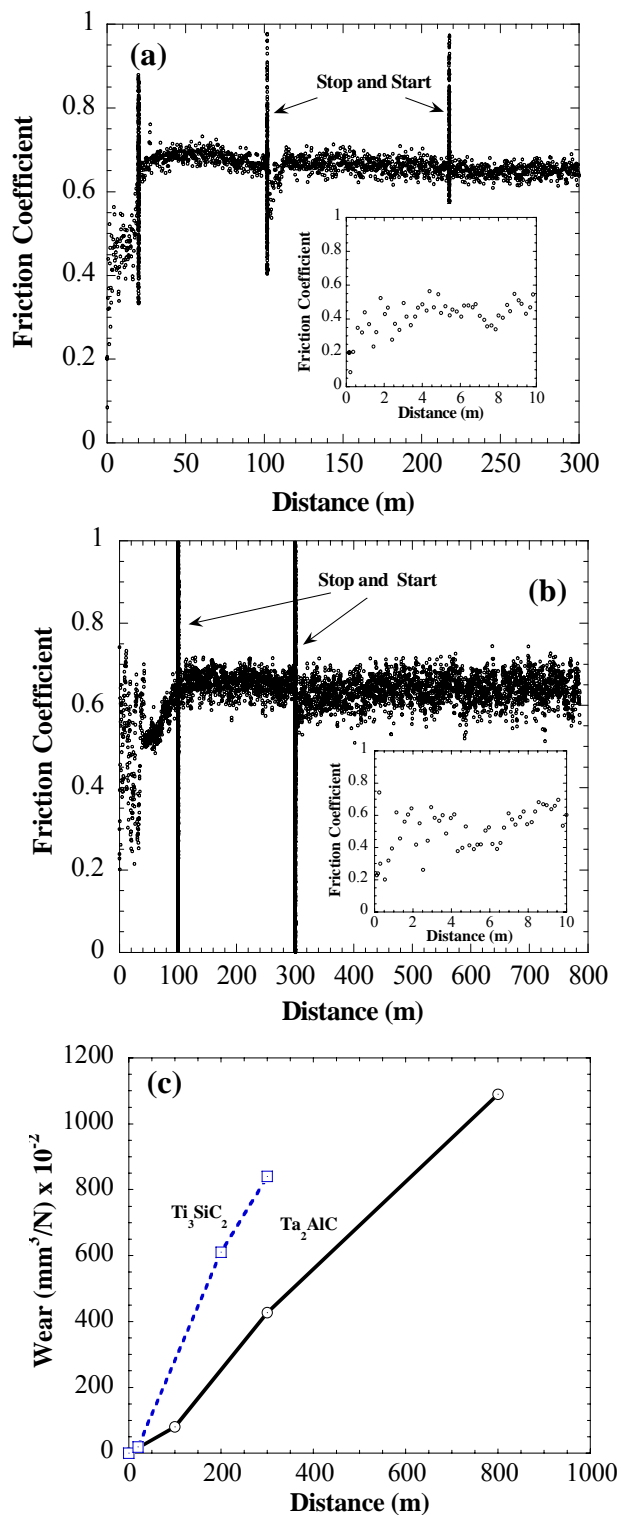


Figure 18: Change in μ as a function of sliding distance, when (a) Ti_3SiC_2 was tested against Inc718, and (b) Ta_2AlC was tested against Inc718. In both a and b, insets show evolution of μ 's during initial 10 m, and, (c) Plot of wear of Ti_3SiC_2 and Ta_2AlC as a function of sliding distance against Inc718. All the experiments were done at standard conditions at 26 °C.

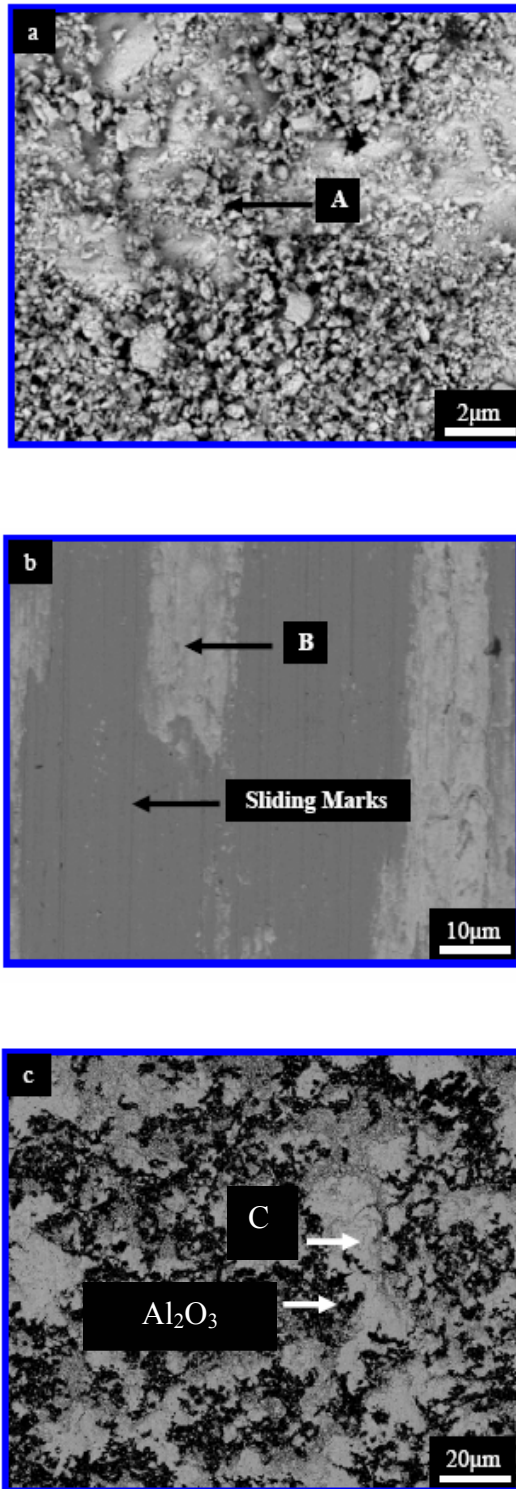


Figure 19: BSE FESEM micrographs of tribosurfaces after dry sliding of Ta₂AlC against Inc718 and at 26 °C: (a) Ta₂AlC surface, (b) Inc718 surface, and, (c) Al₂O₃ surface. In these micrographs, and all other shown in this thesis, letters are used to designate microconstituent.

Table 5: Average of at least 3 EDS readings of a region homogenous at the micro scale. Each alphabet letter represents elemental ratios of “micro constituents”.

Region	O	Al	Ta	Si	Ti	Cr	Fe	Ni	*Averaged Composition*
A (Fig. 19a)	11±4	22±2	50±3	x	x	x	x	x	[Ta _{0.7} Al _{0.3}]O _{0.1}
B (Fig. 19b)	20±1	22±1	43±3	x	x	x	x	x	[Ta _{0.66} Al _{0.33}]O _{0.3}
D (Fig. 19c)	22±3	23±3	41±2	x	x	x	x	x	[Ta _{0.66} Al _{0.33}]O _{0.35}
E (Fig. 21a)	41±8	2.5±2	6.25±5	x	x	11.2	10	27.5±8	[Ta _{0.09} Al _{0.01} Ni _{0.5} Cr _{0.2} Fe _{0.2}]O _{0.7}
F (Fig. 21b)	55±1	x	x	7.5	15	5±0.5	5±0.5	11.5±1	[Ni _{0.25} Fe _{0.1} Cr _{0.1} Ti _{0.35} Si _{0.2}]O _{1.2}
G (Fig. 21c)	50±1	x	x	x	x	11±1	11±1	26±0.5	[Ni _{0.5} Fe _{0.25} Cr _{0.25}]O ₁
H (Fig. 21d)	46±5	x	x	x	x	13±1	11±1	30	[Ni _{0.55} Fe _{0.22} Cr _{0.23}]O _{0.9}
I (Fig. 25)	64±3	12±2	18±3	x	x	x	x	x	[Ta _{0.6} Al _{0.4}]O ₂

3.3.3 Tribology Results at 550 °C

Most of the MAX phases tested against Inc718, and in some cases tested against Inc600, at 550 °C showed negligible ($\leq 10^{-5}$ mm³/N-m) WRs after 2 km of sliding (Table 6). With the exception of Cr₂GaC, the μ_s 's were also < 0.5 . The presence of excess Ga in Cr₂GaC (Table3) may have been detrimental and responsible for its higher WRs. Gouging of the Inc718 surface was also observed in some locations (see below).

Ta₂AlC-Inc718, Ti₃SiC₂-Inc718, Cr₂AlC-Inc718 and Ti₂AlC-Inc718 tribocouples showed most promising results. Extensive EDS and profilometric studies were carried out to characterize the Ta₂AlC, Ti₃SiC₂, Cr₂AlC and Ti₂AlC samples against Inc718. The μ 's were monitored as a function of sliding distance for Ti₃SiC₂ (Fig. 20a) and Ta₂AlC (Fig. 20b). Initially the high values of μ (~ 0.6) were accompanied by a loud metallic noise; once the μ 's decreased to their steady state values of ~ 0.4, the tribo-noises were significantly reduced.

Table 6: Summary of μ and WR's of different tribo-couples at high temperatures.

Static Partner	Dynamic Partner	Experimental Conditions	Temp. (°C)	WR _s (mm ³ /N-m)	WR _d (mm ³ /N-m)	μ_s	Refs.
Ta ₂ AlC	Inc718	Tab on Disc, 3 N, 1 m/s	550	$\leq 1 \times 10^{-6}$	$\sim 10^{-5}$	≈ 0.4	Ch.3
	Al ₂ O ₃			$\leq 1 \times 10^{-6}$	CND	0.9	
Ti ₃ SiC ₂	Inc718			$\leq 1 \times 10^{-6}$	$\sim 10^{-5}$	≈ 0.4	
Cr ₂ AlC				$\leq 1 \times 10^{-6}$		≈ 0.3	
Ti ₂ AlC				$\leq 1 \times 10^{-6}$		≈ 0.4	
Cr ₂ GaC				Inc600		$\approx 5 \times 10^{-4}$	
Cr ₂ GeC	Inc600			$\approx 6 \times 10^{-6}$	≈ 0.35		
Ti ₂ AlN	Inc718			$\approx 3 \times 10^{-5}$	≈ 0.4		
Ti ₄ AlN ₃	Inc600			$\approx 1 \times 10^{-3}$	≈ 0.6		
Si ₃ N ₄	Si ₃ N ₄			Pin on Disc, 10 N, and 1 m/s	800	$\approx 10^{-3\dagger}$	
TiN - Si ₃ N ₄	TiN - Si ₃ N ₄	$5 \times 10^{-5\dagger}$	0.8				
SiC	SiC	400	$\approx 10^{-4\dagger}$		0.7		
SiC - TiC	SiC - TiC		$\approx 10^{-5\dagger}$		0.9		
SiC - TiB ₂	SiC - TiB ₂	$\approx 10^{-6\dagger}$	0.4				

Note:

- WR_s – Specific wear rate of the static tribo-partner.
- WR_d – Specific wear rate of the dynamic tribo-partner.
- † Total WR = WR of pin + WR of disc.

When the surfaces were examined in the SEM after 2 km of sliding against Ta₂AlC, they were slightly gouged, and covered with sporadic and discontinuous tribofilms (Fig. 21a). Under the optical microscope these areas were colored metallic gray (inset in Fig. 21a). EDS of the tribofilm identified it to be an oxide of average composition, E = *[Ni_{0.45}Fe_{0.22}Cr_{0.23}Ta_{0.1}]O_{0.7}* (Table 5). Even at higher magnifications, no phase separation in the oxide layers was observed (inset in Fig. 21a). Similar observations were made on the Inc718 surfaces after 2 km of sliding against Ti₃SiC₂ (Fig.

21b), Ti₂AlC (Fig. 21c) and Cr₂AlC (Fig. 21d). In all cases, the Inc718 surfaces were slightly gouged and covered by spotty, patchy tribofilms. The transfer films formed on the Inc718 surfaces after testing against Ti₃SiC₂ had an average composition F = *Ni_{0.25}Fe_{0.1}Cr_{0.1}Ti_{0.35}Si_{0.2}O_{1.2}*; those against Cr₂AlC, G = *Ni_{0.5}Fe_{0.25}Cr_{0.25}O₁*, and those against Ti₂AlC, H = *Ni_{0.55}Fe_{0.22}Cr_{0.23}O_{0.9}* (Table 5). In other words, with the exception of Ti₃SiC₂, the tribofilm chemistries reflected the chemistries of the elements in the SA.

The Ta₂AlC surfaces - after sliding against Inc-718 at 550 °C for 2 km - were also covered with tribofilms (Fig. 22a) of average composition E = *Ni_{0.45}Fe_{0.22}Cr_{0.23}Ta_{0.1}O_{0.7}*. Even at higher magnifications the tribofilms formed appeared dense and smooth and no evidence for phase separation was observed (Fig. 22b).

Laser profilometry of the worn Inc718 surfaces after testing against Cr₂AlC (Fig. 23a) and Ta₂AlC (Fig. 23b) detected tribofilms and gouges of the order of a few μm's, corroborating the microscopy results. Owing to the stochastic nature of the gouging and tribofilms, it is fairly difficult to estimate the wear of the Inc718 substrates. Nevertheless, using the method outlined in Appendix A, we estimate the WRs of the Inc718 to be ~ 10⁻⁵ mm³/N-m against Cr₂AlC, and ~ 10⁻⁵ mm³/N-m against Ta₂AlC (Table 6). The WRs estimated for the other SA surfaces examined also were of the order of ~ 10⁻⁵ mm³/N-m (Table 6). The R_{RMS} determined from AFM analysis of the post-sliding Ta₂AlC (Fig. 24), Cr₂AlC, Ti₃SiC₂ and Ti₂AlC (not shown) surfaces were ≈ 350 nm, 325 nm, 540 nm and 272 nm, respectively. In other words, the surfaces were extremely smooth.

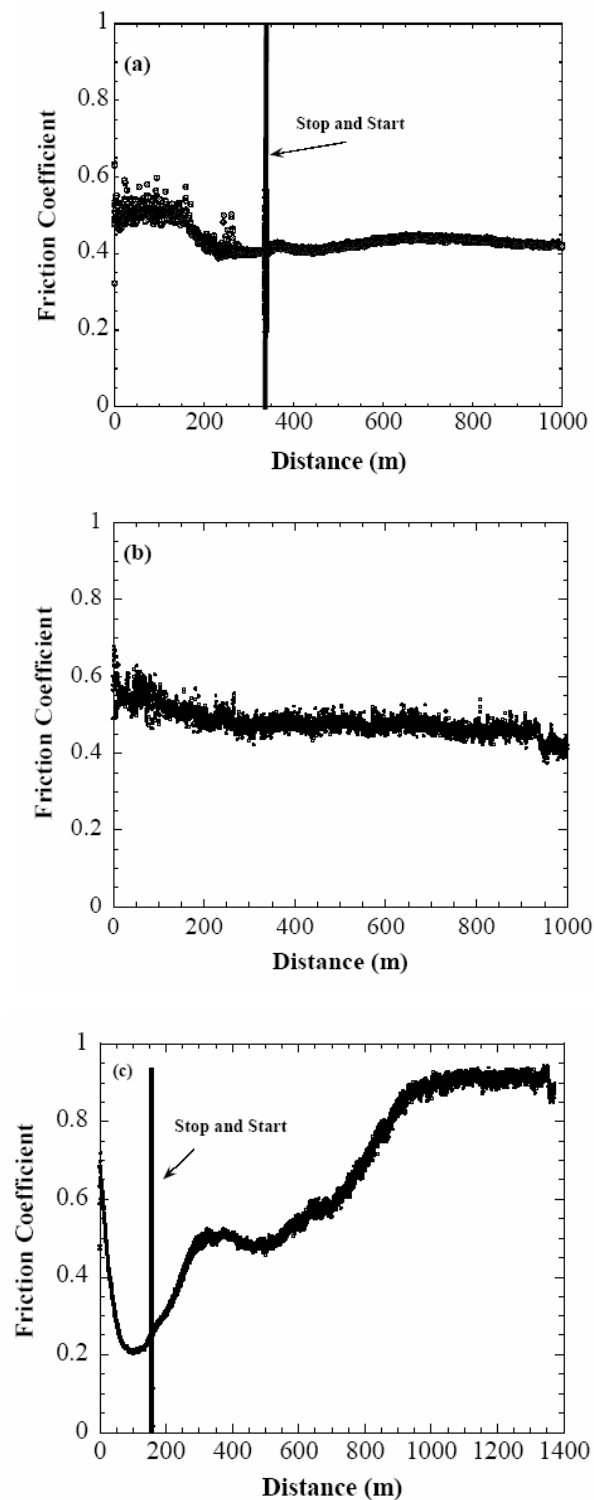


Figure 20: Change in μ as a function of sliding distance, when (a) Ti_3SiC_2 was tested against Inc718, (b) Ta_2AlC was tested against Inc718, and (c) Ta_2AlC was tested against Al_2O_3 . All experiments were done at 550°C , and under standard conditions.

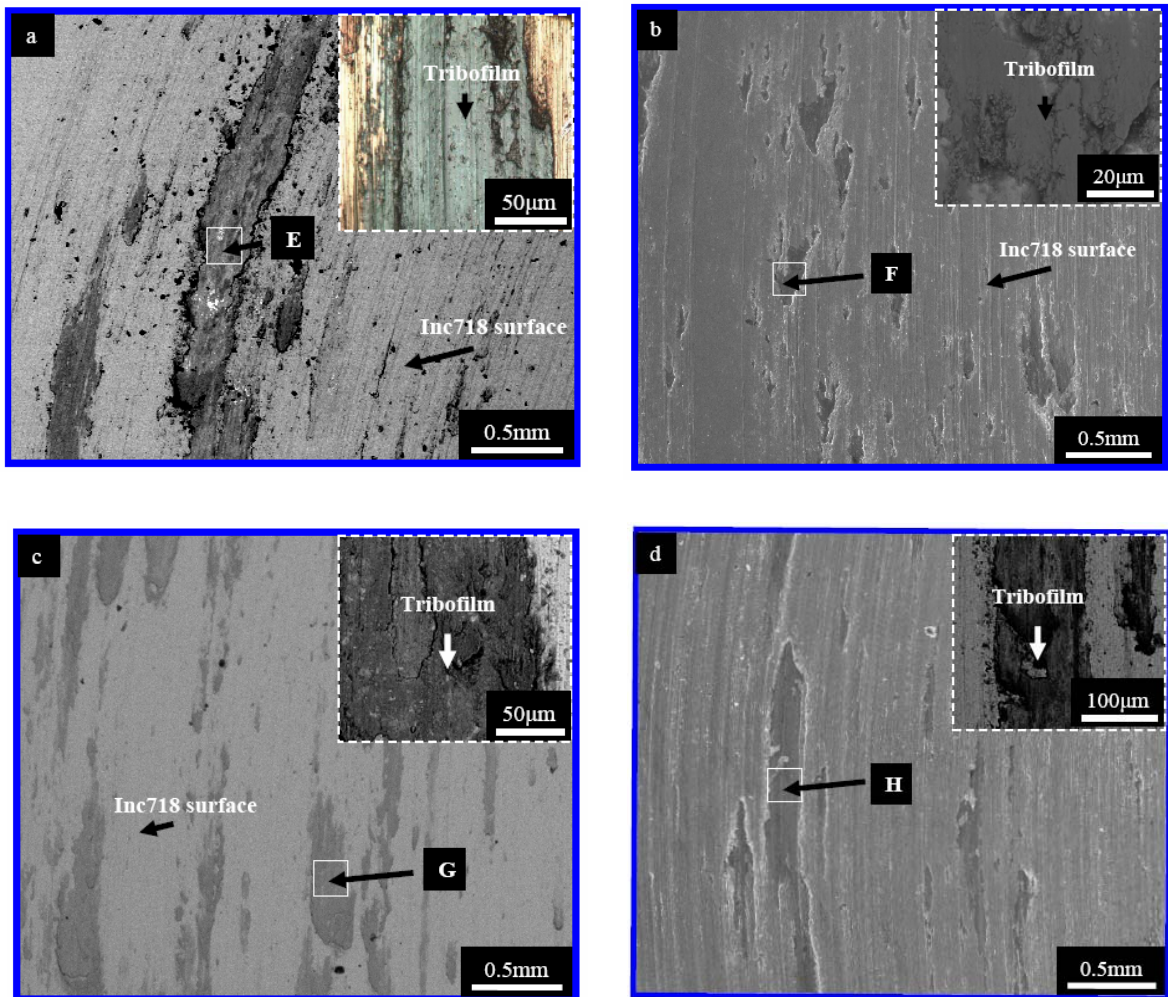


Figure 21: (a) BSE FESEM micrograph showing tribofilms formed on Inc718 surface after 2 km dry sliding against Ta_2AlC . Inset shows the optical micrograph of the tribofilm (light blue) on Inc718 surface, (b) SE FESEM micrograph showing tribofilms formed on slightly gouged Inc718 surface after 2 km dry sliding testing against Ti_3SiC_2 . Inset shows the BSE FESEM micrograph of the tribofilms at higher magnification, (c) BSE FESEM micrograph showing tribofilms formed on Inc718 surface after 2 km dry sliding against Cr_2AlC . Inset shows the BSE FESEM micrograph of the tribofilm at *higher magnification*, and (d) SE FESEM micrograph showing tribofilms formed on Inc718 surface after 2 km dry sliding against Ti_2AlC . Inset shows the FESEM micrograph of the tribofilm. All the tribocouples were tested at 550 °C, and under standard conditions.

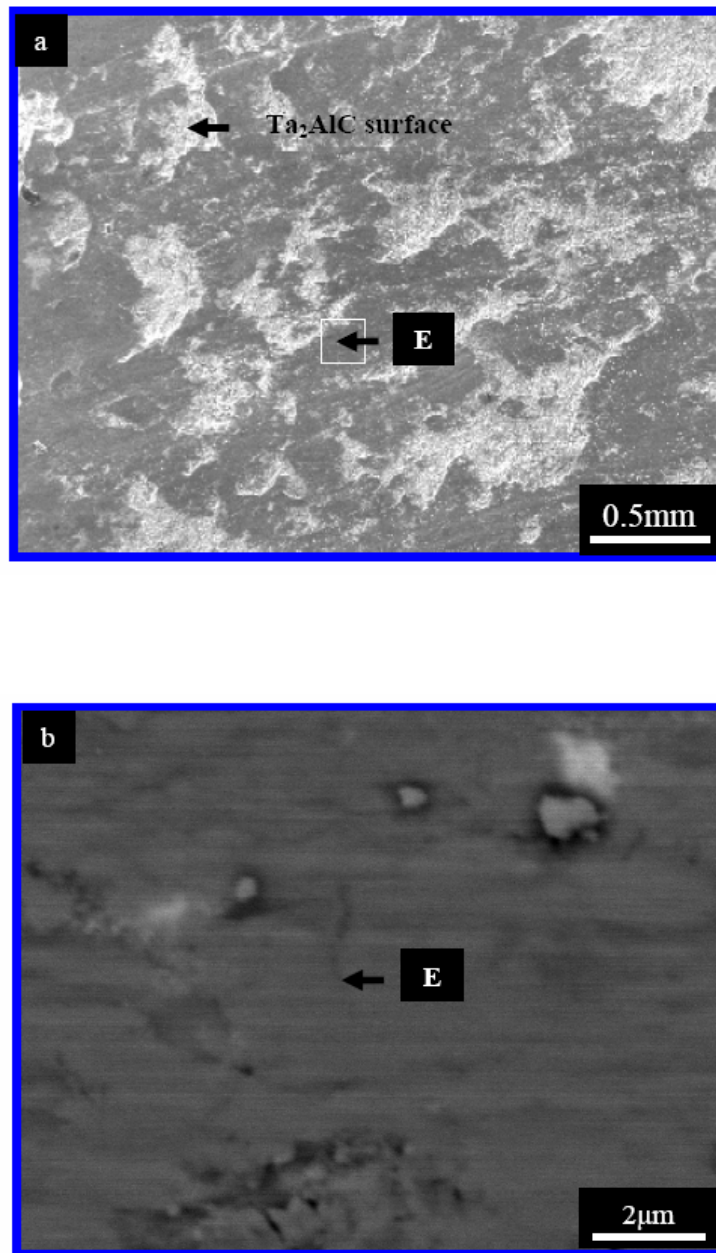


Figure 22: FESEM micrographs showing tribofilms formed on Ta₂AlC surface after dry sliding for 2 km against Inc718 at 550 °C (a) SE image, & (b) BSE image of the region marked E at *higher magnification*. The experiment was done under standard testing condition.

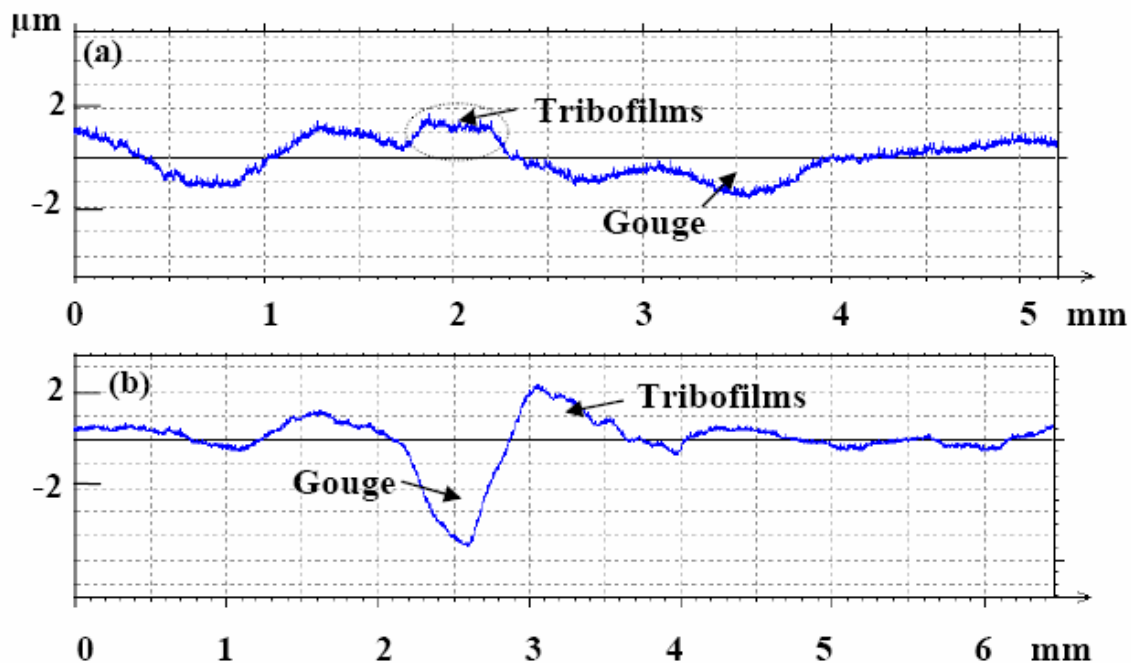


Figure 23: Laser profilometry on Inc718 surfaces after dry sliding for 2 km at 550 °C against, (a) Cr_2AlC , and, (b) Ta_2AlC . All the experiments were done under standard conditions.

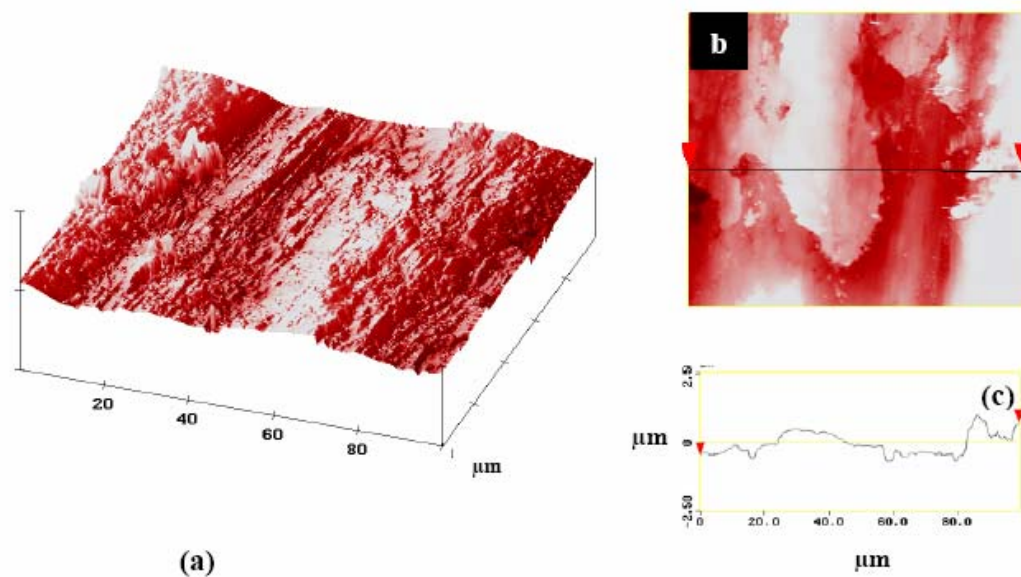


Figure 24: AFM analysis in scanning mode on 100 μm x 100 μm Ta_2AlC surface after testing against Inc718 for 2 km sliding at 550 °C, (a) isometric view, (b) top view, and (c) side view of the profile of the region marked by arrows on top view. All the experiments were done under standard conditions.

When Ta₂AlC was tested against Al₂O₃ at 3N and 1 ms⁻¹, initially μ (~ 0.6) were high, it decreased for few 100 m, then steadily increased to $\mu_s \sim 0.9$ (Fig. 20c, Table 6). The WR of Ta₂AlC was $< 10^{-6}$ mm³/N-m. After sliding for 2 km, the Al₂O₃ surface (Fig. 25a) was covered with spotty tribooxides of the average composition, I = *[Ta_{0.66}Al_{0.33}]O_{1.8}* (Table 5). Similarly, the Ta₂AlC surfaces were smooth and covered with tribooxides of a composition similar to I (Fig. 25b). Note the chemistries of these tribooxides are similar in chemistry to the thermally grown oxides on pure Ta₂AlC [Ch. 2].

3.3.4 XRD

The X-ray diffraction patterns of the surfaces of Ta₂AlC samples after 2 km dry sliding against both Inc718 and Al₂O₃ (Fig. 26) did not reveal any new details compared to the bulk material. The transfer films were either too thin and/or amorphous. The films at 550 °C, were clearly not too thin.

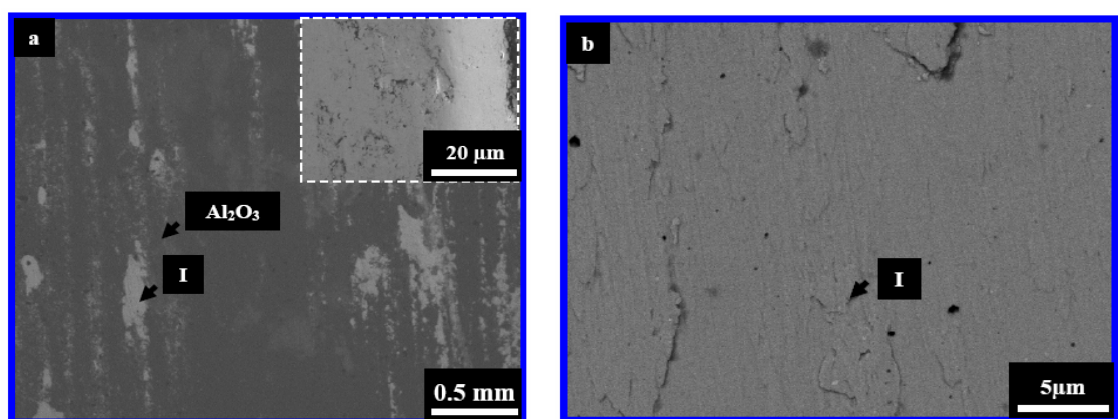


Figure 25: (a) SE FESEM micrographs showing tribofilms formed on alumina surface after dry sliding for 2 km against Ta₂AlC at 550 °C, inset shows the region I at *higher magnification*, and (b) BSE FESEM micrograph of the Ta₂AlC surface. The experiment was done under standard testing condition.

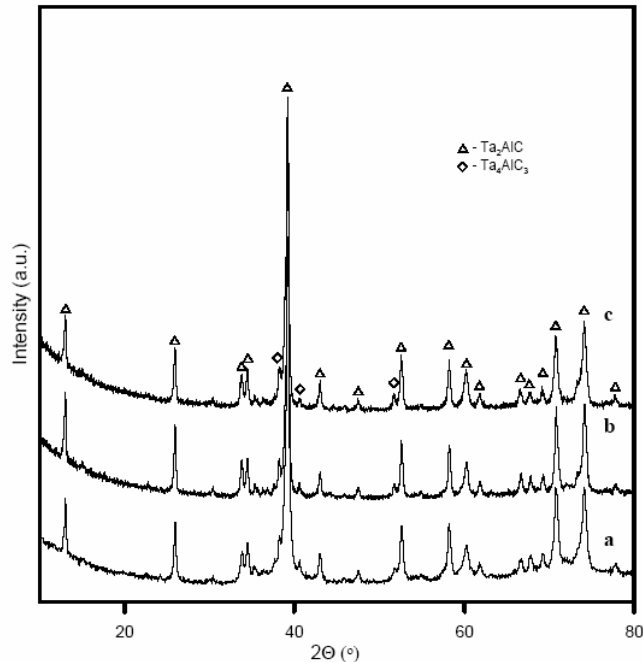


Figure26: XRD patterns of the surfaces of Ta₂AlC counterparts after 2 km sliding: against Inc718 at (a) ambient temperature, and (b) 550 °C; and (c) against Al₂O₃ at 550 °C.

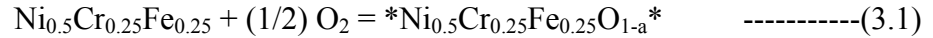
3.4 Discussion

The most important results of this chapter are:

- a) Ti₂AlC, Cr₂AlC, Ta₂AlC and Ti₃SiC₂ tested against Inc718 are excellent tribocouples at 550 °C. The WR's of MAX phases was $\leq 10^{-5}$ mm³/N-m, and that of Inc718 $\sim 10^{-5}$ mm³/N-m. $\mu_s < 0.5$ was observed.
- b) Ta₂AlC tested against Al₂O₃ has a $\mu_s \sim 0.9$, and excellent WR ($< 10^{-6}$ mm³/N-m).
- c) All MAX phases tested against the Ni-based SA's and Al₂O₃ at RT have high WRs ($> 10^{-4}$ mm³/N-m).

3.4.1 Analysis of the 550 °C results

In the case of the Inc718 disc, based on the EDS results, it is reasonable to assume that the following simplified reaction:

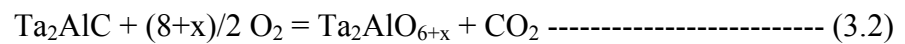


where $a \leq 0.5$.

is occurring on the Inc718 surface (e.g. regions E, F, G and H in Fig. 21 and Table 5). In other words, the friction results in the oxidative wear of the Inc718 surfaces. This layer then apparently smears onto, and coats the MAX-surface (e.g. regions E in Fig. 22).

In some cases, small amounts of elements in the MAX-phases are found in the SA tribosurfaces. For example, phases E and F in Fig. 21 (Table 5).

The tribochemical reaction on the Ta_2AlC surface is most likely (phase I in Table5) :



where $x \leq 0.5$. Similar oxidation reactions can be written for other MAX phases. For simplicity, complete oxidation of MAX phase is assumed in reaction 3.2.

When the Ta_2AlC was sliding against Al_2O_3 , μ_s was ≈ 0.9 (Fig. 20c) and at $< 10^{-6}$ $\text{mm}^3/\text{N}\cdot\text{m}$, the WRs were quite low. A $\text{Ta}_2\text{AlO}_{6+x}$ layer is observed on both the MAX and Al_2O_3 tribosurfaces, for example phase I in Fig. 25 (Table 5) confirming that in the absence of the SA, the transfer films form as a result of reaction 3.2.

3.4.2 Analysis of the room temperature results

Based on the EDS results (e.g. phases A, B and D in Fig. 19), it is reasonable to assume that during dry sliding a partially oxidized, and abrasive third body is formed.

The latter causes high WR of the MAX phases. At this point, it is difficult to deduce an exact tribochemical reaction since the fate of C is not clear.

3.4.3 Proposed Mechanisms and Comparison with Literature

In the literature, it is known that Ni-based binary alloys display a $\mu \sim 0.7$ when sliding against Al_2O_3 at 26 °C. As the temperature is increased, μ drops to 0.3–0.4 because of the formation of lubricious oxides, LO's, like NiO [21, 29]. It is also known that certain oxides, like ZnO and FeO, can be used as solid lubricant at 400 °C, and higher temperatures [Table 7]. Thus it can be concluded that the formation of amorphous LO's due to tribo-oxidation of Inc718 are responsible for ultra-low WRs $\leq 10^{-6}$ mm³/N-m of the MAX phases (Table 6). At $\sim 10^{-5}$ mm³/N-m, the concomitant WR of Inc718 is also low.

Most probably the similarities in hardness of both the MAX phases (4–5 GPa) and Inc718 (5 GPa), and dissimilar nature (former is a ceramics, and latter a superalloy) is beneficial in lowering the adhesive and abrasive wear during initial contact at 550 °C, when μ was 0.6, before decreasing steadily to < 0.5 due to formation of LO's by tribooxidation. Self mated Ni tribocouples (having identical hardness) display $\mu \sim 0.9$ at RT, and retain that value till 700 °C, thereafter it decreases gradually to 0.2 at 900 °C [29]. Self mated tribocouples of Ni-based SA like Nimonic80A (an alloy based on Ni – 20 % Cr) show WR of 10^{-3} mm³/N-m at 26 °C, and it decreases by one order of magnitude at 600 °C [79]. Thus it can be surmised that similar hardness value do not necessarily entail excellent tribological behavior at higher temperatures. It is a complex function of nature of bonding of in solids which influences the formation and adherence of LO's on the tribosurface during dry sliding. In MAX–Inc718 tribocouples, Ni-based LO's generated during tribo-oxidation are retained at the contacts areas and are possibly responsible for the low WR's and μ 's.

In the Ta₂AlC–Al₂O₃ system, the Ta₂AlC surface is tribooxidized at 550 °C to generate oxides similar in composition to thermally grown oxides (Ch. 2). The most probable tribo-reaction is 3.2. These tribooxides have excellent anti-wear properties, but high μ 's. Detailed studies are needed to understand the slip mechanism of these oxides to explain the high μ 's and low WRs.

Table 7: Effect of interfacial film of different chemistries on μ .

Solid Lubricants	Temperature (°C)	μ_s	Ref.
[Ni _{0.45} Fe _{0.22} Cr _{0.23} Ta _{0.1}]O _{0.7}	550	0.3-0.5	Ch.3
[Ni _{0.25} Fe _{0.1} Cr _{0.1} Ti _{0.35} Si _{0.2}]O _{1.2}			
[Ni _{0.5} Fe _{0.25} Cr _{0.25}]O ₁			
[Ni _{0.55} Fe _{0.22} Cr _{0.23}]O _{0.9}			
[Ta _{0.66} Al _{0.33}]O _{1.8}		0.7-0.9	
ZnO	600	0.7	21
NiO	500-800	0.4-0.6	
FeO	300-800	0.6	
CoO	300-600	0.4-0.6	
NiO-FeO	600	0.6	
NiO-TiO ₂	400-800	0.3-0.5	
Ti ₅ O ₉	400	0.8	26-28
Ti ₉ O ₁₇ , γ -Ti ₃ O ₅ , Ti ₉ O ₁₇ , NiTiO ₃	800	0.2-0.8	
SiC _x O _y	400	0.7	26
SiN _x O _y	800	0.6-0.8	

The tribological behavior of some of the MAX phases, but mostly Ti₃SiC₂, at 26 °C has been studied extensively by different groups [47-54]. Different groups have

reported transition in μ from low to high value [48, 52]. Similar transition was also observed in our study (Fig. 18). Souchet et al. [21] studied this transition extensively. It was proposed that the creation and subsequently the microcracking or micro-gouging of an oxy-carbide layer causes this transition. The observance of pulverized oxy-carbide particles on the tested ternary carbides at room temperature indirectly supports this argument. The exact mechanism responsible for the micro-cracking of this oxy-carbide layer is still unclear. More detailed studies on the step-by-step evolution of the oxy-carbide layer, its subsequent delamination and micro-cracking are needed to better understand this dual-regime in μ . Herein, it is reasonable to conclude, that micro-cracking of the partially oxidized layer generates the third body particles, which, in turn, are most probably responsible for the abrasion of the MAX phases and their high WRs at room temperature (Table 4). Along the same lines, it is known that LO's like NiO and ZnO are brittle at room temperature [21].

Interestingly, Hongxiang et al. [54] while studying Ti_3AlC_2 by a block-on-disc method against low carbon steel at 0.8 MPa, but at very high rotation speeds (60 m/s) observed a $\mu \sim 0.1$ and specific WRs $\sim 2.5 \times 10^{-6} \text{ mm}^3/\text{N}\cdot\text{m}$. Self-generating tribofilms, composed of Ti, O, Al and Fe were found in the tribo-contact areas. It can be concluded, brittle oxides at the interfaces can be sheared at room temperature at high rotation speed, most probably because of surface melting. A mapping of the tribological behavior of MAX phases against Inc718 are needed in a wide range of rotation speeds and loading conditions in the entire temperature range [76-79].

Based on the current results, it is tantalizing to visualize a tribosystem running without oil in a system with self-lubricating and self-generating solids as tribo-partners

which are comprised of structural ceramics and SAs, operating continuously at 500 °C and possibly higher temperatures.

3.5 Conclusions

Please refer to Fig. 90 for a schematic understanding of different tribofilms on tribological behavior.

- At room temperature, the tribological behavior of the MAX phases is characterized by high wear rate ($\geq 10^{-4}$ mm³/N-m) and friction coefficients (> 0.4) at room temperature against Al₂O₃ and Inc718. Third body abrasion is believed to be responsible for this behavior.
- At 550 °C, in MAX–Inc718 tribocouples, tribo-oxidation of Inc718 causes formation of Ni_{0.5}Fe_{0.25}Cr_{0.25}O_{1-a} (LO). The formation of this LO at the tribo-contacts is believed to be responsible for the ultra low wear rates of the MAX phases ($< 10^{-6}$ mm³/N-m) and slightly higher WR's of the Inc718 surfaces ($\sim 10^{-5}$ mm³/N-m).
- At 550 °C, in Ta₂AlC–Al₂O₃ tribocouples, tribo-oxidation of Ta₂AlC results in the formation of Ta₂AlO_{6+x} ($x \leq 0.5$) at the tribo-contacts. The formation of these tribo-oxides is responsible for low WRs ($< 10^{-6}$ mm³/N-m) but high μ 's (~ 0.9). There is thus a fundamental difference in the tribological behavior of Ni_{0.5}Fe_{0.25}Cr_{0.25}O_{1-a} and Ta₂AlO_{6+x}.

CHAPTER 4 - SCREENING TESTS TO SELECT BEST COMPOSITIONS FOR FOIL BEARING RIG TESTS

4.1 Introduction

In Ch. 3, the tribological behavior of select MAX phases was studied at 26 °C and 550 °C against Ni-based superalloys (Inc718 and Inc600) and alumina, Al₂O₃. At room temperature (RT), the wear rates, WRs, were relatively high ($\geq 10^{-4}$ mm³/N-m) and no correlation was found between the WRs and the friction coefficients, μ . At 550 °C, the MAX–Inc718 tribocouples displayed $\mu < 0.5$ and $WR < 10^{-5}$ mm³/N-m. Obviously single phase MAX phases cannot be used for oil free turbomachinery because of the relatively high WRs at RT. Furthermore, abrasive third body generated during wear testing at RT could prove disastrous for the engine. It is known in the literature, addition of Ag improves the tribological behavior of composite systems [22]. So Ag was added to the MAX phases to improve their room temperature tribological behavior. Preliminary studies were done, and Cr₂AlC-Ag and Ta₂AlC-Ag composite system against Ni-based SA's were identified as promising tribocouples [55]. In this chapter, the development of the Ag-MAX phase composites from lab scale to prototype samples for testing in actual foil bearing rig is outlined.

4.2 Experimental details

The friction and wear tests were performed using a CSM High Temperature Tribometer capable of going up to 600 °C. The details can be found in Ch. 3.

Compression tests were performed using a hydraulic testing machine (MTS 810, Minneapolis, MN), supplied with a controller (Microconsoler 458.20, MTS), and a 20 kN

capacity load cell. Samples used for testing were cut by diamond wheel into 2 mm^3 cubes. In all tests, a preload, that corresponded to a stress of about 1~2 MPa, was applied to keep the samples aligned. Tensile studies were carried out on the same MTS system. The dimensions of the samples were $50 \times 10 \times 2 \text{ mm}^3$. The tensile creep studies were done at 50 MPa at 550 C for 1h. Strains were measured by a capacitance extensometer (MTS, Minneapolis, MN) with a range 1% strain.

4.3 Synthesis of Ag-based composites

During the course of this work, two types of composites were used for testing; ones prepared at Drexel University and ones in collaboration with 3-ONE-2, Voorhees, NJ. The details of the powders used for the synthesis of the lab samples are described in Table 1. The $\text{Cr}_2\text{AlC}/\text{Ag}$ samples were prepared with different volume fractions of Ag were prepared by pressureless liquid phase (LP) sintering of cold pressed powders at 1200 °C for 10 minutes in an Ar atmosphere. The concentration of Ag in the composite was varied from 5 vol.% to 20 vol.%. Cr_2AlC with 20 vol.% Ag will be henceforth referred to as CrAglab in this thesis. These samples were 10 vol.% porous (Fig. 27a).

The Ta_2AlC powders were not commercially available at the onset of this work. Porous Ta_2AlC samples (10 Vol % porosity) were prepared by hot pressing (HP) stoichiometric amount of Ta (-325 mesh, 99.9% pure), Al (-325 mesh, 99.5 % pure), and graphite (-300 mesh, 99% pure) powders at 1600 °C for 8h under 40 MPa pressure. All the powders were acquired from Alfa Aesar, Ward Hill, MA. Powders were thus prepared by crushing polycrystalline Ta_2AlC samples in our lab by using a mortar and pestle. The resulting powders were mixed with 20 vol.% Ag powder, cold pressed into pellets and

pressureless sintered in an Ar atmosphere at 1200 °C. Henceforth this sample will be referred to as TaAglab. These samples were 10 vol.% porous (Fig. 27b).

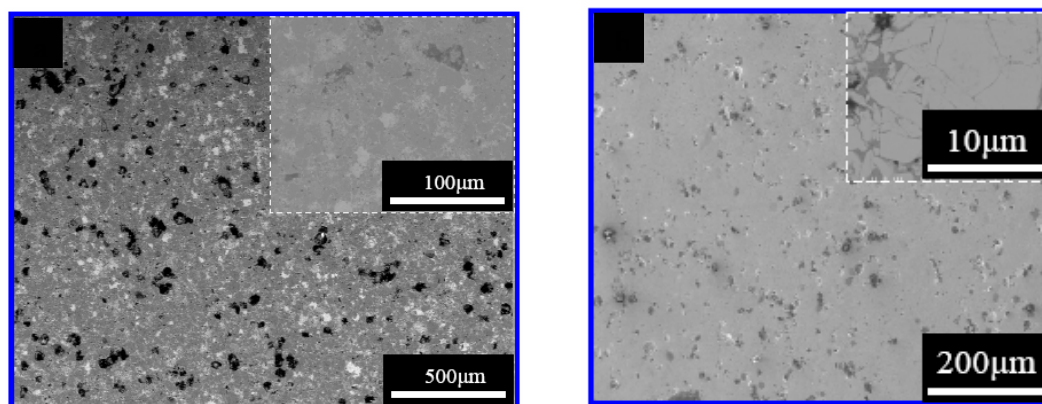


Figure 27: BSE FESEM micrograph of the as-synthesized, (a) CrAglab, and (b) TaAglab samples. Inset of the both figures show the microstructure at higher magnifications.

The details of the powders used for the synthesis of the industrial samples are described in Table 1. The Cr_2AlC -20 vol.% Ag composite samples were obtained by HIPing at 1100 °C for 20 min under ≈ 70 MPa. This sample will be henceforth referred to as CrAg11. The porosity did not exceed 3-5 vol.% (Fig. 28). The Cr_2AlC particles reacted with Ag to form Ag_2Al as the cementing phase. Some of the grains decomposed to Cr_7C_3 .

The first batch of $\text{Ta}_2\text{AlC}/\text{Ag}$ samples were prepared from commercial powders by HIPing at 1100 °C for 20 minutes under 70 MPa. It had a uniform microstructures but they were not fully dense (porosity was about 8-10 vol. %, Fig. 29). This sample will be referred to as TaAg11P. It was not clear why residual pores were found in the first HIP run, but they were most probably related to either degassing, or a breach in the glass envelope used to HIP the samples. This problem was solved by using smaller samples,

which, presumably, prevented the breaching of the glass envelope. The microstructure of the synthesized composite sample is shown in Fig. 30. The Ta_2AlC particles reacted with Ag to form Ag_2Al as the cementing phase. The Ta_2AlC grains were Al-deficient, $Ta_2Al_{1-x}C$ ($x \leq 0.5$). Some of the grains decomposed to Ta_4AlC_3 and Ta_2C . This sample will be referred to as TaAg11. The processing reaction is given by Eq. 2.3.

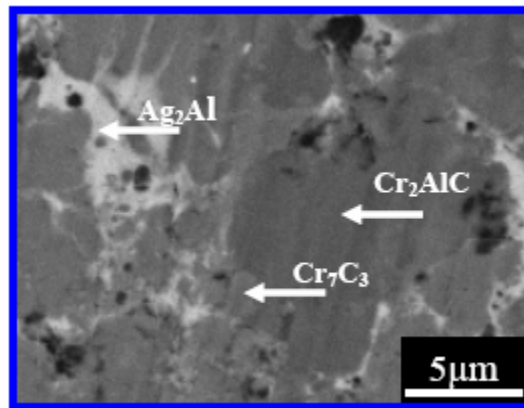


Figure 28: BSE FESEM micrograph of synthesized CrAg11 samples.

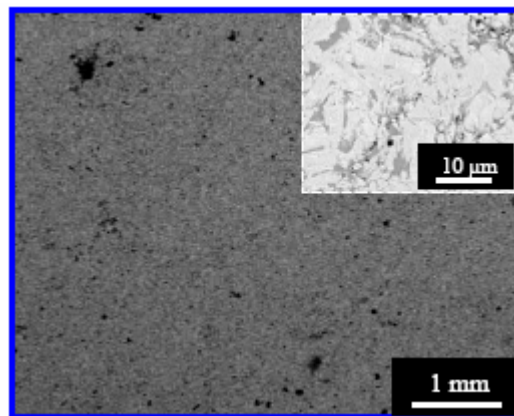


Figure 29: SE FESEM micrograph of the HIPed TaAg11P sample prepared from commercial powders. Inset shows the BSE FESEM micrograph at higher magnification.

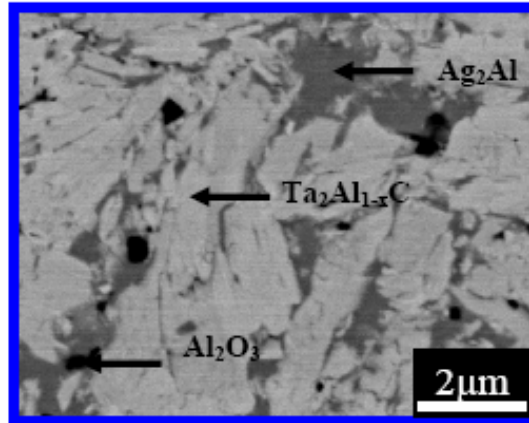


Figure 30: BSE FESEM micrograph of synthesized TaAg11 samples.

4.4 Mechanical properties, μ and WR of the laboratory samples

4.4.1 Influence of Ag additions on μ and WR

The WR of pure Cr_2AlC was $\sim 10^{-3} \text{ mm}^3/\text{N}\cdot\text{m}$, and that of pure Ag was $\sim 2 \times 10^{-4} \text{ mm}^3/\text{N}\cdot\text{m}$ (Table 4). The addition of 5 vol.% Ag to Cr_2AlC reduced its WR at room temperature, by an order of magnitude as compared to pure Cr_2AlC (Fig. 31a). The WR of a Cr_2AlC -20 vol.% Ag sample was $\sim 8 \times 10^{-5} \text{ mm}^3/\text{N}\cdot\text{m}$ (Fig. 31a). The addition of 5 vol.% Ag to Cr_2AlC also reduced μ from 0.65 to 0.5 (Fig 31b). Further increase in Ag content had little effect on μ (Fig. 31b).

It was thus concluded that the tribological properties of MAX-Ag composites with more than 5 vol. % Ag depended weakly on the Ag content. In contrast, the mechanical testing on the composites showed that the 20 vol.% Ag samples had superior compressive strengths as compared to the 10 vol. % Ag composites (Fig. 32). In subsequent sections, the tribological behavior of Cr_2AlC and Ta_2AlC composites with 20 vol.% Ag will be studied. The MP of Ag is $973 \text{ }^\circ\text{C}$. The addition of higher amount of

vol.% of Ag may deteriorate the creep properties of resulting composites at 550 °C. So additions of higher vol.% of Ag were not tried.

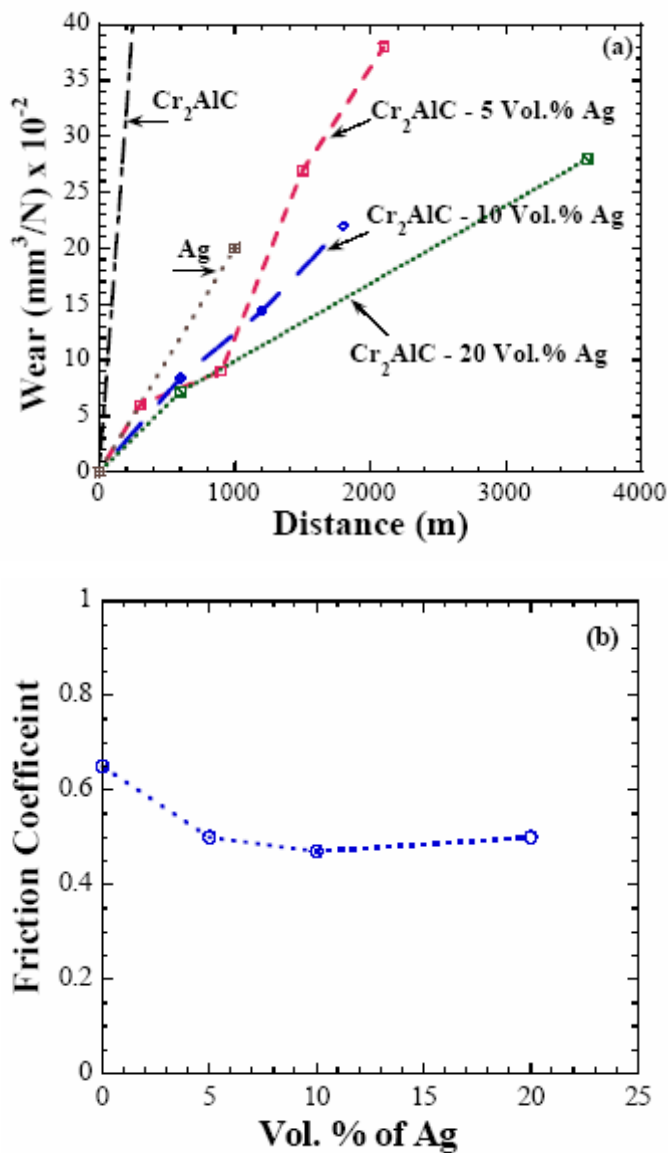


Figure 31: (a) Plot of wear of Cr_2AlC -Ag composite samples as a function of sliding distance against Inc600, and, (b) influence of Ag additions on μ of Cr_2AlC sliding against Inc600. The tribocouples were tested under standard conditions.

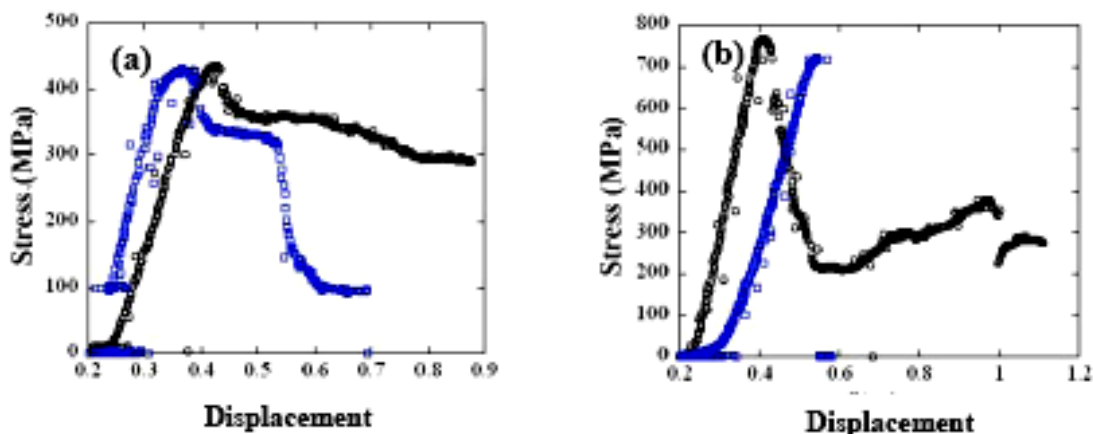


Figure 32: Stress - displacement curves during compression of Cr₂AlC-Ag sample at room temperature with, (a) 10 vol. %, and, (b) 20 vol. % Ag. In each figure, two set of data are plotted to show scatter during testing.

4.4.2 Extensive wear tests of the laboratory synthesized MAX-Ag composites

4.4.2.1 Ta₂AlC-based samples

Extensive tribological and wear tests were performed against Inc600. The tribocouples were subjected to 4 heating and cooling cycles. The maximum temperature at the end of each heating cycle was 500 °C; the average lengths of heating and cooling cycles were about 1300 m and 2500 m, respectively. The total accumulated distance was ≈ 24 km - a distance that is longer than the part would experience during its lifetime. The μ_{mean} was < 0.5 throughout the test, and tended to fluctuate between 0.3 and 0.5 (Fig. 33). The WR after about 5 km was reduced to a value $\leq 5 \times 10^{-6}$ mm³/N-m, and this low WR was maintained till the end of the test (Fig. 33). Based on the profilometric results of the SA discs, their WRs were also quite low. The surface roughness of the superalloy surface did not exceed 5 μm after 24 km of start/stop and 4 thermal cycles (Fig. 34).

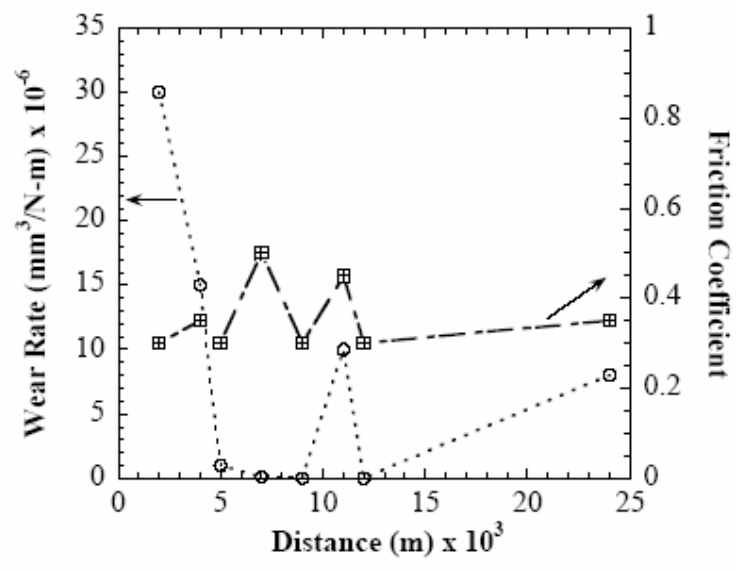


Figure 33: Tribological properties of a TaAglab sample against Inc600. Each data point represents – one heating/cooling down cycle. The test was done under standard conditions.

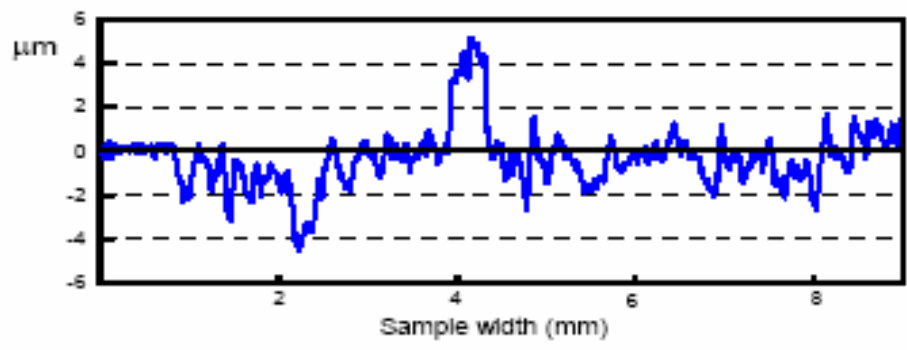


Figure 34: Surface profilometry of Inc600 disc after wear tests against a TaAglab sample for 24 km of dry sliding during thermal cycling.

4.4.2.2 Cr₂AlC-based samples

Figure 35 shows the WR as function of distance after 1 heating and cooling cycle to 500 °C of CrAglab sample against Inc600. During both heating and cooling down

cycles, μ_{mean} was 0.4. At $\sim 10^{-4} \text{ mm}^3/\text{N}\cdot\text{m}$, the WR of this composite was higher than the TaAglab samples.

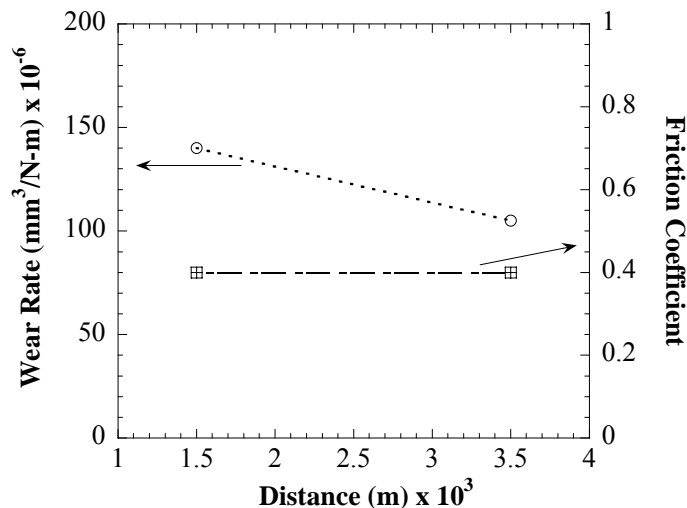


Figure 35: Tribological properties of the a CrAglab sample tested against Inc600. Each data point represents a single heating and cooling down cycle. The tests were done under standard conditions.

4.4.3 μ and WR of MAX-Ag Composites for Rig Testing

The results of wear tests of the TaAglab samples showed that they definitely met the project goal requirements for μ and WRs (Ch. 1). The CrAglab samples also exhibited low μ 's, but their WRs were higher than the Ta-based samples. Despite this fact we decided to make Cr-containing samples because their density – and hence stresses experienced during rig testing or service – was roughly half those of the Ta-containing composites. In the remainder of this chapter we summarize the tribological behavior of these samples.

4.4.3.1 CrAg11 Composites

The results of extensive wear tests during thermal cycling of CrAg11 samples are summarized in the Fig. 36. During thermal cycling, the tribocouple was tested

continuously under dynamic condition, in the temperature range of 26 to 500 °C. The CrAg11 samples exhibited a $\mu_{\text{mean}} < 0.35$ after 8 km. The WR of CrAg11 was $\sim 10^{-4}$ $\text{mm}^3/\text{N}\cdot\text{m}$ during the entire cycling conditions. The wear rate of the Inc718 (Fig. 37) was also low and did not exceed 4-6 μm after 11 km (Fig. 37).

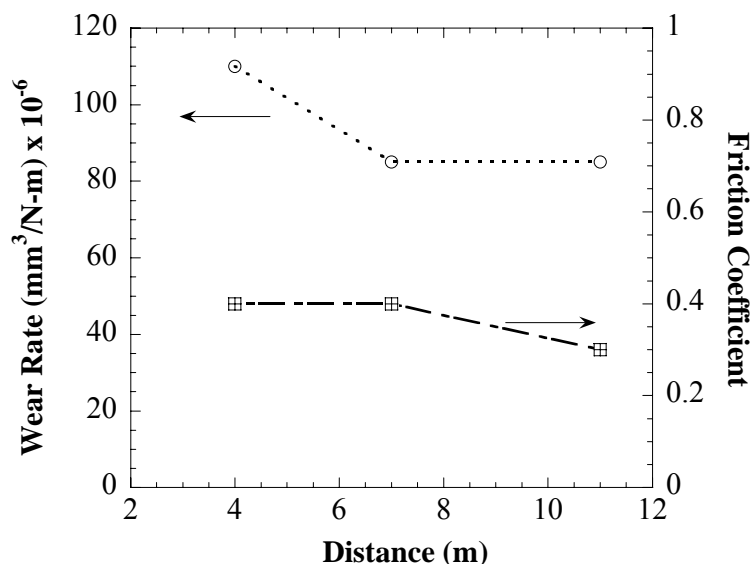


Figure 36: Tribological properties of the CrAg11 sample synthesized from commercial powders tested against Inc718. Each data point represents a heating up and cooling cycle.

4.4.3.2 TaAg11 composites

With a μ of 0.45 the WR of the TaAg11P samples were $\sim 10^{-6}$ $\text{mm}^3/\text{N}\cdot\text{m}$ (Fig. 38), which is considered excellent (Ch. 1). The WR of the Inc600 disc was also low and its dependencies on time and distance were similar to the ones observed when tested against the TaAg11 samples. After the first heating-cooling cycle (or 6 km) it came to the value of 4 μm ; this value was maintained over the later cycles as well (Fig. 39).

The tribological properties of TaAg11 samples tested against Inc718 are shown in Fig. 40. A steady μ of 0.45 was measured during a run of 11 km. The WRs ($\sim 10^{-6}$

mm³/N-m) were also quite good. Although the WRs were found to be higher than for the TaAg11P samples, they were still reasonably low and stable throughout the thermal cycling. Moreover these composites (Fig. 41) had excellent tensile and compressive strength in the 26 to 550 °C temperature range. It is above the minimum safety stresses needed for performance in the rig test (Ch. 1). Creep studies were also performed on these samples. There was negligible creep of this sample after holding at 50 MPa for 1h at 550 °C (Fig. 41d).

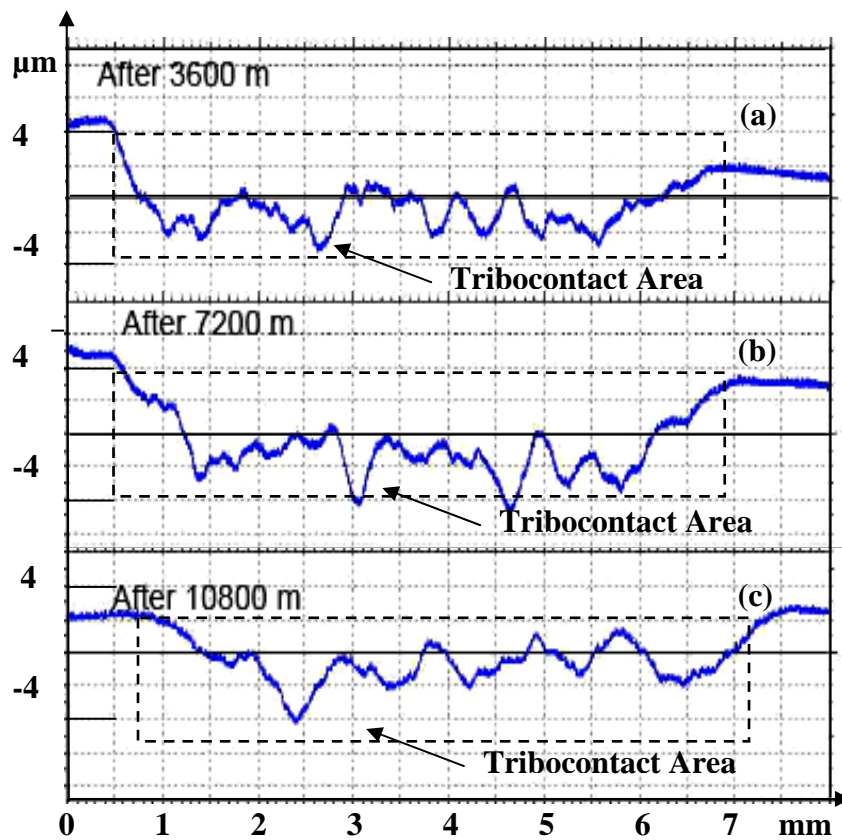


Figure 37: Laser profilometry of the Inc718 surfaces after, (a) first, (b) second, and (c) third heating and cooling cycles during testing against CrAg11 under standard conditions.

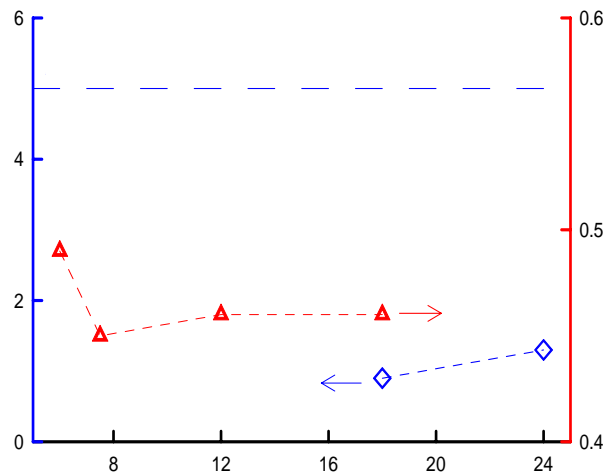


Figure 38: Tribological properties of the TaAg11P sample synthesized from commercial powders.

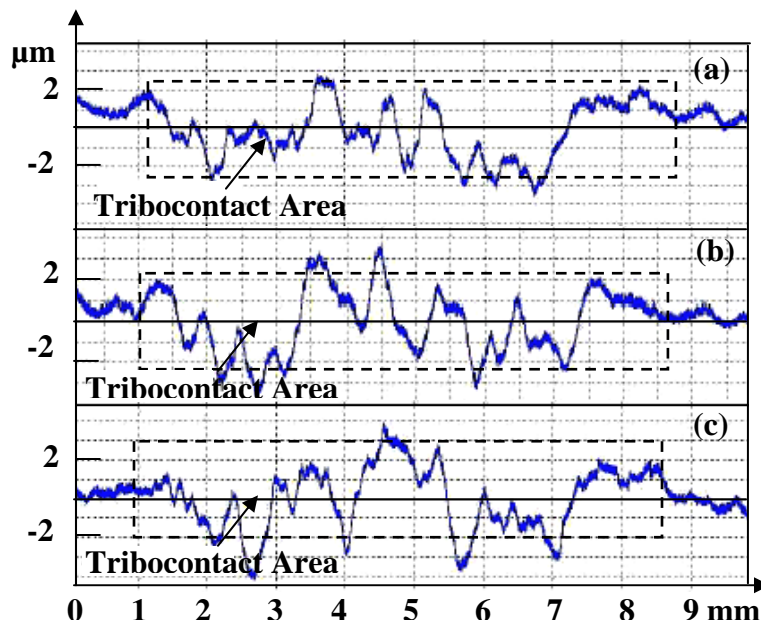


Figure 39: Laser profilometry of the Inc718 surfaces after, (a) first, (b) second, and (c) fourth heating and cooling cycles during testing against TaAg11P samples under standard conditions.

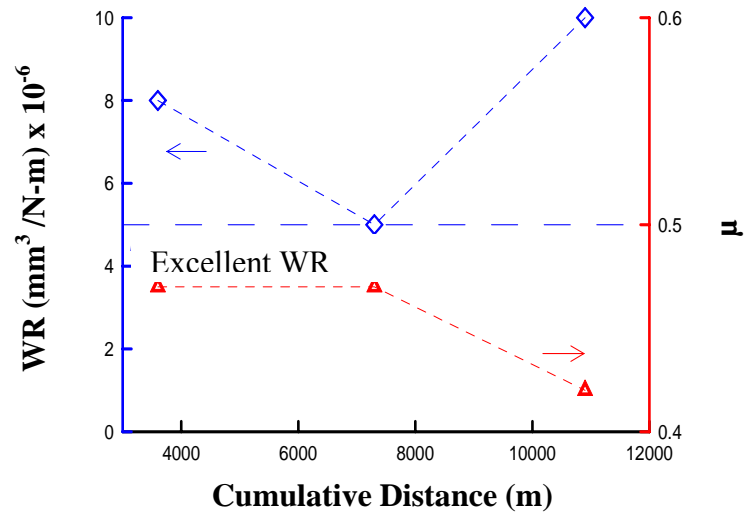


Figure 40: Tribological properties of the dense TaAg11 composites tested against Inc718.

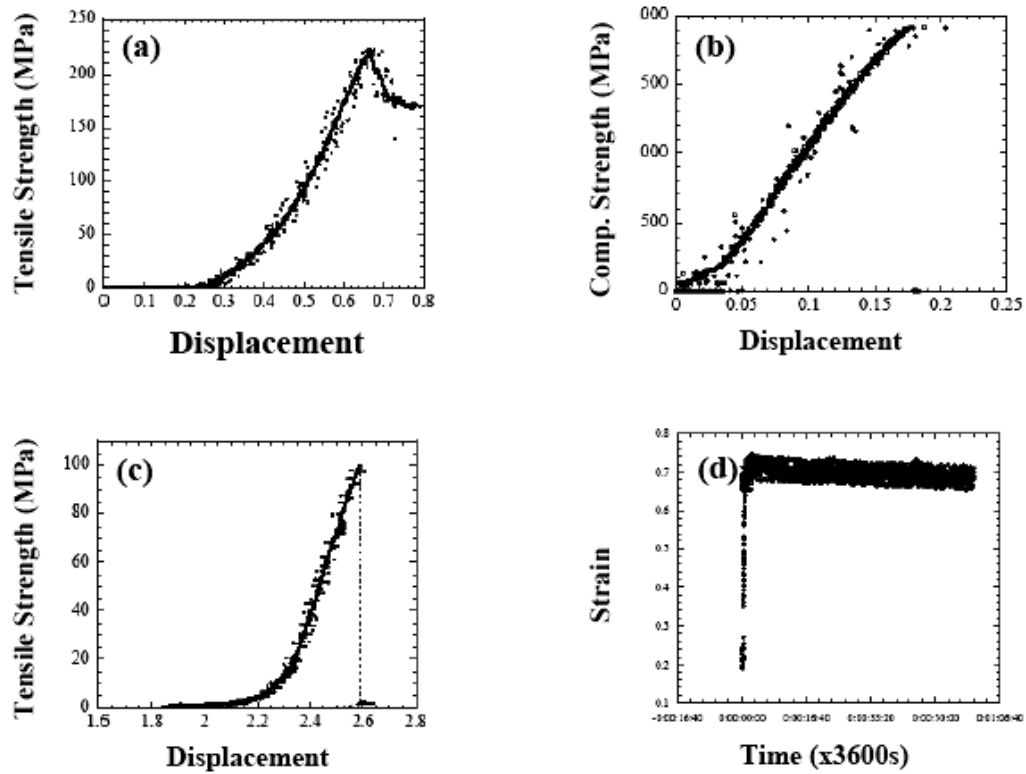


Figure 41: (a) Tensile strength of TaAg11 at 26 °C, (b) compressive strength of TaAg11 composites at 26 °C, (c) tensile strength of TaAg11 composites at 550 °C, and (d) tensile creep resistance of TaAg11 composites tested at 550 °C at 50 MPa for 1h.

4.5 Conclusions

Two MAX-Ag phase composites with 20 vol. % Ag were fabricated using powders fabricated at DU and commercial powders. These were tested against Inc600 and found to have excellent tribological properties. Both the μ 's and WRs were within the design limits imposed by the design engineers as well as having acceptable mechanical strengths at room and 550 °C. The samples were thus identified as candidate materials for further tribological testing in the lab, and subsequently in a foil bearing rig.

CHAPTER 5 - Ta₂AlC/Ag and Cr₂AlC/Ag: PROMISING MATERIALS FOR FOIL/GAS BEARING APPLICATIONS

5.1 Introduction

In Ch. 4, CrAg11 and TaAg11 samples were selected as candidate materials for an exhaustive characterization of their tribological behavior and subsequent testing in a rig. The main goal of this chapter is to study the tribological behavior of MAX/Ag samples against Inc718, and alumina, and to evaluate them as prospective materials for foil bearing applications.

5.2 Experimental Details:

The friction and wear tests were performed using a high temperature tribometer (CSM, Switzerland) capable of going up to 600 °C. The experimental details used for the testing, and characterization of WRs and μ 's were explained in details in Ch. 3. The counter surfaces used for testing were cylindrical (54.5 mm dia x 10 mm thick) discs of Inc718 (High Temp Metals, Inc., Sylmar, CA) or Al₂O₃ (CerCo, OH) or TiAlN (IonBond, Rockaway, NJ) discs. All surfaces were polished to a 1 μ m diamond finish, washed with acetone and dried prior to testing. The MAX/Ag composites were tested in an advanced foil bearing testing rig at a Honeywell's (Torrance, CA) facility.

Shafts were prepared from both CrAg11 and TaAgR samples. Both samples were prepared in collaboration with 3-ONE-2, Voorhees, NJ. Details of the powder used for synthesis of rig samples are listed in Table 1. The required proportion of powders were mixed and sealed in steel cans. The steel cans were subsequently HIPed at 1100 °C for 20 min under 70 MPa pressure (Table 2). Henceforth this sample will be designated as

TaAgR in the rest of the thesis. Foils used during testing of CrAg11-SA tribocouples were chemically etched with FeCl_3 for 10 minutes. The average roughness (R_a) of the tribosurfaces after rig testing was measured in Honeywell's facility.

5.3 Results

5.3.1 Microstructures

The TaAg11 (Fig. 30) and CrAg11 (Fig. 28) composites were > 99 % dense. Due to a reaction between the parent carbide and Ag during processing, the cementing phase at the grain boundary was Ag_2Al . The general composition of matrix Ta_2AlC grains was Al-deficient, i.e. $\text{Ta}_2\text{Al}_{1-x}\text{C}$, where x varied between 0.5 and 1. Small amounts of Ta_4AlC_3 and Ta_2C were also observed (Fig. 42).

In the CrAg11 composite system, some of the Cr_2AlC grains were decomposed to Cr_7C_3 , observed at some of the grain boundaries. Here again, Ag_2Al was the cementing grain boundary phase (Fig. 42).

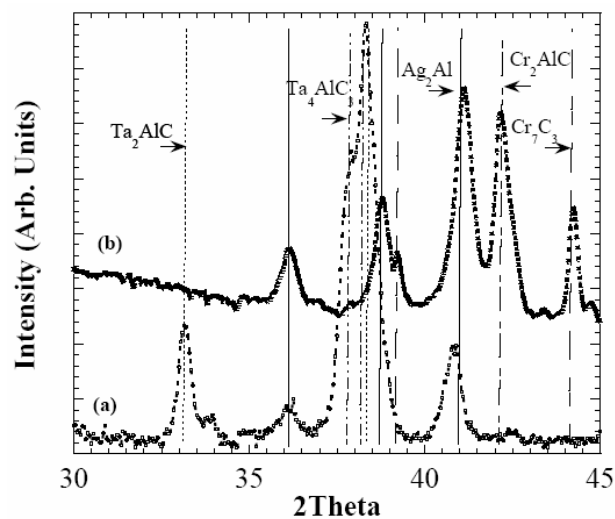


Figure 42: XRD spectra of synthesized, (a) TaAg11, and (b) CrAg11 samples.

5.3.2 μ as a function of sliding distance

5.3.2.1 Room temperature

When the TaAg11 composite was tested against the Inc718, the initial μ was ~ 0.1 , which increased to ~ 0.3 , before reaching $\mu_s \sim 0.6$ (Fig. 43a and Table 8). When tested against harder substrates, such as Al_2O_3 and the TiAlN coated samples, μ was initially low but increased gradually to a $\mu_s \sim 0.35$ (Figs. 43 b and c).

When the CrAg11 samples were tested against Inc718, μ was not stable; μ_s was ~ 0.8 (Fig. 43d). When tested against Al_2O_3 , the initial μ was high, went through a shallow minimum, before gradually increasing to a stable $\mu_s \sim 0.55$ (Fig. 43e).

5.3.2.2 Testing at 350 °C

When the TaAg11 sample was tested against the Inc718, μ_s varied between 0.2 and 0.3. The response was not smooth, however, but was characterized by spikes during which μ increased to ~ 0.6 (Fig. 44a).

When the CrAg11 sample was tested against the Inc718, μ_s varied between 0.4 and 0.5. Here again spikes in μ up to 0.65 were observed (Fig. 44b).

5.3.2.3 Testing at 550 °C

Figures 45a and b present the sliding results of the TaAg11 samples against Inc718 - performed in May and September 2006 - on inner and outer tracks. In both cases, the initial μ 's were relatively high (0.6), but gradually decreased to 0.5. Initially, the μ values were not stable, however, but varied between 0.6 and 0.8 in some locations during the first 600-800 m, before settling in at a $\mu_s \sim 0.5$ (Figs. 45a and b). The experiments were stopped intermittently to satisfy two purposes; mimicking the in service hot start-and-stop conditions, and to measure the wear of the samples as a function of wear distance.

When the CrAg11 samples were tested against Inc718 similar behavior was observed: μ was initially high (~ 0.6) and unstable, before settling in at a $\mu_s \sim 0.35$ (Fig. 45c). When the TaAg11 samples were tested against Al_2O_3 (Fig. 45d), the μ 's were again initially high, before dropping to 0.4. Note, however, that no spikes in μ were observed in this case.

5.3.2.4 Variations in μ during heating and cooling cycles

In service the contact between the foils and the shaft occurs at ambient conditions on startup and at whatever temperature the system is at on shut down. To simulate these conditions in the lab, the tribometer was heated to 500 °C, cooled down to 150 to 250 °C, three times. During the thermal cycling, the μ 's were monitored continuously.

During the first heat up for TaAg11–Inc718 tribocouples, the initial μ 's were low (< 0.1), increased steadily to 0.4, before dropping at 100 °C, and decreased steadily to 0.2 (Fig. 46a). At 200 °C, it steadily increased to 0.5 at 500 °C. The system was then cooled; during the entire cooling cycle, μ varied between 0.5 and 0.6 (Fig. 46a).

The tab was then removed and its weight was measured and surface profilometry was carried out on the Inc718 surface. The pair were then placed again in the tribometer, on the same track, whose temperature had cooled down to ≈ 150 °C. During the subsequent heating cycle, μ started low (< 0.1), before increasing to 0.2. The μ was stable at 0.2 till 250 °C, thereafter it increased steadily to 0.5 at 500 °C (Fig. 46a). During the second cooling cycle, μ was constant at ≈ 0.5 , and in contradistinction to the first cooling down cycle, was much more stable (Fig. 46a). The tab was again reweighed and surface profilometry on Inc718 disc was done. During the third heat up cycle μ increased gradually from 0.2 to 0.4, and was fairly stable during the entire cycle. Unlike the first

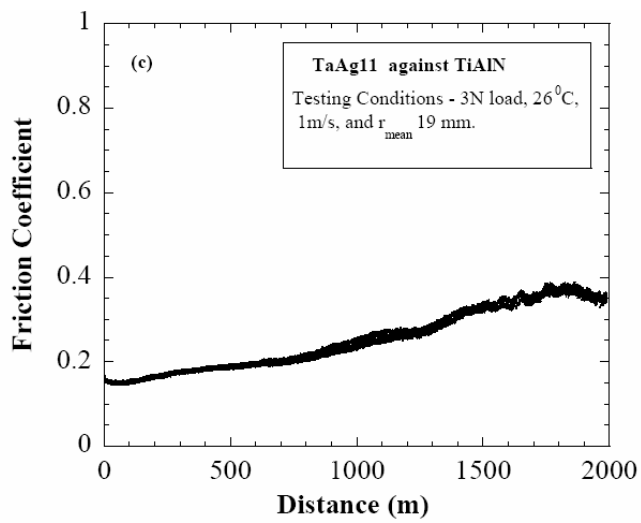
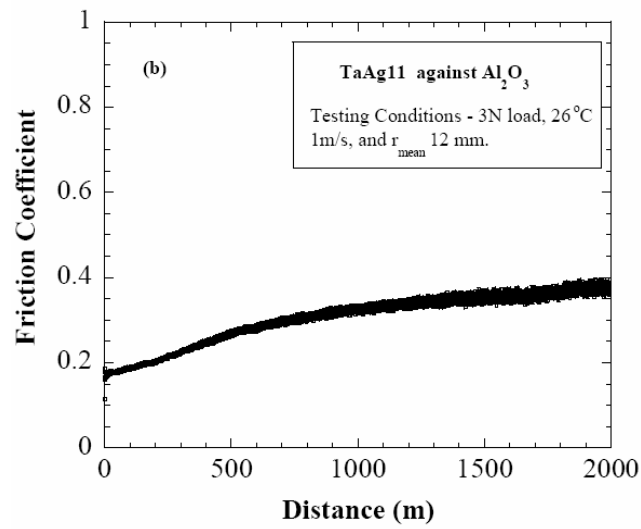
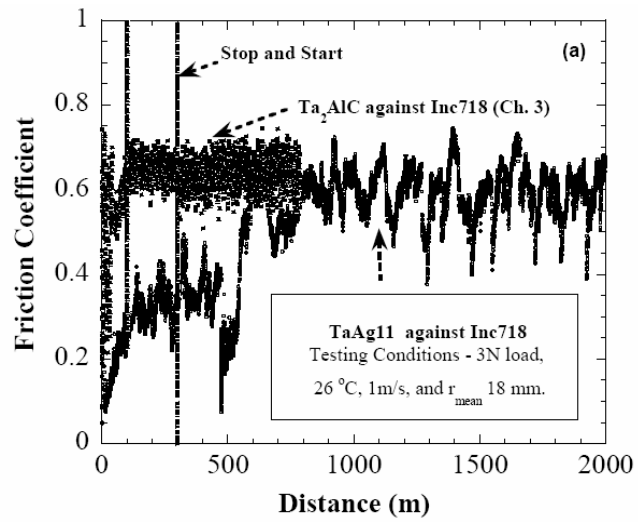
two cycles, μ showed no sharp transition and the final μ was lower than during the first two heating cycles (Fig. 46a). During the third cool down cycle, μ was stable at 0.4 during the entire cycle (Fig. 46a).

During similar testing for the CrAg11–Inc718 tribocouples, the initial starting μ 's were low (< 0.3), increased to 0.8, started dropping from 100 °C, and decreased steadily to 0.3. After 200 °C, it steadily increased to 0.5 at 500 °C (Fig. 46b). During the entire cooling cycle, μ , decreased gradually from between 0.5 and 0.3, in some locations for example between 350 to 400 °C there were some fluctuations (Fig. 46b). During subsequent heat up cycles, μ gradually increased from < 0.3 to ~ 0.5 , mimicking the first heating up cycle. However, unlike the first heat up cycle, no spike in μ was observed (Fig. 46b). Also during subsequent cooling down cycles, μ gradually decreased to 0.3. Some fluctuations in μ were observed (Fig. 46b).

5.3.3 Wear and Wear Kinetics

5.3.3.1 Wear of tribocouples during isothermal studies

The specific WR of the TaAg11 samples, measured after 2 km of sliding at room temperature, was $2 \times 10^{-5} \text{ mm}^3/\text{N}\cdot\text{m}$ (Table 8). The roughness of the SA surface – as measured by the profilometer - is shown in Fig. 47a. No signs of large gouges were observed on the track; the roughening observed was $< 0.5 \text{ }\mu\text{m}$ (Fig. 47a). After isothermal sliding at 350 °C for 1 km, the specific WR of the TaAg11 sample $< 10^{-6} \text{ mm}^3/\text{N}\cdot\text{m}$; no gouging was observed on the Inc718 track (Table 8). The WR of the CrAg11 composites



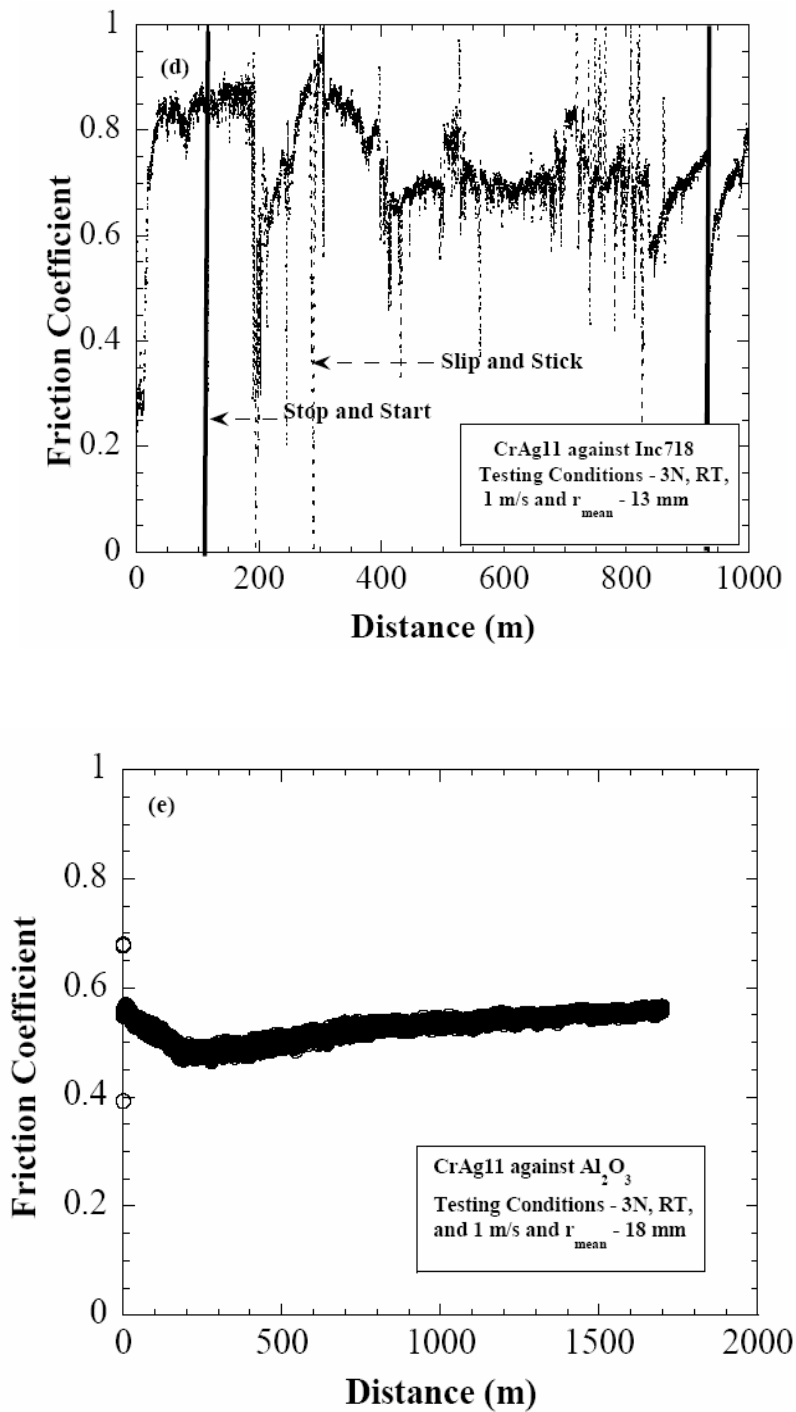


Figure 43: Variation in μ as a function of sliding distance at ambient temperature in different tribocouples; (a) Inc718 – TaAg11, (b) Al_2O_3 - TaAg11, (c) TiAlN coatings - TaAg11, (d) Inc718 - CrAg11, and (e) Al_2O_3 – CrAg11.

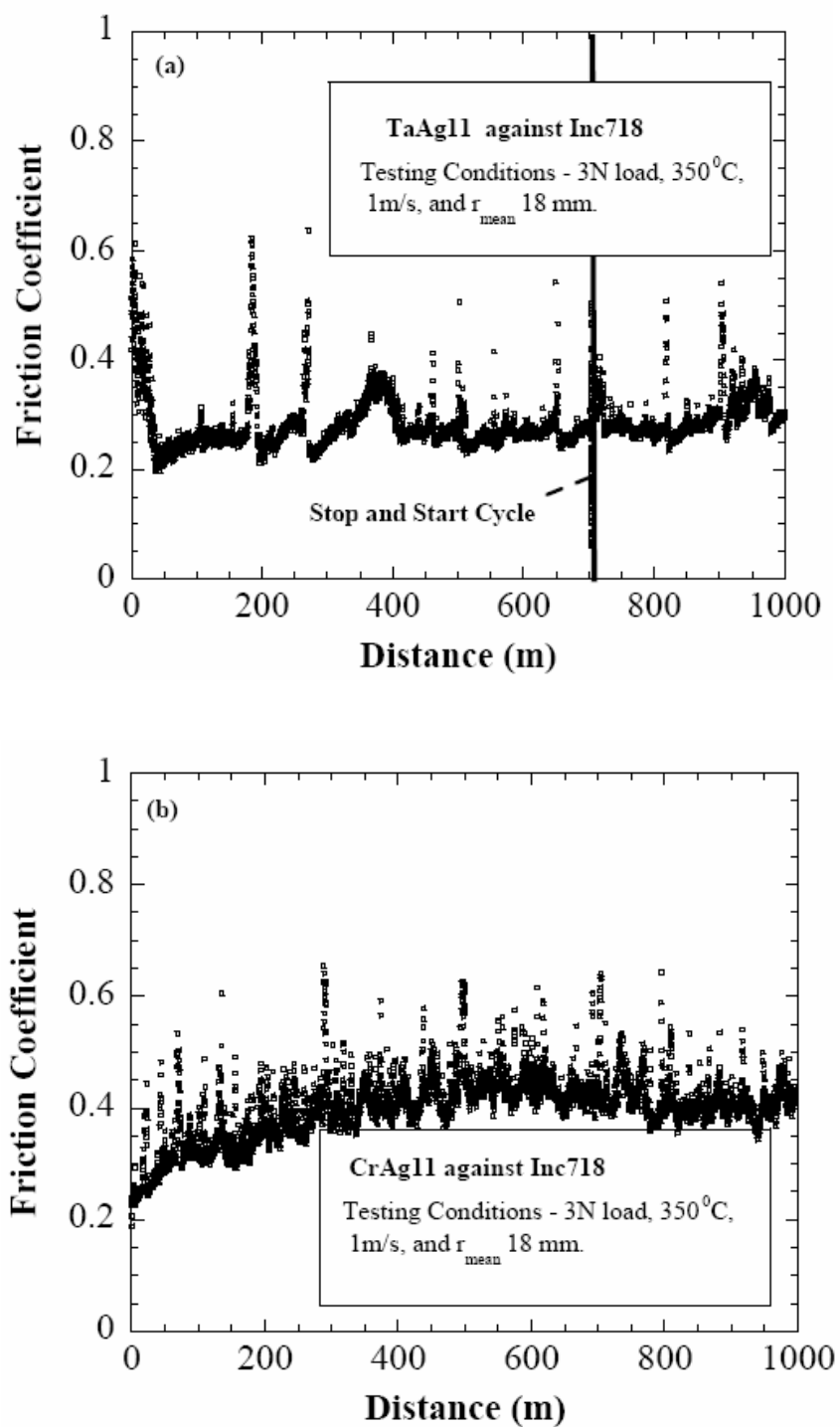
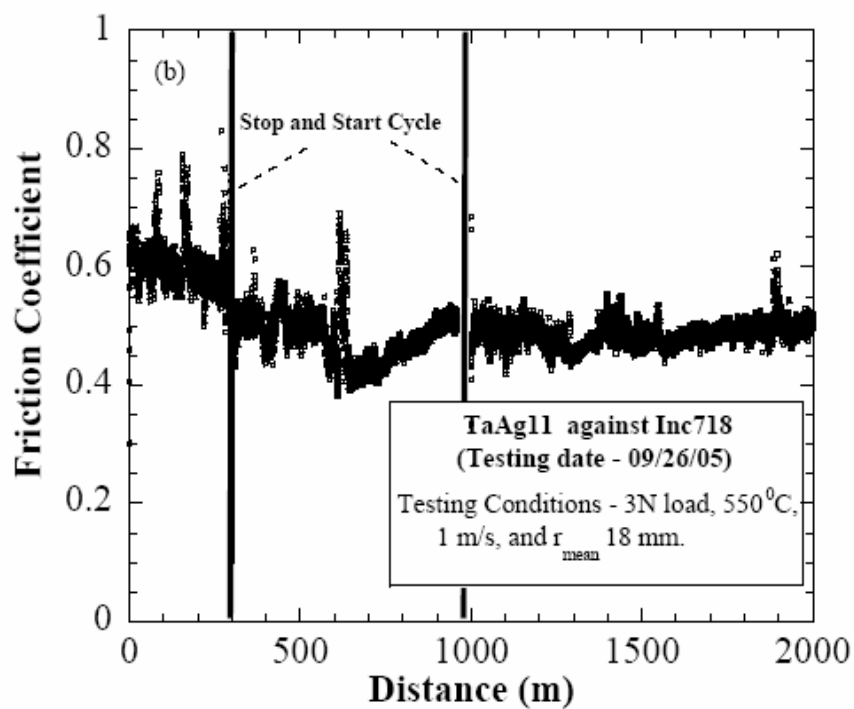
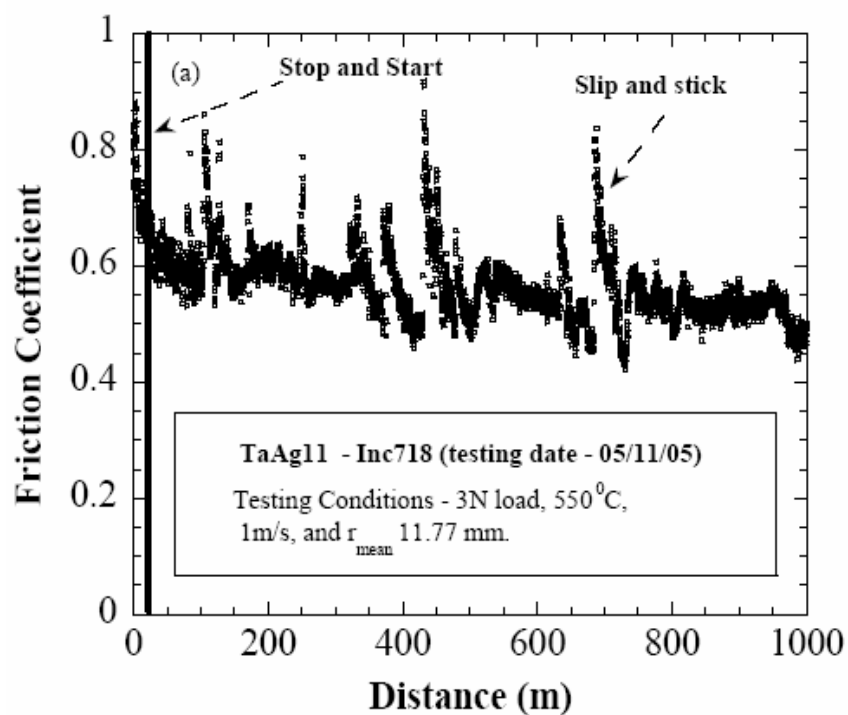


Figure 44: Variation in μ as a function of sliding distance when Inc718 was tested at 350 °C against, (a) TaAg11, and, (b) CrAg11. All the tests were done under standard conditions.



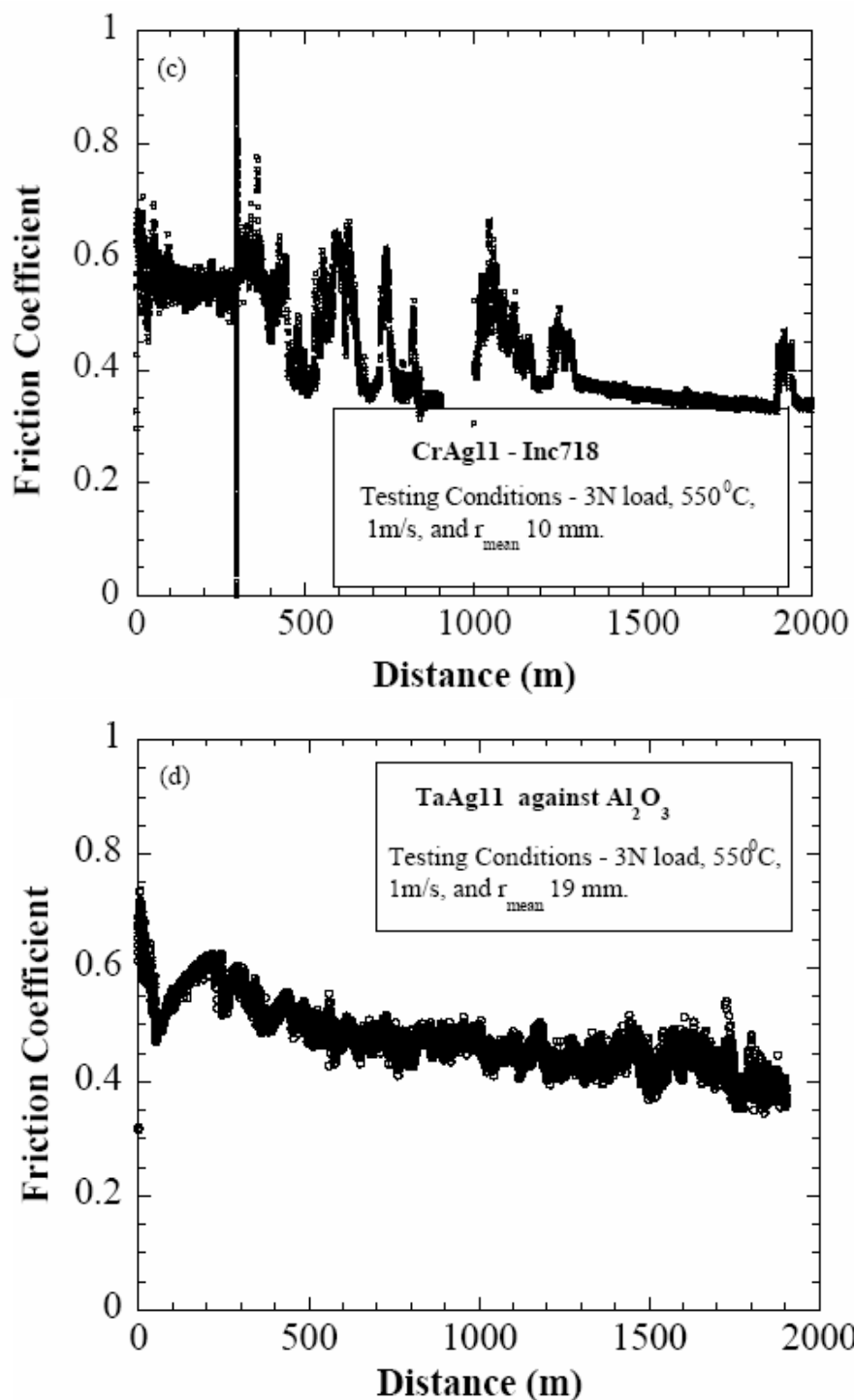
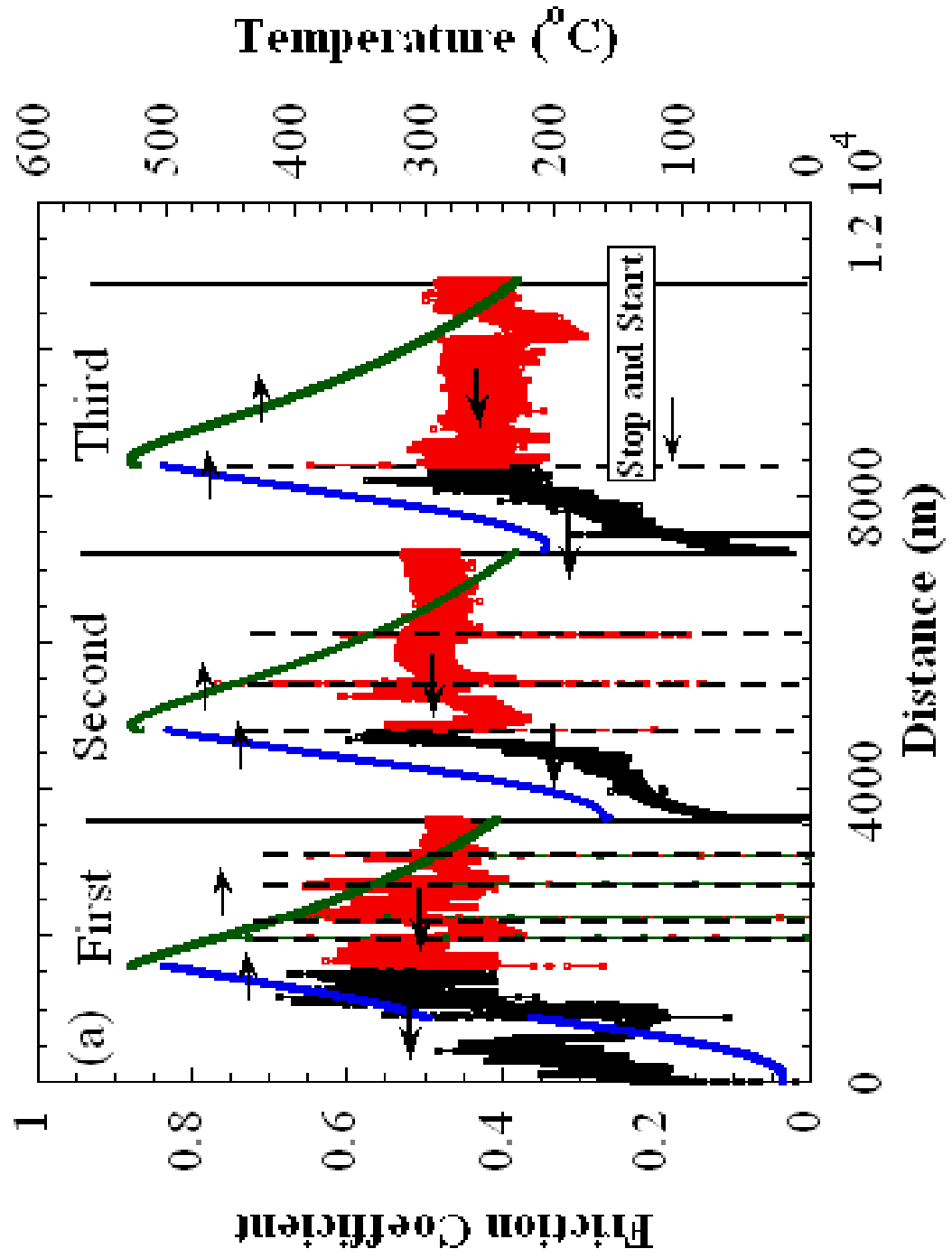


Figure 45: Variation in μ as a function of sliding distance during testing of different tribo-pairs at 550 °C: (a) TaAg11 against Inc718 ($r_{\text{mean}} \sim 12$ mm), (b) TaAg11 against Inc718 ($r_{\text{mean}} \sim 18$ mm), (c) CrAg11 against Inc718 ($r_{\text{mean}} \sim 10$ mm), and (d) TaAg11 against Al_2O_3 ($r_{\text{mean}} \sim 19$ mm). All the tests were done under standard conditions.



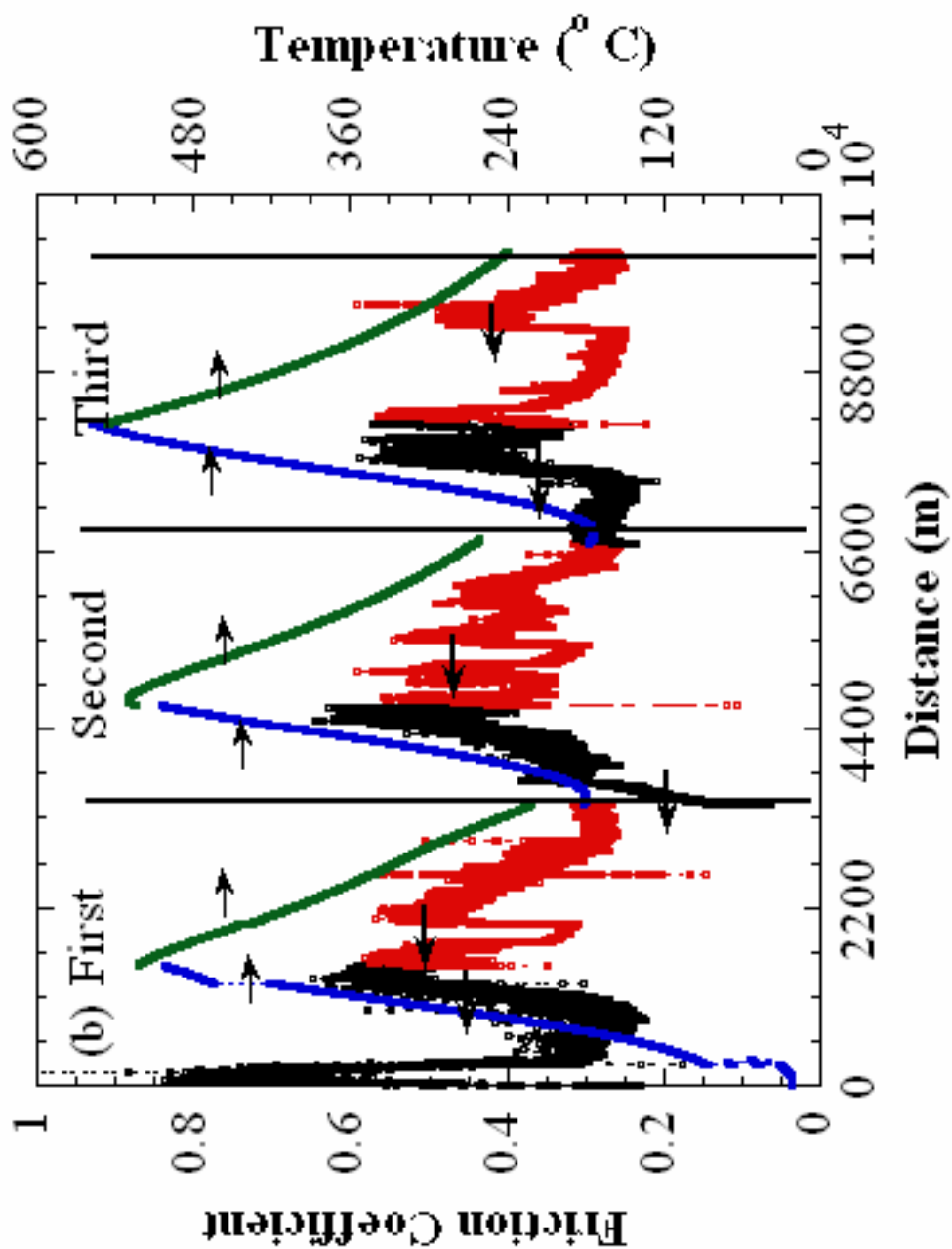


Figure 46: Variation in μ 's of, (a) TaAg11-Inc718 tribocouple, and (b) CrAg11-Inc718 during heating and cooling in 26 to 500 °C temperature range. Black data points represent μ - during heating; red, μ - during cooling; blue - temperature during heating; green - temperature during cooling; black dotted line - stop and start; black solid line - donates end of one cycle, and start of next cycle.

was $\sim 1 \times 10^{-4} \text{ mm}^3/\text{N-m}$ (Table 8).

After sliding for 2 km at 550 °C, the wear on the Inc718 counterpart was markedly higher than at room temperature. Valleys (gouges) and mountains (tribofilms) were observed on the tracks (Fig. 47b). The wear of the tracks of the Inc718 was modeled by assuming a uniform gouge of 2 μm over the entire track (see Appendix A for details). The calculated WR was $\sim 2 \times 10^{-4} \text{ mm}^3/\text{N-m}$. The corresponding WR of the TaAg11 composite tab was $\sim 5 \times 10^{-5} \text{ mm}^3/\text{N-m}$ (Table 8). Using similar assumptions, the WRs of the Inc718 was $\sim 1 \times 10^{-4} \text{ mm}^3/\text{N-m}$ and that of the CrAg11 composites was $\sim 7 \times 10^{-5} \text{ mm}^3/\text{N-m}$ (Table 8).

When the TaAg11 was tested against Al_2O_3 , the wear behavior, as the temperature was increased from ambient to 550 °C was quite different. After 2 km of sliding, the specific WR of the TaAg11 pin increased from ~ 3 to $5 \times 10^{-5} \text{ mm}^3/\text{N-m}$ in the 26 to 350 °C temperature range to $\sim 6 \times 10^{-4} \text{ mm}^3/\text{N-m}$ at 550 °C. In both the cases, the corresponding wear of the Al_2O_3 was negligible as material was visibly transferred from the TaAg11 to the Al_2O_3 surface (Fig. 48).

Figures 49a and b summarize the wear results obtained in this work as a function of temperature. The variations in μ , as a function of temperature, are shown in Fig. 49c. The implications of these results are discussed below.

5.3.3.2 Wear of tribocouples during thermal cycling

After the first heat/cool cycle of the TaAg11–Inc718 tribocouple, - a total distance of 3 km - the WR of the Inc718 was $\sim 2 \times 10^{-4} \text{ mm}^3/\text{N-m}$; after 11 km, it decreased to $\sim 6 \times 10^{-5} \text{ mm}^3/\text{N-m}$ (Figs. 50 a and b). Note assumptions made in Appendix A were used for

Table 8 – Summary of WRs and μ of different tribocouples.

Static	Dynamic	Temp. (°C)	WR _s (mm ³ /N-m)	WR _d (mm ³ /N-m)	μ s	Refs.
Ta ₂ AlC	Inc718	26	1.7×10^{-2}	CND	0.6	Ch.3
		350	3×10^{-5}	CND	0.5	Ch.5
		550	$< 10^{-6}$	$\sim 10^{-5}$	0.4	Ch.3
	Al ₂ O ₃	26	1.8×10^{-2}	Deposition	0.8	
		350	7.5×10^{-4}	Deposition	0.8	
		550	$< 10^{-6}$	Deposition	0.9	
TaAg11	Inc718	26	2×10^{-5}	CND	0.6	Ch.5
		350	$< 10^{-6}$	CND	0.3	
		550	5×10^{-5}	$\sim 2 \times 10^{-4}$	0.5	
	Al ₂ O ₃	26	3×10^{-5}	Deposition	0.4	
		350	5.5×10^{-5}	Deposition	0.45	
		550	6×10^{-4}	Deposition	0.47	
TiAlN	26	8×10^{-6}	Deposition	0.35		
Cr ₂ AlC	Inc718	26	1.6×10^{-3}	CND	0.6	Ch.3
		550	0	$\sim 10^{-5}$	0.35	
CrAg11	Inc718	26	5×10^{-5}	CND	0.8	Ch.5
		350	1×10^{-4}	CND	0.4	
		550	7×10^{-5}	$\sim 1 \times 10^{-4}$	0.45	
	Al ₂ O ₃	26	7×10^{-5}	Deposition	0.55	
Inc750	PS300	26	$(3.9 \pm 0.5) \times 10^{-5}$	$(6.6 \pm 2.5) \times 10^{-5}$	0.23 ± 0.05	35
		500	$(1.3 \pm 0.3) \times 10^{-5}$	$(3.9 \pm 0.3) \times 10^{-4}$	0.29 ± 0.04	
		650	$(3.1 \pm 0.8) \times 10^{-5}$	$(7.1 \pm 1.6) \times 10^{-4}$	0.31 ± 0.04	
	PS304	26	$(0.96 \pm 0.3) \times 10^{-5}$	$(4.8 \pm 0.3) \times 10^{-4}$	0.31 ± 0.05	
		500	$(0.32 \pm 0.5) \times 10^{-5}$	$(2.8 \pm 0.3) \times 10^{-4}$	0.25 ± 0.02	
		650	$(0.38 \pm 0.4) \times 10^{-5}$	$(1 \pm 0.1) \times 10^{-4}$	0.23 ± 0.02	
		800	$(6.9 \pm 2) \times 10^{-5}$	$(2.6 \pm 0.2) \times 10^{-4}$	0.37 ± 0.03	

- WR_s – Wear Rate of Static Partner.
- WR_d – Wear Rate of Dynamic Partner.
- CND – Beyond the resolution of Laser Profilometer.

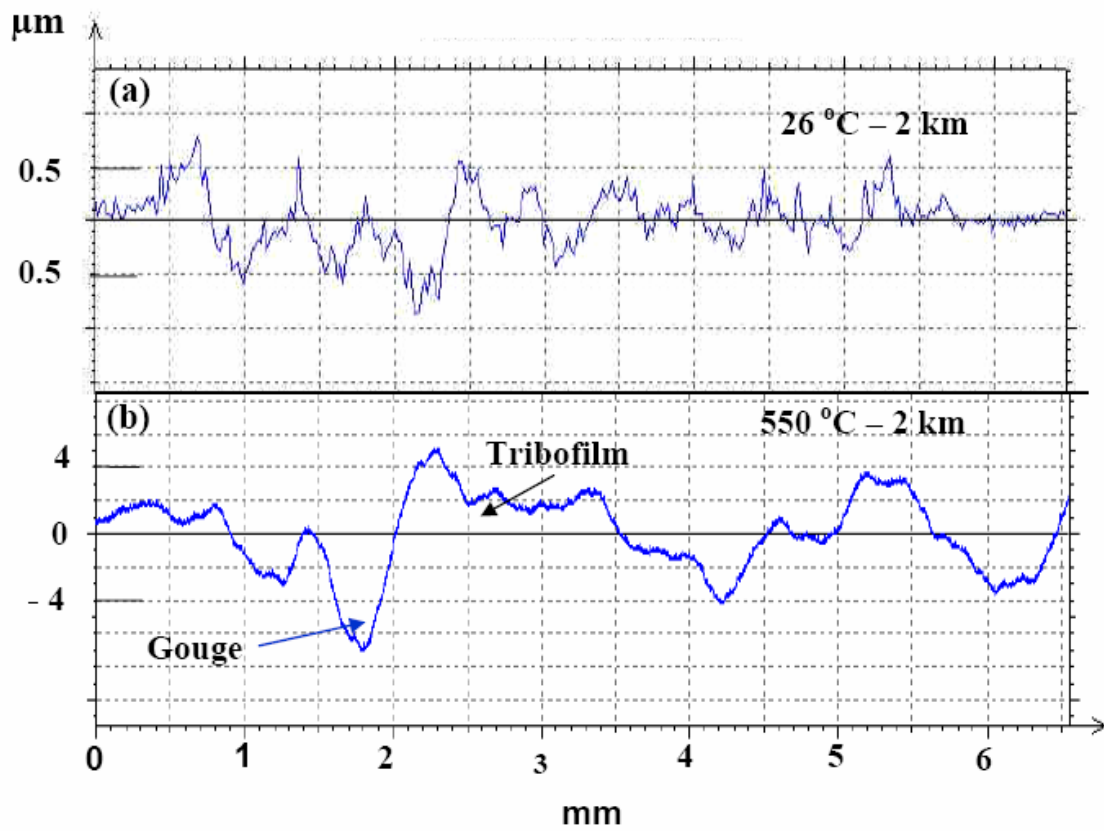


Figure 47: Laser profilometry on Inc718 surfaces after sliding against TaAg11 at, (a) room temperature, and (b) 550 °C.

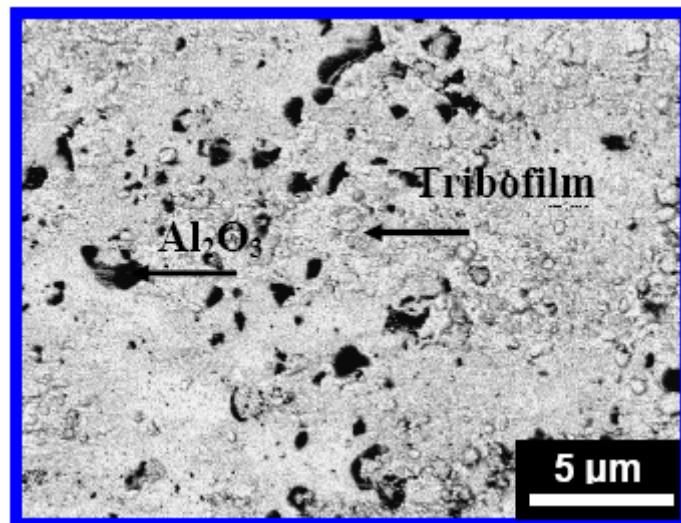


Figure 48: BSE FESEM micrograph showing tribofilms formed on alumina surface after sliding against TaAg11 at 550 °C for 2 km.

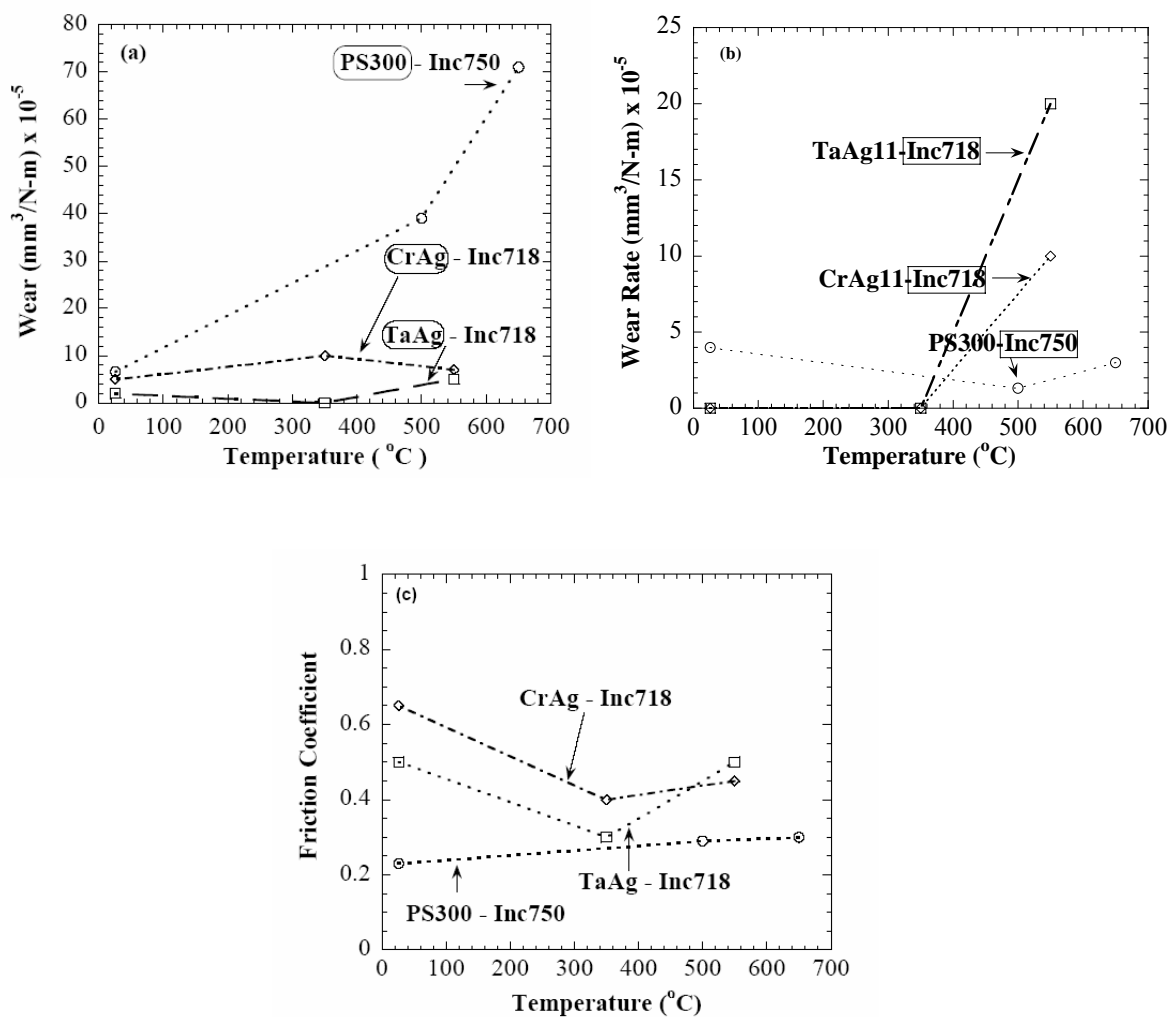


Figure 49: Temperature dependencies of WRs of, (a) different ceramic-based materials, and (b) SA's, and, (c) of μ_{mean} . The WR of the phase encircled with a rectangular box is reported for each (a) and (b).

calculating the WRs of the Inc718. The corresponding WRs of the TaAg11 samples varied between 8 to 10 $\times 10^{-6}$ $\text{mm}^3/\text{N}\cdot\text{m}$ (see Fig. 40 in Ch. 4).

5.3.3.3 Wear Kinetics

At room temperature, the WRs for both the Ta- and Cr-containing samples were

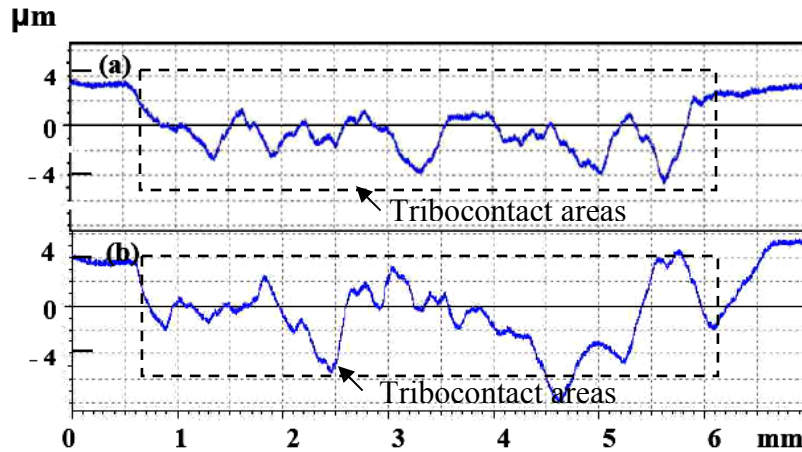


Figure 50: Laser profilometry of the Inc718 surfaces after, (a) one heating and cooling cycle, and (b) three heating and cooling cycles after testing against TaAg11 under standard conditions

linear as a function of sliding distance (Fig. 51a). At 550 °C, the WRs of the CrAg11 and TaAg11 tabs against the Inc718 discs were quite different (Fig. 51b). For the former, the initial wear is relatively high before becoming negligible; for the latter, the wear was linear with sliding distance (Fig. 51b).

The total cumulative WR of the TaAg11 samples against Inc718 is $2 \times 10^{-4} \text{ mm}^3/\text{N}\cdot\text{m}$, after 3 km of continuous sliding, which corresponds to 1 heating up and cooling cycle (Fig. 52a). It decreased to $7 \times 10^{-5} \text{ mm}^3/\text{N}\cdot\text{m}$ after 11 km of sliding (i.e. after the 3rd heat/cool cycle) (Fig. 52a). The μ was less < 0.5 during the entire operation except in some locations where fluctuations were observed (Fig. 46a).

The total cumulative WR for CrAg11/Inc718 tribocouple is $2 \times 10^{-4} \text{ mm}^3/\text{N}\cdot\text{m}$ after the first heat/cool cycles, and decreased to $1 \times 10^{-4} \text{ mm}^3/\text{N}\cdot\text{m}$ at the end of third heat/cool cycles (Fig. 52b); $\mu < 0.5$ for the entire regime (Fig. 52b).

5.3.4 Rig test results

TaAgR and CrAg11 samples were tested in a foil bearing rig against Ni based SA foils. Initially during testing, the TaAgR–SA foil bearing system showed higher starting torque at room temperature, in other words, μ was > 0.5 . During tribological studies of TaAg11-Inc718 tribocouples in the lab, it was shown that with increase in temperature, μ decreases (Fig. 49c). In order to overcome the high starting torque at RT, the system was started at 350 °C. The starting torque decreased, and the tribocouple was tested at that temperature for 5050 cycles. The system was subsequently tested at 550 °C for 2370 cycles, and then at room temperature for 2590 cycles. After the completion of the 10,000 cycles, dark contact areas were observed on the SA surface (Fig. 53a). Before the testing, the surface roughness of SA, R_a was 0.2 μm . It increased to 0.4 μm in contact areas after 10,000 cycles. The tested TaAgR sample appeared smooth (Fig. 53b), before the rig test, R_a was 0.1 μm , and after rig testing - R_a increased to 0.2 μm .

The CrAg11–SA tribocouples system was tested for 3000 cycles in the ambient to 550 °C temperature range. Initially the tribocouple was tested isothermally at 350 °C for 1000 cycles, subsequently at 550 °C, and then at ambient temperature for 1000 cycles. The surfaces finish of FeCl₃ treated SA surface was $R_a \sim 0.9 \mu\text{m}$. After 3000 cycles, dark color tribo-contact areas have $R_a \sim 0.8 \mu\text{m}$ (Fig. 54a). The surfaces of the SA were intentionally roughened to increase the mechanical adhesion of the dark color tribofilms observed during testing. The detailed mechanism for the formation of the tribofilms, and their influence on tribological behavior are discussed in details in Ch.6. Like the TaAgR sample, the CrAg11 sample micro-smooth after testing (Fig. 54b).

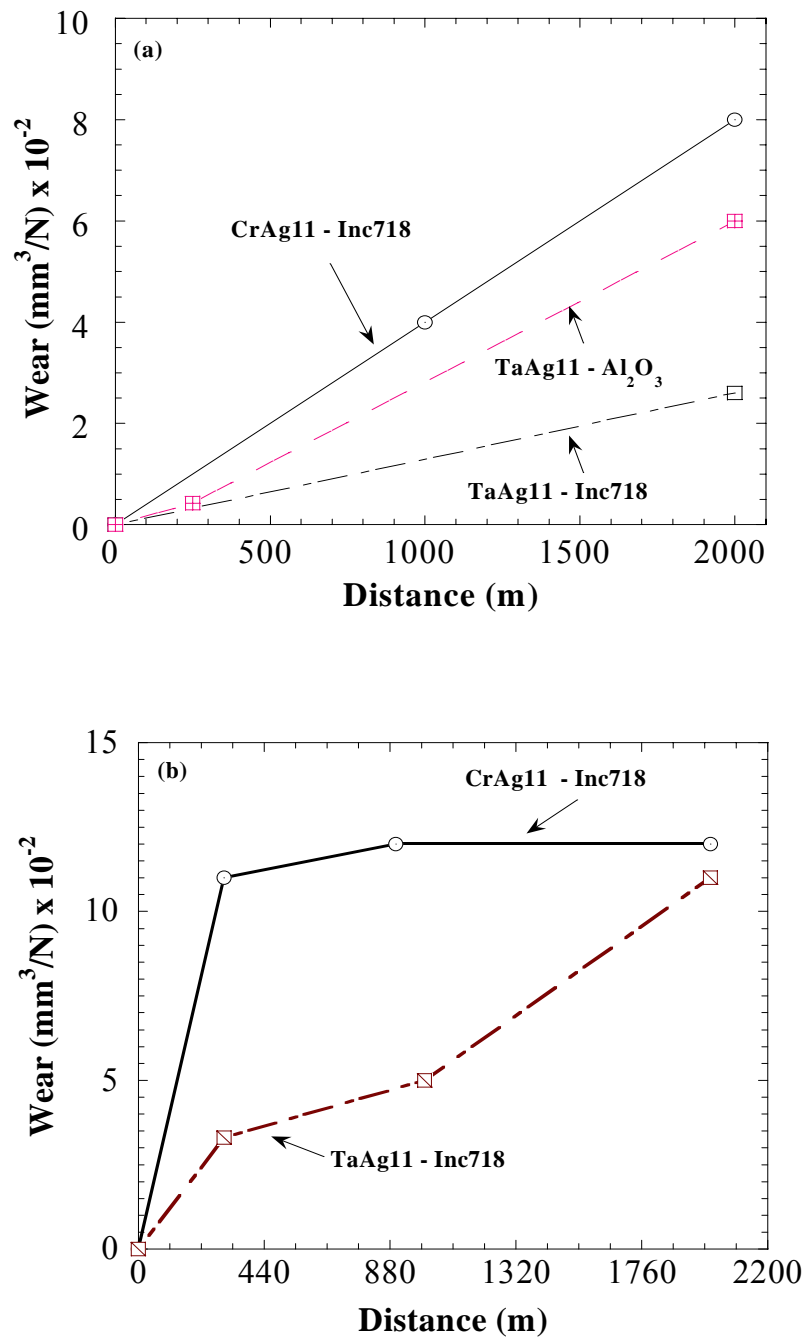


Figure 51: Plot of wear as function of sliding distance of, (a) MAX/Ag composites against different substrates at ambient temperature, and (b) MAX/Ag composites against different substrates tested at 550 °C. All the tests were done under standard condition.

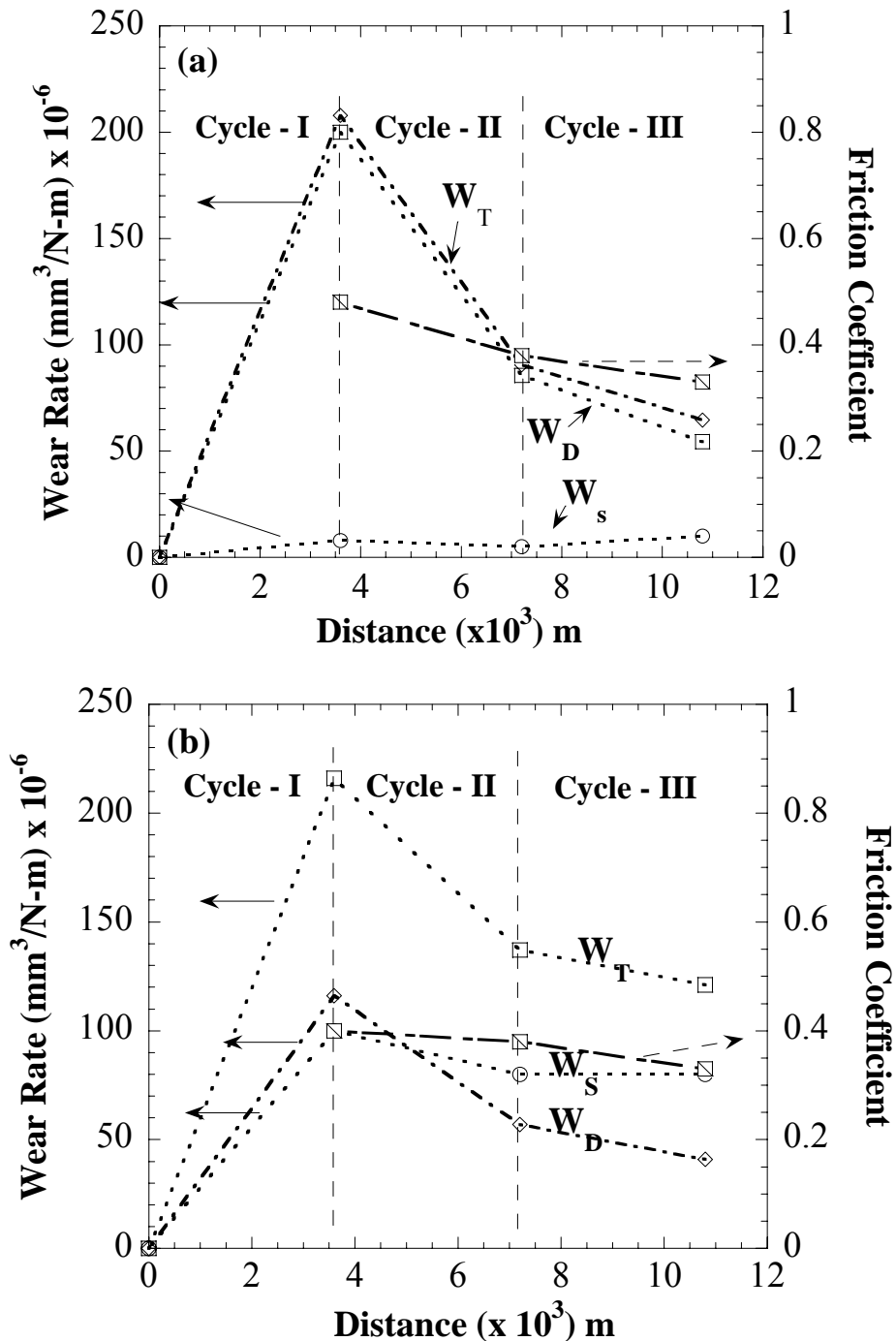


Figure 52: WR as a function of sliding distance for, (a) TaAg11 against Inc718, and (b) CrAg11 against Inc718. Each data point represents, 1 heating and cooling cycle. All the tests were done at standard conditions.

Note: W_s – Wear rate of static partner (Ta₂AlC/Ag or Cr₂AlC/Ag), W_D – wear rate of dynamic partner (Inc718), and $W_T = W_D + W_S$.



Figure 53: (a) Ni-based SA top foil, and (b) TaAgR sample, after testing in foil bearing rig at Honeywell International Facility (Torrence, CA).

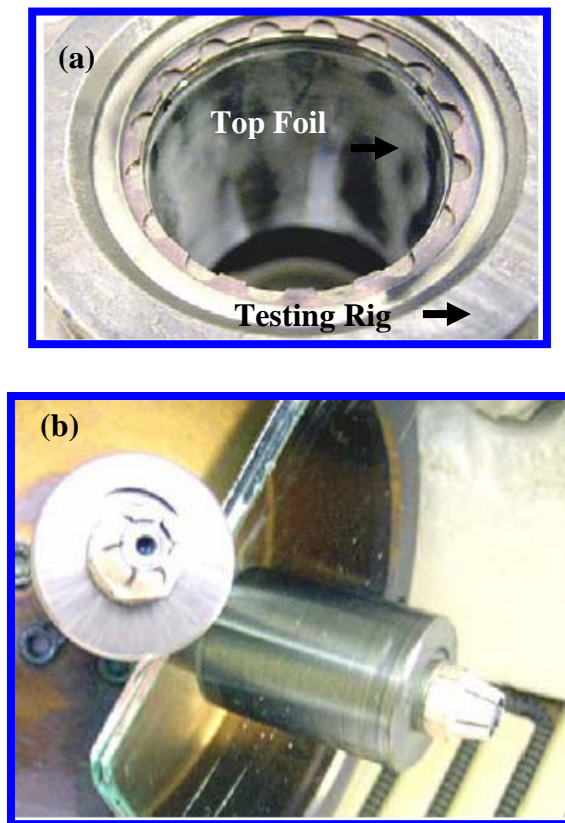


Figure 54: (a) Ni-based SA top foil in testing rig, and (b) CrAg11 sample after testing in foil bearing rig at Honeywell International Facility (Torrence, CA).

5.4 Discussion

The results shown herein clearly show that the MAX/Ag composites are a viable and robust materials that can be used in air-foil bearings in a wide temperature range. As important is the fact that the performance of the tribocouples appear to improve during multiple cycling operations (Fig. 52), a very key consideration and conclusion given the nature of the application. The solution of this 20-year problem in less than 3 years is noteworthy.

Another major accomplishment is the excellent agreement between the lab scale results and rig testing results. Going forward, we have much more confidence in the lab results, which should reduce the expense of further development since we can eliminate the preliminary rig testing used here and go directly to the full blown engine tests.

5.4.1 Comparison with pure MAX phases

The MAX phases by themselves are excellent solid lubricant vs. Inc718 at higher temperatures [Ch. 3]. Ag was added to decrease the WRs at room temperature. If we compare the WRs results at different T's with pure MAX phases, it is obvious that the addition of Ag improves the WRs of the composite materials at room temperature as compared to the pure phases (Table 8). The trend is similar against Al₂O₃ also (Table 8).

When tested at 350 °C against Inc718, the WRs of the pure MAX phases are higher than the composites (currently data is not available for Cr₂AlC at 350 °C). In contradistinction, when tested against Inc718 at 550 °C, the composite WRs are *higher* than the pure MAX phases. This is true despite the fact that the WRs of both CrAg11 and TaAg11 are of the order of 10⁻⁵ mm³/N-m, which is considered quite low (Ch. 1). The

concomitant WRs of the Inc718 substrates were high as compared to the pure MAX phases – the WR of Inc718 was $\sim 10^{-5}$ mm³/N-m after testing against pure MAX phases, and $\sim 10^{-4}$ mm³/N-m after testing against composites (Table 8).

Before adding Ag, the μ 's were stable (Figs. 20 and 43a). The addition of Ag causes variations in μ at RT and 550 °C. Interestingly, the μ was stable – i.e. no slip-stick was observed - when tested against Al₂O₃ in the entire temperature regime tested (Figs. 43b and 45d). The mechanisms responsible for these results will be discussed in Ch. 6.

5.4.2 Comparison with current materials

PS-300, a thermally sprayed coating - pioneered and developed by Dellacorte et al. [34-36] - and its modifications, is the most studied material system for gas/air bearing applications. It is considered to be one of the best materials on the market; we therefore compare our results to it (Table 8). Since in high-speed applications, Ni – based SA's will be the shaft material it makes sense to compare the wear and frictional properties of PS-300 against Inc750.

From the wear data (Table 8), it can be summarized, the tribological performance of TaAg11 and CrAg11 against Inc718 tribocouples were better at room temperature, and that at higher temperatures PS300–Inc750, and TaAg11 or CrAg11–Inc718 showed similar performance.

However in the rig test, CrAg11-Inc718, and TaAg11-Inc718 tribocouples performed better than PS304 (modification of PS300)-ZrN tribocouple during testing at Honeywell International's facility in Torrence, CA. Moreover, PS304-ZrN tribocouples need initial running before actual start of testing, and MoS₂ as a sacrificial lubricant

during initial start up [38]. The wear of PS304 was also higher as compared to TaAg11 or CrAg11 [38].

5.5 Summary and Conclusions

- The authors have been able to design a system which can self-adjust in different temperature regimes, while maintaining a $\mu < 0.5$ and a total cumulative specific $WR \leq 10^{-4} \text{ mm}^3/\text{N}\cdot\text{m}$ in the entire temperature range of 26 °C to 550 °C. The lab-scale results correlated well with pilot testing of the samples under stringent rig conditions.
- The TaAgR samples were successfully tested under rig conditions for 10,000 cycles in the temperature range of 26 to 550 °C. The average surface roughness of TaAgR remained unchanged $\sim 0.2 \text{ }\mu\text{m}$, the average roughness of tribocontact areas on SA surface increased to $0.4 \text{ }\mu\text{m}$. Similarly, the CrAg11 surface after 3,000 cycles appeared smooth, and the average roughness of tribocontact areas on SA surface was $1 \text{ }\mu\text{m}$. Generally, for load bearing studies for applications in oil free turbo-engines, surface finishes of $0.05 - 0.2 \text{ }\mu\text{m}$ are considered best [16]. The thickness of the air thin film that separates the top foil and shaft is $\sim 5 \text{ }\mu\text{m}$ [16]. Based on these parameters, TaAg11 and CrAg11–SA tribocouples may be ideal candidates for load bearing studies in turbomachinery for oil free turbo-engines. Although more studies are needed to improve the surface finish of SA surfaces after testing.
- The aerospace industry may not be ready yet to accept ceramic-based materials for shaft, but they can be used in novel automobile designs to reduce the consumption of eco-toxic oil [80-81]. Trial runs can be made for turbochargers in

diesel truck engines. The high operational temperature of these engines degrades the oil and result in coking [80-81]. However, for aerospace applications, coatings of the same can be thermally sprayed either on the Inconel shafts or foils.

One the last note, the composite systems developed here with the desired properties – which make great strides towards solving a 20 year old problem - were produced in less than 2 years of intensive research effort (continuous screening approach to select the best microstructure) at Drexel University in collaboration with Honeywell International and 3-ONE-2, Voorhees, NJ. Further process optimization both of the composition, and surface properties can cause betterment of the obtained results (see Ch. 7), and considering the fact that some of the pure MAX phases are oxidation resistant till 1000 °C, the temperatures of the systems could be pushed to higher limits further increasing the efficiency of engines, decreasing pollution and saving billion of dollars.

CHAPTER 6 - STUDY OF TRIBOFILMS FORMED BETWEEN Ta₂AlC/Ag OR Cr₂AlC/Ag COMPOSITES AND Inc718 OR Al₂O₃

6.1 Introduction

In Ch. 5, we reported on the wear and frictional behavior - in the 26 to 550 °C temperature range - between a Ni-based superalloy (Inc718) or alumina, on the one hand, and TaAg11 or CrAg11, on the other. When tested against Inc718, the remarkable feature of these tribocouples is their ability to function in the wide temperature range from 26 to 550 °C. The main goal of this chapter is to carefully study the several novel self-lubricated films obtained between TaAg11 or CrAg11 composite samples and a superalloy (Inc718) or alumina, Al₂O₃, and then understand the influence of tribofilm chemistry on the tribological behavior of above mentioned tribocouples.

6.2 Experimental Details

The friction and wear tests were performed using a high temperature tribometer (CSM, Switzerland) capable of going up to 600 °C. Experimental details used for the testing, and characterization of WRs and μ are described in detail in Ch. 3.

The experimental procedure for characterizing the different *microconstituents* in the tribofilms by EDS analysis is also outlined in Ch. 3.

Depth profiles of the tribofilms were obtained using Secondary Ion Mass Spectroscopy, SIMS, (Ion-ToF IV, Germany, also located at the University of SUNY, Stony Brook, NY). Measurements were carried out in a dual beam mode: the crater was etched by a sputter gun (Ar⁺ ions 10 kV 25 nA in positive ion mode or Cs⁺ ions 3 kV 28 nA in negative ion mode; the ion beam was at 45°) and the center of the crater was

analyzed in a non-interlaced mode with a pulsed gun (Ga^+ 15 kV 3 pA; beam at 45°). To enhance image contrast 20 consecutive scans were done on the surfaces.

XRD patterns were obtained at ambient temperatures using a X-ray diffractometer (Siemens D500) using $\text{Cu K}\alpha$ radiation, with a step scan of 0.02° and 1s per step. Si powder was used as an internal standard. The Vickers hardness was measured using 200 g load with a microindenter (LECO* M-400). Thermodynamic calculations were carried out with FACT SAGE software.

6.3 Results

6.3.1 Microscopy of Tribo-surfaces

6.3.1.1 Ambient Temperature Results

TaAg11–Inc718 tribocouple: Figure 55a shows a typical secondary electron, SE, SEM micrograph of the TaAg11 tribosurface after sliding against Inc718 at 26°C under standard testing conditions. No visible mass transfer was observed between the two surfaces. Table 9A summarizes the EDS results on TaAg11-Inc718 and CrAg11-Inc718 tribo-surfaces after dry sliding, where each individual area has been designated with a letter. It is important to note that hereafter the notation *microconstituent* will be used to denote the chemistries of the various regions; this notation is chosen to condense complex multi-element compositions into a reader friendly notation, that is easy to grasp. Along the same lines, the equal sign will be used to refer to the average composition. Referring back to Fig. 55a, the main matrix (light areas), H1 = $*[\text{Ta}_{0.3}\text{Al}_{0.15}\text{Ag}_{0.15}\text{Ni}_{0.25}\text{Cr}_{0.08}\text{Fe}_{0.07}]\text{O}_{0.2}*$. The dark areas, located on the grain boundaries, H2 = $*[\text{Ta}_{0.15}\text{Al}_{0.25}\text{Ag}_{0.4}\text{Ni}_{0.2}]\text{O}_{0.1}*$.

Similarly, no visible transfer film was observed on the Inc718 surfaces (Fig. 55b). This surface has an average composition, J1 = $^*[\text{Ta}_{0.025}\text{Al}_{0.01}\text{Ag}_{0.01}\text{Ni}_{0.55}\text{Cr}_{0.2}\text{Fe}_{0.2}]\text{O}_{0.2}^*$. In some locations, wear debris was observed, the average composition of which was J2 = $^*[\text{Ta}_{0.1}\text{Al}_{0.05}\text{Ag}_{0.05}\text{Ni}_{0.4}\text{Cr}_{0.2}\text{Fe}_{0.2}]\text{O}_{0.45}^*$.

TaAg11–Al₂O₃ tribocouple: A typical backscattered electron, BSE, SEM micrograph of the Al₂O₃ tribo-surface after dry sliding against TaAg11 is shown in Fig. 55c. Table 9b summarizes the EDS results of the microconstituents formed during sliding of TaAg11–Al₂O₃ tribocouples. It was covered with smeared wear debris from the TaAg11 counterpart K = $^*[\text{Ta}_{0.45}\text{Al}_{0.35}\text{Ag}_{0.3}]\text{O}_{1.6}^*$ (Table 9B). This wear debris adhered onto the Al₂O₃ surface to form a discontinuous transfer film.

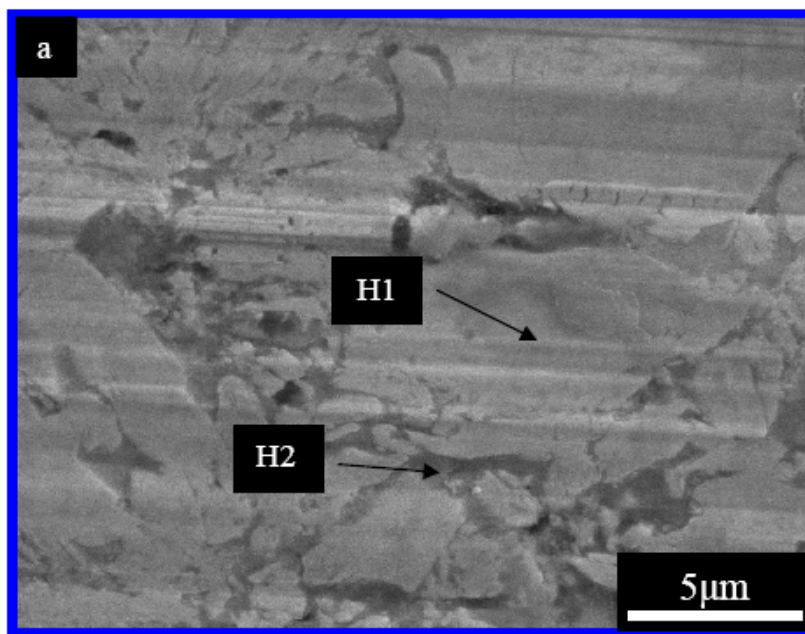


Figure 55: (a) SE FESEM micrograph of TaAg11 surface after testing against Inc718 at room temperature, (b) BSE FESEM micrograph of Inc718 surface after testing against TaAg11 and (c) BSE FESEM micrograph of alumina surface after testing against TaAg11. The experiment was done under standard conditions.

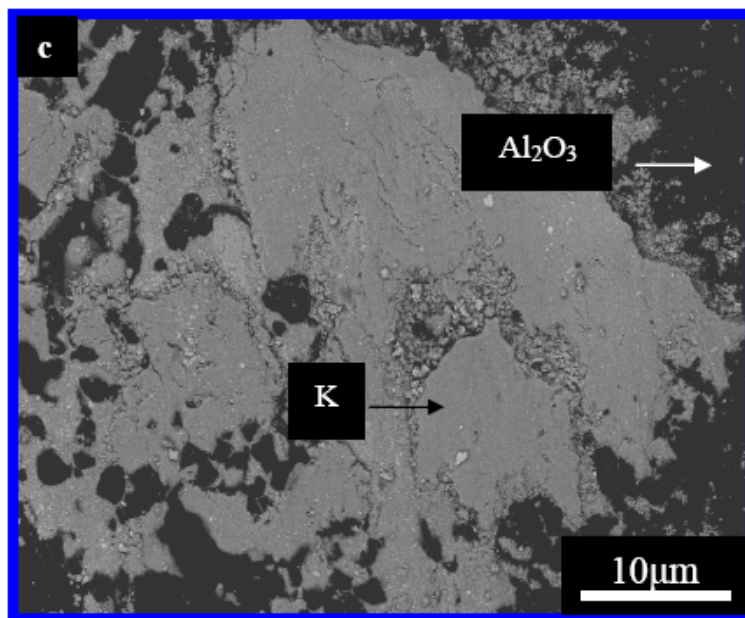
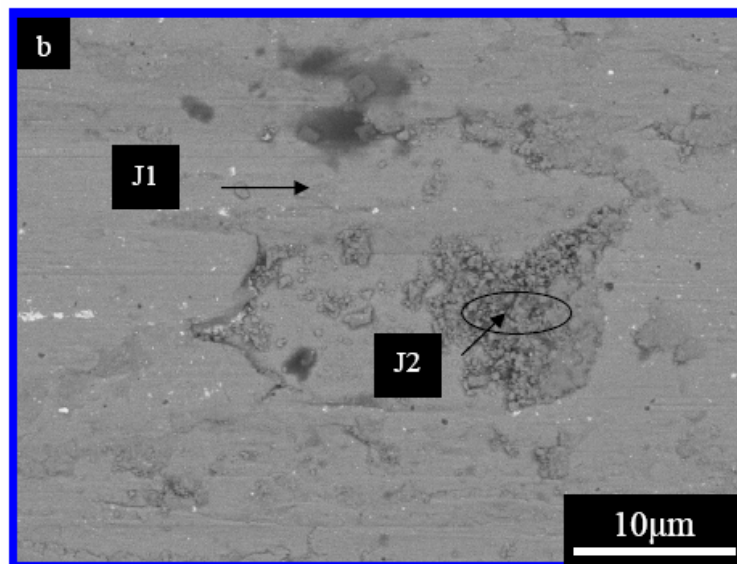


Figure 55: (a) SE FESEM micrograph of TaAg11 surface after testing against Inc718 at room temperature, (b) BSE FESEM micrograph of Inc718 surface after testing against TaAg11 and (c) BSE FESEM micrograph of alumina surface after testing against TaAg11.

Table 9A: Average of at least 3 EDS readings of a region homogenous at the micro scale. Each alphabet letter represents elemental ratios of a *micro constituents*. The regions marked with grey color represent average composition of analyzed tribofilms.

Temp. (°C)	Reg.	*Averaged Composition*	Figure	Tribocouples
26	H1	$[\text{Ta}_{0.3}\text{Al}_{0.15}\text{Ag}_{0.15}\text{Ni}_{0.25}\text{Cr}_{0.08}\text{Fe}_{0.07}]\text{O}_{(0.2)}$	55	TaAg11-Inc718
	H2	$[\text{Ta}_{0.15}\text{Al}_{0.25}\text{Ag}_{0.4}\text{Ni}_{0.2}]\text{O}_{0.1}$		
	J1	$[\text{Ta}_{0.025}\text{Al}_{0.01}\text{Ag}_{0.01}\text{Ni}_{0.55}\text{Cr}_{0.2}\text{Fe}_{0.2}]\text{O}_{(0.2)}$		
	J2	$[\text{Ta}_{0.1}\text{Al}_{0.05}\text{Ag}_{0.05}\text{Ni}_{0.4}\text{Cr}_{0.2}\text{Fe}_{0.2}]\text{O}_{0.45}$		
550	L	$[\text{Ta}_{0.07}\text{Al}_{0.15}\text{Ag}_{0.08}\text{Ni}_{0.3}\text{Cr}_{0.2}\text{Fe}_{0.2}]\text{O}_1$	56	CrAg11-Inc718
	M	$[\text{Ta}_{0.1}\text{Al}_{0.3}\text{Ag}_{0.1}\text{Ni}_{0.3}\text{Fe}_{0.1}\text{Cr}_{0.1}]\text{O}_{0.7}$	57	
	N	$[\text{Ta}_{0.05}\text{Al}_{0.05}\text{Ni}_{0.5}\text{Cr}_{0.2}\text{Fe}_{0.2}]\text{O}_1$		
	R	$[\text{Ta}_{0.3}\text{Al}_{0.125}\text{Ag}_{0.125}\text{Ni}_{0.25}\text{Cr}_{0.1}\text{Fe}_{0.1}]\text{O}_1$		
	LA	$[\text{Al}_{0.2}\text{Ag}_{0.125}\text{Ni}_{0.175}\text{Cr}_{0.5}]\text{O}_{0.66}$	58	
	LB	$[\text{Fe}_{0.05}\text{Al}_{0.4}\text{Ag}_{0.2}\text{Ni}_{0.05}\text{Cr}_{0.3}]\text{O}_{0.66}$	59	
LC	$[\text{Ag}_{0.05}\text{Al}_{0.1}\text{Ni}_{0.4}\text{Cr}_{0.25}\text{Fe}_{0.2}]\text{O}_1$			
Thermal Cyl.	W	$[\text{Ta}_{0.45}\text{Al}_{0.2}\text{Ag}_{0.25}\text{Ni}_{0.05}\text{Cr}_{0.025}\text{Fe}_{0.025}]\text{O}_{0.4}$	61	TaAg11-Inc718
	X	$[\text{Ta}_{0.2}\text{Al}_{0.15}\text{Ag}_{0.1}\text{Ni}_{0.25}\text{Cr}_{0.1}\text{Fe}_{0.2}]\text{O}_1$		
during lab tests	Y	$[\text{Ni}_{0.5}\text{Cr}_{0.3}\text{Fe}_{0.2}]\text{O}_{0.2}$		TaAg11-Inc718
lab tests	Z1	$[\text{Ta}_{0.3}\text{Al}_{0.2}\text{Ag}_{0.1}\text{Ni}_{0.2}\text{Cr}_{0.1}\text{Fe}_{0.1}]\text{O}_1$	62	CrAg11-Inc718
	Z2	$[\text{Ta}_{0.025}\text{Al}_{0.025}\text{Ag}_{0.05}\text{Ni}_{0.5}\text{Cr}_{0.2}\text{Fe}_{0.2}]\text{O}_{0.55}$	62	
Thermal Cyl.	FF1	$[\text{Ta}_{0.5}\text{Al}_{0.2}\text{Ag}_{0.1}\text{Ni}_{0.05}\text{Cr}_{0.03}\text{Fe}_{0.05}]\text{O}_{0.3}$	63	TaAgR-Inc718
	FF2	$[\text{Ta}_{0.4}\text{Al}_{0.3}\text{Ag}_{0.1}\text{Ni}_{0.2}]\text{O}_{0.7}$		
during rig tests	GG1	$[\text{Ni}_{0.7}\text{Cr}_{0.2}\text{Fe}_{0.1}]\text{O}_{0.2}$	64	TaAgR-Inc718
during rig tests	GG2	$[\text{Ta}_{0.05}\text{Al}_{0.1}\text{Ni}_{0.55}\text{Cr}_{0.2}\text{Fe}_{0.1}]\text{O}_{0.55}$		
rig tests	HH1	$[\text{Cr}_{0.6}\text{Al}_{0.4}]\text{O}_{0.25}$	65	CrAg11-Inc718
	HH2	$[\text{Ag}_{0.65}\text{Al}_{0.35}]\text{O}_{0.35}$		
	KK	$[\text{Ag}_{0.075}\text{Al}_{0.1}\text{Ni}_{0.45}\text{Cr}_{0.3}\text{Fe}_{0.075}]\text{O}_{0.6}$	66	
Thermal Cyl. during lab tests	RR1	$[\text{Ta}_{0.12}\text{Al}_{0.04}\text{Ni}_{0.44}\text{Cr}_{0.2}\text{Fe}_{0.2}]\text{O}_{0.5}$	69	TaAg11-Inc718
	RR2	$[\text{Ta}_{0.3}\text{Al}_{0.15}\text{Ag}_{0.15}\text{Ni}_{0.15}\text{Cr}_{0.08}\text{Fe}_{0.08}]\text{O}_{0.5}$		
	SS1	$[\text{Ta}_{0.6}\text{Al}_{0.03}\text{Ag}_{0.12}\text{Ni}_{0.12}\text{Cr}_{0.06}\text{Fe}_{0.05}]\text{O}_{0.2}$		
	SS2	$[\text{Ta}_{0.04}\text{Al}_{0.4}\text{Ag}_{0.01}\text{Ni}_{0.3}\text{Cr}_{0.13}\text{Fe}_{0.14}]\text{O}_{0.8}$		
	SS3	$[\text{Ta}_{0.6}\text{Al}_{0.12}\text{Ag}_{0.1}\text{Ni}_{0.15}\text{Cr}_{0.07}\text{Fe}_{0.07}]\text{O}_{0.3}$		

Table 9B: Average of at least 3 EDS readings of a region homogenous at the micro scale. Each alphabet letter represents elemental ratios of “micro constituents. The regions marked with grey color represent chemistry of analyzed tribofilms.

Temp. (°C)	Reg.	*Averaged Composition*	Figure	Tribocouples
26	K	$[\text{Ta}_{0.45}\text{Al}_{0.35}\text{Ag}_{0.3}]\text{O}_{1.6}$	55c	TaAg11-Al ₂ O ₃
550	S	$[\text{Ta}_{0.2}\text{Al}_{0.1}\text{Ag}_{0.7}]\text{O}_{0.5}$	60	
	T	$[\text{Ta}_{0.45}\text{Al}_{0.2}\text{Ag}_{0.35}]\text{O}_1$		
	U	$[\text{Ta}_{0.5}\text{Al}_{0.3}\text{Ag}_{0.2}]\text{O}_{0.3}$		
	V	$[\text{Ta}_{0.2}\text{Al}_{0.35}\text{Ag}_{0.45}]\text{O}_{0.2}$		

6.3.1.2 Results at 550 °C

TaAg11–Inc718 tribocouple: After testing at 550 °C, the TaAg11 surfaces were covered with an almost continuous transfer film (Fig. 56a). This film was visible to the naked eye (Fig.53b). Figure 56b presents a higher magnification SEM BSE micrograph of the tribofilm. The composition of the main dark areas, L = $*[\text{Ta}_{0.07}\text{Al}_{0.15}\text{Ag}_{0.08}\text{Ni}_{0.3}\text{Cr}_{0.2}\text{Fe}_{0.2}]\text{O}_1*$. It was embedded with areas of composition, M = $*[\text{Ta}_{0.1}\text{Al}_{0.3}\text{Ag}_{0.1}\text{Ni}_{0.3}\text{Fe}_{0.1}\text{Cr}_{0.1}]\text{O}_{0.7}*.$

Figure 57a shows SE SEM and optical (inset) micrographs of the tribofilm formed on Inc718 surface. Figures 57b and 57c present higher magnifications of the transfer films in SE and BSE modes. In the OM micrograph the transfer film is light blue in color. The transfer films were smooth at the micro-scale although in some locations they were slightly gouged (Fig. 57b). As it follows from the BSE micrographs, the tribofilm is composed of two areas: a dark area, N = $*[\text{Ta}_{0.05}\text{Al}_{0.05}\text{Ni}_{0.5}\text{Cr}_{0.2}\text{Fe}_{0.2}]\text{O}_1*$, which is the major constituent, and a minor light area, R = $*[\text{Ta}_{0.3}\text{Al}_{0.125}\text{Ag}_{0.125}\text{Ni}_{0.25}\text{Cr}_{0.1}\text{Fe}_{0.1}]\text{O}_1*$ (Fig. 57c & Table 9A).

CrAg11–Inc718 tribocouple: After testing at 550 °C, the CrAg11 surfaces were covered with an almost continuous transfer film (Fig. 58a). This film was visible to the naked eye. Figure 58b presents a higher magnification SEM SE micrograph of the tribofilm in one location. Inset in Fig. 58b shows the BSE micrograph of the same region. The averaged composition of the area was, LA = $[\text{Al}_{0.2}\text{Ag}_{0.125}\text{Ni}_{0.175}\text{Cr}_{0.5}]\text{O}_{0.66}$. In some regions, light colored areas of average composition, LB = $[\text{Fe}_{0.05}\text{Al}_{0.4}\text{Ag}_{0.2}\text{Ni}_{0.05}\text{Cr}_{0.3}]\text{O}_{0.66}$ were observed (Fig. 58c).

Figure 59a shows a SE SEM micrographs of the tribofilm formed on an Inc718 surface. Figures 59b and 59c present higher magnifications of the transfer films in SE and BSE modes respectively. The transfer films were smooth at the micro-scale (Fig. 59b). From the BSE micrographs, the averaged composition of the tribofilm was, LC = $[\text{Ag}_{0.05}\text{Al}_{0.1}\text{Ni}_{0.4}\text{Cr}_{0.25}\text{Fe}_{0.2}]\text{O}_1$ (Fig. 59c & Table 9A).

TaAg11–Al₂O₃: Figure 60 presents the TaAg11 and Al₂O₃ tribo-surfaces after testing. The Al₂O₃ surfaces were covered with, practically, a continuous transfer layer (Fig. 60a).

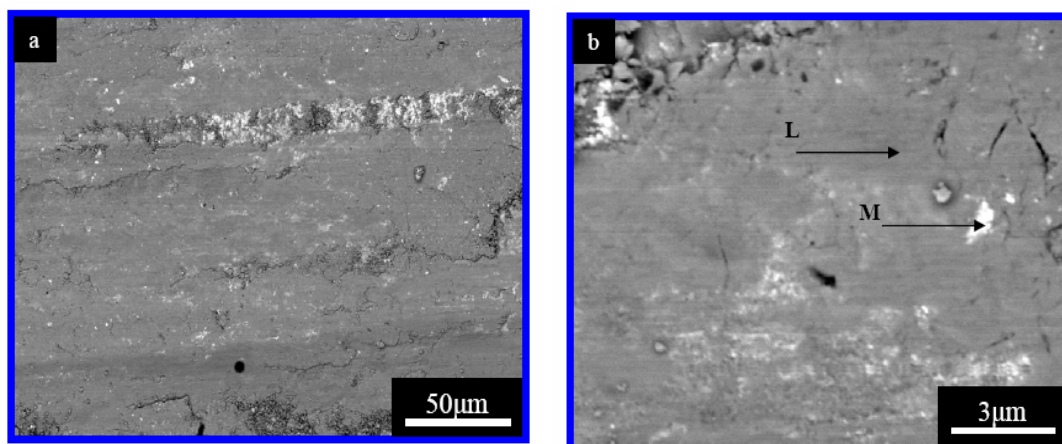


Figure 56: BSE FESEM micrograph of, (a) TaAg11 surface after testing against Inc718 at 550 °C for 2 km, and, (b) at a higher magnification. Experiment was done under standard condition.

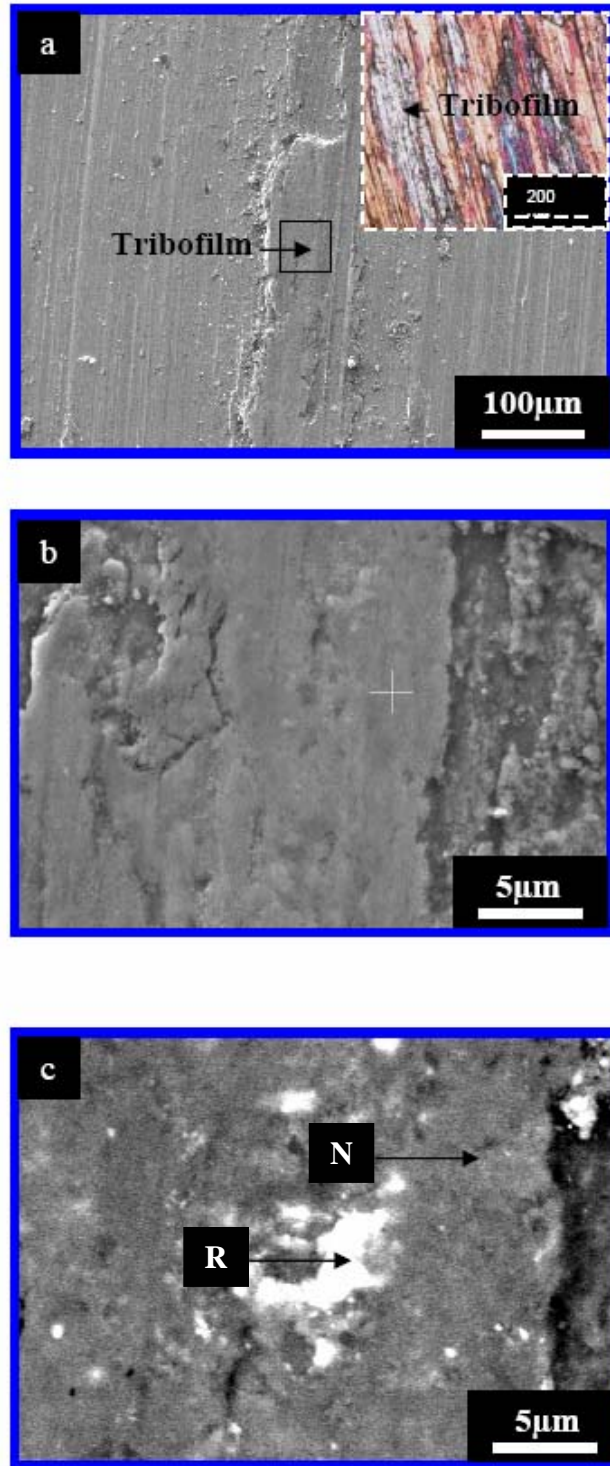


Figure 57: (a) SE micrograph of Inc718 surface after testing against TaAg11 for 2 km at 550 °C. Inset shows the optical micrograph of the tribofilm (blue color), (b) *higher magnification* of the region marked in a, and (c) BSE micrograph of the same region. Experiment was done under standard condition.

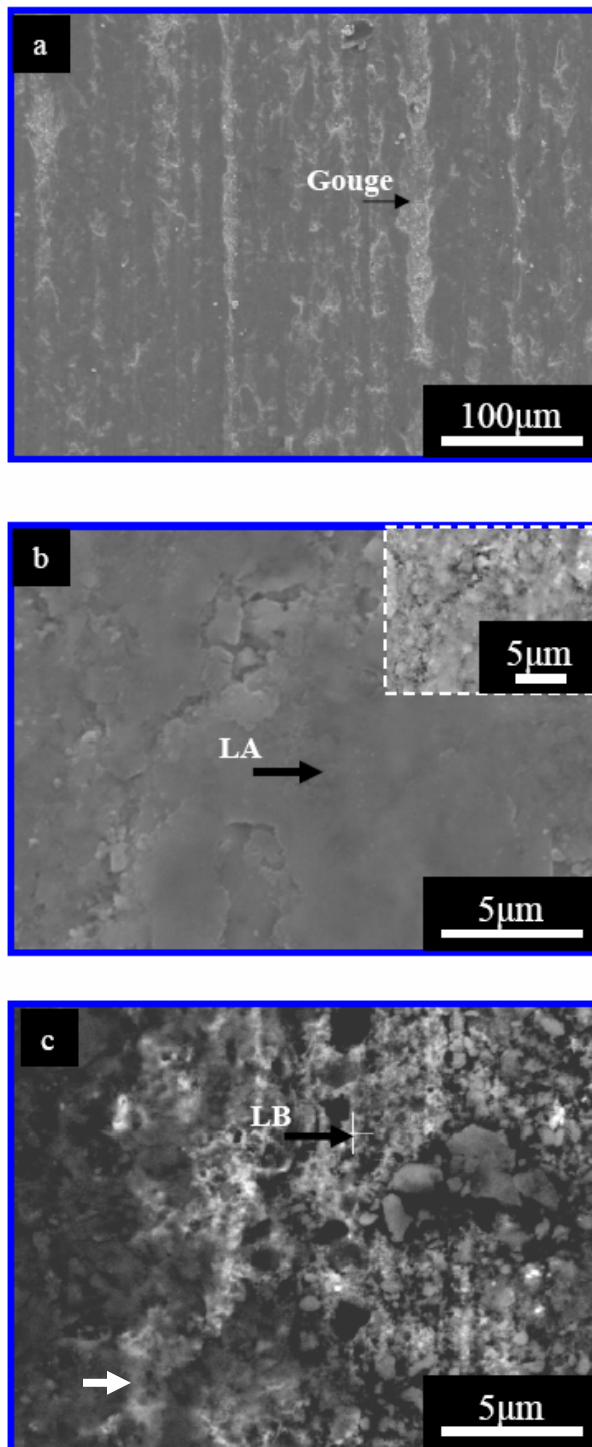


Figure 58: (a) SE micrograph of CrAg11 surface after testing against Inc718 for 2 km at 550 °C, inset shows the optical picture of CrAg11 sample after rig testing, (b) *higher magnification* of the surface in one location in SE, inset shows the BSE image of the same region, and (c) BSE micrograph of another location. This experiment was done under standard conditions.

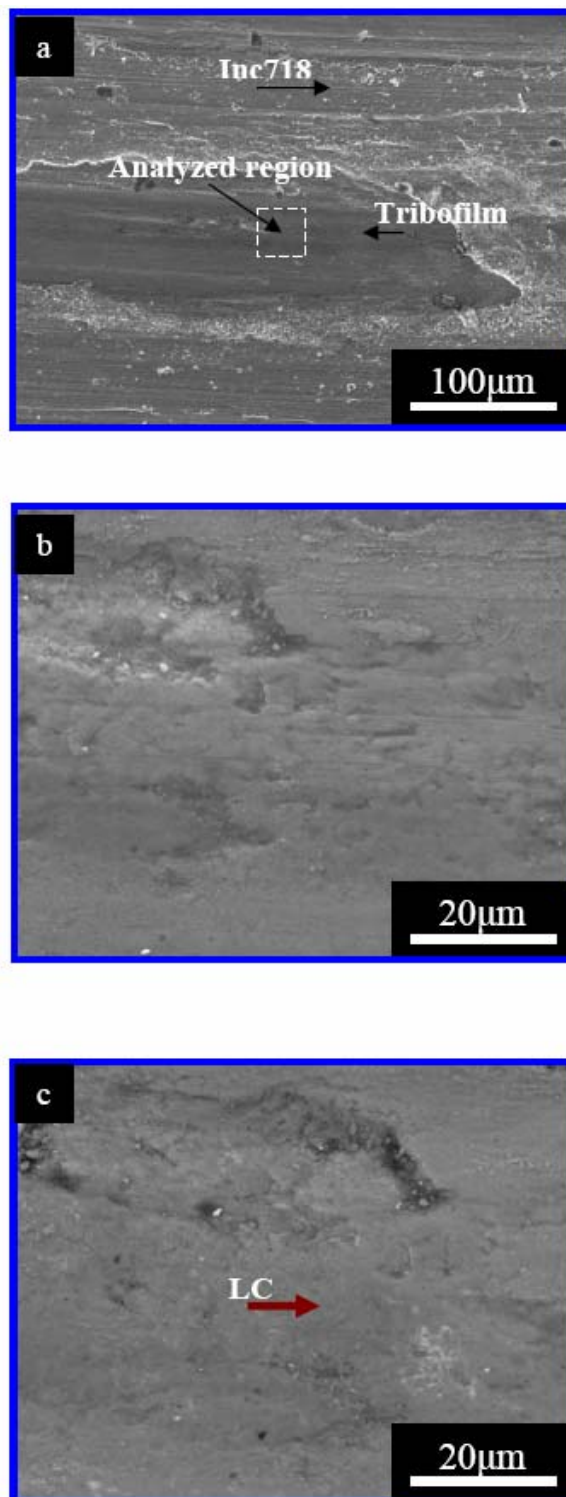


Figure 59: (a) SE micrograph of Inc718 surface after testing against CrAg11 for 2 km at 550 °C, (b) *higher magnification* of the region marked in a in SE, and (c) BSE micrograph of the same region. This experiment was done under standard conditions.

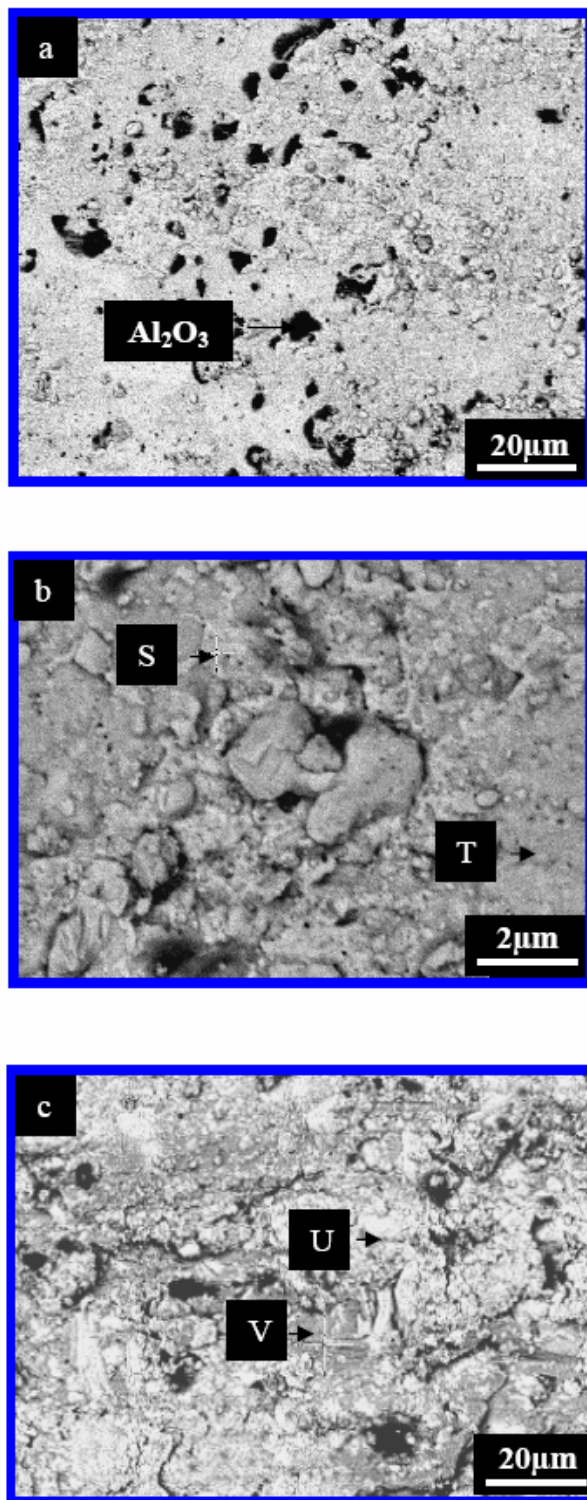


Figure 60: BSE FESEM micrograph of, (a) Al_2O_3 surface after testing against TaAg11 at 550 °C for 2 km, (b) same as a but at higher magnification, and (c) TaAg11 surface after testing. The experiment was done under standard condition.

At higher magnification it is clear that the tribofilm was comprised of two microconstituents (Fig. 60b, Table 9B): light Ag-rich regions, $S = [Ta_{0.2}Al_{0.1}Ag_{0.7}]O_{0.5}$, and dark areas, $T = [Ta_{0.45}Al_{0.2}Ag_{0.35}]O_1$.

Similarly, on the TaAg11 tribo-surface two regions were observed (Fig. 60c, Table 9B): A light area, $U = [Ta_{0.5}Al_{0.3}Ag_{0.2}]O_{0.3}$, and a dark area, $V = [Ta_{0.2}Al_{0.35}Ag_{0.45}]O_{0.2}$.

6.3.1.3 Thermal cycling

Figure 61 presents the TaAg11 surface after dry sliding for 3 heat up and cool down cycles for a cumulative distance of 11 km. In this case the TaAg11 surface is entirely covered with a tribofilm, in which some gouges are visible (Fig. 61a). Figure 61b and 61c present a typical tribofilm micrograph of the TaAg11 surface at higher magnification in SE and BSE, respectively. Similar to the films formed at 550 °C (Fig. 57) the tribofilms formed were composed of two areas (Fig. 61c, Table 9); a light Ta-enriched region, $W = [Ta_{0.45}Al_{0.2}Ag_{0.25}Ni_{0.05}Cr_{0.025}Fe_{0.025}]O_{0.4}$, and a darker region, $X = [Ta_{0.2}Al_{0.15}Ag_{0.1}Ni_{0.25}Cr_{0.1}Fe_{0.2}]O_1$.

Figure 62a presents the Inc718 surface after 11 km continuous cycling. Not surprisingly, a discontinuous tribofilm was observed on the Inc718 surfaces too. As almost all previously described tribofilms, it could be divided into two regions; light, Ta-enriched areas (Table 9A), $Z1 = [Ta_{0.3}Al_{0.2}Ag_{0.1}Ni_{0.2}Cr_{0.1}Fe_{0.1}]O_1$ and darker areas, $Z2 = [Ta_{0.025}Al_{0.025}Ag_{0.05}Ni_{0.5}Cr_{0.2}Fe_{0.2}]O_{0.55}$.

EDS mapping was done on the transfer film. Al (Fig. 62d), Ag (Fig. 62e) and O (Fig. 62f) seem to be rather uniformly distributed in the transfer film, while Ni (Fig. 62b) and Ta (Fig. 62c) are distributed less uniformly.

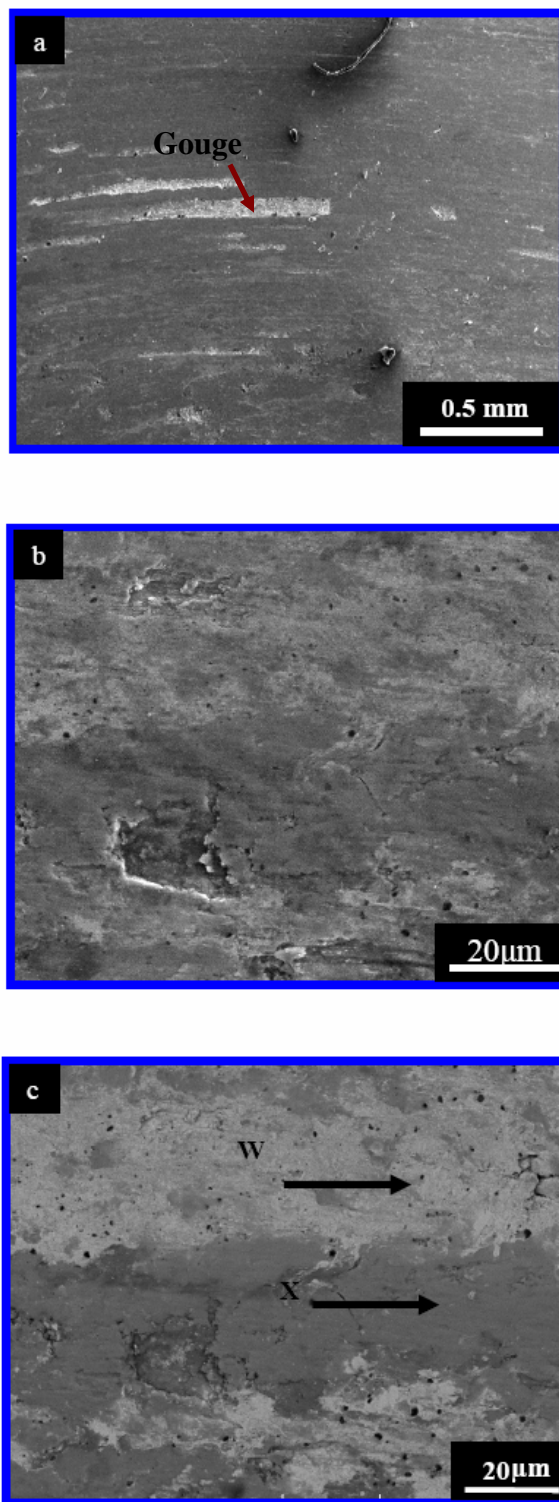


Figure 61: FESEM micrograph of, (a) TaAg11 surface after testing against Inc718 during continuous thermal cycling from the 26 to 500 °C for 11 km in SE, and (b) SE micrograph at higher magnification, and (c) BSE micrograph of the same region. The test was done under standard conditions.

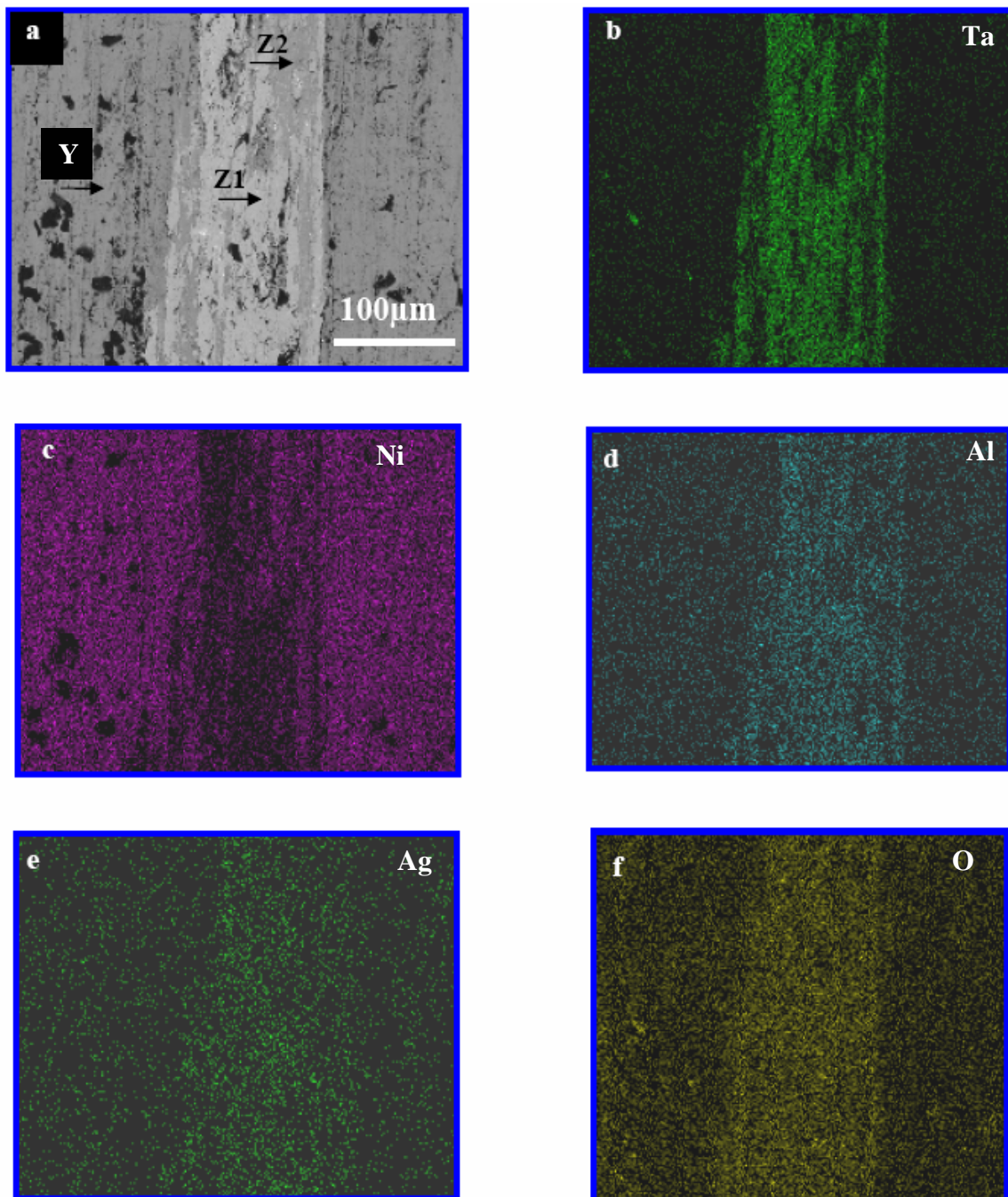


Figure 62: (a) FESEM BSE micrograph of Inc718 surface after sliding against TaAg11 for 11 km after 3 heating and cooling cycles in the temperature range of 26 to 500 °C, and EDS mapping of the Inc718 surface for, (b) Ta, (c) Ni (d) Al, (e) Ag, and (f) Oxygen.

The composition of the non-contacted Inc718 surface (Fig. 62a) was $Y = *[\text{Ni}_{0.5}\text{Cr}_{0.3}\text{Fe}_{0.2}]\text{O}_{0.2}*$.

6.3.1.4 EDS Analysis on rig tested samples

Figure 63 presents the TaAg11 surface after testing in foil bearing rig for 10000 cycles. In this case, the TaAg11 surface is entirely covered with a tribofilm and no wear debris is observed on the TaAgR surfaces (Fig. 63a). Figure 63b and 63c present a typical tribofilm micrograph of the TaAg11 surface at higher magnification in SE and BSE. Similar to the films formed at 550 °C (Fig. 61) the tribofilms formed were composed of two areas (Fig. 63c, Table 9A); a light Ta-enriched region, $\text{FF1} = [\text{Ta}_{0.55}\text{Al}_{0.2}\text{Ag}_{0.125}\text{Ni}_{0.05}\text{Cr}_{0.03}\text{Fe}_{0.05}]\text{O}_{0.3}$ and a darker region, $\text{FF2} = *[\text{Ta}_{0.4}\text{Al}_{0.3}\text{Ag}_{0.1}\text{Ni}_{0.2}]\text{O}_{0.7}*$.

Figure 64 presents the SA (Ni-based superalloy) surface after rig testing. Not surprisingly, a discontinuous tribofilm was observed on the SA surfaces in tribo-contact areas (Fig. 64a). Figure 64b and 64c present typical tribofilm micrographs of the SA surface at higher magnifications in SE and BSE. The averaged chemistry of the tribo-oxide was $\text{GG2} = [\text{Ta}_{0.05}\text{Al}_{0.1}\text{Ni}_{0.55}\text{Cr}_{0.2}\text{Fe}_{0.1}]\text{O}_{0.55}$. The average chemistry of the SA surface was $\text{GG1} = [\text{Ni}_{0.7}\text{Cr}_{0.2}\text{Fe}_{0.1}]\text{O}_{0.2}$ (Fig. 64a).

Figure 65 presents the CrAg11 surface after testing in foil bearing rig for 3000 cycles. The CrAg11 surface was smooth (Fig. 65). Even at higher magnification no wear debris was observed on the CrAg11 surfaces (inset of 65). The averaged composition of dark regions on CrAg11 surfaces was, $\text{HH1} = *[\text{Cr}_{0.6}\text{Al}_{0.4}]\text{O}_{0.25}*$, and light regions had averaged composition $\text{HH2} = *[\text{Ag}_{0.65}\text{Al}_{0.35}]\text{O}_{0.35}*$.

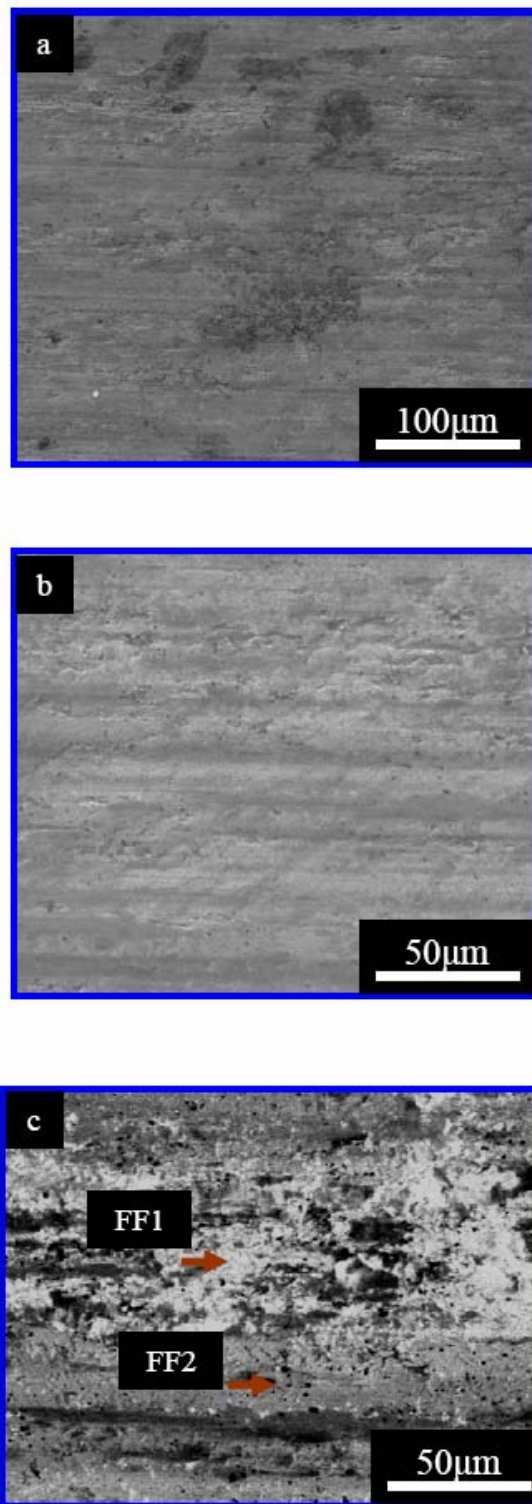


Figure 63: FESEM micrograph of TaAgR surface, (a) after testing against Ni-based SA in *foil bearing rig* for 10,000 cycles in the 26 to 550 °C temperature range in SE, (b) at higher magnification in SE, and (c) BSE micrograph of the same region.

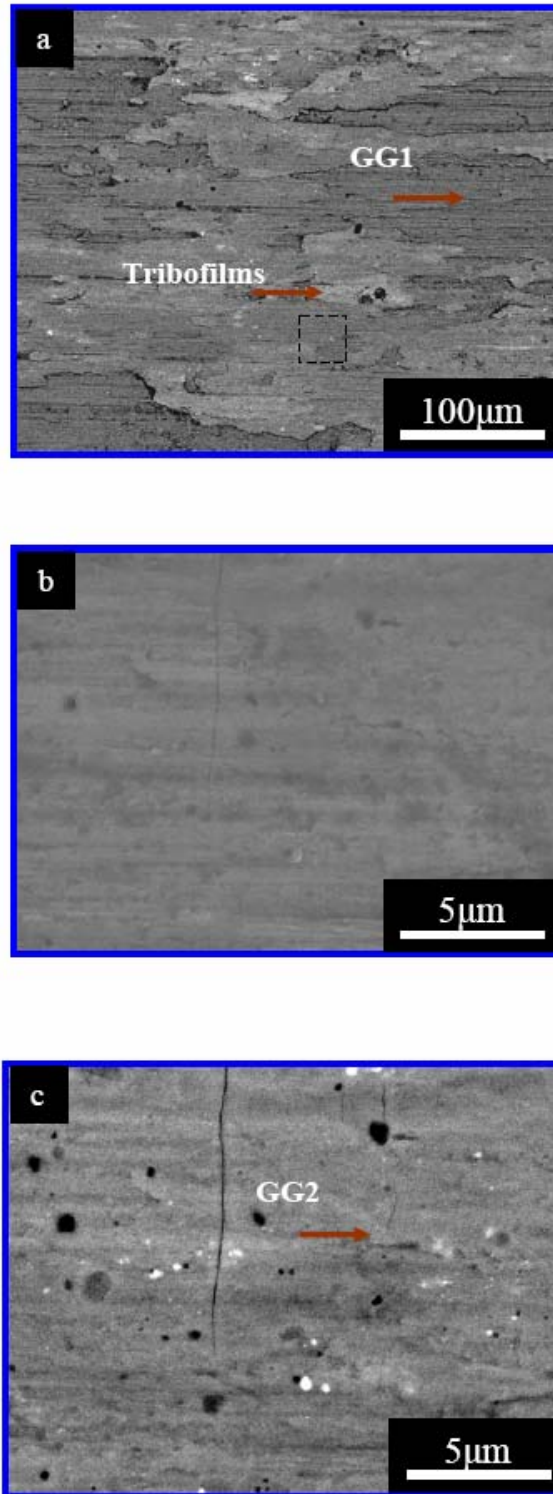


Figure 64: FESEM micrograph of contact regions in Ni-based SA surface, (a) after testing against TaAgR in *foil bearing rig* for 10,000 cycles in the 26 to 550 °C temperature range in SE, (b) at higher magnification of region marked in a in SE, and (c) BSE micrograph of the same region.

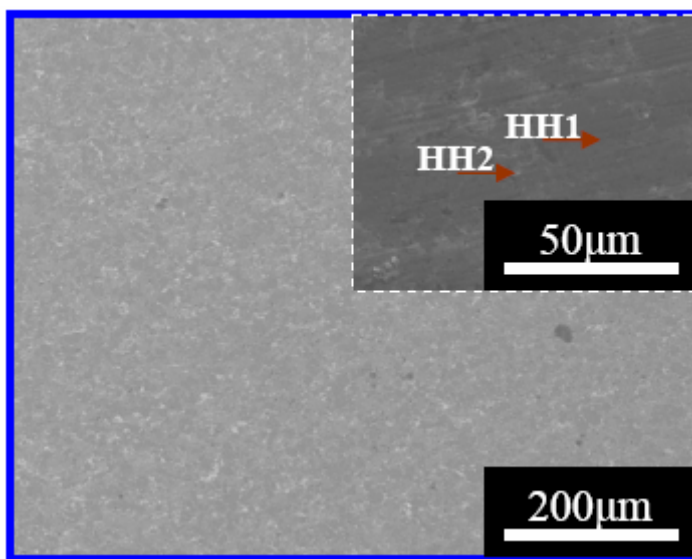


Figure 65: BSE FESEM micrograph of CrAg11 surface after testing against Ni-based SA in *foil bearing rig* for 3,000 cycles in the 26 to 550 °C temperature range. Inset shows the CrAg11 surface at higher magnification in SE.

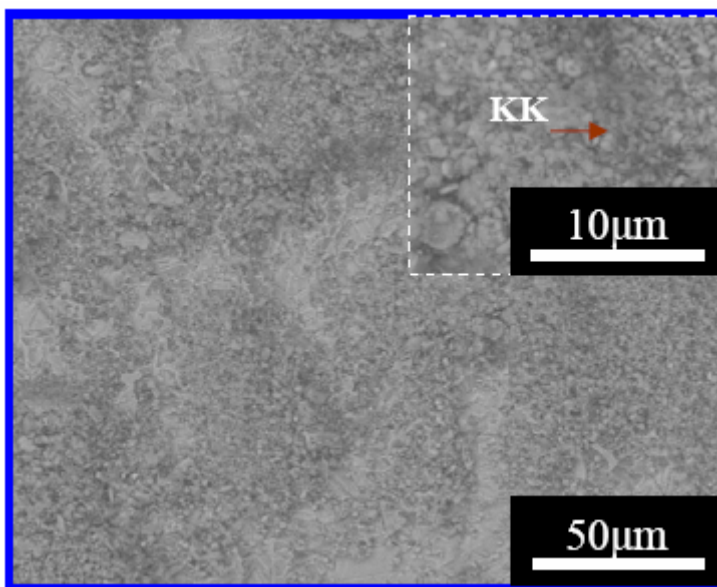


Figure 66: BSE FESEM micrograph of contact regions in Ni-based SA surface after testing against CrAg11 in *foil bearing rig* for 3,000 cycles in the 26 to 550 °C temperature range. Inset shows the Ni-based SA surface at higher magnification in BSE.

Ni-based SA surface after testing (Fig.66) was covered with discontinuous and powdered tribofilm of averaged composition, $KK = [Ag_{0.075}Al_{0.1}Ni_{0.45}Cr_{0.3}Fe_{0.075}]O_{0.6}$.

6.3.2 SIMS Analysis

Three-dimensional depth SIMS profiles of the TaAg11 surface, after 2 km sliding at 550 °C, were obtained in the “light” area designated as L in Fig. 56b, (see Table 9A for composition), which is the contact area. Figure 67 shows positive ions images of Al, Ni, Ag, Ta, TaO from a selected area of 100x100 μm^2 . Figure 68 presents negative ions images of O, AlO and Ag recorded in another location within the same area. Tribosurfaces after testing are rough at the microscale. The images represent the distribution of the elements as a function of depth from the surface. The variation of depth is because the sputtering rate depends on angle between surface and sputtering beam, and it will lead to nonuniformity in depth profile.

The images of the negative ions show that the oxygen concentration decreases drastically, within $\sim 1 \mu m$ from the surface of the transfer films. Even at a $\sim 0.5 \mu m$ depth from the surface the oxygen signal is significantly lower than that on the surface, and separate areas with rather different oxygen contents could be identified (Fig. 68). Concerning the other ions, we can see some increase in the Ag signal, at a $\sim 0.5 \mu m$ depth, followed by a further increase at $\sim 1 \mu m$ (Fig. 67). The positive ion images show a decrease in the Al signal with depth; the Ni signal increased at $\sim 0.5 \mu m$ depth and then decreased at $1 \mu m$ (Fig. 67). It follows from the images, that the element distribution is rather uniform on a 100x100 μm^2 scale.

6.3.3 SEM analysis of the cross-section

From the SIMS result we concluded that after 2 km sliding the tribofilm cross-section was too thin for a proper characterization. To better understand the microstructure of the transfer films formed on the TaAg11 surfaces by SEM and EDS, we characterized

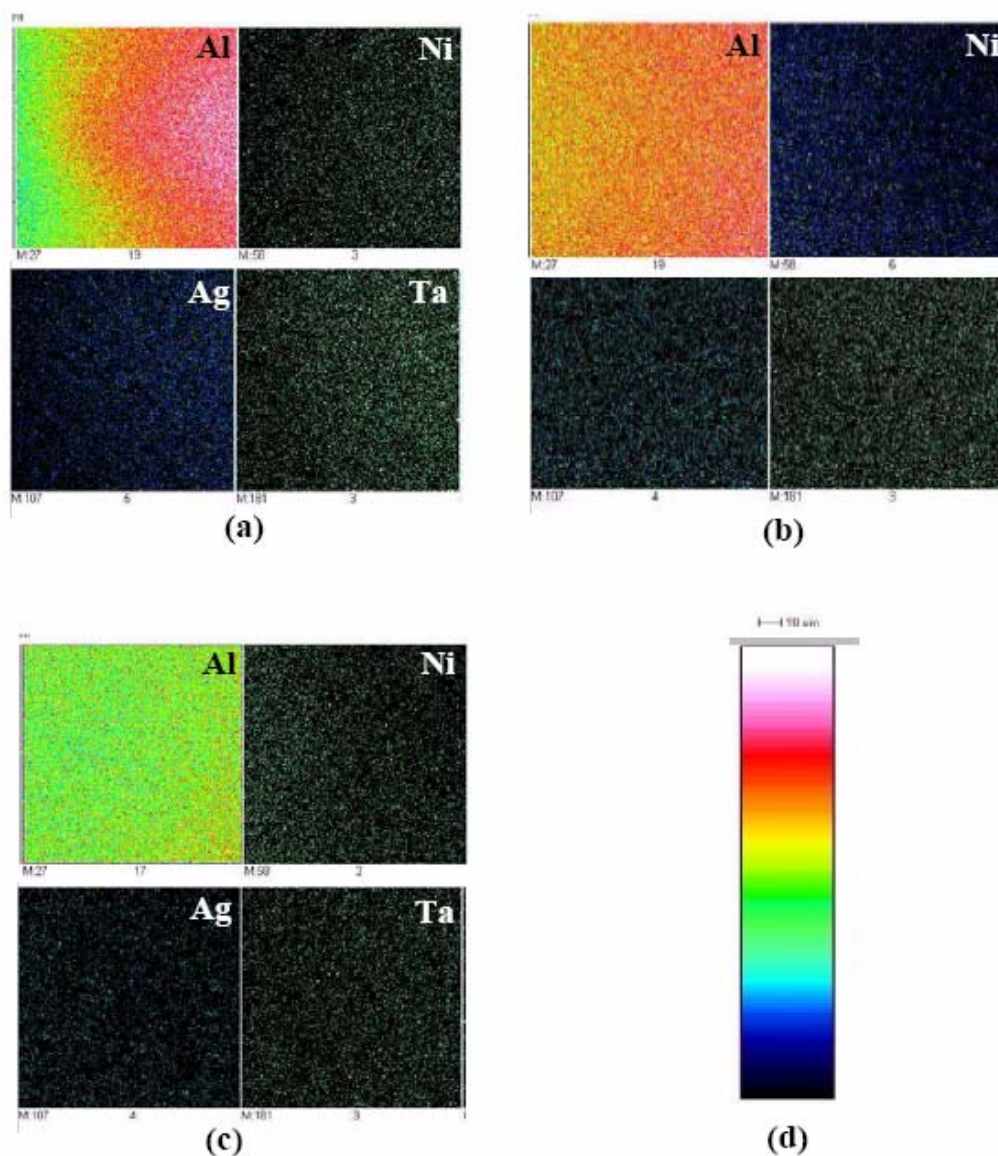


Figure 67: SIMS images of positive ions Al, Ni, Ag and Ta distributions on the surface of TaAg11 (Region L in Fig. 55b) after 2 km sliding against Inc718 at 550 °C, plotted as function of spattering depth, (a) surface, (b) 0.5 μm , (c) 1 μm , and (d) color index to show qualitatively the distribution of ions as a function of depth.

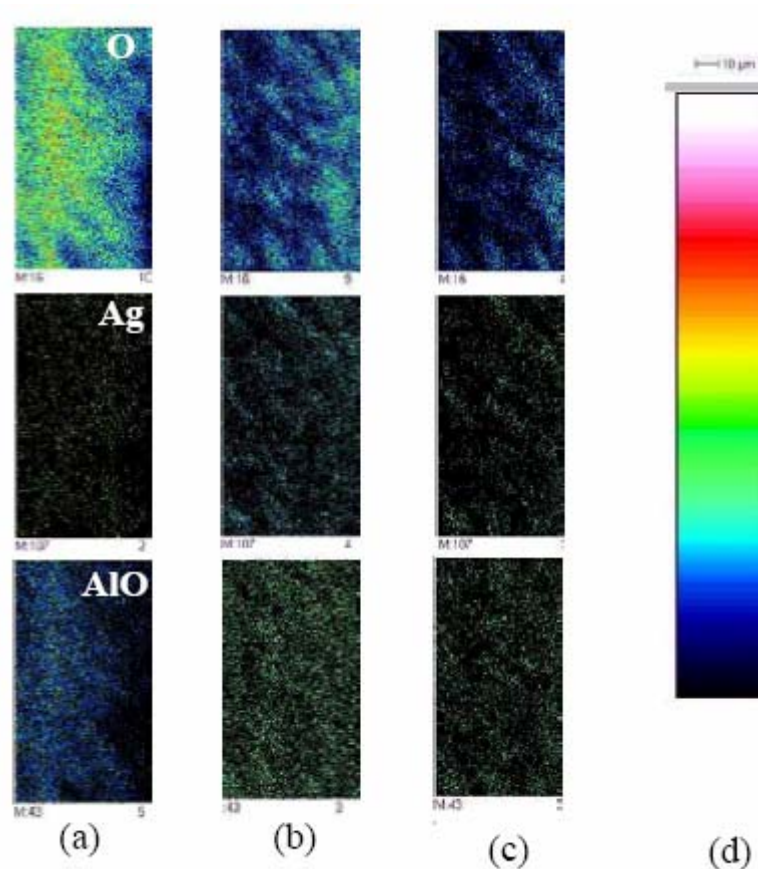


Figure 68: SIMS images of negative ions O, Ag and AlO distributions on the surface of Ta_2AlC/Ag (Region L in Fig. 55b) after 2 km sliding against Inc718 at 550 °C, plotted as function of depth, (a) surface, (b) 0.5 μm , (c) 1 μm and (d) color index to show qualitatively the distribution of ions as a function of depth.

the much thicker tribofilms (2-3 μm) that formed after the 24 km test. The sample that was used for this test was only $\sim 90\%$ dense and made with powders made at Drexel (TaAglab samples - see Ch. 4).

Typical SEM micrographs and EDS analysis after 24 km of sliding against Inc718 are shown in Fig. 69. The total thickness of the tribofilm formed is about 2-3 μm , and is comprised of elements from both counterparts and oxygen. Its microstructure is rather

smearred as a result of the mechanical deformation during formation under tribological conditions, but it is possible to recognize distinct areas - mostly in submicron size - that differ from each other in chemical composition (Fig. 69). These areas may diverge as by oxygen content, as well as, by metal ratios. For example, Ta-rich (SS1 and SS3, Table 9A), Al-poor (SS1 and SS3, Table 9A), Ni- and other Inc718 components rich moderately oxidized (RR1, Table 9A), Ag-rich in presence of Al and Inc718 components (RR2, Table 9A), and some other areas can be identified.

6.3.4 XRD Analysis

XRD analysis of the worn surfaces of TaAg11 composites tested at elevated temperatures against Inc718 (Fig. 70) revealed that the tribofilm was partially crystalline and contained peaks that were not present in the original spectrum, which is almost identical to the one shown in Fig. 70a. The following points are salient:

- all peaks are significantly broadened.
- The appearance of a new peak around 44° , which most likely corresponds to the most intense peak of Inc718. It also overlaps with the nickel oxide 100% peak. This reflects material transfer from the Inc718 counterpart.
- an increase in intensity, of reflections arising, presumably, from the Ta₂C phase.

XRD patterns taken from the worn surfaces of the TaAg11 after being tested against Al₂O₃ at 550°C, basically correspond to the initial bulk material except for the presence of small peak corresponding to Ag (Fig. 70d).

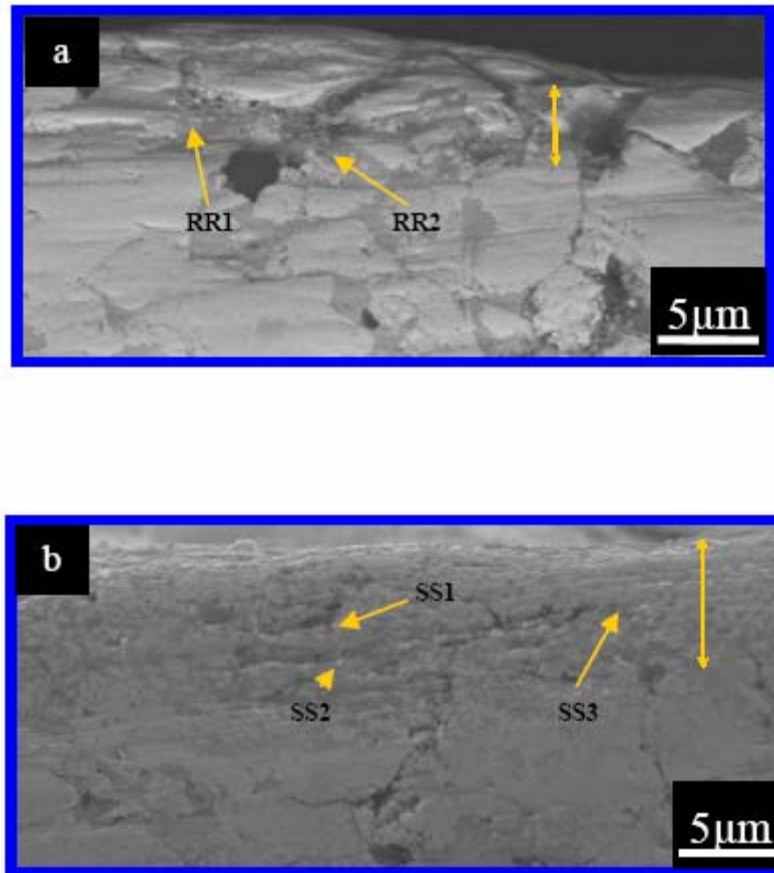


Figure 69: FESEM, (a) BSE micrograph, and (b) SE micrograph of cross-section of TaAg11 sample after 24 km thermocycling sliding against Inc600.

6.3.5 AFM Analysis

For roughness analysis of the tribo-surface of TaAg11 after dry sliding against Inc718 at RT for 2 km at 3 N, AFM mapping (Fig. 71a) on the $100 \times 100 \mu\text{m}^2$ was carried out. The average roughening after the testing was $< 1 \mu\text{m}$ (Figs. 71 b and c). The RMS roughness of the contact area was $\sim 221 \text{ nm}$.

Similar roughening was observed on the TaAg11 surfaces after dry sliding against Inc-718 at 550°C (Fig. 72a). Blue regions are most probably the tribo-contact areas.

Figures 72 b-e represent the linear scans crossing the contact areas. Their height was determined to be about 1-2 μm . The RMS roughness of the contact areas was ~ 450 nm. Similarly, on the Inc718 surfaces, gouges as deep as 4 to 6 μm were observed in some locations (see Fig. 47 in Ch. 5).

6.3.6 Hardness of the transfer films

Vickers hardness indentations were carried out on tribo-films formed after 2 km dry sliding against Al_2O_3 and Inc718, as well as, after 11 km of dry sliding against Inc718 to determine their hardness values. The hardnesses of the tribofilms varied between 7–10 GPa. For comparison the hardness of the $\text{Ta}_2\text{AlC}/\text{Ag}$ surface was 4-5 GPa; that of Inc718, 5 GPa, and that of Al_2O_3 , 15 GPa.

6.3.7 Thermodynamic calculations

The reaction between 2 moles of Ag and 1 mole of Al with 10 moles of O_2 in the temperature range of 26 to 727 $^\circ\text{C}$ (Fig. 73) was simulated in FACT SAGE's software. Ag_2O was stable till 100 $^\circ\text{C}$. Ag was stable in air till 727 $^\circ\text{C}$. Al_2O_3 was the stable oxidation product in the entire temperature range.

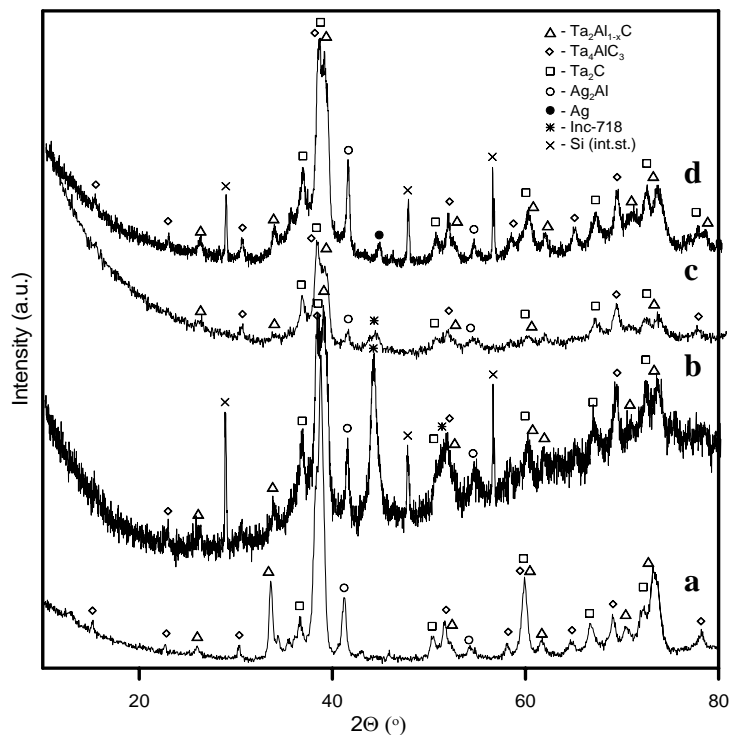


Figure 70: XRD patterns on TaAg11 surfaces after sliding against Inc718, (a) at ambient temperature for 2km, (b) at 550 °C for 2km, (c) for 11 km thermal cycling, and, (d) after 2 km sliding against Al_2O_3 at 550 °C.

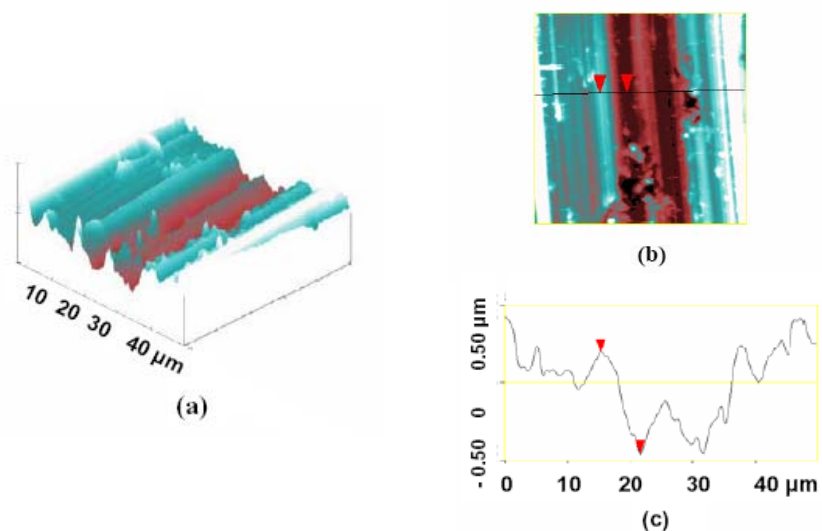


Figure 71: AFM analysis of $100 \times 100 \mu\text{m}^2$ TaAg11 surface after sliding against Inc718 at RT for 2 km, (a) isometric view, (b) top-View, and (c) linear profile of the section marked by line in b.

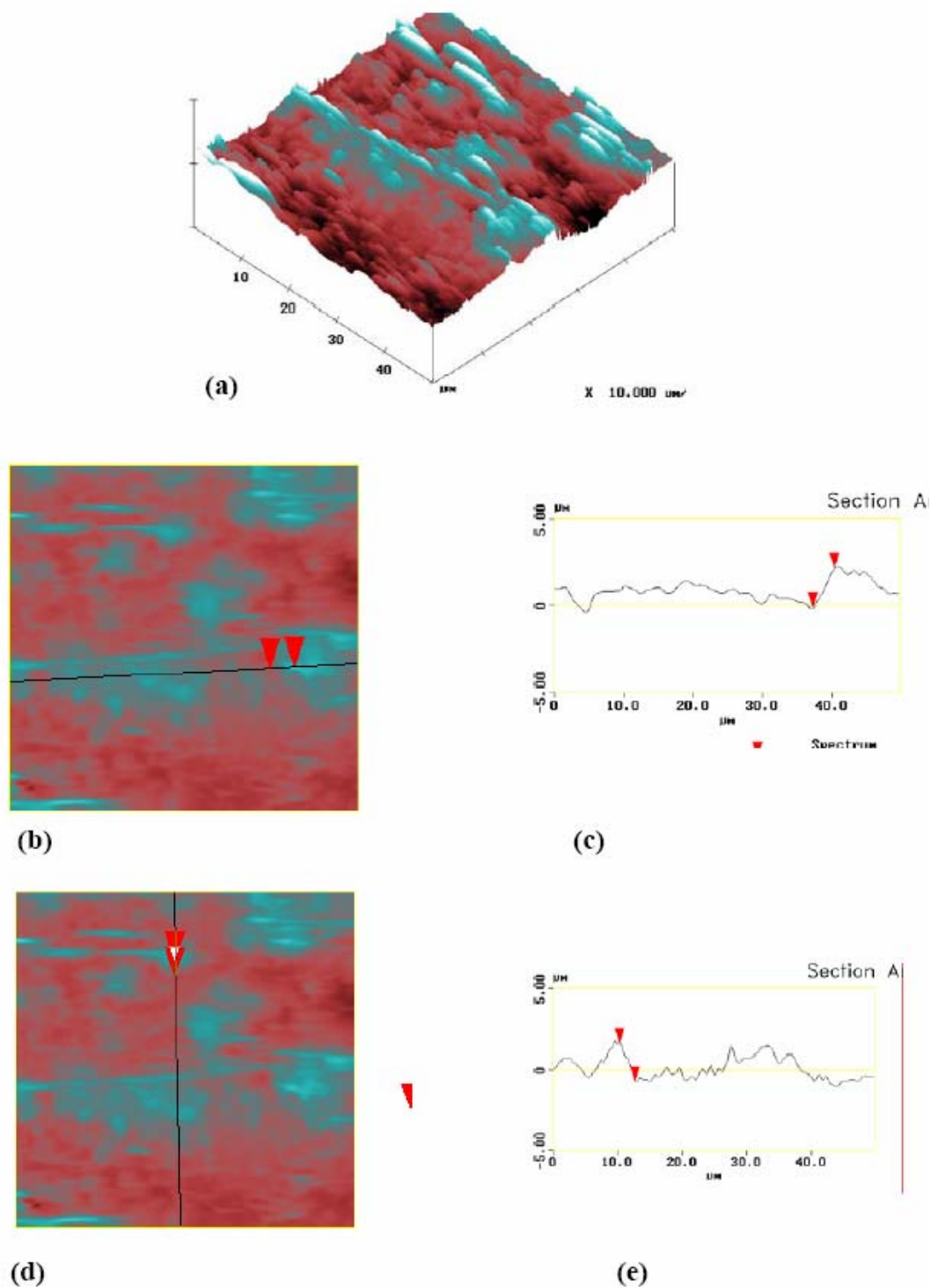


Figure 72: AFM analysis of $100 \times 100 \mu\text{m}^2$ TaAg11 surface after sliding against Inc718 at 550°C for 2 km, (a) isometric view, (b) top view, (c) linear profile of the region marked by line in b, (d) top view, and (e) linear profile of the region marked by line in d.

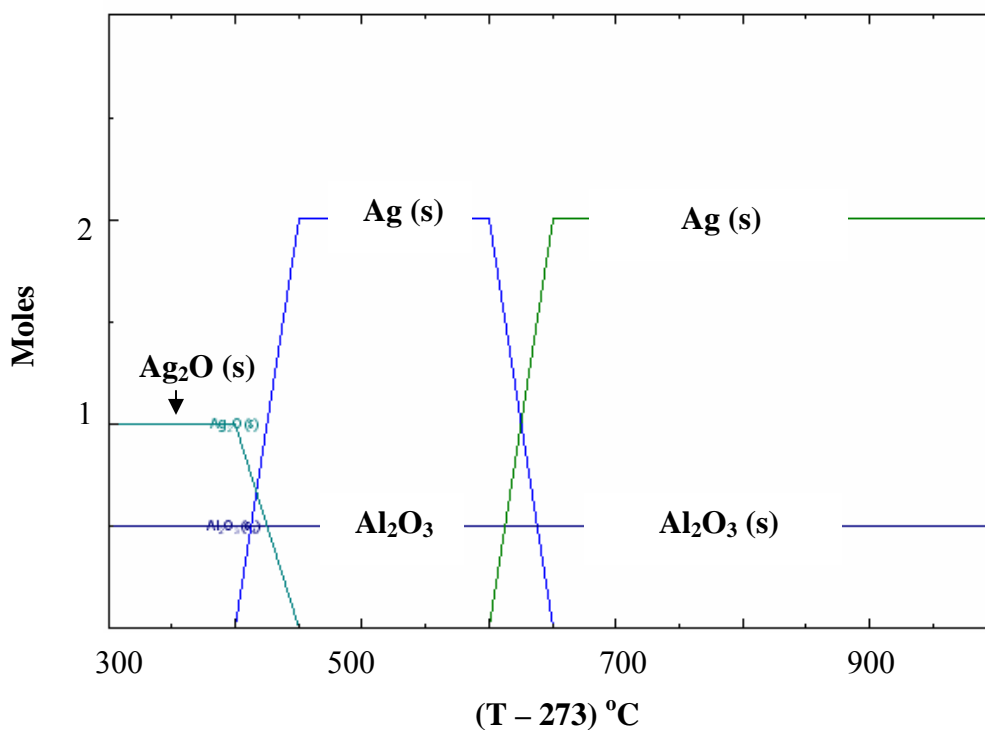


Figure 73: Thermodynamic calculation of 2 moles of Ag and 1 mole of Al reacting with 10 moles of O_2 in 27 to 723 °C temperature range.

6.4 Discussion

The most important results of this chapter are: a) the addition of Ag prevents the formation of a 3rd body against Inc718 at RT, and, b) multi-component, multilayered tribofilms form as a result of thermal cycling. It is because of these layers that the μ 's and WRs gets better with time (Fig. 52 in Ch.5). In the following discussion the underlying mechanisms responsible for these results will be presented. For simplicity, in the tribological reactions, the starting composition of TaAg11 will be assumed $Ta_2Al_{0.5}C$ and Ag_2Al .

6.4.1 Correlating tribochemistry with μ and WR

6.4.1.1 Ambient Temperature

No clearly visible transfer films were observed on either the TaAg11 or Inc718 surfaces after testing at room temperature. However, from EDS analysis, it can be concluded that surface oxidation of the Inc718 surface and its partial transfer onto the TaAg11 surface is taking place (Fig. 55). The transfer layer formed is thin enough so that the underlying TaAg11 substrate is clearly visible (Fig. 55a). The absence of any new details in the XRD pattern compared to the bulk TaAg11 indicates that the transfer film is either extremely thin or, more likely, x-ray amorphous (Fig. 70).

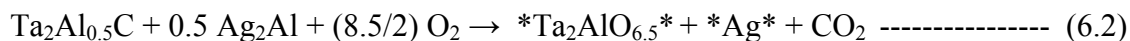
Based on these results the most probable, but simplified, tribochemical reaction occurring at room temperature is:



Most probably the presence of Ag_2Al as the cementing phase in the grain boundaries prevents the formation of the abrasive third bodies. As a result, the WR of the TaAg11 pin was reduced by 3 orders of magnitude (Table 8) as compared to pure Ta_2AlC . The inability of the surfaces to form visible, coherent, low-shear transfer film explains the instabilities in μ (Fig. 43).

In the case of the TaAg11- Al_2O_3 tribocouples, visible and smooth transfer films were detected on the Al_2O_3 surface after testing (Fig. 55c). Based on the EDS data (Table 9, μ -constituent, K) it is reasonable to conclude that the tribofilm is comprised of almost completely oxidized Al and Ta, - viz. Al^{3+} and Ta^{5+} - and metallic silver, viz. Ag^0 .

Based on these results the most probable, but simplified, tribochemical reactions occurring at room temperature are:

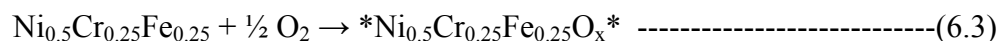


The nonstoichiometric phase $\text{Ta}_2\text{Al}_{1-x}\text{C}$ is presumably more easily oxidized than the stoichiometric carbide Ta_2AlC and may thus be providing a lubricating oxide layer. The presence of Ag may also help in lubricating the interfaces. It appears that $* \text{Ag} *$ and $* \text{Ta}_2\text{AlO}_{6.5} *$ are mixed in the nanoscale. Note - $* \text{Ta}_2\text{AlO}_{6.5} *$ is not single phase oxide, it is a multicomponent oxide system. These factors are responsible for lowering of the WR and μ as compared to pure Ta_2AlC -Inc718 tribocouples (Table 8). Henceforth, this kind of complex transfer film will be referred to as lubricating mixture (LM).

6.4.1.2 At 550 °C and thermal cycling

Testing of the TaAg11 against Inc718 at 550 °C resulted in the formation of tribo-oxides on their surfaces (Fig. 56). From the SIMS depth profiling it can be concluded, that the average thickness of the tribo-oxide layer was less than 500 nm (Fig. 68). And even at this thickness, the non-uniformity in oxygen distribution is rather large (Fig. 68).

From the EDS analysis of the tribofilm surfaces formed after sliding between TaAg11 and Inc718 at 550 °C, (e.g., μ -constituents, L, M, N and R in Table 9A), it can be concluded that the transition metals like Ni, Cr, and Fe are almost completely oxidized. According to EDS analysis, the tribo-oxide film formed on the Inc718 surface is predominantly, oxidized Inc718. Based on these results the most probable, but simplified, tribochemical reactions on the Inc718 surfaces is:



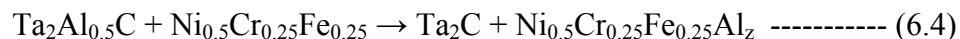
where, $x > 0.5$.

Similarly from EDS analysis on the CrAg11 surfaces (eg. LC in Table 9A), it can be concluded, tribo-oxides are predominantly formed by tribo-oxidation of Inc718 surfaces by reaction 6.3.

What happens to the MAX/Ag surface was slightly more complex. For example, on the TaAg11 surfaces; the tribo-oxide formed is essentially oxidized Inc718, in which small amounts of TaAg11 by tribo-oxidation constituents are observed. These constituents are Al-rich (e.g. L and M in Fig. 56, and Table 9A). SIMS analysis on the TaAg11 surface also detected Al - enrichment on the tribosurfaces (Fig. 67). By SIMS analysis, an increase in the intensity of Ni was also observed at a 0.5 μm depth as compared to surface (Fig. 67). Results of XRD analysis (Fig. 70) on the TaAg11 surface showed broadening of peaks and increase in intensities of Ta_2C peaks. The presence of pristine/oxidized Inc718 was also detected (Fig. 70). Similarly on the CrAg11 surfaces - transference of tribo-oxides from Inc718 surfaces were observed (LC in Table 9A), and Al-enrichment in some areas were observed (LB in Table 9A). The fundamental mechanisms responsible for these results become clearer after inspecting the tribofilms formed during thermal cycling.

The tribofilms formed during thermocycling were non-homogenous at the microscale. The presence of μ -constituents, like W and X (Fig.61c and Table 9A) on the TaAg11 surfaces after 11 km sliding against Inc718 clearly demonstrates the chemical non-uniformity of the tribo-oxide films. The surfaces were covered with tribo-oxides formed from both counterpart surfaces. The TaAg11 surface is tribo-oxidized by a reaction similar to 6.2; the Inc718 surface by reactions similar to 6.3 (eg. W and X in Fig. 61c). Results of XRD analysis (Fig. 70) on the TaAg11 surface showed broadening of

peaks and a possible increase in intensities of Ta₂C peaks; the presence of pristine/oxidized Inc718 was also detected but its intensity was smaller as compared to 550 °C (Fig. 70). Tribofilms of thickness ~ 2 to 5 μm were formed on the porous TaAg11 sample after cycling for 24 km (Fig. 69). As shown by SEM/EDS analysis, in some areas, Inc718 particles have penetrated into the tribofilms (Fig. 69). Most probably, these particles are tribo-particles that are partially oxidized (e.g., RR1 in Table 9A). These particles reacted with some Ta₂Al_{1-x}C grains to form Ta-rich regions (e.g. SS1 and SS3 in Table 9A). Most probably these regions are Ta₂C. Based on these results the most probable, but simplified, tribochemical reactions of Inc718 particles with the TaAg11 matrix is:



where, $z \leq 0.5$.

The tribofilms formed during rig testing of TaAgR samples against SA's were also non-homogenous at the microscale. They were composed of tribo-oxidized products from both tribo-surfaces (e.g. FF1, FF2 and GG2 in Table 9A).

During rig testing material was transferred from the CrAg11 onto the SA surfaces (e.g. KK in Table 9A). The resulting tribofilms formed on SA surfaces were powdery, and composed of tribo-oxides from both the surfaces (e.g. KK in Table 9A).

Based on these important observations, and results, it can be concluded:

- The tribofilms formed at 550 °C, and during thermal cycling are partially crystalline and, as it was noted earlier, the XRD reflections are significantly broadened presumably due to the small crystallite size and/or structural defects (Fig. 64).

- The tribo-layer is not uniform through its thickness (Figs. 61 and 63). It is most probably multi-layered, with tribo-oxide layers on top, and carbide-containing layers beneath it. The latter presumably includes binary and ternary carbides, which are most probably nonstoichiometric. The high value for the hardness of transfer films formed on the Inc718 surfaces ($\sim 8 - 10$ GPa) could also be related with binary carbide and/or oxide formation.
- At 550 °C, the TaAg11–Inc718, and CrAg11–Inc718 tribocouples showed the formation of a tribo-oxide layer according to Eq. 6.3 by the tribo-oxidation of the Inc718. The presence of this layer is responsible for the relatively high WR ($\sim 10^{-4}$ mm³/N-m), and μ 's ~ 0.5 . The exact role of the carbide-rich sublayer is not clear, most possibly, it forms a semi-continuous hard substrate on which lubricating tribooxide (LO's) can be sheared easily.
- During continuous *thermocycling* operations, the TaAg11–Inc718 tribocouples maintained their intrinsic self-lubricating property. The μ 's are ≤ 0.5 and the WRs are $\sim 10^{-4}$ mm³/N-m. The tribolayer was composed of Ni_{0.5}Cr_{0.25}Fe_{0.25}O_{1-a} formed by tribo-oxidation of Inc718 (Eq 6.3), and triboxidized TaAg11 surfaces (Eq. 6.2). The exact role of the carbide-rich sublayer is not clear, most possibly, it forms a semi-continuous hard substrate on which lubricating tribooxide (LO's) can be sheared easily.
- During rig testing of TaAgR against SA's - the tribolayer was composed of Ni_{0.5}Cr_{0.25}Fe_{0.25}O_x formed by the tribo-oxidation of Inc718 (Eq 6.3), and triboxidized TaAg11 surface (Eq. 6.2). The formation of these lubricating tribo-

oxides is responsible for the negligible WR of the TaAg11 surfaces, and the small amounts of wear of the SA surfaces.

- During rig testing of CrAg11 against chemically treated SA's, powdered tribofilms composed of tribo-oxides from both the surfaces were observed.

6.4.1.3 TaAg11 against alumina at 550 °C

When the TaAg11 was tested against Al₂O₃ (Figs. 60b and c), phase separation in the tribo-layer was observed: Ag-rich regions essentially separated out (S and T, Table 9) and Ag peaks were detected in the XRD spectra (Fig. 70). A similar effect was observed during the thermal oxidation of TaAg11 sample at 600 °C for 96 h, which resulted in the selective oxidation of Al in Ag₂Al to form Al-rich oxides and the formation of a O-deficient phases at the oxide/carbide interface (Ch. 2). Also during XRD analysis, an increase in the intensity of the Ta₂C peaks (Fig. 70) was observed.

The transfer film formed on TaAg11 was harder (~ 9 GPa) as compared to the as-synthesized TaAg11 samples. Thus, it is fair to propose that at 550 °C, tribo-oxidation of the TaAg11 surfaces is similar to triboreaction 6.2. Most probably due to higher contact temperatures as compared to room temperature, the LM formed at room temperature separates into the Ag-rich phases and Ta-Al based mixed oxide (Fig. 60). Most probably due to O- gradient in the transfer films, some of the Ta-Al rich phases are not completely oxidized. This can account for the origin of Ta₂C peaks in XRD. The phase separated tribo-layer is abrasive as compared to the LM generated at RT, and high WR ~ (10⁻⁴ mm³/N-m) and $\mu_s < 0.5$, are observed (Table 8). Henceforth, this particular kind of tribofilm will be referred to as AM (abrasive mixture). Similar μ_s and WRs are observed during testing of MAX/Ag-Inc718 tribocouples due to formation of LO's. The

fundamental difference between AM and LO is tribochemistry. AM are generated by phase separation of LM's (LM's are formed by tribo-oxidation of MAX/Ag surfaces), and LO's by tribo-oxidation of both Inc718 and MAX/Ag surfaces.

6.5 Conclusions

In the present work, we have considered the several novel self-lubricated tribocouples based on TaAg11 and CrAg11 composites. The remarkable feature of these tribocouple is their ability to work continuously in the wide temperature range from 26 to 550 °C. Based on the dominant tribological reactions, which are taking place during the friction, a classification of the different type of tribofilms was developed. Please refer to Fig. 91 for schematics of the different tribofilms formed during dry sliding.

- During the tribological study of TaAg11-Inc718 tribocouples under standard conditions at RT, the presence of Ag₂Al as the cementing phase in the grain boundaries prevents the formation of abrasive third bodies. As a result, the WR of the TaAg11 pin was reduced by 3 orders of magnitude as compared to pure Ta₂AlC (Table 8).
- During tribological study of TaAg11-alumina tribocouples under standard conditions at RT, LM are formed by tribooxidation of the TaAg11 surfaces (Eq. 6.3). This tribolayer is responsible for lowering of the WRs and μ 's as compared to pure Ta₂AlC-Inc718 tribocouples (Table 8).
- At 550 °C, the TaAg11-Inc718, and CrAg11-Inc718 tribocouples formed a LO according to reaction in 6.3 by the tribo-oxidation of the Inc718. The presence of this layer is responsible for low WR of MAX/Ag surfaces ($\sim 10^{-5}$ mm³/N-m,

Table 8), and the relatively high WR of Inc718 surfaces ($\sim 10^{-4}$ mm³/N-m, Table 8), and μ 's ~ 0.5 . The exact role of the carbide-rich sublayer is not clear, most possibly, it forms a semi-continuous hard substrate on which lubricating tribooxide (LO's) can be sheared easily.

- During continuous thermocycling operation, the TaAg11–Inc718 the tribocouples maintained their intrinsic self-lubricating property; μ 's ≤ 0.5 and WR $\sim 10^{-4}$ mm³/N-m are observed. The tribolayer was composed of Ni_{0.5}Cr_{0.25}Fe_{0.25}O_x formed by tribo-oxidation of Inc718 (see eq 6.3), and triboxidized TaAg11 particles (see eq. 6.2). The exact role of the carbide-rich sublayer not clear, most possibly, it forms a semi-continuous hard substrate on which lubricating tribooxide (LO's) can be sheared easily.
- During rig testing of TaAgR against SA's - the tribolayer was composed of Ni_{0.5}Cr_{0.25}Fe_{0.25}O_x formed by tribo-oxidation of Inc718 (Eq 6.3), and triboxidized TaAg11 surfaces (Eq. 6.2). The formation of these lubricating tribo-oxides is responsible for the negligible WR of the TaAg11 surfaces, and the small amount of wear of the SA surfaces.
- During rig testing of CrAg11 against SA's – the roughening of the SA surfaces resulted in powdered tribofilms composed of tribo-oxides from both the surfaces. The tribo-couple successfully passed the rig testing.
- During tribological study of TaAg11-alumina tribocouples at 550 °C, tribo-oxidation of TaAg11 surfaces results in formation of AM's on the tribo-surfaces.

CHAPTER 7: TRIBOFILM ENGINEERING OF SELF-LUBRICATING Ta₂AlC/Ag–Inc718 or Cr₂AlC/Ag–Inc718 TRIBOCOUPLE

7.1 Introduction

In Ch.6 several novel self-lubricated films obtained between TaAg11 and CrAg11 composite samples and a superalloy (Inc718) or Al₂O₃ were studied. It was established that the tested tribocouples can generate multilayered tribofilms that self-adjust to the dynamically changing tribological conditions, more specifically temperature cycling. Furthermore, based on the dominant tribological reactions taking place during dry friction, an understanding of the different types of tribofilms was developed.

The goal of this chapter is to engineer the tribofilms by changing the surface roughness, load, and test temperatures of TaAgR, CrAg11 and TaAg11 samples against Inc718.

7.2 Experimental Details

The friction and wear tests were performed using a high temperature tribometer (CSM, Switzerland) capable of going up to 600 °C. The experimental procedure of the testing and characterization of the WRs and μ 's were detailed in Ch. 3. The sliding speed during all the experiments was 1 m/s. The procedure for characterizing the different *microconstituents* in the tribofilms by EDS analysis was also explained in Ch. 3. TaAg11, CrAg11 and TaAgR samples were used for characterization.

All surfaces were polished to a 1 μ m diamond finish, washed with acetone and dried prior to testing. During some experiments, roughening of the Inc718 surfaces was done by sandblasting or chemical etching. Sandblasting of the surfaces was done by

Al_2O_3 grits for 30s. Chemical etching was done with a 40 vol.% ferric chloride solution (Fisher Scientific) for 10 minutes. Henceforth, treated Inc718 surface will be designated either as Inc718 (sandblasted) or Inc718 (FeCl_3).

7.3 Results

7.3.1 Sample Chemistry

Both TaAgR and TaAg11 have similar chemistries (Fig. 74). The main matrix is $\text{Ta}_2\text{Al}_{1-x}\text{C}$ ($x \leq 0.5$), which is surrounded by Ag_2Al as a cementing phase. Small amounts of Ta_4AlC_3 and Ta_2C were also detected.

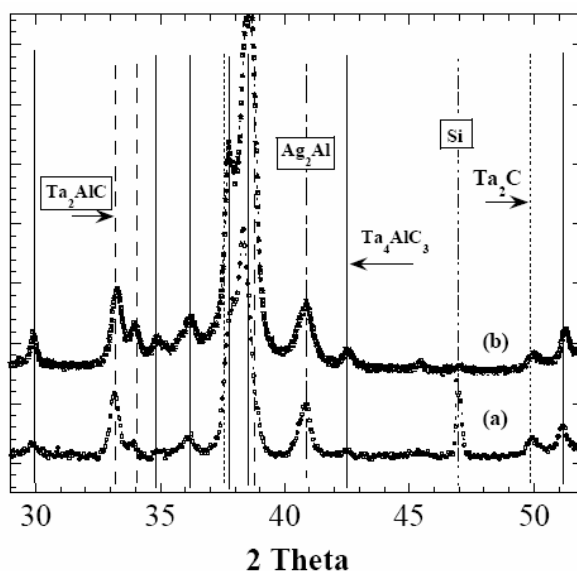


Figure 74: XRD of as-synthesized, (a) TaAg11, and (b) TaAgR.

7.3.2 Variation of μ as a function of sliding distance

When the TaAgR-Inc718 tribocouple was tested under standard conditions at RT, it initially displayed a $\mu \sim 0.9$ (Fig. 75), which decreased sharply to 0.4 after ~ 350 m, thereafter it increased gradually again to 0.9, and maintained that steady state value till 1

km. When the TaAg11-Inc718 tribocouple was tested under similar condition it displayed a $\mu_s \sim 0.6$ (Fig. 75).

When the TaAgR-Inc718 tribocouple was tested under standard conditions at 550 °C (Fig. 76) it displayed an initially high $\mu \sim 0.6$, that decreased to a $\mu_s \sim 0.4$.

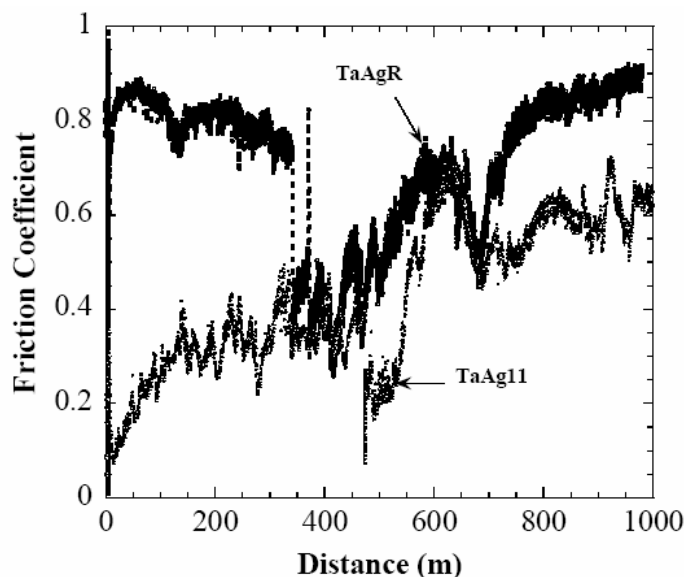


Figure 75: Variation of μ as a function of sliding distance when the TaAg11 and TaAgR samples were tested against Inc718 at 26 °C. Experiments were done under standard conditions.

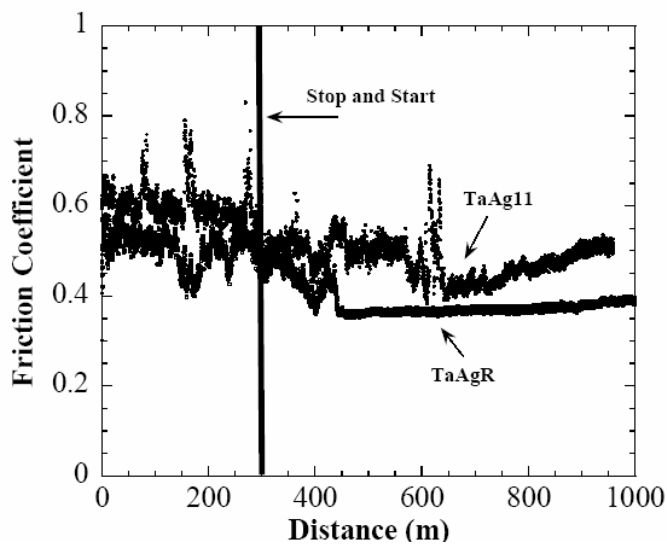


Figure 76: Variation of μ as a function of sliding distance when the TaAgR and TaAg11 samples were tested against Inc718 at 550 °C under standard conditions.

7.3.3 Change in μ with load

At 26 °C, the TaAg11-Inc718 tribocouple displayed a $\mu_s \approx 0.6$ at 3 N load. It decreased to 0.3 when the load was increased to 8 N, while retaining all the other parameters similar (Table 10).

The TaAgR-Inc718 and CrAg11-Inc718 tribocouples were also tested extensively under variable loading conditions at 26 °C: at 3N load, μ_s was ~ 0.8 - 0.9 in both the cases; it decreased to 0.3 at 8 N although fluctuation in μ was observed (Fig. 77). At 18 N, μ_s was 0.3, and μ became stable. The TaAgR-Inc718 was also tested under different loading conditions at 550 °C. At 3 N, μ_s was ≈ 0.4 and it increased to ~ 0.5 as the load was increased to 18 N (Fig. 77).

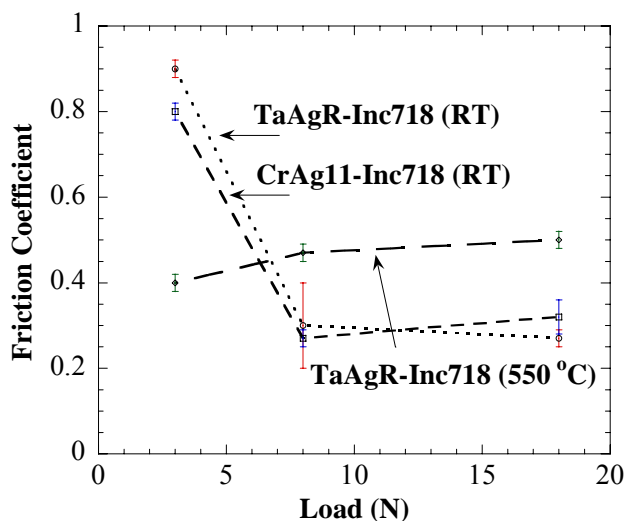


Figure 77: Dependence of μ on normal applied load when TaAgR and CrAg11 were tested against Inc718 at 26 °C, and TaAg11 was tested against Inc718 at 550 °C.

7.3.4 Effect of cycling on μ :

When the TaAgR-Inc718 tribocouple was tested at RT under 18 N for 1 km, μ_s was 0.3 (Fig. 78). The tribocouple was subsequently

tested at 3 N, on the *same* track, μ gradually increased to 0.6; it was not stable though

Table 10: Summary of WR's and μ 's when TaAg and CrAg composites were tested against Inc718 under different loading and temperature.

Static Partner	Dynamic Partner	Conditions	Temp. (°C)	WR _s (mm ³ /N-m)	μ_s	Ref.	
TaAg11		8 N and 1 m/s		2×10^{-4}	0.3		
TaAgR	Inc718	3 N and 1 m/s	26	6×10^{-6}	0.9	Ch. 7	
	Inc718 (Sandblasted)	3 N and 1 m/s		4×10^{-5}	0.3		
	Inc718 (FeCl ₃ treated)	3 N and 1 m/s		2.5×10^{-5}	0.5		
		3 N and 1 m/s		550	2.5×10^{-5}		0.6
		8 N and 1 m/s	26	5×10^{-5}	0.3		
		18 N and 1 m/s [‡]	26	3×10^{-4}	0.3		
		3 N and 1 m/s	26	2.5×10^{-5}	0.6		
		3 N and 1 m/s	550	1.5×10^{-5}	0.5		
		3 N and 1 m/s	26	2.5×10^{-5}	0.5		
		8 N and 1 m/s ^{‡‡}	550	9×10^{-5}	0.5		
		3 N and 1 m/s	26	$< 10^{-6}$	0.12		
		18 N and 1 m/s	550	3×10^{-4}	0.5		
		Inc718 (Sandblasted)	3 N and 1 m/s ^{‡‡‡}	550	5×10^{-5}		0.5
			3 N and 1 m/s	26	3×10^{-5}		0.3
TaAg11	Inc718	3 N and 1 m/s	26	2×10^{-5}	0.6	Ch. 5	
			350	$< 10^{-6}$	0.3		
			550	5×10^{-5}	0.5		
	Al ₂ O ₃		26	3×10^{-5}	0.3		
			350	5.5×10^{-5}	0.45		
			550	6×10^{-4}	0.47		
			TiAlN	26	8×10^{-6}		0.3
CrAg11	Inc718	3N and 1 m/s	26	5×10^{-5}	0.8	Ch.5	
		8N and 1 m/s		4×10^{-5}	0.3	Ch.7	
		18N and 1m/s		6×10^{-5}	0.3		

- Method- 1[‡], method - 2^{‡‡}, method - 3^{‡‡‡}

and large fluctuations were observed (Fig. 78a). The tribometer was then heated to 550 °C, and the tribocouple was tested for 2 km. μ_s was 0.5 during this experiment (Table 10).

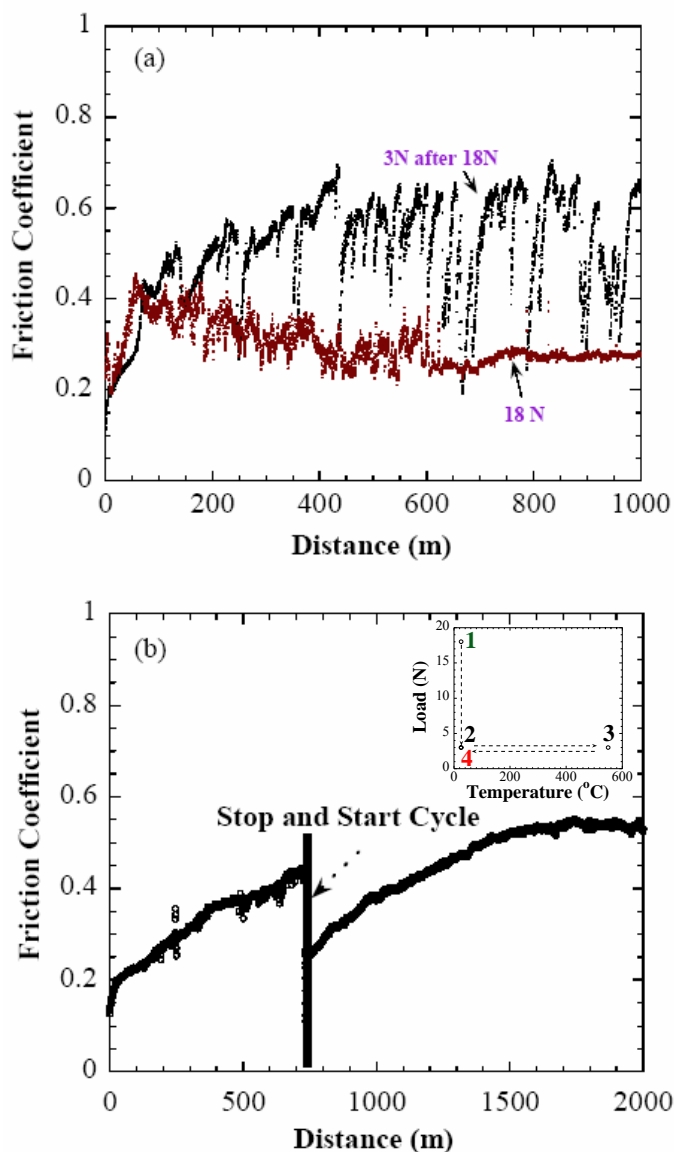


Figure 78: (a) Variations in μ_s as a function of sliding distance when TaAgR was tested against Inc718 at 18 N load for 1000 m at 26 °C, and subsequently tested at 3N load, and (b) variations in μ_s as a function of sliding distance when the same sample was tested against Inc718 at 3 N load for 2000 m at 26 °C after being cycled at conditions described in Fig. 78a, then at 550 °C for 2 km at 3 N load. Inset shows the schematic representation of the cycle, 1 is the starting point of the cycle, and 4 is the end point.

The tribometer was then cooled down. On the same track, the sample was tested at 3N and 1 m/s. The fluctuation in μ decreased, μ started from < 0.2 , and gradually increased to 0.4. The experiment was stopped and started again to mimic cold stop and start condition, whereupon μ increased from < 0.2 and attained a $\mu_s \sim 0.5$ (Fig. 78b). This entire cycle will be henceforth referred to as method 1. Inset in Fig.78b shows schematic representation of the entire cycle.

When the TaAgR-Inc718 tribocouple was tested at 8 N and 550 °C, μ was 0.6, and gradually decreased to $\mu_s \sim 0.5$ (Fig. 79a). The tribometer was then cooled down, and the sample was tested at 3 N and 26 °C. μ marginally increased from 0.1 to 0.15 after 1 km of dry sliding. This cycle will be henceforth referred to as method 2 (Fig.79b).

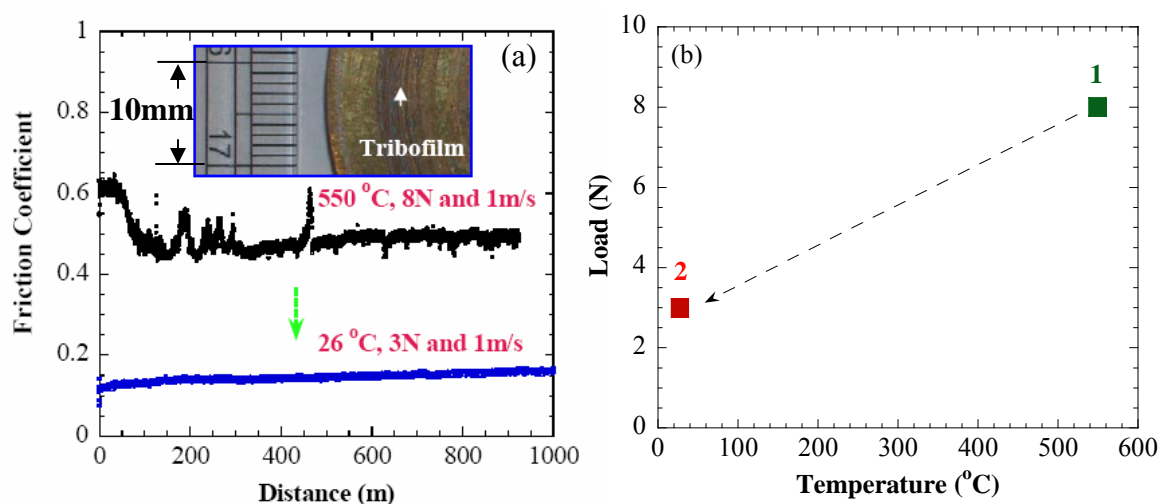


Figure 79: (a) Variation in μ 's as a function of sliding distance when TaAgR-Inc718 tribocouple was tested at 550 °C, and 8N. On the same wear track, the tribocouple was subsequently tested at 26 °C, and 3 N. Inset shows the tribofilms formed on the Inc718 surface. (b) Schematic representation of this cycle which is referred to as method-2 in the text.

7.3.5 Effect of surface roughness and thermal cycling on μ

During testing of TaAgR against Inc718 (sandblasted) at RT, under standard conditions, μ gradually increased from < 0.2 , to $\mu_s \approx 0.5$ (Fig. 80a). Material was transferred from the TaAgR surface onto the Inc718 (sandblasted) surface (inset of Fig. 80a).

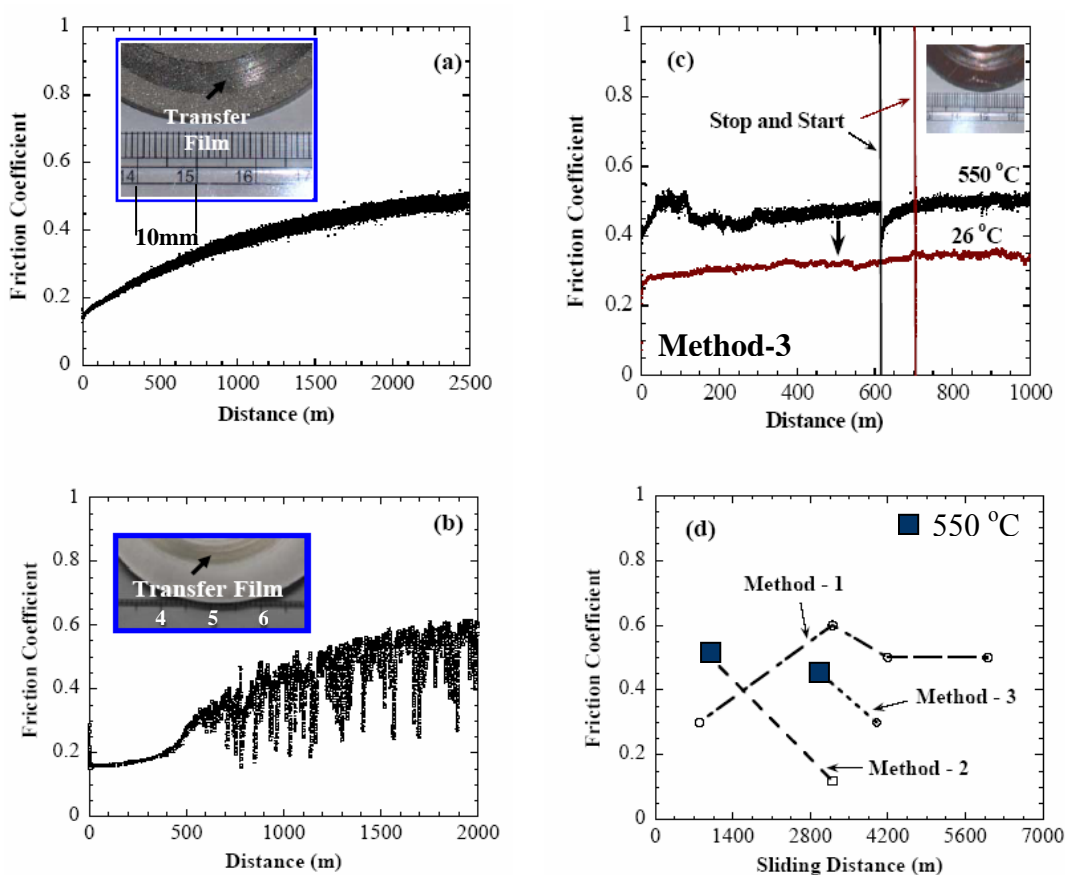


Figure 80: Variation in μ 's as a function of sliding distance when TaAgR was tested against, (a) Inc718 (sandblasted), and (b) Inc718 (FeCl₃ treated) under standard conditions at RT. Inset in a and b shows the tribofilms formed on Inc718 surface. (c) Variation in μ 's as a function of sliding distance when TaAgR was tested against Inc718 (sandblasted) by *method-3* described in text. Inset shows the digital picture of transfer film formed on Inc718 surface. (d) Variation in μ 's as a function of sliding distance when TaAgR-Inc718 tribocouple was tested by method 1, 2 and 3.

When μ of TaAgR at RT was monitored as function of sliding distance against Inc718 (FeCl₃) under standard conditions, it increased from < 0.2 to a $\mu_s \approx 0.6$ (Fig. 80b). Huge fluctuations in μ 's were observed after 500 m. A transfer film was observed on the Inc718 (FeCl₃) surface (inset of Fig. 80b).

When TaAgR was tested against Inc718 (sandblasted) at 550 °C under standard conditions, μ was initially ~ 0.4 , before attaining a $\mu_s \approx 0.5$ (Fig. 80c). The tribometer was then cooled down. The tribocouple was subsequently tested at RT under standard conditions. μ was 0.3 during the entire sliding distance (Fig. 80c). This entire cycle will be henceforth referred to as method 3. A summary of μ as a function of sliding distance observed during methods 1, 2, and 3 is shown in Fig. 80d.

7.3.6 Wear

7.3.6.1 Wear of Ta₂AlC/Ag composites

7.3.6.1.1 WRs as a function of variable load and surface roughness

The WRs of TaAg11 was $2 \times 10^{-5} \text{ mm}^3/\text{N-m}$ after testing against Inc718 under standard conditions (Table 10, Fig. 81). At 8 N, the WR increased to $2 \times 10^{-4} \text{ mm}^3/\text{N-m}$. Similarly, the WRs of TaAgR was $\sim 6 \times 10^{-6} \text{ mm}^3/\text{N-m}$ after testing against Inc718 at RT under standard conditions. It increased to $\sim 5 \times 10^{-5} \text{ mm}^3/\text{N-m}$ at 8N, and finally to $3 \times 10^{-4} \text{ mm}^3/\text{N-m}$ at 18 N load. The WRs of TaAgR was $5 \times 10^{-5} \text{ mm}^3/\text{N-m}$ when it was tested against Inc718 (sandblasted), and $2.5 \times 10^{-5} \text{ mm}^3/\text{N-m}$ when tested against Inc718 (FeCl₃) (Table 10). WR of CrAg11 when tested against Inc718 under standard conditions was $5 \times 10^{-5} \text{ mm}^3/\text{N-m}$. Increase in load from 3 to 18 N has small effect on WR. In other words, increase in loads had no effect on WR of CrAg11 (Fig. 81).

At 550 °C, the WR of TaAgR was $3 \times 10^{-5} \text{ mm}^3/\text{N-m}$ after testing under standard conditions (Table 1, Fig. 75). It increased to $9 \times 10^{-5} \text{ mm}^3/\text{N-m}$ at 8N, and finally to $3 \times 10^{-4} \text{ mm}^3/\text{N-m}$ at 18 N load.

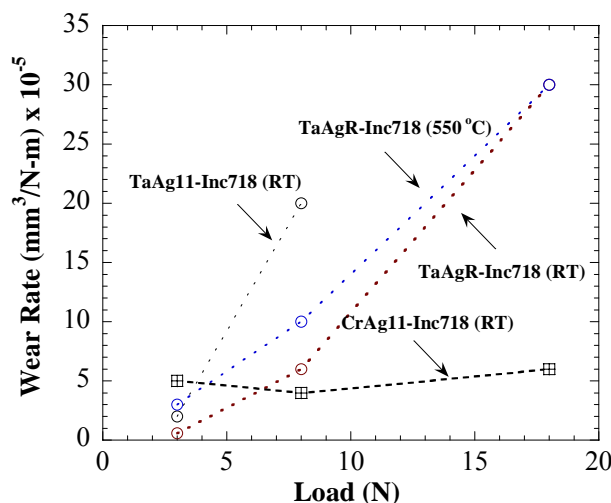


Figure 81: WR of MAX/Ag as a function of normal loads when tested against Inc718 at 26 and 550 °C.

7.3.6.1.2 Evolution of wear at RT

Figure 82a summarizes the evolution of wear as a function of sliding distance when the TaAgR and TaAg11 samples were tested against Inc718, both polished and surface treated. During all the testing conditions, wear was linear as a function of sliding distance (Fig. 82a).

7.3.6.1.3 Evolution of wear at 550 °C

The TaAg11 and TaAgrR samples had similar WRs, when tested under standard conditions at 550 °C (Table 10). The WR kinetics of TaAg11 tested against polished and

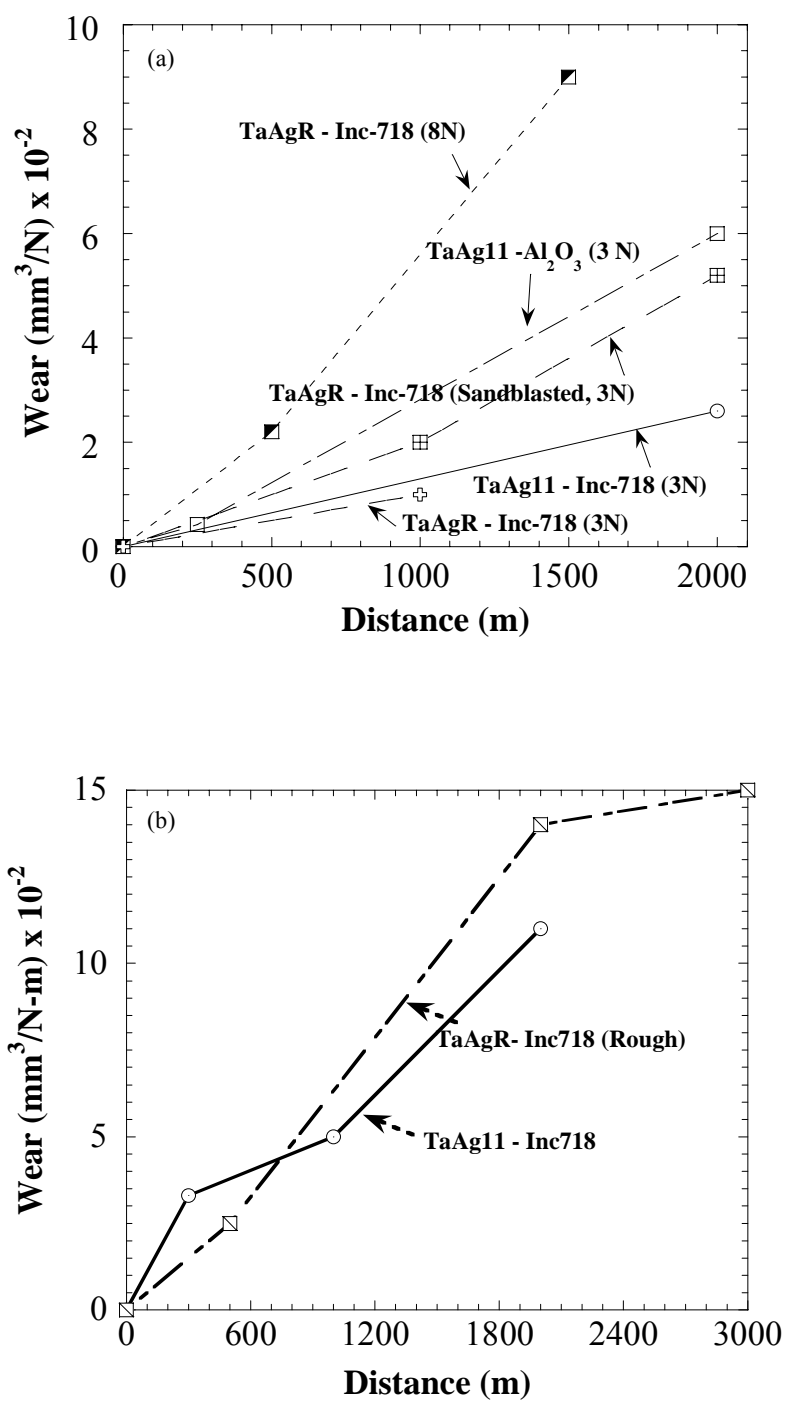


Figure 82: Evolution of WR of TaAg composites tested under different normal loads, (a) at RT, and (b) at 550 °C.

sandblasted Inc718 tested under standard condition were initially linear (Fig. 82b). The WR of the TaAgR samples decreased after 2 km.

7.3.6.1.4 Evolution of wear during cyclic conditions

The WRs of TaAgR, as a function of sliding distance tested by method 1, 2 and 3 are summarized in Table 10 and Fig. 83. During method 1 - after testing at 26 °C and 18 N - the WR of TaAgR was $3 \times 10^{-4} \text{ mm}^3/\text{N}\cdot\text{m}$. It decreased to $< 5 \times 10^{-5} \text{ mm}^3/\text{N}\cdot\text{m}$ during subsequent dry sliding. During method 2, the WR was $\sim 9 \times 10^{-5} \text{ mm}^3/\text{N}\cdot\text{m}$, after testing at 8 N, 1 m/s and 550 °C. It decreased to $< 10^{-6} \text{ mm}^3/\text{N}\cdot\text{m}$ during subsequent testing at 26 °C. When tested by method 3, the WR of TaAgR was $5 \times 10^{-5} \text{ mm}^3/\text{N}\cdot\text{m}$ after testing against Inc718 (sandblasted) at 550 °C for 3 km. It decreased subsequently to $3 \times 10^{-5} \text{ mm}^3/\text{N}\cdot\text{m}$ after testing at 26 °C for 1 km (Fig. 83).

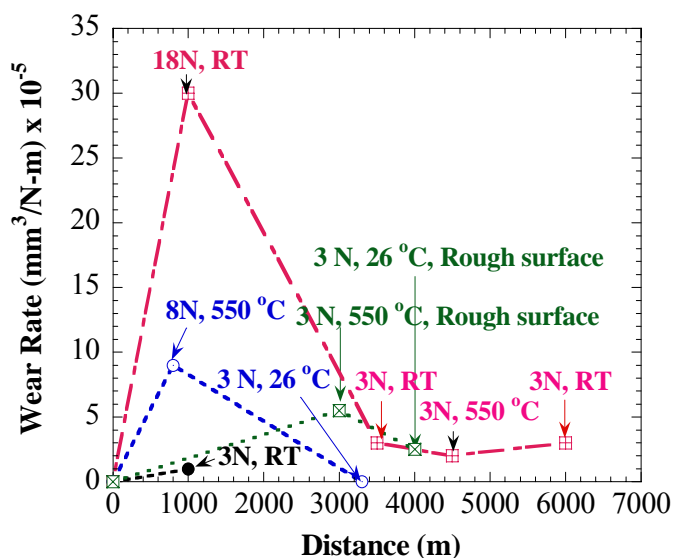


Figure 83: Evolution of WRs of TaAgR after testing under cyclic conditions - method 1 (Red), 2 (Blue) and 3 (Green).

7.3.6.1.5 Wear of Inc718

7.3.6.1.5.1 RT

Surface roughening was observed on the Inc718 surface after testing against TaAg11 under standard conditions after 2 km dry sliding. In some locations gouges as deep as $\sim 0.5 \mu\text{m}$ were observed (Fig. 47a). On the Inc718 surfaces, after testing against TaAgR at 8N, 1 m/s sliding speed and after 800 m dry sliding, in some locations, gouges as deep as $\sim 1 \mu\text{m}$ was observed (Fig. 84).

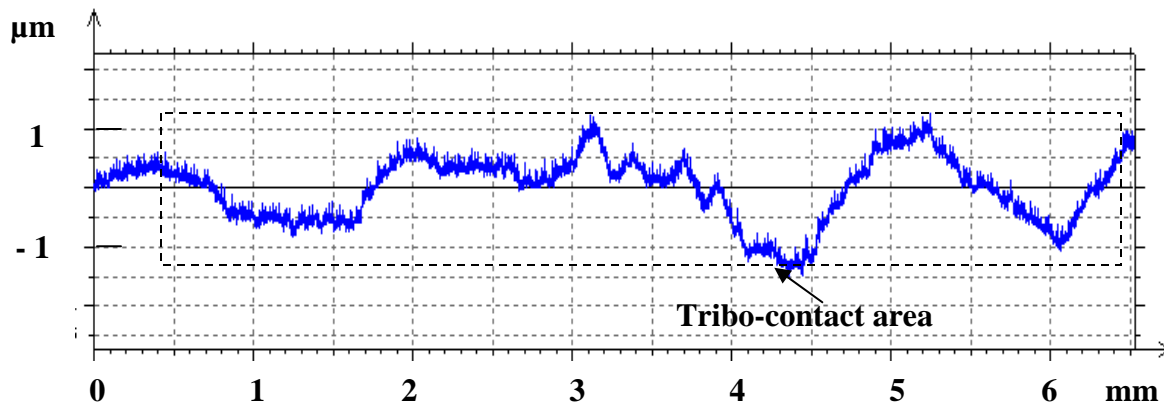


Figure 84: Laser profilometry of Inc718 surfaces after testing against TaAgR at 8 N load at 26 °C.

7.3.6.1.5.2 After testing at 550 °C

The Inc718 surfaces were covered with tribofilms and in some locations gouges were observed after testing against TaAg11 under standard conditions after 2 km dry sliding (Fig. 47b). The surfaces of the Inc718, after testing by methods 1 and 2, were covered with tribofilms; in some locations gouges were observed (Fig. 85).

7.3.6.1.5.3 Surface treated Inc718

In the Inc718 (sandblasted) surfaces gouges as deep as 5 μm were seen (Fig. 86a). In the tribo-contact area, the maximum depths of the gouges after testing against TaAgR at RT under standard conditions decreased to $\sim 2 \mu\text{m}$. The Inc718 (FeCl_3) surfaces - *after* testing against TaAgR at RT - showed no significant change in the surface roughness from the surface treated samples prior to testing (Fig. 86b). On the Inc718 (sandblasted) surfaces tested by method 3, tribofilms and gouges like those observed in methods 1 and 2 were observed.

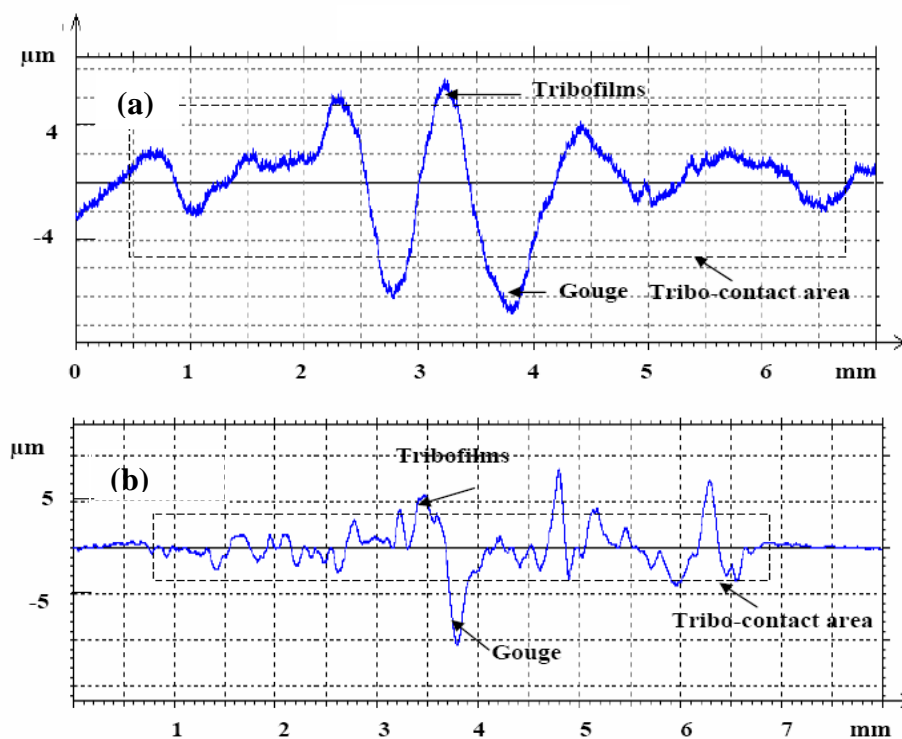


Figure 85: Laser profilometry of Inc718 surfaces after testing by, (a) method 1, and (b) method 2.

7.3.7 Microscopy and EDS analysis

The Inc718 and TaAgR surfaces after testing at RT and under 8 N load were studied by

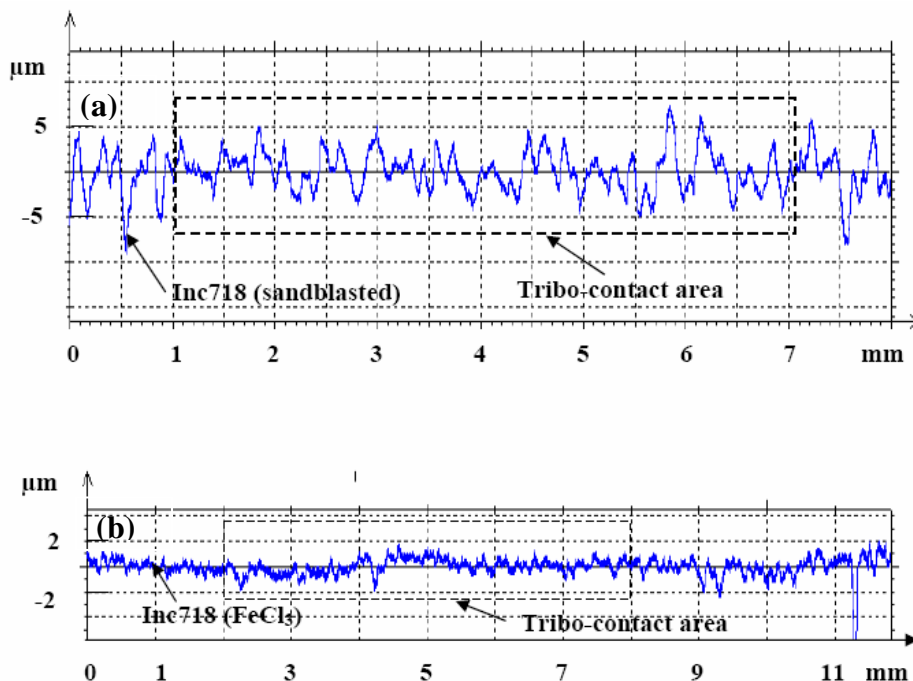


Figure 86: Laser profilometry of the Inc718 (surface treated) tested against TaAgR, (a) sandblasted and, (b) FeCl₃ treated under standard conditions at RT.

microscopy (Figs. 87a and b). The Inc718 surfaces were covered with a discontinuous transfer film of average composition AB, $^*[\text{Ta}_{0.4}\text{Al}_{0.2}\text{Ag}_{0.2}\text{Ni}_{0.1}\text{Cr}_{0.05}\text{Fe}_{0.05}]\text{O}_1^*$ (Table 11, inset of Fig. 87a). The average composition of the Inc718 surface, where there was no tribofilm was AA = $^*[\text{Ta}_{0.1}\text{Al}_{0.05}\text{Ag}_{0.05}\text{Ni}_{0.4}\text{Cr}_{0.2}\text{Fe}_{0.2}]\text{O}_{0.25}^*$ (Table 11, Fig. 87a). The TaAgR tribosurface was composed of 2 regions (Fig. 87b); dark regions, AC = $^*[\text{Ta}_{0.4}\text{Al}_{0.25}\text{Ag}_{0.2}\text{Ni}_{0.05}\text{Cr}_{0.05}\text{Fe}_{0.05}]\text{O}_{0.5}^*$, and light regions, AD = $^*[\text{Ta}_{0.35}\text{Al}_{0.2}\text{Ag}_{0.35}\text{Ni}_{0.03}\text{Cr}_{0.03}\text{Fe}_{0.03}]\text{O}_{0.1}^*$.

TaAgR and Inc718 (sandblasted) surfaces after testing under standard conditions at RT were examined (Fig. 88). Inc718 (sandblasted) were covered with tribofilms of chemistry AL1 = $[\text{Ta}_{0.1}\text{Al}_{0.1}\text{Ag}_{0.05}\text{Ni}_{0.4}\text{Cr}_{0.2}\text{Fe}_{0.15}]\text{O}_{0.3}$, and AL2 =

$[\text{Ta}_{0.3}\text{Al}_{0.25}\text{Ag}_{0.1}\text{Ni}_{0.1}\text{Cr}_{0.1}\text{Fe}_{0.1}]\text{O}_{0.7}$ (Fig. 88a). The TaAgR surface was smooth, and no third body was visible on the surface. The average chemistry of the surface was AN = $[\text{Ta}_{0.6}\text{Al}_{0.25}\text{Ag}_{0.15}]\text{O}_{0.15}$ (Fig. 88b).

The Inc718 and TaAgR surfaces after testing by method 2 were examined (Fig. 89). The average chemistry of the bare Inc718 surfaces, AE (dark regions), = $*[\text{Ta}_{0.05}\text{Al}_{0.05}\text{Ag}_{0.05}\text{Ni}_{0.5}\text{Cr}_{0.2}\text{Fe}_{0.2}]\text{O}_{0.5}*$ were covered with scatted tribofilms of composition, AF = $*\text{Ta}_{0.2}\text{Al}_{0.07}\text{Ag}_{0.07}\text{Ni}_{0.25}\text{Cr}_{0.2}\text{Fe}_{0.25}]\text{O}_1*$ (Table 11, Fig. 89). Sliding marks were present on the TaAgR surface (inset of Fig. 89c), which was composed of two constituents: AG (dark regions) = $*\text{Ta}_{0.15}\text{Al}_{0.07}\text{Ag}_{0.07}\text{Ni}_{0.4}\text{Cr}_{0.15}\text{Fe}_{0.15}]\text{O}_1*$ and AH (light regions) = $*\text{Ta}_{0.3}\text{Al}_{0.2}\text{Ag}_{0.1}\text{Ni}_{0.2}\text{Cr}_{0.1}\text{Fe}_{0.1}]\text{O}_{0.7}*$ (Fig. 83).

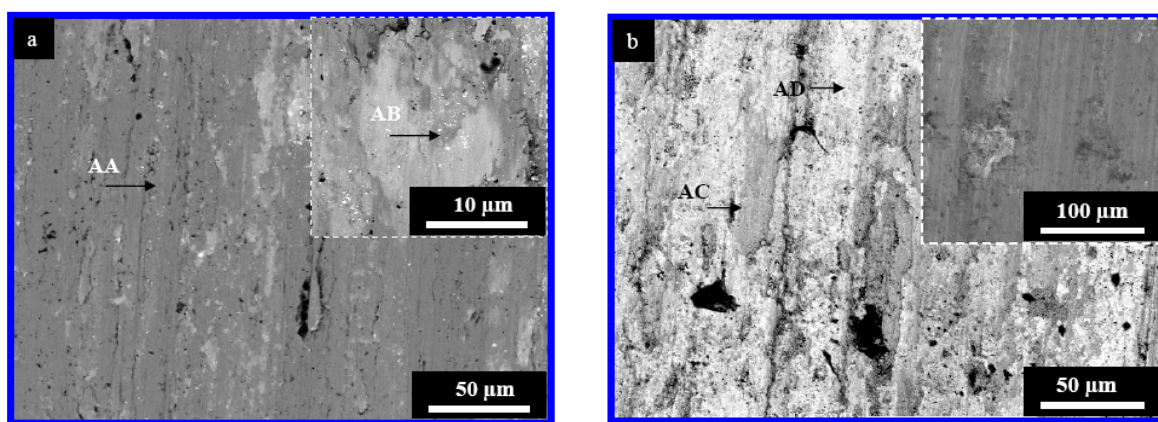


Figure 87: BSE FESEM micrograph of, (a) Inc718 surface after being tested against TaAgR. Inset shows the higher magnification of the transfer film formed on Inc718 surface, and, (b) TaAgR surface. Inset shows the SE FESEM micrograph of the TaAgR surface. The experiment was done at RT and 8N load.

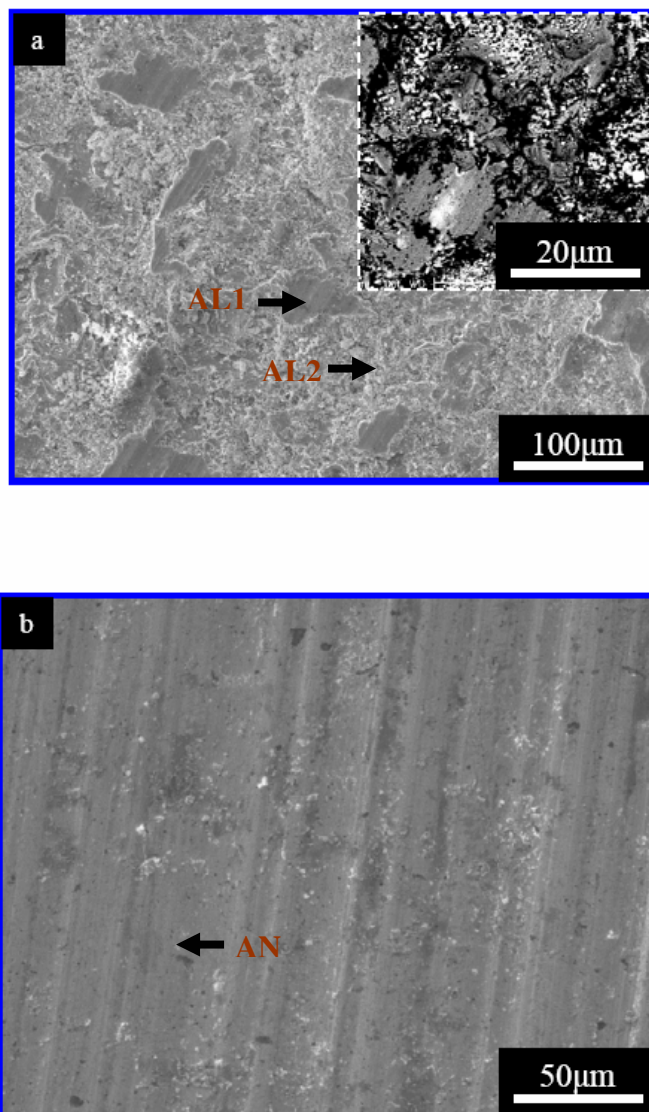


Figure 88: SE FESEM micrograph of, (a) Inc718 (sandblasted) surface after being tested against TaAgR. Inset shows the BSE micrograph at higher magnification of the transfer film formed on Inc718 surface, and, (b) TaAgR surface. Inset shows the SE FESEM micrograph of the TaAgR surface. The experiment was done under standard conditions.

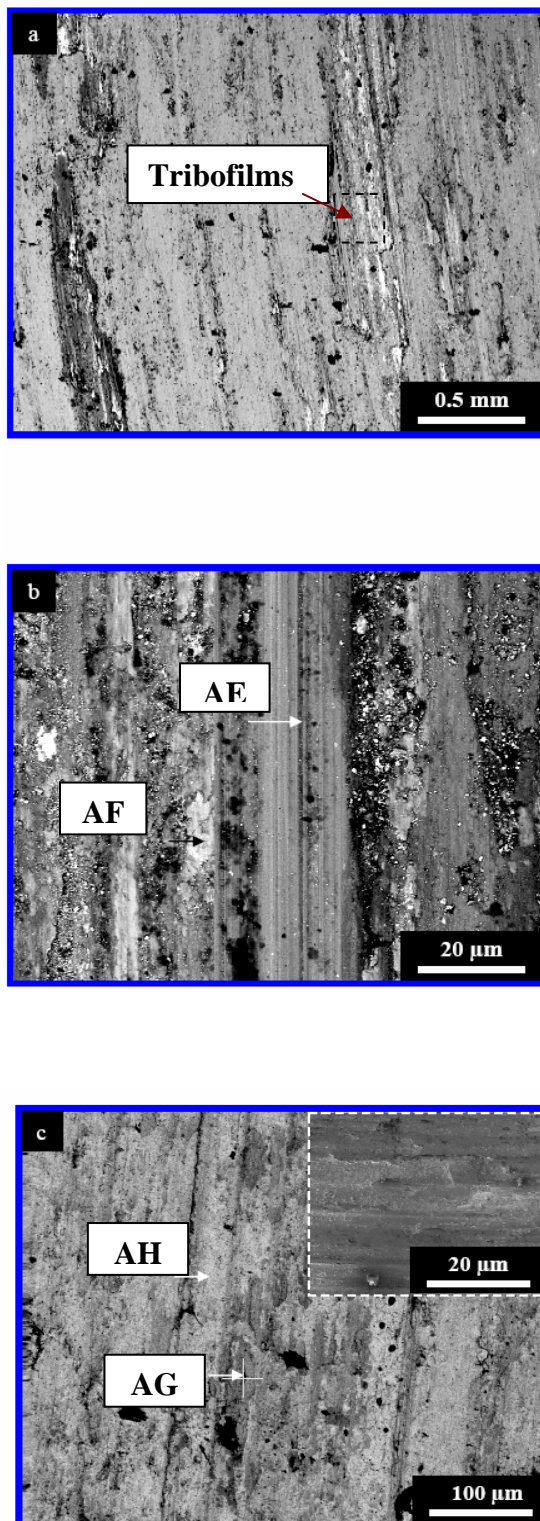


Figure 89: BSE FESEM backscattered micrograph of, (a) Inc718 surface, (b) higher magnification of Inc718 surface, and (c) TaAgR surface. The TaAgR-Inc718 tribocouple was tested by method 2.

Table 11 Average of at least 3 EDS readings of a region homogenous in micro scale, each alphabet letter represents elemental ratios of “micro constituents”. The areas highlighted with grey areas denote chemistries of tribofilms.

Reg.	O	Al	Ta	Ag	Cr	Fe	Ni	*Averaged Composition*
AA	22±0.5	3	5	2	15±1	12.5±0.5	36	[Ta _{0.1} Al _{0.05} Ag _{0.05} Ni _{0.4} Cr _{0.2} Fe _{0.2}]O _{0.25}
AB	52±0.5	8±1	16	8±5	2±0.5	3±1	5±1	[Ta _{0.4} Al _{0.2} Ag _{0.2} Ni _{0.1} Cr _{0.05} Fe _{0.05}]O ₁
AC	31±8	14±1	22	12±2	3±1	3±1	3.5±1	[Ta _{0.4} Al _{0.25} Ag _{0.2} Ni _{0.05} Cr _{0.05} Fe _{0.05}]O _{0.5}
AD	9±1	17±2	28	31±8	2±1	1±1	2±1	[Ta _{0.35} Al _{0.2} Ag _{0.35} Ni _{0.03} Cr _{0.03} Fe _{0.03}]O _{0.1}
AL1	22	7	6	2.5	15	13	30	[Ta _{0.1} Al _{0.1} Ag _{0.05} Ni _{0.4} Cr _{0.2} Fe _{0.15}]O _{0.3}
AL2	42	15	20	5	7	6	5	[Ta _{0.3} Al _{0.25} Ag _{0.1} Ni _{0.1} Cr _{0.1} Fe _{0.1}]O _{0.7}
AN	12	21	49	12	1	1	2	[Ta _{0.6} Al _{0.25} Ag _{0.15}]O _{0.15}
AE	33±2.5	2±0.2	2	1	11±1	14±1	34±1	[Ta _{0.05} Al _{0.05} Ag _{0.05} Ni _{0.5} Cr _{0.2} Fe _{0.2}]O _{0.5}
AF	51±3	5±1	10	5±0.5	7±1	10±6	12±2	[Ta _{0.2} Al _{0.07} Ag _{0.07} Ni _{0.25} Cr _{0.2} Fe _{0.25}]O ₁
AG	48	5	8	3±1	8±0.5	7	18±2	[Ta _{0.15} Al _{0.07} Ag _{0.07} Ni _{0.4} Cr _{0.15} Fe _{0.15}]O ₁
AH	40±3	11±1	17	5	5.5±1.5	4.5±0.5	11±0.5	[Ta _{0.3} Al _{0.2} Ag _{0.1} Ni _{0.2} Cr _{0.1} Fe _{0.1}]O _{0.7}

7.4 Discussion

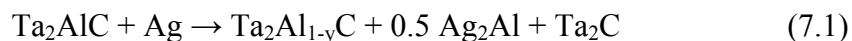
The important results of this chapter are:

- (a) The tribofilms formed at higher temperature are more effective in lowering the WRs and μ , as compared to the tribofilms formed at RT.
- (b) The μ 's and WR's can be tailored by altering the surface roughness of the SA.

In what follows, the fundamental mechanisms responsible for these results are discussed.

7.4.1 Effect of sample chemistry on μ and WR

According to XRD analysis, the TaAg11 and TaAgR samples have similar chemistries owing to the occurrence of a similar reaction during processing, namely:



where y depends on processing conditions.

At this point it is not clear why the two nominally identical samples had different tribo-responses. The TaAg11–Inc718 tribo-couple had lower μ 's as compared to TaAgR–Inc718 at RT tested under different load regimes. Under similar testing conditions TaAgR was more wear resistant than TaAg11 (Table 10). Both the tribo-couples have similar WRs at 550 °C when tested under standard conditions. μ is more stable for TaAgR as compared to TaAg11 (Fig. 76). The simplest explanation is that the tribochemistry is a complicated function of the proportions of different phases the different phases present: Al-deficient $Ta_2Al_{1-y}C$, Ta_2AlC , Ta_4AlC_3 , Ta_2C , Ag and Ag_2Al . However, it is known that tribo-chemistry is highly complex, and it will take extensive studies to understand the synergy of these phases on the tribological properties, which is beyond the scope of the current work.

7.4.2 Tribochemical Reaction and Mechanism

7.4.2.1 RT

At 3N loads, there is negligible mass transfer between the Inc718 and TaAg11 surfaces. Increase in loads from 3 to 8 N resulted in a decrease in μ (Fig.77). EDS analysis of the tribo-surfaces of the TaAgR–Inc718 tribocouples after testing at 8N showed tribofilms predominantly of chemistry AB (Table 11). The tribochemical reaction at the contact areas is similar to triboreaction 6.2 (Ch. 6). It results in the formation of a LM in the contact areas of the tribocouples. Owing to the lubricious nature of the LM, it became relatively easier to shear the interface – which accounts for the lowering of μ at higher loads. It is interesting to note that TaAg11 tested against harder substrates like Al_2O_3 and

TiAlN displays $\mu \sim 0.3$ at 3N (Table 8, Ch. 6). Most probably, the higher hardness of Al_2O_3 at the micro contacts promotes the formation of LM (Table 9, Ch.6).

Along the same lines, the increase in roughness of the Inc718 surfaces by sandblasting or chemical treatment increases the WRs of TaAgR (Table 10). However, that leads to the formation of a LM from the TaAgR surface to surface treated Inc718 (AL1 and AL2 in Table 11). These LM's were able to heal the surfaces of TaAgR (Fig. 88b). Even chemically treated Inc718 surfaces with tailored roughness of $< 1 \mu m$ (Fig. 86b) was able to induce the formation of visible tribofilms (Fig. 80), which lowered μ from 0.9 to 0.5 – 0.6 (Table 10 and Fig. 74). Thus it can be concluded that under these conditions, the TaAgR and TaAg11 surfaces are the source of the solid lubricant (LM). The formation of LM's lowers μ . But the tribofilms formed by formation of LM's are not able to lower the WR kinetics with distance, and they are linear during the entire testing duration (Figs. 81 and 82).

CrAg11-Inc718 tribocouple system during at RT under variable loads also showed decrease in μ from 0.8 to 0.3 as load was increased from 3 to 8N (Fig.77). Most probably due to formation of LM at the tribo-contacts is responsible for this behavior. Interestingly, the WR of CrAg11 doesnot increase with increase in load (Fig. 81).

7.4.2.2 Testing at 550 °C

In Ch. 6, it was established that formation of LO's imparted the TaAgR-Inc718 tribocouples with $\mu \leq 0.5$ and $WR \sim 10^{-4} mm^3/N\cdot m$ (Table 8). In this chapter, it was shown change in load has negligible effect on μ (Fig. 77), although the WRs increase linearly with load (Fig. 81). Thus it can be deduced that the LO based tribofilms formed at 550 °C are difficult to shear as compared to LM's formed at RT.

7.4.2.3 Cyclic testing conditions

Three cyclic tests were done by 3 different methods. From the WR results (Fig. 83), it can be concluded, the tribological performance of TaAgR-Inc718 tribocouple at 550 °C was similar during all the testing conditions. However, method 2 gave best tribological performance at RT as compared to other methods (Figs. 79 and 83). In other words, the tribofilms formed at higher temperature and loads are more efficient in improving the tribological performance as compared to tribofilms formed at RT. Both the TaAgR and Inc718 surfaces were examined after testing by method 2 (Fig. 89). Based on the EDS analysis of the tribosurfaces, it can be concluded that the tribofilms are most probably formed by the simplified triboreactions 6.2 and 6.3 discussed in Ch. 6. Note, at lower loads predominantly Inc718 surface contribute to formation of LO (viz. Eq. 6.3 in Ch. 6). In the last section, it was shown that only tribofilms from TaAgR surfaces are formed at RT during testing at higher loads. Basically, tribofilms generated by this technique were used in method 1 for cyclic test. Thus, it can be summarized, “the best tribological performance of TaAgR–Inc718 tribocouples can be attained by forming tribofilms at higher temperatures”. Based on these results successful rig tests of TaAgR samples against SA’s were done after generating tribofilms at higher temperature (Ch. 5).

Tribofilm formation at higher temperatures at the comparatively lower load of 3 N can be accelerated by roughening the Inc718 surfaces (viz. method 3). This conclusion implemented in the rig test by roughening the foils, was also confirmed during testing of CrAg11– Inc718 tribocouples in rig (Ch.5).

7.5 Comparison with literature

It is known in literature, oxides like NiO, ZnO are excellent LO's at 550 °C [21,22]. However, at room temperature, these oxides are ineffective as solid lubricants, due to fracture, and the cracking of the oxides [21]. In this chapter, it was demonstrated that tribo-oxides are excellent solid lubricants at room temperature, if a soft metal like Ag is present in the tribolayer to form LM with LO. The role of the Ag is not entirely clear at this time, but it most probably was able to alleviate the stresses which cause fracture of the oxide layers.

7.6 Conclusions

Please refer to Fig.91 for schematic understanding of different tribofilms.

- For reasons that are not clear, the tribological behavior of the TaAg-Inc718 tribocouple depended on processing conditions and varied from sample to sample. More studies are needed to understand the effect of processing conditions on tribological properties in this system.
- Increasing in load from 3 to 18 N decreased μ from 0.9 to ≤ 0.3 at RT at 1 m/s sliding speed because of intensification of the tribofilm formation. It resulted in the formation of LM from TaAgR surfaces. The LM's formed were highly shearable. The presence of Ag as microconstituents is responsible for this behavior. Increasing the surface roughness of the Inc718 also lowers μ from 0.9 to ≤ 0.5 presumably for the same reasons. Refer to Fig. 91 for the schematic understanding of formation of tribofilms under these conditions.

- At 550 °C, the μ 's were slightly increased as the load was increased from 3 to 18 N. Thus it can be inferred that LO formed at HT are not as shearable as the LM formed at RT.
- It was further shown the tribofilms generated at higher loads (≥ 8 N) were composed of tribo-oxidized product formed from both surfaces. Moreover, these tribofilms operate better than tribofilms formed at RT. Interestingly, tribofilms formation at 550 °C can be accelerated by roughening the surfaces (viz. method – 3).

CHAPTER 8 – CLASSIFICATION OF TRIBOFILMS

8.1 Introduction

In this chapter, important conclusions from Chs. 2–7 have been summarized to develop a classification of tribo-films. Based on these conclusions, a novel philosophy for optimizing the tribological behavior of MAX/Ag-Inc718 tribocouples has been proposed.

8.2 Classification of tribofilms

8.2.1 MAX Phases against Inc718 and Al₂O₃

Classifications of tribofilms in this section are based on studies done in Ch. 3.

8.2.1.1 Tribofilm – I

During dry sliding of MAX-Inc718 and MAX-Al₂O₃ tribocouples under standard conditions at RT, *partially oxidized wear debris* is formed by tribo-oxidation of the MAX surfaces. The wear debris acts as a third body and causes abrasion of the MAX phases (Figs. 90a1 and c1).

Consequently, the tribological behavior of the MAX-Inc718 and MAX-Al₂O₃ tribocouples are characterized by high WRs ($\geq 10^{-4}$ mm³/N-m) and $\mu > 0.4$, at room temperature.

8.2.1.2 Tribofilm - II

During dry sliding of MAX-Inc718 tribocouples under standard conditions at 550 °C, *tribo-oxidation of Inc718 surfaces* results in the formation of Ni_{0.5}Cr_{0.25}Fe_{0.25}O_{1-a} (where $a \leq 0.5$) which acts as a LO at the tribocontact areas. It is because of this tribo-oxidation that the WRs of the Inc718 was relatively high ($\sim 10^{-5}$ mm³/N-m). However,

because these oxides are lubricious, the WRs of the MAX phases are low $< 10^{-5}$ mm³/N-m, with $\mu's \leq 0.5$ (Table 6, and Fig. 90b1).

8.2.1.2 Tribofilm - III

During dry sliding of Ta₂AlC-Al₂O₃ tribocouples under standard conditions at 550 °C, *tribo-oxidation of the Ta₂AlC surfaces* results in the formation of the tribooxides Ta₂AlO_{6.5-x} ($x < 0.5$) at the tribocontact areas. It is because of formation of this tribo-oxides that WRs $< 10^{-6}$ mm³/N-m and $\mu's \sim 0.9$ are observed (Fig. 90d1).

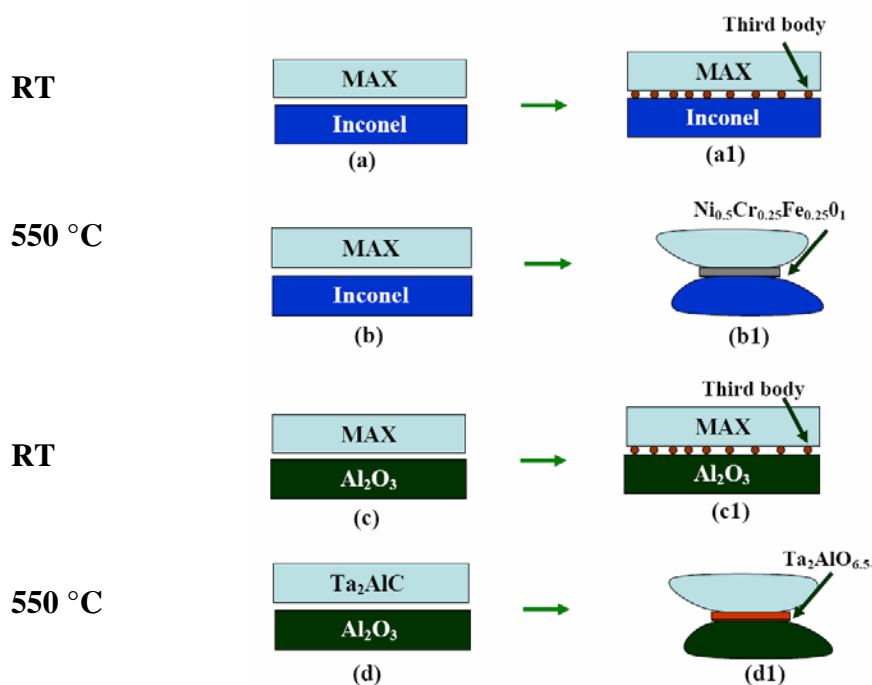


Figure 90: Schematic presentation of tribo-interactions of MAX phases against different tribo-partners: (a) and (a1) MAX-Inc718 tribocouples before and after dry sliding experiments at RT, (b) and (b2) MAX-Inc718 tribocouples before and after dry sliding experiment at 550 °C, (c) and (c1) MAX-alumina tribocouples before and after dry sliding experiment at RT, and (d) and (d1) MAX-alumina tribocouples before and after dry sliding experiment at 550 °C. All the tests were done under standard conditions.

8.2.2 MAX/Ag composites against Inc718 and Al₂O₃

8.2.2.1 Tribofilm IV

During dry sliding of TaAg11-Inc718 tribocouples under standard conditions at RT, negligible mass transfer was observed between the surfaces (Fig. 91a1). Thus the presence of Ag₂Al stops third body abrasion. Although during this sliding, partial oxidation of the Inc718 surface was detected. This partially oxidized Inc718 forms an extremely thin, or more likely x-ray amorphous layer (Fig. 70). Compared to pure Ta₂AlC tested against Inc718, the addition of Ag reduces the WR by 3 orders of magnitude (Table 8).

8.2.2.2 Tribofilm V

- During dry sliding of the TaAg11-Al₂O₃ tribocouples under standard conditions at RT, material is transferred from the TaAg11 surface to Al₂O₃, and a smooth transfer film – a lubricious mixture, LM – composed of tribooxides and Ag is formed at the interface (Fig. 91c1 and Eq. 6.2 in Ch.6). Low WRs ($\sim 2 \times 10^{-5}$ mm³/N-m), and μ 's of ~ 0.4 are observed (Table 8).
- During dry sliding of TaAg11, CrAg11 or TaAgR-Inc718 tribocouples at RT under 8N and higher loads, LM's are also formed on the tribo-surfaces mainly by tribo-oxidation of MAX/Ag (Fig.91a2). These LM's are responsible for low μ 's ~ 0.3 . The WRs of the TaAg composites varied between $\sim 10^{-4}$ - 10^{-5} mm³/N-m (Table 10).
- During dry sliding of TaAgR-Inc718 against sandblasted or FeCl₃ etched Inc718, LM's are formed on the tribo-surfaces mainly by abrasion of the TaAgR surfaces by the roughened Inc718 surfaces, and consequently the tribo-oxidation of the

TaAgR. These LM's are responsible for $\mu \sim 0.5 - 0.6$ in these tribocouples; the WRs of TaAgR was $\sim 10^{-5}$ (Table 10). Clearly the presence of Ag renders the Ta-Al oxide lubricious.

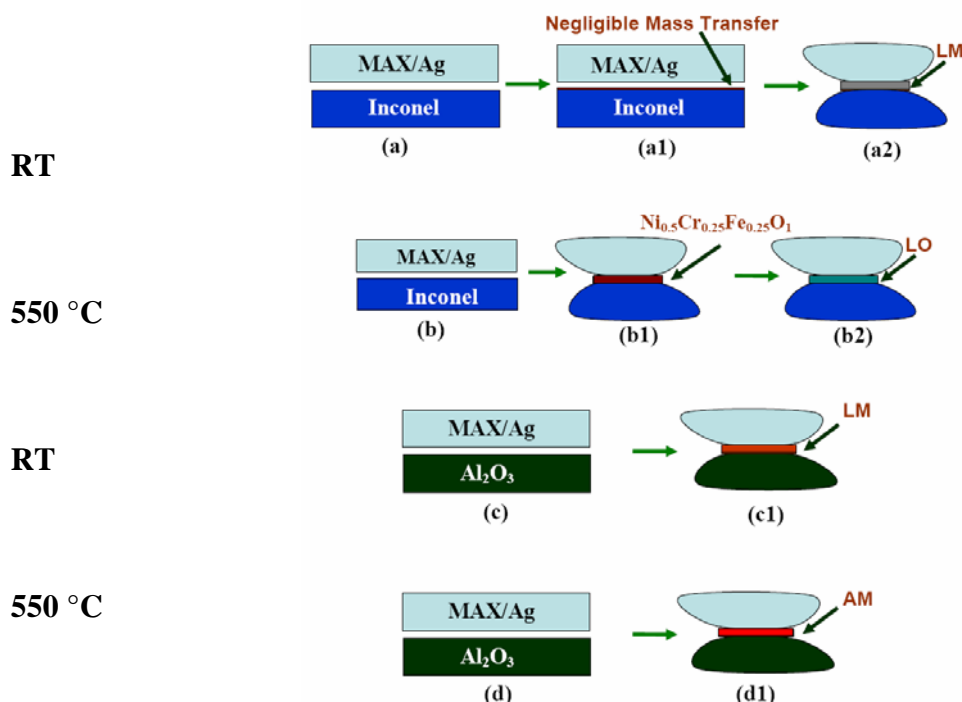


Figure 91: Schematic presentation of tribo-interaction of MAX/Ag against different tribo-partners: (a) and (a1) MAX/Ag-Inc718 tribocouples before and after dry sliding experiment at RT under standard conditions, (a2) MAX-Inc718 tribocouples after dry sliding experiment at RT and 8N load, (b) and (b2) MAX/Ag-Inc718 tribocouples before and after dry sliding experiment Inc718 at 550 °C under standard conditions, (b2) MAX-Inc718 tribocouples after dry sliding experiment at 550 °C and 8N load, (c) and (c1) MAX/Ag-alumina tribocouples before and after dry sliding experiment at RT under standard conditions, and, (d) and (d1) MAX/Ag-alumina tribocouples before and after dry sliding experiment at 550 °C under standard conditions.

8.2.2.3 Tribofilm VI

During dry sliding of TaAg11-Inc718 and CrAg11-Inc718 tribocouples under standard conditions at 550 °C, essentially the *tribo-oxidation of the Inc718 surfaces*

results in the formation of the LO ($\text{Ni}_{0.5}\text{Cr}_{0.25}\text{Fe}_{0.25}\text{O}$) at the tribocontact areas. It is because of the formation of this tribo-oxides that the WRs $\sim 10^{-4} \text{ mm}^3/\text{N}\cdot\text{m}$ are observed on Inc718 surfaces, and since these oxides are acting as LO, the WRs of the MAX phases are lower $< 10^{-5} \text{ mm}^3/\text{N}\cdot\text{m}$ (Table 8 and Fig. 91b1). Philosophically, tribofilm-VI is similar to tribofilm-II. However, the constitution of tribofilms-VI is more complex as compared to tribofilm-II. Owing to the interaction between Inc718 particles and TaAg11 matrix, Ta_2C -rich sublayers are developed beneath the LO (*Triboreaction 6.4* in Ch.6). In other words, the tribolayer is multilayered.

8.2.2.3 Tribofilm VII

- During thermal cycling of TaAg11-Inc718 tribocouples under standard conditions in the ambient to 550 °C temperature, *tribo-oxidation of the Inc718 (tribo-reaction 6.3) and TaAg11 (tribo-reaction 6.2) surfaces* results in the formation of LO at the tribocontact areas (Fig. 91b2). It is because of the formation of these tribo-oxides that WRs $\sim 10^{-4} \text{ mm}^3/\text{N}\cdot\text{m}$ are observed on the Inc718 surfaces. Since these oxides are lubricious, the WR's of of the MAX phases are low ($\leq 10^{-5} \text{ mm}^3/\text{N}\cdot\text{m}$) (Table 8 and Fig. 91b2). Moreover, these tribo-oxides maintain their lubricious nature over a wide temperature range continuously.
- During dry sliding of TaAgR-Inc718 tribocouples at 550 °C, and 8N loads, *tribo-oxidation of Inc718 (tribo-reaction 6.3) and TaAg11 (tribo-reaction 6.2) surfaces* results in the formation of a LO (eg. AE and AF in Table 11) at the tribocontact areas (Fig. 91b2). When these tribofilms were cycled at RT, the lowest $\mu \leq 0.15$, and $\text{WR} \leq 10^{-6} \text{ mm}^3/\text{N}\cdot\text{m}$ were observed during the course of this work.

- During rig testing of TaAg11-Inc718 tribocouples, *tribo-oxidation of Inc718 (tribo-reaction 6.3) and TaAg11 (tribo-reaction 6.2) surfaces* results in the formation of a LO (eg. FF1 and FF2 in Fig. 63) at the tribocontact areas (Fig. 91b2). It resulted in negligible WR of TaAgR surfaces, and roughening of SA surfaces, $R_a \sim 0.4 \mu\text{m}$ (Ch.5).
- During rig testing of CrAg11-Inc718 tribocouples, tribo-oxidation of both the surfaces result in formation of LO on SA surfaces (Fig. 66). SA surface was intentionally roughened to increase the tribofilm formation. It resulted in formation of powdery tribofilm (Inset of Fig. 66).

8.2.2.4 Tribofilm VIII

During dry sliding of the TaAg11- Al_2O_3 tribocouples, under standard conditions, at 550 °C, material is transferred from the TaAg11 surface to Al_2O_3 , and a transfer film – composed of tribooxides and most probably Ag are formed at the interface (Fig. 84d1 and *tribo-reaction 6.2*). Due to high tribo-contact temperature, the tribo-oxides separate into Ag-rich, and Ta-Al-based oxide rich regions (e.g. S and T in Fig. 60b). This results in WR's that are higher ($\sim 10^{-4} \text{ mm}^3/\text{N}\cdot\text{m}$) than observed in RT in similar tribocouple, $\mu_s < 0.5$. Philosophically, this kind of transfer film can be referred to as AM (abrasive mixture).

8.3 Philosophy of forming tribofilms

Based on studies done in Chs. 5 -7 - the conditions required for generating a tribofilm can be summarized as follows (Fig. 85).

- **Processing** – CrAg11, TaAg11, CrAg11 and TaAgR were studied against SA's in detail. The TaAg11 and CrAg11 were prepared by liquid phase

sintering. The TaAg11 and CrAg11 samples were prepared by reactive HIPing in glass, and the TaAgR by reactive HIPing in steel cans, at the same temperature. But apparently, subtle change in processing conditions influenced the tribological behavior. For application in oil free engines, dense samples are needed since porous samples cannot tolerate high rotation speeds (Ch. 4).

- **Substrates** – Substrates like Inc718, that provide the Ni, Cr and Fe atoms needed for the formation of LOs, work best against MAX/Ag based composites (Ch.6).
- **Surface** – The adherence of tribofilms on the Inc718 surfaces can be increased by controllably roughening the Inc718 surfaces by sandblasting or etching. This conclusion was proved during testing of CrAg11 against SA (chemically etched) during rig tests (Ch.5).
- **Temperature** – Tribofilms formed at high temperature are better in reducing the WR's during cyclic conditions than those formed at RT (Ch.7).

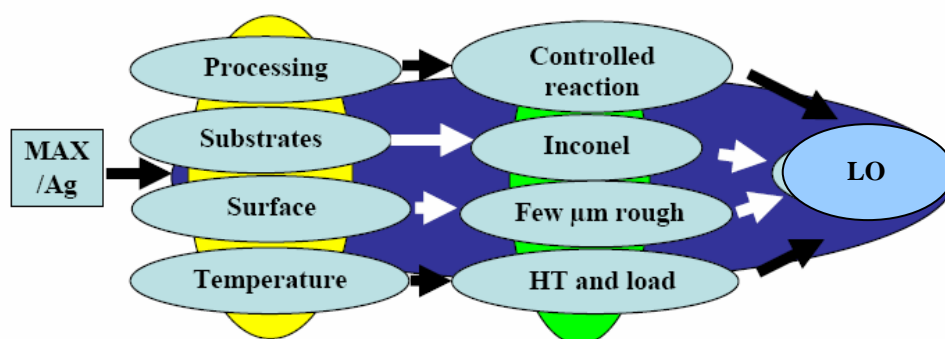


Figure 92: Schematic presentation showing different parameters required for forming LO's during tribochemical interaction of MAX/Ag composites against Inconel.

Based on these conclusions, some of the important characteristics of an excellent tribofilm that can be used over a wide temperature range are:

1. Composed of tribooxides from TaAg11 or CrAg11 and SA surfaces.
2. Tribofilm should be able to cover the Inc718 surfaces uniformly.
3. Well adhered tribofilms on both the tribosurfaces.

Based on these parameters, the best tribofilm observed during this study is summarized in section 8.2.2.3. It is classified as tribofilms VII.

CHAPTER 9-CONCLUSIONS AND FUTURE WORK

9.1 Conclusions

- At room temperature, the tribological behavior of the MAX phases is characterized by high wear rate ($\geq 10^{-4}$ mm³/N-m) and friction coefficients (> 0.4) at room temperature against Al₂O₃ and Inc718. Third body abrasion is believed to be responsible for this behavior.
- At 550 °C, in MAX–Inc718 tribocouples, tribo-oxidation of Inc718 causes formation of Ni_{0.5}Fe_{0.25}Cr_{0.25}O_x (LO). The formation of this LO at the tribo-contacts is believed to be responsible for the ultra low wear rates of the MAX phases ($< 10^{-6}$ mm³/N-m) and slightly higher WR's of the Inc718 surfaces ($\sim 10^{-5}$ mm³/N-m).
- At 550 °C, in Ta₂AlC–Al₂O₃ tribocouples, tribo-oxidation of Ta₂AlC results in the formation of Ta₂AlO_{6+x} ($x \leq 0.5$) at the tribo-contacts. The formation of these tribo-oxides is responsible for low WRs ($< 10^{-6}$ mm³/N-m) but high μ 's (~ 0.9). There is thus a fundamental difference in the tribological behavior of Ni_{0.5}Fe_{0.25}Cr_{0.25}O_x versus Ta₂AlO_{6+x}.
- During the tribological study of TaAg11–Inc718 tribocouples under standard conditions at RT, the presence of Ag₂Al as the cementing phase in the grain boundaries prevents the formation of abrasive third bodies. As a result, the WR of the TaAg11 pin was reduced by 3 orders of magnitude (Table 8) as compared to pure Ta₂AlC.

- During tribological study of TaAg11-alumina tribocouples under standard conditions at RT, LMs are formed by tribo-oxidation of the TaAg11 surfaces (Eq. 6.3). This tribolayer is responsible for lowering of the WRs and μ 's as compared to pure Ta₂AlC-Inc718 tribocouples (Table 8).
- At 550 °C, the TaAg11–Inc718, and CrAg11-Inc718 tribocouples formed a LO according to reaction in 6.3 by the tribo-oxidation of the Inc718. The presence of this layer is responsible for the relatively high WR ($\sim 10^{-4}$ mm³/N-m), and μ 's ~ 0.5 . The exact role of the carbide-rich sublayer is not clear, most possibly, it forms a semi-continuous hard substrate on which lubricating tribooxide (LO's) can be sheared easily.
- During continuous thermocycling operation, the TaAg11–Inc718 the tribocouples maintained their intrinsic self-lubricating property. The observed μ 's ≤ 0.5 and WR $\sim 10^{-4}$ mm³/N-m are observed. The tribolayer was composed of Ni_{0.5}Cr_{0.25}Fe_{0.25}O_x formed by tribo-oxidation of Inc718 (see eq 6.3), and tribo-oxidized TaAg11 particles (see eq. 6.2). The exact role of the carbide-rich sublayer not clear, most possibly, it forms a semi-continuous hard substrate on which lubricating tribooxide (LO's) can be sheared easily.
- The TaAgR samples were successfully tested under rig conditions for 10,000 cycles in the temperature range of 26 to 550 °C. The average surface roughness of TaAgR remained unchanged ~ 0.2 μ m, the average roughness of tribocontact areas on SA surface increased to 0.4 μ m. Similarly, CrAg11 surface appeared smooth, and the average roughness of tribocontact areas on SA surface was 1 μ m. Generally, for load bearing studies for applications in oil free turbo-engines,

surface finishes of 0.05 – 0.2 μm are considered best [16]. The thickness of the air thin film that separates the top foil and shaft is $\sim 5 \mu\text{m}$ [16]. Based on these parameters, TaAg11 and CrAg11–SA tribocouples may be ideal candidates for load bearing studies in turbomachinery for oil free turbo-engines.

- During rig testing of TaAgR against SA's - the tribolayer was composed of $\text{Ni}_{0.5}\text{Cr}_{0.25}\text{Fe}_{0.25}\text{O}_x$ formed by tribo-oxidation of Inc718 (Eq 6.3), and tribooxidized TaAg11 surfaces (Eq. 6.2). The formation of these lubricating tribo-oxides is responsible for the negligible WR of the TaAg11 surfaces, and the small amount of wear of the SA surfaces.
- During rig testing of CrAg11 against SA's – the roughening of the SA surfaces resulted in powdered tribofilms composed of tribo-oxides from both the surfaces. The tribo-couple successfully passed the rig testing.
- During tribological study of TaAg11-alumina tribocouples at 550 °C, tribo-oxidation of TaAg11 surfaces results in formation of AM's on the tribo-surfaces. Most probably due to high contact temperatures, the tribo-oxides separate into Ag-rich, and Ta-Al based oxide rich regions. It results in $\text{WR} \sim 10^{-4} \text{ mm}^3/\text{N}\cdot\text{m}$ and $\mu_s < 0.5$.
- Increasing in load from 3 to 18 N decreased μ from 0.9 to ≤ 0.3 at RT at 1 m/s sliding speed because of intensification of the tribofilm formation. It resulted in the formation of LM from TaAgR surfaces. The LM's formed were highly shearable. Most probably the presence of Ag as a microconstituent is responsible for this behavior. Increasing the surface roughness of the Inc718 also lowers μ

from 0.9 to ≤ 0.5 presumably for the same reasons. Refer to Fig. 91 for the schematic understanding of formation of tribofilms under these conditions.

- At 550 °C, the μ 's were slightly increased as the load was increased from 3 to 18 N. Thus it can be inferred that LO formed not as shearable as the LM formed at RT.
- It was further shown the tribofilms generated at higher loads (≥ 8 N) were composed of tribo-oxidized product formed from both the surfaces. Moreover, these tribofilms operate better than tribofilms formed at RT. Interestingly, tribofilms formation at 550 °C can be accelerated by roughening the surfaces (viz. method – 3).
- Finally based on these results, a classification of tribofilms has been developed.

9.2 Future work

- The controlled effect of second phases like, carbides and intermetallics on the tribological behavior of pure MAX phases against different SA and ceramic based substrates need to be explored.
- The effect of grain size on the tribological behavior of the MAX phases against different SAs and ceramic-based substrates needs to be understood.
- The effect of moisture on the tribological behavior of the MAX phases against different SA and ceramic-based substrates needs to be understood. Also the effect of moisture on the properties of the tribofilms.
- More studies are needed to understand the influence of addition of metals like Au, Ni, and Co on the tribological behavior of MAX phases against different SA and ceramic-based substrates.

- Further characterization of the tribofilms by nanoindentation, Raman and TEM can provide insight on the constitution of the tribofilms.
- During this thesis, TaAg11 and TaAgR composites were tested exhaustively against Inc718. Further studies are needed on the tribological behavior of Cr and Ti-based MAX phases with Ag as additives.

LIST OF REFERENCES

1. S. Korcek, J. Sorab, M. D. Johnson and R. K. Jensen, *Industrial Lubrication and Tribology*, 52, 5, 209 (2000).
2. C. Dellacorte and M. J. Valco, *Proc. of the ISABE Conference, ISABE-2003-* 1182 (2003).
3. W. Bathie, *Fundamental of Gas Turbines*, John Wiley & Sons (1996).
4. <http://www.grc.nasa.gov/WWW/K-12/airplane/Animation/turbpar/enex.html>.
5. FAG Kugelfischer, Georg Schafer, KGaA Schweinfurt, *Rolling Bearing and their Contribution to the Progress of Technology*, Lewis Books (1986).
6. *Gas Lubricated Bearings*, Eds. N. S. Grassam, and J. W. Powell (1964).
7. *Gas Film Lubrication*, W. A. Gross, John Wiley & Sons (1962).
8. C. Dellacorte and M. J. Valco, *Trib. Trans.* **43**, 4, 795-801 (2000).
9. *Advanced Foil Bearing Program*, www.grc.nasa.gov/WWW/Oilfree/bearings.htm.
10. G. L. Agrawal, *Mech. Eng.* **120**, 7, 78-80 (1998).
11. C. -P. R. Ku and H. Heshmat, *ASME J. Trib.* **114**, 394-400 (1992).
12. H. Heshmat, *ASME J. Trib.* **116**, 287-295 (1993).
13. M. Salehi and H. Heshmat, *Trib. Trans.* **43**, 2, 318-324 (2000).
14. M. Salehi and H. Heshmat, *Trib. Trans.* **44**, 3, 458-464 (2001).
15. Personal communications with Dr. Dellacorte.
16. K. C. Radil and C. Dellacorte, *Trib. Trans.* **45**, 199-204 (2002).
17. H. Termuehlen, *100 years of power plant development*, ASME Press, New York (2001).

18. Gas turbines for autos and trucks (selected papers through 1980), Prog. Tech. Series, Soc. Aut. Eng. Inc (1980).
19. H. Heshmat, P. Hryniewicz, J. F. Walton, J. P. Willis, S. Jahanmir, and C. Dellacorte, Trib. Intern. **38**, 1059-1075 (2005).
20. B. Bhushan and B.K.Gupta, Chapter 5, Handbook of Tribology (Materials, Coatings, and Surface Treatments), Kreiger Publishing Company (1997).
21. A. Erdemir, Chapter-22, Modern Tribology Handbook, CRC Press LLC (2003).
22. H. E. Sliney, Trib. Intern. **15**, 303-315 (1982).
23. R. S. Gates, S. M. Hsu and E. E. Klaus, Trib. Trans. **32**, 3, 357-363 (1989).
24. T. E. Fisher and H. Tomizawa, Wear, **105**, 29-45 (1985).
25. M. Woydt, Chapter -4, Surface Modifications and Mechanisms, 59-79, Marcel Dekker (2003).
26. A. Skopp and M. Woydt, Tribol. Trans. **38**, 233-242 (1995).
27. M. Woydt, A. Skopp, I. Dorfel and K. Witke, Tribol. Trans. **42**, 21-31 (1999).
28. W. Woydt, Tribol. Letts. **8**, 117-129 (2000).
29. M. B. Peterson, S. J. Calabrese, S. LI, and X. Jiang, J. Mater. Sci. Techno., **10**, 313 – 320 (1994).
30. Nicholas J. Barnick, Thierry A. Blanchet, W. Gregory Sawyer and James E. Gardner, Wear, **214**, 1, 131-138 (1998).
31. M. B. Peterson, S. F. Murray and J. J. Florek, ASLE Trans., 2, 225-233 (1960).
32. H. E. Sliney, ASLE Trans., **29**, 3, 370-376 (1986).
33. B. Bhusan, Wear. **75**, 333-356 (1982).
34. C. Dellacorte, Surf. Coat. Technol. **86-87**, 486-492 (1996).

35. C. Dellacorte and J. A. Fellenstein, Trib. Trans. **40**, 639-642 (1997).
36. C. Dellacorte, Trib. Trans. **43**, 257-262 (2000).
37. T. A. Blanchet, J. Kim, S. J. Calabrese and C. Dellacorte, Trib. Trans. **45**, 4, 491-498 (2002).
38. Personal communication with Keith Hurley.
39. M. W. Barsoum and M. Radovic, in *Encyclopedia of Materials Science and Technology*, edited by R. W. C. K. H. J. Buschow, M. C. Flemings, E. J. Kramer, S. Mahajan and P. Veysiere (Elsevier, Amsterdam, 2004).
40. M. W. Barsoum and T. El-Raghy, J. Amer. Cer. Soc. **79**, 1953-56 (1996).
41. M. W. Barsoum, Prog. Solid State Chem **28**, 201-281 (2000).
42. M. Radovic, M. W. Barsoum, T. El-Raghy, S. M. Wiederhorn, and W. E. Luecke, Acts Materialia **50**, 1297-1306 (2002).
43. M. Radovic, M. W. Barsoum, T. El-Raghy, and S. M. Wiederhorn, J. Alloys and Compds. **361**, 299-312 (2003).
44. T. El-Raghy, M. W. Barsoum, a. Zavaliangos, and S. R. Kalidindi, J. Amer. Cer. Soc. **82**, 2855-2860 (1999).
45. T. Zhen, M. W. Barsoum, S. R. Kalidindi, M. Radovic, Z. M. Sun, and T. El-Raghy, Acta Mater. **53**, 4963-4973 (2005).
46. T. Zhen, M. W. Barsoum, and S. R. Kalidindi, Acta Mater. **53**, 4163-4171 (2005).
47. S. Myhra, J.W.B. Summers and E.H. Kisi, Mater. Lett. **39**, 6 (1999).
48. T. El-Raghy, P. Blau and M.W.Barsoum, Wear **238(2)** (2000).
49. Z. M. Sun, Y.C. Zhou and S. Li, J. Mat. Sci. Tech. **18(2)**, 142-145 (2002).
50. Y. Zhang, G. P. Ding, Y. C. Zhou and B. C. Cai, Mat. Letts. **55**, 285-289 (2002).

51. H. Z. Zhai, Z.Y. Huang, Y. Zhou, Z. L. Zhang, Y. Wang & M. Al, *J. Mat. Sci.* **39** (21) 6635-6637 (2004).
52. A. Souchet, J. Fontaine, M. Belin, T. Le Mogne, J.-L. Loubet and M.W. Barsoum, *Tribo. Letts.*, **18**, 341-352 (2005).
53. D. Sarkar, B. Basu, S. J. Cho, M. C. Chu, S. S. Huang and S. W. Park, *J. Amer. Cer. Soc.* **88** (11), 3245-3248 (2005).
54. Z. Hongxiang, H. Zhenying, A. Zingxing, Z. Yang, Z. Zhilli and L. Shibo, *J. Amer. Cer. Soc.* **88** (11), 3270-3274 (2005).
55. T. Palanisamy, S. Gupta, M. W. Barsoum, and C. W. Li, US Patent (Pending).
56. S. Gupta, T. Palanisamy M. W. Barsoum, and C. W. Li, US Patent (Pending).
57. S. Gupta and M. W. Barsoum, *J. Electrochem. Soc.*, 151 [2] D24-D29. (2004)
58. X. H. Wang, Y. C. Zhou, *J. Mater. Chem.* 12 [9] 2781–2785 (2002).
59. M.W. Barsoum, *J. Electrochem. Soc.*, 148 [8] C544-C550 (2001).
60. M. W. Barsoum, N. Tzenov, A. Procopio, T. El-Raghy, M. Ali, *J. Electrochem. Soc.*, 148 [8] C551-C562 (2001).
61. I. Salama, T. El-Raghy, M. W. Barsoum, *J. Electrochem. Soc.*, 150 [3] C152-C158 (2003).
62. M. Desmaison-Brut, N. Alexandre, J. Desmaison, *J. Europ. Ceram. Soc.*, 17 [11] 1325-1334 (1997).
63. P. Kofstad, *High Temperature Corrosion*, p. 309, Elsevier Applied Science Pub. Co., NY, 1988.
64. S. Wu, H. M. Chan, M. P. Harmer, *J. Am. Ceram. Soc.*, 88 [11] 2369–2373 (2005).

65. S. Maeng, L. Axe, T. Tyson, A. Jiang, *J. Electrochem. Soc.*, 152 [2] B60-B64 (2005).
66. V. B. Voltovich, V. A. Lavrenko, V. M. Adejev, E. I. Golovko, *Oxid. Met.*, 43 [5-6] 509-526 (1995).
67. R. Chandrasekharan, I. Park, R. I. Masel, M. A. Shannon, *J. App. Phys*, 98 [11] 114908 (2005).
68. S. Chakraborty, T. El-Raghy, M.W. Barsoum, *Oxid. Met.*, 59 [1-2] 83-96 (2003).
69. M. W. Barsoum, L. H. Ho-Duc, M. Radovic, T. El-Raghy, *J. Electrochem. Soc*, 150 [11] B166-B175 (2003).
70. Y. S. Touloukian, R. K. Kirby, R. E. Taylor and T. Y. R. Lee, *Thermal Expansion, Nonmetallic Solids*, IFI/Plenum Press, NY, 1977.
71. Q. Yang, T. Senda, N. Kotani and A. Hirose, *Surf. Coats. Tech.* **184**, 270-277 (2004).
72. T. El-Raghy, S. Chakraborty, and M. W. Barsoum, *J. Eur. Cer. Soc.* **20**, 2619 (2000).
73. A. T. Procopio, M.W.Barsoum and T. El-Raghy, *Metall. Mater. Trans. A* **31A**, 333-337 (2000).
74. Z. M. Sun, S. Gupta, H. Ye and M. W. Barsoum, *J. Mater. Res.* **20**, 2618-2621 (2005).
75. M. Godet, *Wear*, **100**, 437-452 (1984).
76. T. F. J. Quinn, *Wear*, **18**, 413-419 (1971).
77. T. F. J. Quinn, *Tribol. Inten.* **16**, 257-271 (1983).

78. S. C. Lim and M. F. Ashby, *Acta. Metall.* **35**, 1-24 (1987).
79. F. H. Scott, *New Direction in Tribology, Planery and Invited papers from the first World Tribology Congress, London*. Ed. I. Hutchings, 391-401.
80. A. Tanaka, *Proceedings of Japan International Tribology Conference, Nagoya*, 1339-1344 (1990).
81. S. A. Howard, *Trib. Trans.* **42**, 174 - 179 (1999).

APPENDIX A

- **Calculation of WR of Inc718 tested against MAX tribocouples:**

Gouges in the Inc718 substrates were observed in localized regions on the wear track. If one assumes, the average gouge is of uniform depth that is $\sim 0.5 \mu\text{m}$ (Fig 23) throughout the tested wear track then the volume of worn material is 0.018 mm^3 on a 36 mm^2 area in the track. The normal load is 3 N , using r_{mean} (mean radius of track) $\sim 10 \text{ mm}$ for Ta_2AlC or r_{mean} (mean radius of track) $\sim 12 \text{ mm}$ for Cr_2AlC , 6 mm sample length, and using the formula written below, it can be shown, the WR of the Inc718 is $\sim 10^{-5} \text{ mm}^3/\text{N}\cdot\text{m}$.

$$\text{WR} = [0.018 / \{3 \times (2000 / 2 \times 3.14 \times r_{\text{mean}}) \times 6\}] \text{-----}(\text{A1.1})$$

- **TaAg11 sliding against Inc718 at 550 °C:**

Assuming a $2 \mu\text{m}$ uniform gouge throughout the track diameter (Fig. 47), and using similar assumptions used above after a 2 km sliding distance, 3 N , $r_{\text{mean}} = 18 \text{ mm}$, and 6 mm length of sample;

$$\text{WR} = [2 \times 10^{-6} \times 36 \times 10^3 / \{3 \times (2000/2\pi \times 18) \times 6\}] = 2 \times 10^{-4} \text{ mm}^3/\text{N}\cdot\text{m}\text{--}(\text{A1.2})$$

- **TaAg11 sliding against Inc718 during thermal cycling:**

- (a) **After 3 km dry sliding:**

Assuming, conservatively, that a $6 \mu\text{m}$ uniform gouge throughout the track diameter after 3 km sliding distance, 3 N load, $r_{\text{mean}} = 10 \text{ mm}$, and 6 mm length (Fig. 50) then,

$$\text{WR} = [6 \times 10^{-6} \times 36 \times 10^3 / \{3 \times (3000/2\pi \times 10) \times 6\}] = 2 \times 10^{-4} \text{ mm}^3/\text{N}\cdot\text{m}\text{--}(\text{A1.3})$$

(b) After 11 km dry sliding:

Assuming, conservatively, that a 6 μm uniform gouge exists throughout the track diameter after 3 km sliding distance, 3N load, $r_{\text{mean}} = 10$ mm, and 6 mm length (Fig. 50) then,

$$WR = [6 \times 10^{-6} \times 36 \times 10^3 / \{3 \times (11000/2\pi \times 10) \times 6\}] = 6.5 \times 10^{-5} \text{ mm}^3/\text{N-m} \quad (\text{A1.4})$$

Similar calculation were used for calculating WR of CrAg11 against Inc718 during thermal cycling.

APPENDIX B1: EDS analysis of different “micro-constituents” formed during tribology study of MAX/Ag composites against SA’s.

Reg	O	Al	Ta	Ag	Nb	Cr	Fe	Ni	*Averaged Composition*
H1	18±5	11±5	23	12±5	x	6±5	4±1	20±1	[Ta _{0.3} Al _{0.15} Ag _{0.15} Ni _{0.25} Cr _{0.08} Fe _{0.07}]O _(0.2)
H2	7	21	14	36		1	2	12	[Ta _{0.15} Al _{0.25} Ag _{0.4} Ni _{0.2}]O _{0.1}
J1	12±1	1.5±1	1	1		17±2	15±2	49±2	[Ta _{0.025} Al _{0.01} Ag _{0.01} Ni _{0.55} Cr _{0.2} Fe _{0.2}]O _(0.2)
J2	31±22	3±1	5	2.5±0.5		12±5.5	11±5.5	31±14	[Ta _{0.1} Al _{0.05} Ag _{0.05} Ni _{0.4} Cr _{0.2} Fe _{0.2}]O _{0.45}
L	52±8	7.5±1	5±1	5±1	x	8±1	7±1	16±1	[Ta _{0.07} Al _{0.15} Ag _{0.08} Ni _{0.3} Cr _{0.2} Fe _{0.2}]O ₁
M	43±3	17±1	6.75±1	4.5±1	1	6±1	7±1	15±1	[Ta _{0.1} Al _{0.3} Ag _{0.1} Ni _{0.3} Fe _{0.1} Cr _{0.1}]O _{0.7}
N	52±1	2.5±1	3	x		9	8±1	23±1	[Ta _{0.05} Al _{0.05} Ni _{0.5} Cr _{0.2} Fe _{0.2}]O ₁
R	50±4	6.25±1	10	6.25±1		5±1	5±1	12.5±1	[Ta _{0.3} Al _{0.125} Ag _{0.125} Ni _{0.25} Cr _{0.1} Fe _{0.1}]O ₁
LA	41±1.5	16	x	2.5±0.5		28±2	2	10.5±0.5	[Al _{0.2} Ag _{0.125} Ni _{0.175} Cr _{0.5}]O _{0.66}
LB	33	25	x	13	x	22	2	5	[Fe _{0.05} Al _{0.4} Ag _{0.2} Ni _{0.05} Cr _{0.3}]O _{0.66}
LC	50±3	5±2	x	2±2		12±2	10±3	18±3	[Ag _{0.05} Al _{0.1} Ni _{0.4} Cr _{0.25} Fe _{0.2}]O ₁
W	27±10	13±4	28	13.5±2		2	6	2	[Ta _{0.45} Al _{0.2} Ag _{0.25} Ni _{0.05} Cr _{0.025} Fe _{0.025}]O _{0.4}
X	51±3	6.5	10	4		5	9	12±1	[Ta _{0.2} Al _{0.15} Ag _{0.1} Ni _{0.25} Cr _{0.1} Fe _{0.2}]O ₁
Y	16	0	0	0	1	20	18	45	[Ni _{0.5} Cr _{0.3} Fe _{0.2}]O _{0.2}
Z1	49±3	9	14	5±1	x	3±1	4±1	9±1	[Ta _{0.3} Al _{0.2} Ag _{0.1} Ni _{0.2} Cr _{0.1} Fe _{0.1}]O ₁
Z2	35±10	1	1	2		13±2	13±2	33±2	[Ta _{0.025} Al _{0.025} Ag _{0.05} Ni _{0.5} Cr _{0.2} Fe _{0.2}]O _{0.55}
FF1	22±7	13±0.5	34±0.5	8±3		2±0.5	3±1	3±2.5	[Ta _{0.5} Al _{0.2} Ag _{0.1} Ni _{0.05} Cr _{0.03} Fe _{0.05}]O _{0.3}
FF2	39±2	16±2	19±3	4.5±1		2±0.5	2.4±0.5	9±0.5	[Ta _{0.4} Al _{0.3} Ag _{0.1} Ni _{0.2}]O _{0.7}
GG1	16.5±1	1.6	1	1		14.5±0.5	8	55±1.5	[Ni _{0.7} Cr _{0.2} Fe _{0.1}]O _{0.2}
GG2	34±4	5±1	4.5±2	2±1		11±1	6±1	34±4	[Ta _{0.05} Al _{0.1} Ni _{0.55} Cr _{0.2} Fe _{0.1}]O _{0.55}
HH1	19	31	x	x		50	x	x	[Cr _{0.6} Al _{0.4}]O _{0.25}
HH2	25	26	x	48		x	x	x	[Ag _{0.65} Al _{0.35}]O _{0.35}
KK	36±12	8±2	x	4±2.5	x	19±6	4±1	29±19	[Ag _{0.075} Al _{0.1} Ni _{0.45} Cr _{0.3} Fe _{0.075}]O _{0.6}
RR1	33	3	8	0		13	13	30	[Ta _{0.12} Al _{0.04} Ni _{0.44} Cr _{0.2} Fe _{0.2}]O _{0.5}
RR2	33	10	22	10		6	4	10	[Ta _{0.3} Al _{0.15} Ag _{0.15} Ni _{0.15} Cr _{0.08} Fe _{0.08}]O _{0.5}
SS1	20	2	56	10		4	6	10	[Ta _{0.6} Al _{0.03} Ag _{0.12} Ni _{0.12} Cr _{0.06} Fe _{0.05}]O _{0.2}
SS2	40	24	2	1		8	8	18	[Ta _{0.04} Al _{0.4} Ag _{0.01} Ni _{0.3} Cr _{0.13} Fe _{0.14}]O _{0.8}
SS3	25	8	41	8		4.5	4.5	9	[Ta _{0.6} Al _{0.12} Ag _{0.1} Ni _{0.15} Cr _{0.07} Fe _{0.07}]O _{0.3}

APPENDIX B2: EDS analysis of different “micro-constituents” formed during tribology study of MAX/Ag composites against alumina.

Reg	O	Al	Ta	Ag	*Averaged Composition*
K	58±1	12±1	16	8±1.3	[Ta _{0.45} Al _{0.35} Ag _{0.3}]O _{1.6}
S	33±4	8±0.1	11	48±13	[Ta _{0.2} Al _{0.1} Ag _{0.7}]O _{0.5}
T	51±3	10±1	16	17±4	[Ta _{0.45} Al _{0.2} Ag _{0.35}]O ₁
U	25±2	20±2	32	12±1	[Ta _{0.5} Al _{0.3} Ag _{0.2}]O _{0.3}
V	17±6	26±0.5	14	37±9	[Ta _{0.2} Al _{0.35} Ag _{0.45}]O _{0.2}

VITA

Name: Surojit Gupta

Education:

- PhD in Materials Science and Engineering, Drexel University, Philadelphia, PA-19104.
- B. Sc (Tech) in Ceramic Science and Technology from University of Calcutta.

Professional Experience:

- 2001-2005 – Research Fellow, Drexel University, Department of Materials Science and Engineering.
- 2003-2005 – Visiting Researcher in Honeywell International, Morristown, NJ.

Activities:

- **Co-Chair** for the session; *Adsorption/Desorption Phenomenon and Frictional Performance*, 29th International Conference on Advanced Ceramics and Composites, Cocoa Beach, January 23-28, 2005 (Invited).
- Member of DAT (Disaster Action Team) for *American Red Cross*.
- Featured article in the “Physics Update” section of the February 2005 issue of *Physics Today*.
- Student member of ASME, MRS and Materials Advantage [Joint member of ASM, ACERS and TSM].

Publications and Patents:

- 15 papers in archival journals (published or under print), proceedings and confidential reports.
- 5 papers on tribology to be submitted.
- Two patents in the highly competitive field of solid state lubrication (pending).

Conferences and Presentations:

- Conference presentations in various international conferences on Material Science and Engineering.